Micro-scale Studies on Hydrodynamics and Mass Transfer of Dense Carbon Dioxide Segments in Water

by

Ning Qin

A thesis
presented to the University of Waterloo
in fulfillment of the
thesis requirement for the degree of
Doctor of Philosophy
in
Mechanical and Mechatronics Engineering

Waterloo, Ontario, Canada, 2017

Author's Declaration

I hereby declare that I am the sole author of this thesis. This is a true copy of the thesis, including any required final revisions, as accepted by my examiners.

I understand that my thesis may be made electronically available to the public.

Examining Committee Membership

The following served on the Examining Committee for this thesis. The decision of the Examining Committee is by majority vote.

External Examiner: Dr. Baixin Chen, Senior Lecturer

          School of Engineering & Physical Sciences,
          Mechanical, Process & Energy Engineering,
          Heriot-Watt University, Edinburgh, UK

Supervisor: Prof. Carolyn Ren, Professor

          Department of Mechanical and Mechatronics Engineering,
          Faculty of Engineering,
          University of Waterloo, Canada

Internal Member: Prof. Sean Peterson, Associate Professor

          Department of Mechanical and Mechatronics Engineering,
          Faculty of Engineering,
          University of Waterloo, Canada

External Member: Prof. Yuri Leonenko, Associate Professor

          Department of Earth and Environmental Sciences,
          Faculty of Science,
          University of Waterloo, Canada

External Member: Prof. Maurice Dusseault, Professor

          Department of Earth and Environmental Sciences,
          Faculty of Science,
          University of Waterloo, Canada

Abstract

Microfluidic technologies have started to show their potential in assisting with the probes into the complicated mechanical-chemical interactions of multiphase fluids at microscale geometries (e.g., regular channels, porous media micromodels). The benefits of appropriately implementing microfluidics in such research efforts may include, but are not limited to: (1) small-dimensions facilitated analogous mechanical behaviors, (2) precise and reliable controls over relevant operating parameters of the fluids, (3) approximated reproduction of the hydrostatic or hydrodynamic circumstances, and (4) implementations of advanced visualization technologies such as microscopic imaging in order to reveal the dynamic processes involved in those multi-fluid interactions. Following the early studies on two-phase flow such as oil and water in microscale devices driven by the understanding of oil recovery process and mechanisms, carbon dioxide (CO_2) has drawn increasing attention because of their environmental impact such as greenhouse gas effects. Most studies target either enhancing the chemical reactions by using pressurized CO_2 as a solvent or revealing physical properties as well as mass transfer performance of gaseous CO_2 in common hydrodynamic scenarios. However, dense CO_2 including liquid and supercritical states are rarely touched, which is mainly due to the technical difficulties in working with extreme pressures (tens to hundreds times of atmospheric pressure) and elevated temperatures ($> 31°C$). Driven by the literature voids, this thesis presents some preliminary studies of the hydrodynamic issues and mass transfer of dense CO_2 in a form of flowing segments in microchannels.

Prior to the commencement of any experimental work concerning dense CO_2, a system capable of working at extreme pressures reliably and safely needs to be build first. Chapter 3 details the building of an experimental system which is dedicated to two phase microfluidic studies, especially for those related to extreme pressure/temperature conditions. Based on two principles of being extreme conditions durable and leakage free., a few goals, namely, reliability, flexibility and coordinability of this system are achieved.

The first part of this thesis (Chapter 4) presents an experimental study of a fluid pair, namely, liquid CO_2 and deionized (DI) water, in a micro T-junction, where liquid CO_2 and DI water are injected from the side and the main channel of the T-junction, respectively. Drop flow and co-flow are identified as two main flow regimes subjected to the various flow rate ratios applied. By focusing on the drop flow, a full period of liquid CO_2 drop generation is divided into three stages, and each

stage is meticulously described in terms of the interfacial developments (e.g., interface profile, pressures across the interface, size variations). The mass transfer mechanisms including CO_2 hydration, diffusion on a perpendicular dimension of the interface and the advection parallel to the interface are considered and discussed in terms of their effects in CO_2 molecules transport. An overall theoretical analysis of such mechanisms verifies that the transported CO_2 portion is a small quantity compared with the bulk CO_2 stream. Based on this verification, the generated liquid CO_2 drop size, speed, and the spacing development within one drop generation period are probed. A formulation of drop size with the flow rate ratio shows a magnified effect of the later factor, which is interpreted by the extended time scale of an 'elongating-squeezing' stage of the period. Drop speed results show that they can be approximated by dividing the total flow rates over the channel cross-sectional area. And the speed differences between the generated drop and the emerging one in the T-junction lead to a model which details the spacing development within one drop generation period. The model is well validated by experimental results.

The second (Chapter 5) and the third part (Chapter 6) of the thesis are devoted to the investigations of hydrodynamics and mass transfer of liquid CO_2 and $scCO_2$ drops traveling simultaneously with water in a long straight microchannel (~15mm long), respectively. The production of such CO_2 drops is realized by using the aforementioned micro T-junction. Distinctly, these studies focus on the drop size and drop speed at three specified positions of the channel and the mass transfer caused shrinkage of the CO_2 drop quantified by the decreasing drop length. In order to calculate the mass transfer coefficient of CO_2 drops, the detailed geometries of a Taylor drop in the square microchannel with a presence of wall films that separate the drop from the channel wall are considered, and consequently, the surface area and the volume of the drop are formulated based on the drop dimensions, channel geometries, contact angle and estimated film thicknesses. Furthermore, a specific mathematical model is developed to calculate the mass transfer coefficients based on the drop length reductions and drop flowing time in the channel. Discussions on these results indicate that surface-volume ratio and drop flow time are the two main factors in controlling the hydrodynamic shrinkage of the liquid CO_2 and $scCO_2$ drops. In addition, pressure declines of segmented flows in microchannels are considered and their effects are evaluated based on a pressure decline model and the Peng-Robinson equation of state (Eos) as well as the estimated initial pressures at the T-junction. Calculations of the resulted volume changes from the pressure declines show that the influences are small, and the observed CO_2 drop shrinkage is confidently attributed to the mass transfer across the interface between the CO_2 phase and water phase.

The last part (Chapter 7) presents a numerical study of the hydrodynamics of one single liquid CO_2 drop and one single $scCO_2$ drop traveling in a straight microchannel simultaneously with water as the carrier fluid. A two-dimensional (2D) computational domain of the straight microchannel is configured based on the experimental observations. Three liquid CO_2 cases and three $scCO_2$ cases are studied. It is found that the computed drop is disk-like shape encapsulated by thin films that separate the drop from the channel walls. The predicated film thicknesses agree very well with the literature. Besides, the flow domain within CO_2 drops could be mainly composed of a few vortex regions, and small vortex regions at the front and the back cap of the drop start to vanish with increased velocities. Analysis of the mechanisms causing the vortexes is provided. The interfacial CO_2 distributions of the drop show that both diffusion and local relative convection at the meniscus regions contribute to the concentration profile. Although no significant drop shrinkage is observed for typical Taylor drops, the one for the case with the highest capillary number (Ca ~ 10^{-2}) defined from its pure diffusional gradient profile showed a similar development tendency over time as its experimental counterpart in Chapter 6.

Acknowledgements

Total time of my stay at Waterloo amounts to fourteen terms (each term was four months), which is definitely a long stage in my twenty-year study career; however, it is so short when I turn back to see those joys and depressions along the way of my academic life that they seemingly took place as if yesterday. I am feeling grateful and proud to be a student in the University of Waterloo where I have learned so much from wandering across the boundaries of different disciplines and from putting my thoughts in real practices. The first of my gratefulness goes to my supervisor, Dr. Carolyn Ren, for giving me the opportunity to join her excellent lab in 2012, for encouraging me to overcome the many difficulties especially at the early stage of my PhD study, for always answering yes to my purchase requests for equipment and materials, and for her trusts on me in managing research well. My understandings of research and knowledge growth in the field will not be possible without Dr.Ren's guidance and support, which are always kept in my mind.

Also, I would like to thank my comprehensive exam and thesis committee members, Prof. Sean Peterson, Prof. Yuri Leonenko and Prof. Maurice Dusseault, for their roles in the committee and their insightful suggestions and comments. Without their contributions, a few key problems in this thesis might have been ignored. I am also grateful to Dr. Baixin Chen for being an external examiner of the thesis examining committee, and his in-person participation from Edinburgh, UK is especially appreciated.

These several years would not be so enjoyable if I have not met so many wonderful colleagues and friends. I thank my colleagues in the Waterloo Microfluidics Laboratory, including Dr. Cody Chen, Alexander Brukson, Gurkan Yesiloz, Pegah Pezeshk, Anna T. Nguyen, Sahil Kashyap, David Wong, and Matthew Courtney for helpful weekly discussions, and Dr. Chao Jin, Dr. Peng Peng, Ran Peng, Quanquan Pang from other labs for their help in my work. I thank a lot for the help on component fabrications from lab technicians including Jason Benninger, Robert Wagner and Jorge Cruz.

I am also grateful to the help from Dr. Bo Bao, Dr. Huaping Xu and Harlan Kuntz during the microchip fabrications in the University of Toronto, as well as the help from Dr. Brian Cahill, Nobu Karippai, Yingjia Li and Qilin Lian during my research internship at Heilbad Heiligenstadt, Germany.

My endless gratefulness go to my parents and my beloved Dr. Pei Zhao whose love, support and trust have been and will be throughout my life. I am enormously blessed and any of my successes is dedicated to them.

Dedication

To my parents,

my father Yúanjīng Qín and my mother Mùyún Jǐan,

for their lifelong endless love and hard work.

Table of Contents

xi

List of Figures

List of Tables

Chapter 1

Introduction

1.1 Background and Motivation

As one of the three primary greenhouse gases (carbon dioxide (CO_2), methane (CH_4), nitrous oxide (N_2O)), global CO_2 had increased rapidly from 280 ppm in pre-industrial times (before 1760) to around 405 ppm by February 2017 (see https://www.esrl.noaa.gov/gmd/ccgg/trends/global.html). partly due to anthropogenic activities [1]. The combustion of coals, natural gas and oil contributed approximately 67% of the total anthropogenic emissions [2,3]. Increasing CO_2 concentration could be detrimental to the global climate by virtue of continuous aggravation of greenhouse effects and a resulted rising mean global temperature [4,5,6]. Possible consequences may include, but are not limited to the rising of sea levels in response to glacier ablations [7], the flooding of low elevation regions [8] and damage to vulnerable ecosystems [9]. As given by [3], the average increase rate of the atmospheric CO_2 concentration was (2.0±0.1) ppm/year during 2002 to 2011 which predicts that CO_2 concentration within the next 50 years will exceed the levels set for protections of low elevation coastal regions and sensitive ecosystems [2]. Therefore, CO_2 emissions must be substantially reduced, which can be carried out from three aspects, i.e., (1) high-efficiency production and current fuels, (2) energy source shift to low- or non-carbon fuels, and (3) carbon capture and storage (CCS) [2,5,10].

Among the proposed strategies above, CCS has been considered a practical and an optimal strategy in the near or medium term for reducing CO_2 emissions [10,11,12,13]. The conception of CCS originated from the late 1970s when CO_2 was exploited for enhanced oil recovery (EOR) in the US and has been regarded as one of the most promising climate mitigation strategies since the early 2000s. As its name suggests, CCS proceeds chronologically in the sequence of capture, transport and storage (see Figure 1.1). First, CO_2 is purified and captured from the effluent gases and then compressed to a dense phase (e.g., a liquid or a supercritical state); secondly, the dense CO_2 will be transported to stringently selected storage locations through transportations (e.g., on-shore or offshore pipelines); and lastly, CO_2 is injected through the wells drilled at the storage sites and is sequestered in the storage reservoirs [5,14,15,16].

Capture & Compression ⟶ Transport ⟶ Injection & Sequestration
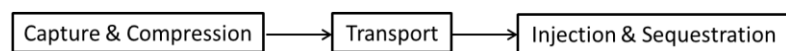
Figure 1.1 Schematic of the three main steps of carbon capture and storage (CCS).

Among the different storage strategies, such as soils [17,18], ocean [19,20], mineral carbonation [21,22,23] and geological underground storage [24-29], geological storage of CO_2 is advantageous over others considering storage capacity, environmental hazards and cost. The promising geological formation candidates for CO_2 storage mainly include: (1) active or depleted oil and gas reservoirs, (2) unminable coal beds, (3) deep aquifers, and (4) mined salt domes or rock caverns [27,30]. Deep saline aquifers (depth $\geq$ 800m) are a better option for long-term storage due to their largest storage capacities, a much larger worldwide distribution and even local availabilities. Since 1996, other than the pilot and demonstration projects carried out by a number of organisations [31-34], several benchmarking large scale commercial projects have been implemented [5,35-41], including the Chevron operated Gorgon Project where the CO_2 will be injected and stored in the Dupuy Formation that is more than 2 kilometers beneath Barrow Island in Australia [5,41].

After CO_2 is injected into the deep underground saline formations, a number of physical and geochemical mechanisms work collaboratively in guaranteeing permanent immobilizations of CO_2 over long time. These trapping mechanisms include structural trapping, capillary (residual) trapping, dissolution trapping and mineral trapping. Despite the collaboration of these four mechanisms, they may play different roles in immobilizing CO_2 over different time scales [5]. As indicated in the special report on CCS by the Intergovernmental Panel on Climate Change in 2005 [5], the trapping mechanisms and their impacts on the fluids and rocks are the primary knowledge gaps out of the eight scientific knowledge gaps in total, although there are some studies having evaluated parameters such as permeability to understand storage mechanisms [42]. Because potential CO_2 leakage is a primary concern of structural trapping, numerical simulation has been extensively employed in probing the CO_2 plume distributions as a function of multiple factors (e.g., the formation structural heterogeneity, anisotropic permeability, CO_2 dissolution in the *in situ* water, and the capillary forces within pore space) in the reservoir over up to thousands of years [43-49]. Core flooding experiments and simulations (e.g., using Tough2) have been widely used in studying the displacement process of water (or brine) by CO_2 [50], in measuring the essential parameters (e.g., relative permeability, saturation, CO_2 distribution etc.) based on x-ray computed tomography scanner (CT) and/or magnetic resonance imaging (MRI) [51,52], and in assessing the geochemical and geo-mechanical interactions between CO_2, water and solids [53,54]. Enabled by microfluidic fabrication technologies, pore-scale networks or channels etched on micromodels for modeling the characteristic porous medium or pore-throat structures have also been utilized for studying storage-related two-phase flow problems [55-62], Moreover, pore network modelling (PNM) has also been employed to investigate the wettability

2

heterogeneity effects on saturation patterns [16,63]. Besides the unique features of micromodels such as enhanced heat and mass transfer, flexible process controls and shorter operation time [42], advances in fabrication enable the production of micromodels to replicate the real reservoir conditions (extreme pressures and temperatures) and the more-alike geometrical features of the pore network.

CO_2 will become either liquid or supercritical state when stored deeper than 800 meters with a temperature higher than 31 °C. Due to its mild critical conditions (critical pressure P_c = 7.38Mpa, critical temperature T_c = 31°C) and other advantages such as non-toxic non-flammable and tunable physiochemical properties, $scCO_2$, has been widely used as solvents in various chemical reactions [64-67]. However, detailed interactions between $scCO_2$ and aqueous fluid are underexplored due to the use of macro-scale systems. Microfluidic platforms where a network of microchannels, electrodes, sensors can be integrated offer unique advantages to investigate the interactions by confining the interface and using advanced fabrication and detection technologies. This shift of research from macroscale to microscale devices is the so-called 'Lab-on-a-Chip' (LOC), which is characterised by the advantages such as faster analyses and reactions, less sample and reagent consumptions, less waste products, higher throughputs and portability. In addition, analytic techniques and control systems can also be integrated to the microscale 'laboratory', which further enables real-time monitoring of the on-chip processes, fast mass and heat transfer and prompt controls of the operation conditions. More importantly, extreme conditions (e.g., very high pressures and temperatures) can be introduced to the microreactors more reliably and securely due to the small-sizes of the devices and small quantities of the reactants, which may be, in comparison, difficult to be achieved in macroscale systems. Despite of their huge potentials, microreactors that are compatible with extreme pressures and temperatures did not incur much attention until the mid-2000s, and there are a limited number of reported cases available in literature. The pioneering work include the use of dense CO_2 for chemical reactions [68-75], for improving reaction performance [76], in assisting with nanomaterial productions [77-79], and in measuring the solubility of CO_2 in water and brine [80]. Benefiting from the advanced visualization techniques, CO_2 drop shrinkage and their mechanisms are also of great interests [81-82]. It should be noted that CO_2, particularly the gaseous CO_2, as one of the two-phase fluids has been studied extensively in the realm of microscale fluid dynamics and chemical processes over the past 12 years [83-91]. However, the dense CO_2 including liquid and supercritical CO_2 has not been studied equivalently. Besides its applications in CCS, it is also scientifically rich to investigate the hydrodynamics and mass transfer of CO_2 in microreactors with extreme temperature and pressure conditions, especially about a discrete form of the CO_2.

For this purpose, issues as listed below will be addressed in this thesis:

- an experimental system equipped with a silicon-glass microchip will be built for studies related to transient micro-processes particularly at extreme pressure and elevated temperature conditions;

- a silicon-glass microchip featured with a micro T-junction is applied to model instantaneous contacts between liquid CO_2 and water, and the potential drop flow will be specifically focused and discussed;

- liquid and supercritical CO_2 drops which are produced by the T-junction will be monitored in a long straight microchannel in Taylor flow regime, and for the first time, the shrinkage effect resulted from the interfacial mass transfer with water will be probed by experiments;

- by numerical simulations, hydrodynamics of a single liquid CO_2 drop and a single supercritical CO_2 drop will be studied in a long straight microchannel, the flow patterns within CO_2 drops as well as in the interfacial regions and the interfacial distributions of CO_2 are the main focuses.

1.2 Thesis Outline

This thesis is structured into eight chapters as follows:

In Chapter 1, the background and motivation of this thesis are introduced. It starts with the introductions of various aspects of carbon capture and storage (CCS) as a promising CO_2 mitigation method and the knowledge gaps of the storage mechanisms in porous reservoirs. The potentials and applications of pore-scale micromodels especially those with extreme pressures/temperatures conditions are briefly reviewed. Also by surveying on the microfluidic studies involving gaseous CO_2 that cover the hydrodynamics and mass transfer resulted shrinkage, the lack of microscale studies related to dense CO_2 including liquid and supercritical CO_2, the exact forms of CO_2 stored in geological formations, is pinpointed, which also prompts this thesis. The thesis outline is provided as well.

In Chapter 2, a literature review is provided mainly on: (1) two-phase microfluidic flows including the relevant forces, dimensionless numbers, interfacial effects, common geometries and flow regimes, (2) hydrodynamic issues of drops (and/or bubbles) in microchannels including flow resistance, thin film presence and Taylor bubble/drop speed, (3) conventional equations of state (Eos), and (4) classic mass transfer models.

In Chapter 3, an experimental system specifically built for the two phase microfluidics working at extreme pressures/temperatures is introduced, and the fabrication of silicon-glass microchips is detailed. Also specifically introduced are several key issues encountered during the system building, such as a design calculation of the square microchannel geometry in terms of mechanical strengths, a design of a 'plug-and-play' connector, a general assembly of the microchip with the connector, calibrations of a back pressure transducer, and additions of 2-µm filters for preventing microchannel clogging.

In Chapter 4, liquid CO_2 and de-ionized (DI) water are engineered into a micro T-junction, in which the liquid CO_2 stream is a dispersed fluid encountering the water stream at the T-junction in a perpendicular manner. A drop flow regime has been analyzed in details in terms of the comprising stages of one representative drop generation period and the generated drop size, speed and spacing development over time. In order to justify our discussions on such parameters, the involved transport mechanisms including CO_2 hydrations, interfacial diffusion and relative strength of advection are analyzed, and the overall CO_2 mass loss into water is verified as small.

In Chapter 5, shrinkage of liquid CO_2 segments that are produced in the micro T-junction are studied by following its traveling locations in a long straight microchannel. A mathematic model is developed for calculating the mass transfer coefficients on the drop side. Pressure decline of the segmented flow in microchannel is considered. By using the Peng-Robinson equation of state (Eos) for describing the CO_2 drop, the pressure decline effect over the drop volume changes are analyzed which are proved to be an extreme small quantity.

In Chapter 6, an analogous experimental study to that in Chapter 5 is performed towards supercritical CO_2 (scCO_2) segments travelling in the same long straight channel. Based on a similar methodology as in Chapter 5, the shrinkage phenomenon of scCO_2 is confirmed and relevant hydrodynamic issues are analyzed. It is made clear, based on the experimental results in this chapter, that surface-to-volume ratio and the flowing time of scCO_2 drops in the channel are the two main factors governing the overall mass transfer processes which mainly occur at the interface between the drops and the neighboring water.

In Chapter 7, a numerical study on the hydrodynamic issues of one single liquid CO_2 drop and one single scCO_2 drop is presented. The numerical problem is described first and the applied numerical method is then detailed. Three liquid CO_2 drop cases and three scCO_2 drop cases, of which the operating conditions are analogous to that in the experimental work, are considered, respectively. The

computed drop profiles and thin film (at the channel wall) formations are presented and discussed. And the flow fields both within the drops themselves and at the drop meniscus regions are shown. The generated toroidal vortexes in those regions are generally attributed to the shear stresses in the thin films as well as that local ones in the vicinity of the drop meniscuses. Interfacial distributions of CO_2 indicate the effects of both diffusion and local convections.

In Chapter 8, a summary of this thesis is given and future studies following the current work are recommended.

Chapter 2
Literature Review

2.1 Introduction

Two phase flow, as an important topic in fluid mechanics, has been studied for a long history since the pioneering work of Young and Laplace on the fluid cohesions in capillary tubes in the early nineteenth century [92]. Based on the forms of the substances involved in research and applications, two phase flows can be grouped into four classes, namely, gas-liquid flows, liquid-liquid flows, gas-solid flows and liquid-solid flows. The most important two types of two phase flow, despite the regular involvements of solids as mediums or walls, are gas-liquid and liquid-liquid flows, which have been extensively implemented in industrial applications, such as the transportation of oil-gas mixtures in pipelines, heat exchangers, boilers in power plants and refrigeration systems [93,94]. Specifically, two-phase microflows as a subfield of the broad two phase flows are referred to the fluidics involving two immiscible or partially miscible fluids in microscale (<1mm) devices. The characteristics of two-phase microfluidic flows, such like relatively large interfacial area, fast mixing and reduced mass transfer limitations [95], outweigh them over conventional bench-scale systems and lead to numerous applications in biomedical engineering, high throughput chemistry and 'digital microfluidics' [96]. Among all potential flow regimes subjected to either the geometries of the microchannels, physical properties of the fluids or the flow conditions, micro segments (such as drops and bubbles) featured two phase flows have attracted more attention in research dedicated to enhancing heat and mass transfer between fluids, which is mainly due to the stable hydrodynamic characteristics (e.g., size, speed, morphology and monodispersity etc.) of these segments and the shortened heat and mass transfer path [95,97-102].

When CO_2 is considered one of the fluids in liquid-liquid and gas-liquid systems, it could be either a gas phase, a liquid phase or even a supercritical one. Whatever phase the CO_2 is, these fluid-fluid systems may not be immiscible but instead partially miscible. Moreover, when liquid or supercritical CO_2 are considered, the ideal gas law may not be applicable. Therefore, appropriate methods are needed to describe the applied CO_2 and to characterize the mass transfer involving CO_2 during the dissolution processes. Last but not the least, hydrodynamic issues of CO_2 segments when flowing in the microchannels, such as speeds, presence of thin films, and pressure decline, are necessary to be considered as well.

7

2.2 Fundamentals of Two-Phase Microfluidics Flows

When compared with single-phase flows, two-phase microfluidic flows may be advantageous in terms of larger interfacial areas, shorter transfer distances and more intensive mixing [96]. The properties of two-phase flows in microfluidic channels are generally determined by the following parameters: geometries of channels, properties of the involved fluids, and the flow conditions [95]. These parameters can be integrated into and taken account of by using dimensionless parameters, which have been normally used to characterize the two-phase flows. On the other hand, as a result of the phases introduced, interfaces between different fluids and solids are very likely to arise that can be characterized by such factors as interfacial tension, contact angle and capillary pressure which are able to significantly show effects to the hydrodynamics of the fluids and mass transfer between them.

2.2.1 Forces and Dimensionless Numbers

Interfaces are usually under the scenarios of balance and imbalance which are subjected to forces involved. There are generally four types of force related to two phase microfluidic flows, i.e., inertial, viscous, gravitational and interfacial forces. Interactions of these forces result in flow instabilities and a number of fluid distributions. Relative importance of each force of a pair can be described by the ratio of the two forces, which exactly defines a dimensionless number. Reynolds number (Re), as shown in equation (2.1), compares the relative intensity between inertial forces and viscous forces,

$$Re = \frac{\rho v d}{\eta} ,$$

(2.1)

where ρ is the fluid density, kg/m^3; v is the characteristic velocity, m/s; d is the characteristic length, m; and η is the dynamic viscosity, Pa·s. Re number for microfluidics is generally much smaller than 100 and often is less than 1 [103-107]. This indicates a general weaker role of inertia relative to the viscous forces, which is mainly resulted from the restricted velocities of the fluids in the microscale channels.

As the viscous forces compared to the interfacial tension, capillary number (Ca) is introduced to quantify the relativeness of the viscous forces. Capillary number is defined as follows

$$Ca = \frac{\eta v}{\sigma} ,$$

(2.2)

in which η and v are the same as that used for the definition of Re, and σ (in N/m) is the interfacial tension between the fluids. Due to a dominant role of interfacial tension under the presence of

interfaces as well as under a usually hydrodynamic scenario, the Ca number is a key dimensionless number in microfluidics, especially when it comes to the droplet generation, coalescence and transports.

Based on Re and Ca, the other two parameters, i.e., Ohnesorge number (Oh) and Weber number (We) can be induced. Oh number is defined as the ratio of viscous forces to inertial and interfacial forces, and We number compares the inertial forces to the interfacial tension.

$$Oh = (\frac{Ca}{Re})^{1/2} = \frac{\eta}{(\rho d \sigma)^{1/2}}; \quad We = ReCa = \frac{\rho d v^2}{\sigma}. \tag{2.3}$$

However, due to the very dominant role of interfacial tension, these two dimensionless number are rarely considered in microfluidics. On the gravitational dimension, there are two other dimensionless numbers, namely, Bond number (or called 'Eötvös number') and Grashof number have been introduced to evaluate the gravitational forces to the interfacial forces (equation (2.4)) and the buoyancy to the viscous forces (equation (2.5)), respectively, as shown below

$$Bo = \frac{\Delta \rho g d^2}{\sigma} = \frac{(\rho_l - \rho_g) g d^2}{\sigma}, \tag{2.4}$$

$$Gr = \frac{g \beta (T_s - T_\infty) d^3}{(\eta/\rho)^2}, \tag{2.5}$$

in which $\Delta \rho$ is a density difference between the liquid phase (ρ_l) and the gas phase (ρ_g), g is the gravitational acceleration, m^2/s; (T_s-T_∞) is a temperature difference between the surface and the bulk fluid, and β is a coefficient of thermal expansion that is correlated with 1/T. Because of the microscale dimensions and the high-order scaling between the dimensions and these two numbers, Bond number and Grashof number are typically out of considerations. Nevertheless, Bond number has been applied to identify a prevalent flow regime in two-phase microfluidic flows-Taylor flow [108], and Grashof number may outstand itself when there exist flows significantly driven by a density difference [109].

In addition, there are some other dimensionless numbers commonly used in microfluidics, which are related to the fluid properties and flow conditions, such as the density ratio (ρ), the viscosity ratio (μ) and the flow rate ratio (φ), as shown below

$$\rho = \frac{\rho_c}{\rho_d}, \quad M = \frac{\eta_c}{\eta_d}, \quad \varphi = \frac{Q_c}{Q_d} \tag{2.6}$$

Here, Q is the flow rate of the fluid, m^3/s. The subscripts in equation (2.6) 'c' and 'd' indicate the continuous fluid which is preferred by the solid walls upon wettability and carries the other fluid segments that are exactly the dispersed fluid, respectively. Moreover, dimensionless drop or bubble

9

sizes (L_d/W) quantified by comparing their lengths (L_d) to the characteristic width (or hydrodynamic diameter) of the channel (W) are usually used in quantitative analyses.

2.2.2 Interfacial Effects: Surface Tension, Contact Angle, Capillary Pressure

Given the general flow velocities (~ mm/s) being worked with, interfacial effects become a dominant factor that significantly affects the flow, as evidenced by the order of magnitude of the capillary number (Ca). When two immiscible fluids contact with each other, they are generally separated by a very thin layer called the 'interface' [110]. As discussed by Defay and Prigogine [111], a spherical cap of a bubble or a drop is subjected to surface tension σ at the base of the cap and pressures P' and P'' at each point on the surface, as shown in Figure 2.1 The effect of the surface tension is to contract the bubble or drop to resist a potential deformation resulted from an imbalance of forces. If the surface tension is uniformly distributed on the surface (i.e., same value of σ on all points), σ is called the surface (or interfacial) tension of the surface. It can be deemed as either the force per unit length of an arbitrary line on the interface or the energy for creating a unit area of the interface [112], thus the dimension of surface tension can be either force per unit length or energy per unit area, with the units 'N/m' and 'J/m^2', respectively.

Other than a uniform scenario, differences of the surface tension among at different positions on the interface could lead to another type of stress working to re-balance the interface, i.e., Marangoni stresses, which can be brought in thanks to a temperature difference or a presence of surfactants [113,114]. But in this thesis, the effects of variable temperatures on interfacial tension are ruled out and only uniform cases are assumed and considered.
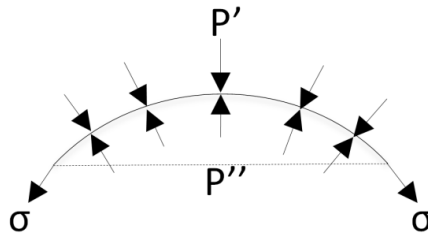
Figure 2.1 Capillary equilibrium of a spherical cap (after Defay and Prigogine [111]).

There are usually two types of interfaces for immiscible fluid pairs, i.e., fluid-fluid (often gas-liquid and liquid-liquid) and fluid-solid involved in two phase microfluidic flows, where the wetting characteristics of fluid-solid interfaces determine whether the subjected flow regime is ordered or disordered. In general, complete and partial wetting between the continuous phase and the

microchannels result in an ordered and a disordered flow pattern, respectively. Considering a liquid drop on a smooth and planar surface, as shown in Figure 2.2, the interface between the liquid and gas intersects with the solid surface at an angle 'θ' which is called the contact angle [115]. On the interfaces of gas/liquid, gas/solid and liquid/solid, there are three surface tensions interacting with each other, namely, σ_{lg}, σ_{sg} and σ_{sl}, respectively. A force balance among these surface tensions results in a stable gas/liquid/solid system, which is based on equation (2.7) (i.e., Young-Dupre equation or Young's equation)

$$\sigma_{lg} cos\theta = \sigma_{sg} - \sigma_{sl}. \tag{2.7}$$

where σ_{lg}, σ_{sg}, and σ_{sl} are the surface tensions of liquid/gas, solid/gas and solid/liquid, respectively. θ is the contact angle between gas and liquid phase, which ranges from 0° to 180°. Equation (2.7) can be rearranged as equation (2.8) to give contact angle θ, as shown below

$$cos\theta = \frac{\sigma_{sg} - \sigma_{sl}}{\sigma_{lg}}. \tag{2.8}$$
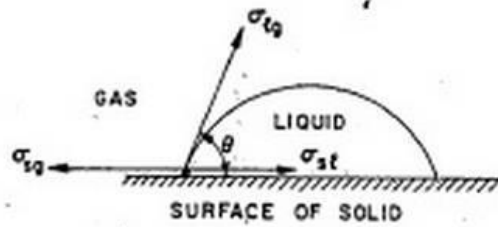
Figure 2.2 A force balance at a meeting point between a gas-liquid pair and a solid surface (after Dullien [110]).

Contact angle is an important characteristic parameter of interfaces in microfluidics, which quantitatively characterizes the hydrophilicity or hydrophobicity of the solid surface with respect to the fluids in contact. When the contact angle is smaller than 90°, the solid surface is hydrophilic; while the surface is hydrophobic as the contact angle is larger than 90°. Moreover, additions of surfactants at certain concentrations can alter the contact angle [116], for example, when the concentration of sodium dodecyl sulfate (SDS) as a surfactant is higher than the critical micelle concentration (CMC) in water, the surface of poly methyl methacrylate (PMMA) will change from being hydrophobic to be hydrophilic [117].

By this point, interfacial effects between fluid phases and solid surface, i.e., surface tension and contact angle, can be described by Young-Dupre equation (or Young's equation) in a combined way.

Generally, the solid-fluid interactions are specified to be 'wettability'. It has significant effects on the flow of two immiscible fluids in porous medium and microchannels as well as in other applications (e.g., coating applications), which also have been studied in petroleum industry for a long time due to its key role in oil recovery processes [115]. Although interfacial tensions of fluid/solid might not be likely to be measured easily, the interfacial tension and contact angle between the two fluids can be measured. Take water and oil as an example, they compete with each other to contact the solid surface. Typically, the system is considered as (preferentially) water wetting if $0° \leq \theta < 90°$ (where water is the wetting fluid), or oil wetting if $90° \leq \theta \leq 180°$ (where water is the non-wetting fluid). And a contact angle of $90°$ corresponds to an intermediately wetting state when $\sigma_{sg} = \sigma_{sl}$. Practically, a contact angle between $65°$ to $105°$ is deemed as an intermediate wetting state. Another case is a mixed wettability where the surface wettability varies among positions of the surface. It is also noted that the cases when $\sigma_{sg} - \sigma_{sl} \geq \sigma_{lg}$ ($S_{lg} = \sigma_{sg} - \sigma_{sl} - \sigma_{lg}$, and is called 'spreading coefficient', see Figure 2) can be possible as well, and thus there is a spontaneous spreading of the liquid on the solid surface since the adhesive forces of liquid/solid is larger than that of gas/solid [110,115,118].

As a consequence of a combined effect from surface tension and contact angle, another key parameter, capillary pressure, can be raised which defines the pressure difference across the interface between two immiscible fluids. By considering a non-wetting phase displaces a wetting phase inside a capillary [119], as shown in Figure 2.3, the horizontal forces are under an equilibrium state such that a stable interface between the two fluids can be formed, as described by equation (2.9)

$$P_{nw}(\pi R^2) + \sigma_{ws}(2\pi R) - P_w(\pi R^2) - \sigma_{nws}(2\pi R) = 0, \tag{2.9}$$

where R is the radius of the capillary and subscripts 'nw' and 'w' refer to the non-wetting and wetting fluid, respectively. Equation (2.9) can be rearranged as

$$P_{nw} - P_w = \frac{2(\sigma_{nws} - \sigma_{ws})}{R}, \tag{2.10}$$
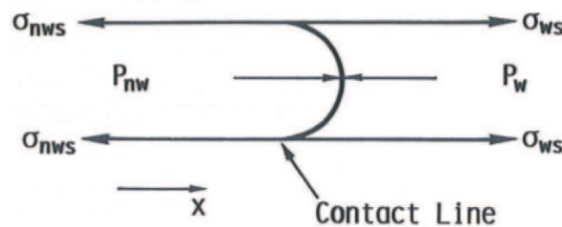
Figure 2.3 Equilibrium at a contact line between two fluids and a solid surface in a capillary (after G.P. Willhite [119]).

Integrate equation (2.10) with equation (2.7), equation (2.11) is obtained

$$P_{nw} - P_w = \frac{2\sigma_{nw,w}cos\theta}{R},$$ (2.11)

which is exactly the Young-Laplace equation for capillary pressure P_c, as formulated below

$$P_c = \frac{2\sigma_{nw,w}cos\theta}{R}.$$ (2.12)

For a more general interface, it can be written as

$$P_c = 2\sigma_{nw,w}cos\theta(\frac{1}{R_1} + \frac{1}{R_2}),$$ (2.13)

where R_1 and R_2 are the principal radii of the curvature of the interface. In practices, R_1 and R_2 may be determined by considering the geometries of the channels and the contact angle simultaneously.

2.3 Common Geometries and Flow Regimes of Two-Phase Microfluidic Flows

In this section, the commonly used geometries to facilitate the immediate contact of two fluids in microfluidic flows are introduced. The resulted flow regimes for gas-liquid and liquid-liquid systems are briefly discussed.

2.3.1 Common Geometries

There are generally two groups of methods, i.e., passive and active ones, to facilitate the interactions of the involved fluids, which rely on purposely designed geometries in the devices and external forces (e.g., electrical, magnetic, ultrasonic), respectively. Among passive methods, the applied geometries can be further categorized into three types, i.e., cross-junctions (including T- and Y- junction), flow focusing and co-flowing devices. Figure 2.4 shows the three main microfluidic geometries used in liquid-liquid and gas-liquid flows, namely, T-junctions, flow focusing and co-flowing.

Cross-junctions
Cross-junction, especially the type of T-junction, is the most applied geometry in microfluidic flows involving immiscible fluids, in which one fluid intersects with the other in a certain angle (e.g., 90° for T-junction) [117,120-122]. It is generally composed of one side channel from which the fluid is dispersed into the junction and a main channel where there is a continuously flowing fluid. At the interface as these two fluids encounter, shear stresses, pressure gradients and interfacial tension dominate the stream breakups and possible droplet formations. For liquid-liquid flows, T-junction can be further divided into two types: cross-flowing and perpendicular flowing. In cross flowing, as

shown in Figure 2.4 (A)b, the dispersed fluid is induced from a side channel into the main channel, where the continuously flowing fluid shears off the dispersed flow and generates droplets [123]. In perpendicular flowing (see Figure 2.4 (A)c), however, the dispersed fluid flows in the main channel and the continuous one is induced from the side channel [124].

| (A) | (B) | (C) |
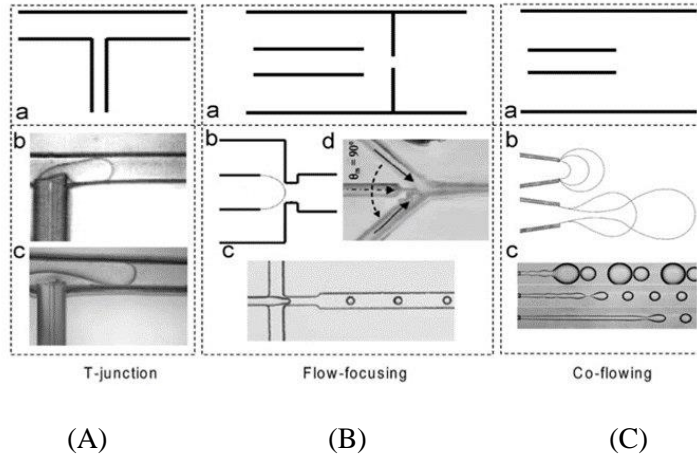
Figure 2.4 Three common geometries of the microfluidic devices for two-phase flows: (A) T-junction, (B) flow focusing and (C) co-flowing devices (after Zhao and Middelberg [96]).
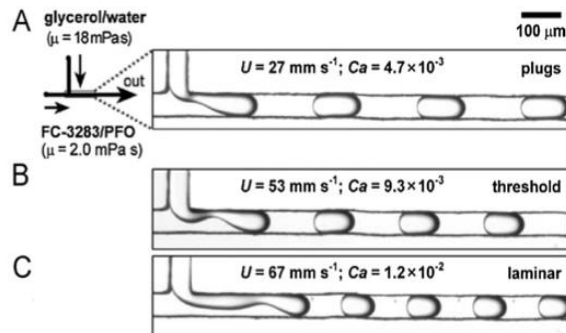
Figure 2.5 Three regimes of the two-phase liquid-liquid flows in a cross-flowing micro T-junction subjected to increasing flow velocities and capillary numbers (after Tice et al. [126]).

In a cross-flowing T-junction, three regimes are reported for various flow rates, as shown in Figure 2.5. When the flow velocity is low, interfacial tension is the dominant force that rapidly breaks up the plugs. As the flow velocity increases, viscous force becomes significant and interfacial tension is not sufficient to break up plugs. This is evidenced by the long neck and postponed breakups in Figure 2.5 (B) and (C). Similar regimes of the droplet formation in a T-junction were also reported in a numerical study [125], and the regimes including squeezing, dripping and jetting were identified.

14

The other prominent type of the cross-junction is Y-junction, of which the interaction angle of the side and the main channel is an obtuse one [127,128]. Steegmans et al. [127] characterized the monodisperse emulsifications at a Y-junction, and based on a force balance analysis, a model was derived which correlated the droplet size with the channel depth and the capillary number. In addition, by using a correlation of the droplet sizes with static interfacial tensions, the apparent dynamic interfacial tensions in various surfactant systems were estimated, where the liquid-liquid interface were controlled by the shear stresses and a dominant convective transport of the surfactants [128].

Flow focusing

The other mostly used geometry is a flow focusing device which has been extensively applied for forming spherical monodisperse droplets [129], as that shown in Figure 2.4 (B). In a typical flow focusing design, the dispersed and the continuous fluid flow coaxially at the exit of an inner microchannel and an outer microchannel, and then focused by a confining small orifice. The dispersed fluid is squeezed by the continuous fluid and breaks into spherical droplets or bubbles. Compared with T-junctions, flow focusing devices are generally used to produce droplets rather than plugs because the dispersed fluid is confined in the central region of the channel. Nevertheless, adhesions or damages of the droplet might be possible due to contact with the channel walls. There are primarily three flow regimes in flow focusing devices, i.e., squeezing, dripping and jetting, depending on the flow rate ratios of the dispersed fluid and that of the continuous one, which is analogous to T junction [130]. And the formations of these regimes can also be interpreted by using the capillary number [130,131], which compares the viscous force with the interfacial tension.

Co-flowing

Co-flowing is generally a second method to produce monodisperse droplets, as shown in Figure 2.4 (C). The disperse phase flows through a capillary or a needle tube which is an inner capillary into the continuous phase that is flowing in an outer capillary, and the droplets or bubbles are produced by a combinatorial effect of interfacial tension and shear stress [132]. In a co-flowing design, droplets can be produced at the tip of the tube (i.e., dripping regime) or at a certain distance from the end of the tube (i.e., jetting regime). These regimes are similar to the dripping and the jetting regime in a flow focusing device. Umbanhowar et al. [103] reported the droplet formation in the dripping regime for the first time. Utada et al. [133] experimentally studied the dripping to jetting transition and concluded that the transition regime occurs when the Ca number of the continuous phase is around 1.

Other geometries

Straight-through microchannels, membranes and micro-fabricated channel arrays are other geometries used by researchers in microfluidics. Straight-through microchannels take advantage of an array of vertical holes that are uniformly distributed in silicon surface to produce monodisperse droplets [134]. For membranes, the dispersed phase is driven through the uniform pores into the continuous phase under a certain pressure. Despite low energy inputs and low shear stresses, coefficients of variation (COV) of the droplets in membrane emulsification are much higher than those in other geometries (e.g., T-junction, flow focusing, co-flowing, straight-through) [96]. Other geometries have also been developed, such as array microchannels [135] and parallel droplet formation channels [136].

Active methods based on external forces

Other than the interfacial instabilities based geometries as a passive method driven by viscous forces and interfacial tensions, the interactions between fluids can also be achieved and controlled by using external forces, e.g., electro-wetting [137], dielectrophoresis [138,139], thermo-capillary and magnetic actuation [140]. Electrical forces are the mostly used external forces in droplet formation. The application of interfacial electrical forces offers several advantages in droplet formation, e.g., adjustable droplet sizes, flexible geometries of the channel etc. [141-145]. Moreover, the size and the production rate of the droplets could be adjusted under different liquid flow rates or voltage differences. Thermal energy is another method to control droplet flow in microchannels. Temperature changes can lead to changes of viscosities and interfacial tensions, which contribute to the manipulation of the droplet [146,147]. In recent years, surface acoustic waves (SAWs) based on acoustics and ultrasonics at high frequencies (10 ~ 1000 MHz) have been utilized to conduct ultrafast microfluidics. It is a superior alternative to conventional methods in producing rapid actuations, extremely fast motions of drops and significant inertia within drops. Therefore, it is of particular significance to the manipulation of drops in an atomized and fast way as well as in enhancing the mixing performance within droplets, especially with respect to the small particles in droplets. On the topics of SAWs integrated with microfluidics, readers are referred to the references such as Yeo and Friend [148], Friend and Yeo [149], Ding et al. [150], Yeo and Friend [151].

2.3.2 Flow Regimes

One key feature of two-phase flows is the interface between the two phases. The interface, especially that of a gas-liquid system, is very likely to take various forms subjected to multiple factors. And due

to the interfacial effects, it tends to be a curved shape. Thus, it is appropriate to describe two-phase flows according to the various types of distributions of these interfaces. Consequently, the concept of 'flow regime' or 'flow pattern' has been conceived [152]. Analogous to the conventional two phase flows at macroscale, there exist various flow regimes (or patterns) of the gas-liquid and liquid-liquid systems in the microscale geometries. These flow regimes are of enormous importance to the main design parameters and the common modeling methods of two phase flow systems. In this section, common flow regimes of gas-liquid and liquid-liquid two phase microfluidics are introduced. Note that, since the layouts of the capillaries (e.g., vertical, horizontal or inclined) and flow directions (e.g., downward or upward) can have a significant influence on the flow regimes, the discussions here are limited to two phase flows in planar microchannels (i.e., horizontal). Also, Taylor instability is not applicable in capillaries and microchannels.

2.3.2.1 Gas-liquid flow regimes

Gas-liquid flow is the mostly studied subject of two-phase microfluidic flow. It has been attempted in all of the aforementioned geometries. Similar to that in the early studies in the capillaries (of which the diameter is on the order of magnitude of 1 mm [153,154]), the flow regimes in microchannels are mainly determined by viscous and interfacial forces as well as inertial forces when Re approaches 1. Besides, wetting properties of the wall are very important for the gas-liquid flows as well.

Early research work was mostly done in circular capillaries with inner diameter around or below 1mm [153,155-157]. For most cases, five major flow regimes have been identified in experiments, namely, bubbly flow (including dispersed and general bubbly flow with respect to the bubble size), slug flow, churn flow, slug-annular flow and annular flow [157], as shown in Figure 2.6. Bubbly flow (Figure 2.6 (A-B)) is characterized by discrete bubbles of equivalent diameters smaller than that of the capillary, which usually occurs at very high liquid velocity and a simultaneously low gas velocity. As the gas velocity increases relatively to the liquid one, slug flow starts to be developed which is characterized by a cylindrical slug of an equivalent diameter larger than that of the capillary and by a certain film separating the slug from contacting the wall (see Figure 2.6 (C-D)). The slug is generally featured by two semi-circular shaped caps at the front and the back end, though a difference between the dynamic contact angles of the front and the end cap leads to a shape difference, as shown by Figure 2.6 (D). Note that slug flow is often referred as Taylor flow or intermittent flow which may be identified based on a critical Bond number [108]. As gas velocity further increases to be several times of the liquid one and the total flow rate of two fluids increases as well, churn flow can be formed in

17

which the caps of the bubbles in slug flow become unstable and disrupt into smaller satellite bubbles (see Figure 2.6 (E-F)). As a result of the coalescence of the long bubbles, a flow regime called slug-annular or wavy-annular flow emerges in which there are rare liquid segments to separate the bubbles from one another, as shown in Figure 2.6 (G-H). It is not stable at the interface as well. When the gas velocity further increases, the wavy interface starts to be flattened and the trend line of the overall interface seems as parallel to the channel wall, the flow regime at this moment is named annular flow (represented in Figure 2.6 (I-J)).
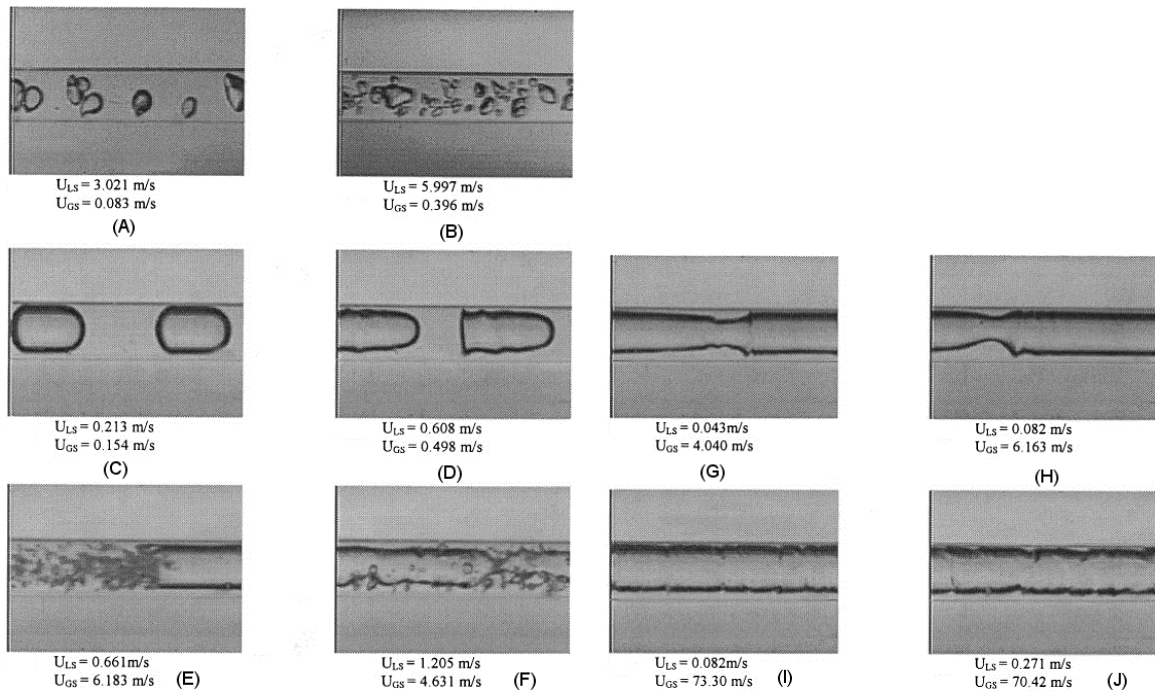
Figure 2.6 Some representative photos of various flow regimes of gas-liquid flows in a 1.097mm diameter circular capillary: (A-B) bubbly, (C-D) slug, (E-F) churn, (G-H) slug-annular, (I-J) annular (after Triplett et al. [157]).

However, 1mm diameter channel serves more like an upper boundary of the microscale channels, as argued by Rebrov [158], and the dominance of either interfacial tension or inertial force in microchannels may not complicate the flow regimes when compared with those in millimeter scale capillaries. Thus the flow regimes might be able to be divided into three groups, i.e., the one dominated by interfacial tension, the one dominated by inertial forces, and the rest as a result of a competition between interfacial tension and inertial force. Despite of this categorization, there are mainly six flow regimes in microchannels, as shown in Figure 2.7, most of which are analogous to

that already reported in the 1mm dimeter capillaries. However, the early transition from slug to slug-annular flow may be further differentiated from the general slug-annular flow and called slug-ring, in which certain curvatures still exist at the interface. When the gas and the liquid both have a high velocity, a regime of dispersed phases of both fluids can be generated.

(A)   (B)
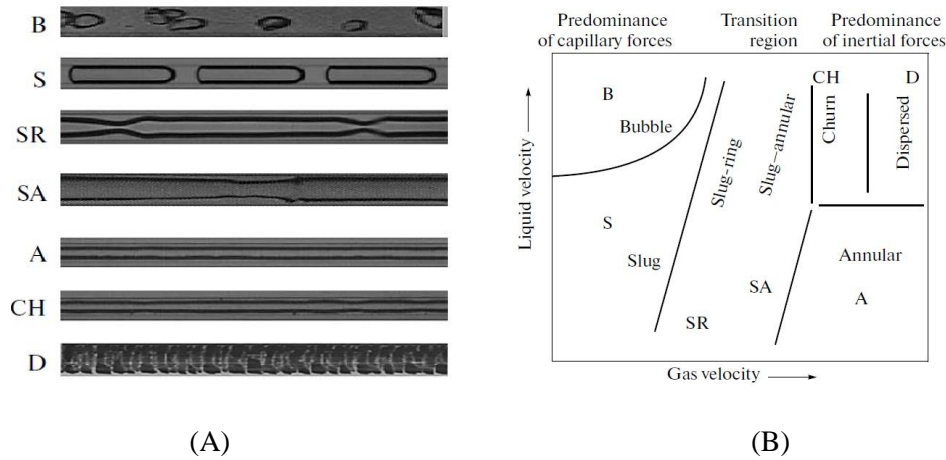
Figure 2.7 A generalized schematic of various flow regimes in microchannels: (A) representative photos of each flow regime designated with first letters: bubbly-B, slug-S, slug-ring-SR, slug-annular-SA, annular-A, churn-CH, dispersed-D; (B) a typical mapping of flow regimes against superficial velocities of the gas and the liquid. (after Rebrov [158]).

There have been a large number of publications on the flow regimes of gas-liquid flows in microchannel in the past 15 years, and many parameters have been verified as influential on the flow regimes as well as the transitions between regimes. These parameters generally include, but are not limited to: (1) the geometries of the mixer and the microchannels (e.g., [159-162]), (2) the wetting properties of the channel wall surface (e.g., [163-165]), (3) the surface tension (e.g., [166-168]), and (4) the liquid viscosities [166]. Regarding the effects of such parameters, readers are referred to a review work by Rebrov [158].

2.3.2.2 Liquid-liquid flow regimes

Liquid-liquid flow is distinguished from the gas-liquid one in terms of: (1) the viscosities of both fluids are non-negligible, (2) both fluids are incompressible, and (3) wetting issues are related with both fluids [95]. In view of the research history, water and various oils (e.g., silicon oil, toluene, decane, tetradecane, hexadecane etc.) have been the mostly used liquid pairs in liquid-liquid flow, which is mainly due to their excellent immiscibility and easy availability.

Thorsen et al. [123] reported diverse patterns of water droplets at a T-junction under various water and oil pressures. Such different droplet patterns, other than the pure water or oil streams, include separated droplets, jointed droplets, double and triple droplet layers and elongated droplets. And they dedicated the instability of those vesicle formations to a competition of the shear forces with the surface tension. Dreyfus et al. [169] investigated the effects of wetting properties of the oil and water relative to the channel walls over the flow patterns. In a complete wetting case, the flow patterns were ordered and determined by the flow rates, these patterns were divided into isolated water drops, pearl necklace, pears and stratified flow, as shown in Figure 2.8 (B). In a same complete wetting case but with no surfactant added, the flow patterns could not be exactly defined, as shown in Figure 2.8 (C). Moreover, the concentration of the surfactant showed an influence on the interfacial tension and further resulted in a transition from disordered patterns to an ordered separated drop pattern.

(A) (B)

(C) (D)
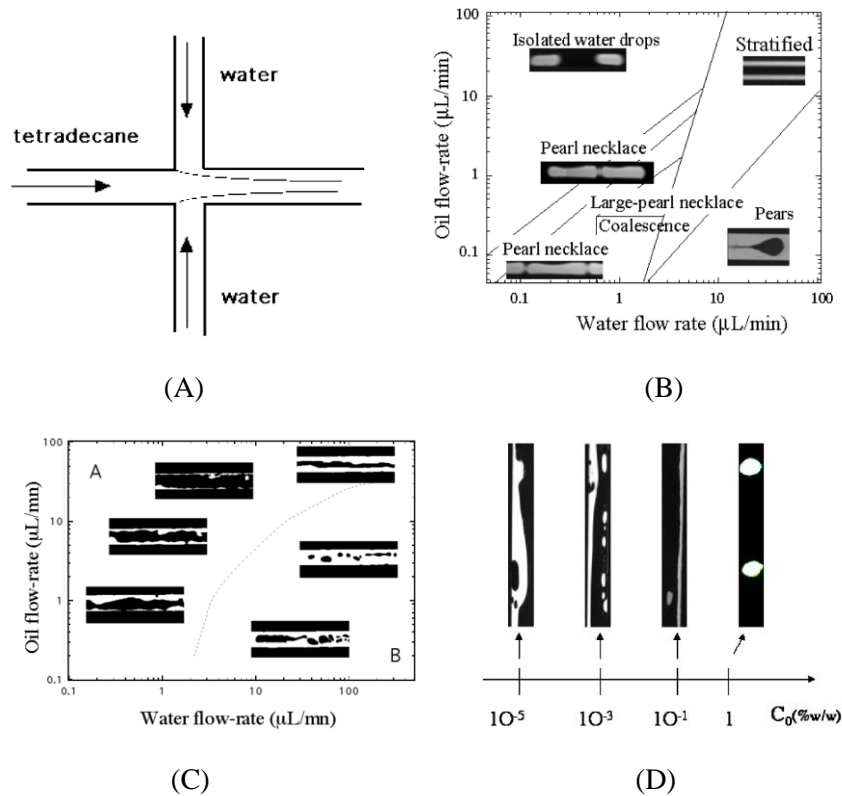
Figure 2.8 Obtained ordered and disordered flow patterns with and without using surfactants: (A) a flow-focusing device using water and tetradecane as a liquid-liquid system; (B) ordered flow patterns at a complete wetting scenario; (C) disordered patterns without using surfactants; (D) flow pattern evolution as a result of increasing the concentration of the surfactant SPAN 80 (after Dreyfus et al. [169]).

Zhao et al. [170] reported liquid-liquid flow patterns at a T-junction in a rectangular microchannel. The flow patterns had been specified as slug flow, monodispersed droplet flow, droplet populations, parallel flow and annular flow (see Figure 2.9 (A)), which were correlated with the Weber numbers of the water and oil phase (see Figure 2.9 (B)). Similar to the gas-liquid system, the flow patterns of liquid-liquid one can also be divided into three groups, namely, (1) interfacial tension dominated group including slug and monodispersed droplet flow, (2) inertial and interfacial forces combined group including parallel flow and droplet populations, and (3) inertial forces dominated group including parallel and annular flow. Slug flow and parallel flow have been identified as the two main flow patterns in T- and Y-shaped glass microchips using deionized (DI) water and dyed oil phases (i.e., toluene and hexane) [171]. The formation of these two patterns was attributed to a competition between the viscous force and interfacial tension (i.e., mean capillary number and Reynold number). A similar finding of the predominance of slug flow and stratified flow as main flow patterns was reported by Cherlo et al. [172], and the Weber number was deemed the key factor in controlling the flow patterns as well.

(A)   (B)
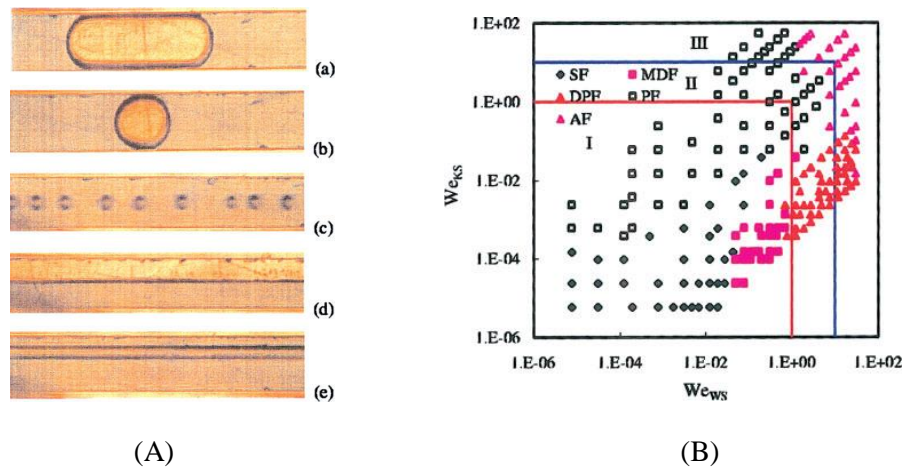
Figure 2.9 Flow patterns of liquid-liquid systems at a micro T-junction: (A) representative photos of the flow pattern including slug flow (a), monodisperse droplet flow (b), droplet populations (c), parallel flow (d), annular flow (e); (B) a mapping of the flow patterns against the Weber numbers of the water and kerosene (after Zhao et al. [170]).

2.4 Mechanisms of Droplet/Bubble Formations in Two-phase Microflows

Droplet/bubbly flow as well as slug flow have been the common flow regimes shared by both gas-liquid and liquid-liquid system in microfluidic studies. These flow regimes have fascinated

21

researchers working on the heat and mass transfer, thanks to well-defined interfaces, increased surface-volume ratios, convective motions within the slugs and the droplets, interfacial diffusion between the slugs of different fluids, reduced distances of mass and heat transfer, etc. [173-175]. In order for better controls and applications, the mechanisms of droplet/bubble/slug formations need to be studied. As indicated in a review work [96], droplet formation is generally determined by the following parameters: (1) channel geometry, structure and surface property (e.g., channel type, dimension and hydrophobicity); (2) fluid properties (e.g., density, viscosity, interfacial tension and contact angle); and (3) operating conditions (e.g., pressure, flow rate ratio, temperature, electric field, etc.). These parameters can be integrated and expressed by using dimensionless numbers. Due to the proportional relation with the characteristic length of the microchannel, Reynolds number is usually very small, which indicates that the inertial effects compared with viscous forces can be ignored. Capillary number is a key dimensionless number in microfluidic studies and has been used to reveal the mechanisms of droplet/bubble formations.

Three typical formation regimes have been identified in the common geometries, namely, squeezing, dripping, and jetting. For droplet breakup in a T-junction, two dynamic models, i.e., 'rate-of-flow-controlled' breakup and shear-driven breakup are proposed by Garstecki et al. [122,176] and Thorsen et al. [123], respectively. For low capillary numbers (< 0.01), shear stress is smaller compared with interfacial tension. Therefore, droplet breakup results from the pressure difference across the droplet or bubble under a simultaneous presence of interfacial tension. Garstecki et al. [122,176] named the mechanism of droplet formation in squeezing regime 'rate-of-flow-controlled' breakup, which may be applicable to droplet breakups in confined T-junctions and flow-focusing geometries as well. Table 2-1 lists a few scaling laws of the droplet/slug size for liquid-liquid flows when Ca < 0.01 at a squeezing regime. A dimensionless length of the droplet/slug is defined by a ratio of the absolute length L over the channel width W, and is generally correlated as a function of the flow rate ratio Q_d/Q_c, which corresponds to the 'rate-of-flow-controlled' mechanism.

For Ca > 0.01, shear stress starts to contribute to the droplet formations. The mechanism can be characterized as a shear-driven breakup [123]. Droplets are generally produced in an unconfined way [101,177], and the flowing pattern is somewhat similar to the dripping regime as that arises in co-flowing or unbounded T-junction [103,123,132]. According to Zhao and Middleberg [96], droplet diameter (d_d) can be correlated to Ca by '$d_d \propto (1/Ca)$'. Therefore, the droplet size is inversely proportional to the continuous phase flow rate, bulk flow rate, and the viscosity of the continuous phase. Some publications have contributed in probing the mechanisms of droplet formation under

Table 2-1 Scaling laws of the droplet/slug size under low capillary numbers and a squeezing regime.

Conditions	Authors	Scaling laws	Annotations
1. Low Ca (Ca < 0.01); 2. Squeezing regimes in confined T- junctions and flow-focusing	Tice et al. [183]	$L/W = 1.9 + 1.46\, Q_d/Q_c$	
	Garstecki et al.[122]	$L/W = 1 + Q_d/Q_c$	Main channel (width × depth): 100 µm×33 µm; side channel (width × depth): 50 µm × 33 µm; Ca: 8×10^{-5}~8×10^{-3}
	Xu et al. [124]	$L/W = 4.07\, (Q_d/Q_c)^{-5}$	A T-junction microchannel; continuous phase: oil, channel: 200×150 (µm^2); dispersed phase: water; quartzose capillary (inner diameter: 40 µm) into the perpendicular channel 200× 150 (µm^2)
	Xu et al. [184]	$L/W = \varepsilon + \delta\, Q_d/Q_c$	

Note: 'L' is the length of the immiscible droplet/slug; 'W' is the width of the channel; 'Q$_d$' and 'Q$_c$' are the flow rate of the disperse and continuous phase, respectively; 'ε' and 'δ' are fitting parameters depending on the T-junction geometry.

Table 2-2 Scaling laws of the droplet/slug size under large capillary numbers and a dripping regime.

Conditions	Authors	Scaling laws	Annotations
1. Large Ca (> 0.01); 2.Dripping regimes in an unconfined way in T-junctions and co-flow devices.	Xu et al., [184]	$\dfrac{d_d}{d_i} \approx \dfrac{1}{Ca'} = \dfrac{1}{Ca}\dfrac{wh - 0.785d^2_d}{wh}$ (Modified Ca: $Ca' = Ca\,\dfrac{wh}{wh-0.785d^2_d}$)	A modified Ca incorporates the effect of the droplet size; Ca: 0.06 to 0.8.
	Xu et al. [117]	$d_d \propto (\dfrac{1}{Ca})^{0.3}$	Applied to d > h; for d < h, $d_d \propto \dfrac{1}{Ca}$
	van der Graaf et al. [185]	$V = V_{crit,ref}Ca^m + t_{neck,ref}Ca^nQ_d$ (m = n = -0.75)	For both confined & unconfined droplet formation.
	Xu et al. [184]	$L/W = \varepsilon + \kappa(\dfrac{Q_d}{Q_c})^\alpha(\dfrac{1}{Ca})^\beta$	Applicable to a transient regime between squeezing and dripping.

d_d, d_i: diameters of the droplet and the inner microchannel; w, h: width and height of the microchannel; V: volume of the droplet; V$_{crit, ref}$ and t$_{neck, ref}$ are the critical volume and the necking time at Ca=1.
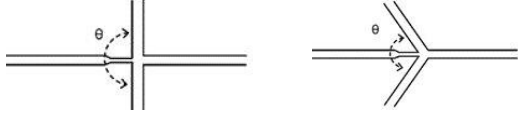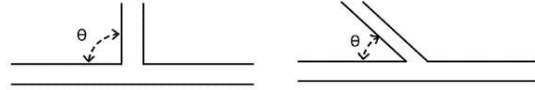
a large capillary numbers (Ca > 0.01) at the dripping regime in unconfined T-junctions and co-flowing, as shown in Table 2-2. In a short summary, the confined breakup is based on the 'rate-of-flow-controlled' mechanism, which relies on the pressure difference across the plugs in the T-junction or the droplets in a flow-focusing geometry. And the unconfined breakup is controlled by a shear-driven mechanism where capillary number determines the final droplet size.

Generally, microfluidic gas-liquid flows are a gas-in-liquid type, which may be unstable and difficult to control as compared with liquid-liquid flows. A number of experimental studies have been done on bubble formation mechanisms in gas-liquid microfluidic flows, as shown in Table 2-3. In addition to the experimental studies, a number of numerical studies on the hydrodynamics and mechanism of the bubble formation process have also been reported [e.g., 178-182].

Table 2-3 Scaling laws and some studies of bubble size in gas-liquid microfluidic flows.

Authors	Scaling laws or findings	Annotations
Gañán-Calvo [186]	$d_b/D = 1.1\,(Q_g/Q_l)^{0.4}$; d_b: bubble diameter; D: diameter of the orifice	Microbubbles produced by a capillary flow-focusing device.
Cubaud et al., [187]	$d_b/h = 1 + Q_g/Q_l$; h-channel height	A flow-focusing device with four-crossed square channels; water + air; water + SDS/air
Xiong et al. [188]	$d_b/h = 1 + Q_g/Q_l$	A co-flowing microchannel; Not effective at large Q_g/Q_l, since small Q_l hardly contributes to bubble formation in co-flowing.
Yasuno et al., [189]		Bubble size is independent of surface tension in the range of 36.2-48.9 mN/m using SDS; Using proteins as surfactant, droplets get different sizes even under the same interfacial tension due to the effect of viscoelasticity; Averaged bubble size is inversely proportional to viscosity ratio.
Xu et al. [190]		A T-junction microchannel; Bubble size $\propto \dfrac{1}{\text{flow rate of continuous phase}}$ or $\dfrac{1}{\text{viscosity of continuous phase}}$; Bubble size is independent of surface tension; Different surfactants lead to varied bubble formation process due to various wetting and dynamic interfacial properties.
Fu et al. [191]		A flow-focusing microchannel; Low influence of surface tension on bubble size; Bubble breakup is controlled by the bubble collapse stage; collapse rate of thread neck and collapse time are influenced by the gas and liquid flow rates as well as the liquid phase viscosity.

Table 2-3 Scaling laws and some studies of bubble size in gas-liquid microfluidic flows (continued).

Dietrich et al. [192]	$V_b/W_g = 300\left(\dfrac{\theta}{\theta_c}\right)^{-\frac{1}{6}}(\dfrac{Q_g}{Q_l})^{\frac{1}{4}}$ V_b: bubble volume; W_g: width of gas channel; θ: angle of flow focusing channel; θ_c: contact angle of the liquid on the channel	A dimensionless correlation of the bubble volume.
Tan et al. [193]	$L/W = 0.5\left(\dfrac{1}{Ca}\right)^{-\frac{1}{5}}\left(\dfrac{Q_g}{Q_l}\right)^{\frac{1}{2}}$ L: gas plug length Ca: capillary number	A T-junction with a side rupturing flow; the angle θ formed by the disperse gas phase channel and the continuous liquid phase is introduced to correlate the former equation,
Xiong and Chung [194]	$L/W = 1 + a\left[\dfrac{2\rho_l(Q_g + Q_l)h}{\mu_l}\right]^b\left(\dfrac{Q_g}{Q_l}\right)^c$ h: height of the channel; a, b, c: fitting parameters	A T-junction channel with high aspect ratio; Gas phase is injected from the side channel.
Zhang and Wang [195]	Pressure rather than the gas phase flow rate is used to interpret the mechanism of bubble formation; An empirical relation is used for predicting the bubble volume in a confined T-junction channel; capillary number significantly affects the bubble volume.	

2.5 Hydrodynamics of Drops/Bubbles (Taylor types) in Microchannels

In this section, some hydrodynamic properties of the droplets/bubbles after their formations, including an existence of a thin film, pressure drop determination and moving speeds, in either a circular or rectangular microchannel (the high aspect ratio is on the order of 1) are discussed. Here, it is assumed that there exists a complete wetting scenario of the channel wall with respect to the continuously flowing liquid (or called 'carrier fluid'). In addition, our discussions focus on Taylor type bubbles and droplets with a cylindrical shape. The equivalent diameters of such segments are several times of the hydrodynamic diameter of the channel, as shown in Figure 2.10. The capillary number ranges from 10^{-4} to 10^{-2}.

2.5.1 Thin Film in capillaries and square microchannels

(A)   (B)

(C)   (D)
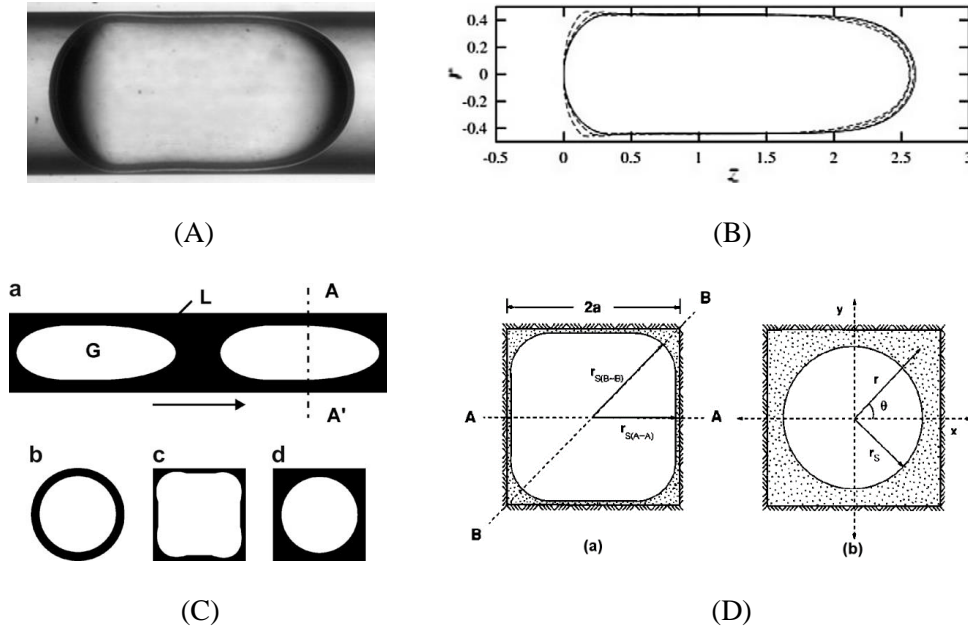
Figure 2.10 A single Taylor bubble/droplet in a microchannel: (A) an image of a typical water droplet in hexdecane; (B) outlines of a bubble at Ca = 0.04 for various Re (1 ~ 200); (C) schematics of the cross-sectional profile of a gas bubble (a) in circular capillaries (b), in a square microchannel at low Ca ($O(10^{-3})$) (c), and in a square microchannel at high Ca ($O(10^{-1})$) (d); (D) geometries of a bubble in a square tube when it is non-axisymmetric (a) and axisymmetric (b), respectively. (after Gupta et al. [196], Kreutzer et al. [197], Fries et al. [198], Kolb and Cerro [199])

2.5.1.1 Thin film in capillaries

When a Taylor bubble or droplet flows in either a circular or a square microchannel, it is always enclosed and separated from the channel wall by a thin film which is sometimes referred a lubrication film. The presence of this thin film is mainly a consequence of: (1) the wettability preference towards the continuously flowing liquid (i.e., the slug phase between two consecutive bubbles/droplets) and (2) the interfacial tension between the bubble/droplet fluid and the slug phase [200]. As the bubble/droplet is featured by a speed v_d, based on a homogeneous model of the interface between two phases and the boundary layer theory, there exists a velocity gradient of the thin film from the wall to the interface which leads to a viscous drag in a reverse direction of the velocity. The dragging effect of the viscous forces also contributes to the deposition of the continuous phase at the wall. Moreover, according to the Young-Laplace equation, there also exists a pressure jump from inside the

bubble/droplet to the thin film which can be estimated by equation (2.11). The effect of the capillary pressure is more like to push the interface toward the wall and expel the thin film liquid into the bulk. Therefore, the thin film is controlled by both the viscous force and the interfacial tension as well as the wettability and the radial size of the drop (see Figure 2.10 (D)), simply, the Ca number of the bubble/drop [201]. Some early studies of the thin film thickness for gas-liquid systems in capillaries demonstrated that the capillary number of the bubbles is a dominant role, which were summarized by Angeli and Gavriilidis [108], as shown in Table 2-4. Other than viscous and interfacial force, inertial force may become important when Ca reaches 10^{-2}, and during then, the film can be thickened to a certain portion of the channel diameter. This effect may be accounted for by the Weber number [202].

Table 2-4 Film thickness of gas-liquid systems in circular capillaries. (after Angeli and Gavriilidis [108]).

Dimensionless film thickness, δ/r	Range of Ca	Measuring technique
$0.5\,Ca^{1/2}$	$5 \times 10^{-5} \leqslant Ca \leqslant 3 \times 10^{-1}$	Movement of indicator bubble/conductimetry
$\left(0.89 - \dfrac{0.05}{U_g^{1/2}}\right)Ca^{1/2}$ U_g in cm/s	$7 \times 10^{-6} \leqslant Ca \leqslant 2 \times 10^{-4}$	Conductimetric technique
$1.34\,Ca^{2/3}$	$10^{-3} \leqslant Ca \leqslant 10^{-2}$	Volumetry
$0.36[1 - \exp(-3.08(Ca^{0.54}))]$	$9.5 \times 10^{-4} \leqslant Ca \leqslant 1.9$	Light absorption
$\dfrac{(1.34Ca^{2/3})}{1 + 2.5(1.34Ca^{2/3})}$	$10^{-3} \leqslant Ca \leqslant 1.4$	Video recording

2.5.1.2 Thin film in square microchannels

The film thickness of a gas-liquid system in square microchannels can be different from that in capillaries, especially when the Ca number is low (< 0.01), such as that shown in Figure 2.10 (D)-a. There are two regions of the thin film, i.e., a wall film region and a corner film region (or called 'gutter region'), which are of different dimensions [198]. Kolb and Cerro [199] measured the film thickness of both the wall film and on the diagonal direction (see Figure 2.10 (D)) at various Ca numbers. The results showed that the corner regions accounted for ~22% of the total cross-sectional area for the flow and the wall film thickness (δ_{film}) could be 0.08·r_s. Thulasidas et al. [203] measured the film thickness in a square capillary, and a dimensionless film thickness (δ_{film}/r_s) could range from 0.05 to 0.2 depending on the Ca number (0.022 to 1.11). The film thickness in square tubes has been also investigated in numerical simulations (e.g., Hazel and Heil [204]). Kreutzer et al. [197] summarized the data of these work and plotted the film thicknesses in wall film region and corner

27

region against the capillary numbers, see Figure 2.11. They noted that the results on the diagonal direction agreed well and even when the velocity was very low (approaching to 0) the film would not disappear; on the other hand, when Ca > 0.04 the bubble size would be uniform in diagonal direction and at the side wall (see Figure 2.10 (D)b), i.e., the bubble is axisymmetric. Additionally, a correlation of the bubble size in the diagonal direction was provided as follows

$$\frac{d_{b,B-B}}{d_{channel}} = 0.7 + 0.5\exp(-2.25Ca^{0.445}), \tag{2.14}$$

in which $d_{b,B-B}$ is the bubble diameter in the diagonal direction and $d_{channel}$ is the width of the square channel.
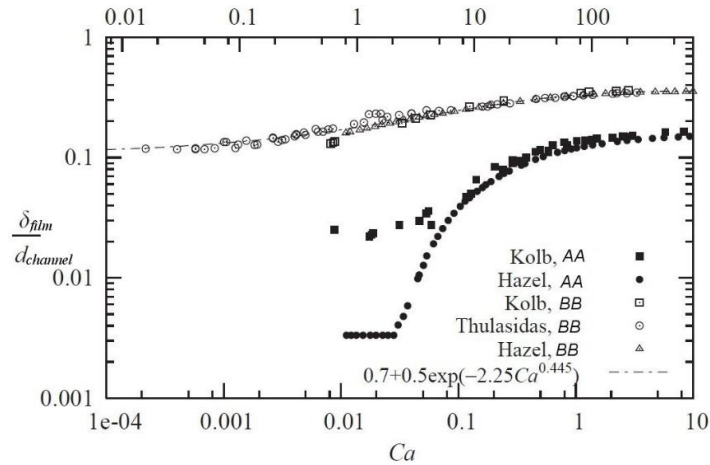
Figure 2.11 Film thickness versus Ca number in square microchannels (after Kreutzer et al. [197]).

Fries et al. [198] compared their experimentally measured film thickness in the corner by using confocal laser scanning microscopy and laser induced fluorescence with the predicated results by using equation (2.14), and found that the correlations provided slightly overestimated data. The deviations were more pronounced under low Ca numbers (< 0.001) when very short bubbles were presented. Nevertheless, the tendency of the film thickness in the corner region with Ca number was well predicted. Despite the limited resolution of the thin film in wall region (or say, in the observation plane), Fries et al. [198] approximated the film thickness in the wall region as $0.02 \cdot d_{channel}$ where the $d_{channel}$ is the hydraulic diameter of the channel. Using CO_2/water and N_2/water in a rectangular microchannel (aspect ratio is 2.68), Yao et al. [205] focused on inertial effects on the gas slugs formation and on the film thickness in both the wall region and the corner region, and argued that when inertial effects were significant (Weber number: 0.21 to 12.5) with a Weber number exceeding 3.1 the film thicknesses might be underestimated by the aforementioned models. This argument was

evidenced by their measurements under a Ca number over 0.01 together with significant inertia involved. Still, the previous models worked well when Ca < 0.01. However, inertia and geometry (e.g., represented by aspect ratio) can be two other important factors showing influence on the film thicknesses. As discussed by others [206,207], the effects of inertia and gravitational forces could be pronounced as well, especially when flow rates and dimensions were increased.

Other than experiments, numerical studies based on self-developed and commercial codes have been probing the effects of various factors on the thin film thickness, such as that summarized by Talimi et al. [208]. These numerical studies generally cover a Ca range of 0.001 to 10 for gas-liquid flows in microscale capillaries and square as well as rectangular channels. More information can be referred to this review and the references there. By comparing the dimensionless film thickness (relative to the channel hydraulic radius) between simulated results and model predicted ones, as shown by Abadie et al. [209] and Gupta et al. [196], the numerical methods could be reliable for providing more insights to the thin film.

Comparatively, liquid-liquid two phase flows in capillaries and square microchannels have not received equivalent attention as the gas-liquid counterparts in terms of both the thin film and the related hydrodynamics (e.g., pressure drop). In recent years, liquid-liquid two-phase flows, especially in a droplet/slug flow regime, have been increasingly reported in: (1) assisting the mass transfer based extraction between liquids (e.g., [210-212]), (2) facilitating the heat transfer from outside channel wall and among the liquids and the solid walls [213-215]. Focusing on the thin film in liquid-liquid systems, Kashid and Agar [216] estimated the pressure drop along a capillary by considering the wall film, of which the thickness was calculated based on Bretherton's law. Using laser induced fluorescence, Ghaini et al. [217] measured the wall film thickness of water/kerosene in a glass capillary (inner diameter (ID) = 1mm) and showed that the film were (0.006~0.016) times of inner diameter of the capillary. Jovanović et al. [218] measured the film thickness in a liquid-liquid slug flow and compared it to the predicted one by Bretherton's law, however, the measured data were mostly lower than the predictions. Additionally, there was an effect of the gravity which led to an asymmetrical distribution of the film thickness. A similar comparison was made by Gupta et al. [196]. In the sector of numerical simulations, liquid-liquid two-phase flows have not been studied extensively neither, as reviewed by Talimi et al. [208]. Despite of the efforts on slug formation and flow pattern studies, there are very limited insights into the issues such as thin film, pressure drop and heat transfer.

2.5.2 Pressure Drop

The pressure drop of gas-liquid flows in Taylor flow regime in micro capillaries and channels has been extensively investigated since 1960s [219]. The gas is typically a gas plug surrounded by the liquid (slugs as well as the thin film), and is mainly subjected to both a friction of the liquid and the pressure drop over the gas plug thanks to the surface tension along the curvature-featured front and back meniscus, as discussed by [197,198,220,221]. Comparatively, the pressure drop in liquid-liquid Taylor flows has not been studied at an equivalent scale [196,216,218,222]. As argued by Eain et al. [219], an increased viscosity of the drop phase in liquid-liquid flows relative to the gas counterpart in gas-liquid flows may result in a significant interfacial shear that shows effects on the pressure drop, which essentially complicates the pressure drop predication.

2.5.2.1 Pressure drop of liquid-liquid Taylor flow

Without considering the thin film, Kashid and Agar [216] proposed a theoretical model and dedicated the total pressure drop in micro capillary to be a sum of: (1) the frictional pressure drop of the drop and the continuous phase and (2) the interfacial pressure drop due to the curvatures of the drop meniscuses. As the thin film is considered, the pressure drop caused by this thin film is deemed a dominant one compared to the frictional pressure drop of the continuous phase and the interfacial one. The two cases discussed by Kashid and Agar [216] are summarized as follows

$$\Delta P_t = \begin{cases} = \Delta P_{fr,c} + \Delta P_{fr,d} + \Delta P_{in,d} = L_t \cdot \frac{8\eta_c \bar{v}(1-\alpha)}{R_h^2} + L_t \cdot \frac{8\eta_d \bar{v}\alpha}{R_h^2} + \frac{2L_t-(L+L_{s,w})}{(L+L_{s,w})} \cdot \frac{2\sigma}{R_h} \cos\theta_c, & \text{no film} \\ = \Delta P_{in,d} = \frac{1-\alpha}{1-(R_h-\delta)^4/R_h^4} \cdot \Delta P_{sin} & \text{with film} \end{cases}, \quad (2.15)$$

where the frictional pressure drops, i.e., $\Delta P_{fr,c}$ and $\Delta P_{fr,d}$, of the continuous and the drop phase can be determined according to assumptions of fully developed Hagen-Poiseuille flow of single phase. L_t, η_c, η_d, $\bar{v}$, α and R_h are the total length of the microchannel, dynamic viscosities, mean velocity of the flow ($\bar{v} = (Q_c + Q_d)/(DW)$), length fraction of the drop phase and hydrodynamic radius, respectively. The interfacial pressure drop $\Delta P_{in,d}$ can be calculated by the Young-Laplace equation, as shown by the third term on the right side of the expression under no film case, in which $(L + L_{s,w})$ indicates the length of a flow unit composed by a drop (L) and a continuous slug ($L_{s,w}$), and σ represents the interfacial tension. On the other hand, when the thin film of the continuous phase is considered, its thickness δ that may be estimated by the Bretherton's Law [220] together with Hagen-Poiseuille equation for the pressure drop of the single phase can be applied to calculate the total pressure drop.

Jovanović et al [218] pointed out the Kashid and Agar model could overestimate the pressure drop values, owing to (1) the interfacial pressure drop was calculated based on a constant static contact angle, however, an advancing and a receding contact angle might exist and be different from the one under a dry wall case; (2) the effects of the front and back meniscus of the drop on pressure drop were summed up, but should had been subtracted instead of being summed up since the contributions of these two meniscuses to the pressure drop in the flowing direction were contrary; (3) the superficial velocity of the continuous fluid was applied to determine frictional pressure drops, whereas the dispersed drop flowed faster than the continuous fluid due to the existence of the thin film. Based on the pressure drop model for a single bubble in a capillary proposed by Bretherton [220] and by accounting for the thin film thickness and velocity, Jovanović et al [218] developed a stagnant film and a moving film model of the pressure drop of a slug Taylor flow, as follows

$$\Delta P_t = \Delta P_{fr,c} + \Delta P_{fr,d} + \Delta P_{in,d} = L_t \cdot \frac{8\eta_c \bar{v}(1-\alpha)}{R_h^2} + L_t \cdot \frac{8\eta_d \overline{v_d}\alpha}{(R_h-\delta)^2} + \frac{L_t}{(L+L_{s,w})} \cdot 7.16(3Ca)^{2/3}, \quad \text{stagnant film,} \quad (2.16\text{-}1)$$

$$\Delta P_t = \Delta P_{fr,c} + \Delta P_{fr,d} + \Delta P_{in,d}$$

$$= L_t \cdot \frac{8\eta_c \bar{v}(1-\alpha)}{R_h^2} + L_t \cdot \frac{4\overline{v_d}\alpha}{[R_h^2 - (R_h-\delta)^2]/\eta_c + [0.5(R_h-\delta)^2]/\eta_d} + \frac{L_t}{(L+L_{s,w})} \cdot 7.16(3Ca)^{2/3}, \text{moving film,}$$

$$(2.16\text{-}2)$$

The model, particularly the moving film one as shown in equation (2.16-2), has been used in a few work [196,222,223] for comparisons with either experimental or numerical results. As reported, the moving film model works well only at low flow rates (resulted $Ca \ll 10^{-2}$) and for long drops which narrows the length difference between the thin film and the drop. But as the flow becomes faster, inertia effects start to challenge the validity of Bretherton's estimation of the interfacial pressure drop which is indeed overestimated. The overestimation by Bretherton's law further leads to an overestimation by using the moving film model, which has been evidenced by the comparisons with experimental data [222,223] as well as with CFD simulation data [73]. These comparisons suggest that a revision of the above factor accounting for a more accurate film thickness could improve the performance of the moving film model.

In a recent review [219], the above models were used to compare the calculated pressure drops to the experimentally measured ones. Not very surprisingly, neither of the models gave a within ±15% accurate prediction of the experimental results. The authors concluded that the models failed in correctly calculating the interfacial pressure drops because of not accounting for the inertia effects. In view of an obvious viscosity ratio (may be from 0.3 up to 100 relative to water) of the liquids in

liquid-liquid Taylor flows, pressure drop models specifically developed for gas-liquid flows might be applicable to liquid-liquid ones as well, depending on the viscosity ratio range.

2.5.2.2 Pressure drop of gas-liquid Taylor flow

For a single bubble in a round capillary, Kreutzer et al. [197] investigated the effects of drop length (as well as the continuous slug length), inertia and interfacial tension on the interfacial pressure drop of a bubble, and considered $\Delta P_{in,d}$ a function of: (1) non-dimensional length of the continuous slug L_c^* ($L_c^* = L_{s,w}/(2R_h)$), (2) the capillary number Ca of the bubble, and (3) the Reynold number Re calculated by the superficial velocity $\bar{v}$. A non-dimensional form of this model is given as

$$f_c Re_{\bar{v}} = 16 + \frac{a}{L_c^*}\left(\frac{Re_{\bar{v}}}{Ca}\right)^{0.33}, \tag{2.17}$$

where f_c is a friction factor of the continuous fluid. The first term on the right-hand side originates from a fully developed Hagen-Poiseuille flow of a single fluid; the factor 'a' in the second term is a constant that can be 2.72 or 1.12 according to experiments or numerical simulations, respectively. The discrepancy of 'a' between experimental and numerical results, as suggested, is thanks to the Marangoni effect caused by the impurities in the liquids applied in the experiments. Walsh et al. [224] proposed a revised factor of 'a' (a = 1.92) and noted that the two terms on the right-hand side of the model formulation (equation 2.17) stemmed from a single phase Poiseuille flow and an empirically derived Taylor flow limit, respectively. 'a = 1.92' was coincidently an average of those two values obtained by Kreutzer et al. from experiments and simulations [197]. Eain et al. [219] verified that the pressure drop model proposed by Walsh et al. [224] might be applicable to the liquid-liquid counterparts as well as long as there was a viscosity ratio $\eta_c/\eta_d > 4.5$. A more recent model of pressure drop for gas-liquid Taylor flows in round capillaries was developed by Warnier et al. [221]. This model considers similar issues as in Kreutzer's model. One difference between these two models is that the effect of the gas bubble velocity on the pressure drop is included in Warnier's model. Based on mass balance between the continuous slug and the gas bubble plus the thin film, Warnier's model is developed and incorporates the effect of a non-negligible thin film thickness in Bretherton's Law [202,220], it is specified as follows

$$\Delta P_t = L_t \frac{32\eta_c \bar{v_c}}{(2R_h)^2}\left[1 + \frac{7.16\times 3^{\frac{2}{3}}}{32}\frac{1}{L_c^*}\frac{A_c}{A_d}\frac{1}{(Ca_d^{\frac{1}{3}}+3.34Ca_d)}\right], \tag{2.18}$$

32

where A_c and A_d are the channel and the bubble cross sectional area, respectively. As shown by Eain et al. [219], this model yielded a better agreement than Walsh's model in spite of a few scatterings still out of its ±20% bandwidths. In fact, Eain et al. [219] suggested a curvature parameter of 8.16 instead of 7.16 to be used in order for an improved approximation. This modification results in a modified Warnier's model. As a result, Warnier's model extends the application range: $1.45 \leq \text{Re} \leq 567.59$, $4.5 \times 10^{-5} \leq \text{Ca} \leq 0.067$, $0.76 \leq L_c^* \leq 46.83$, $1.05 \leq L_d^* \leq 14.25$, and can be applicable to liquid-liquid Taylor flows in micro capillaries as well. Nevertheless, as noted by Warnier et al. [221], one part of their model is based on the work of Bretherton [220] and that of Aussillous and Quéré [202]. Thus the model is unlikely to be applicable to circumstances such as non-axisymmetric channels, non-laminar flows of continuous phase, strong inertia, nor non-ignorable velocity of the thin film that separates the bubble from touching the channel wall.

2.5.3 Speeds of Taylor Bubbles/Drops

As a consequence of the thin film and the pressure drop in the flow direction, the moving speed of the Taylor bubble or droplet in either a capillary or a square microchannel can be distinguished from that of the neighboring continuously flowing slug. A dimensionless number, m, is usually used to characterize the motion of the bubble/drop relative to the superficial slug speed, as expressed below

$$m = \frac{v_d - v_s}{v_d}, \tag{2.19}$$

in which v_d and v_s are the moving speed of the bubble/drop and the averaged slug speed (from the total flow rates of both fluids), respectively. Fairbrother and Stubbs [225] correlated m with Ca as m = $1.0 \cdot \text{Ca}_d^{1/2}$, which was valid for $7.5 \times 10^{-5} < \text{Ca}_d < 0.014$. Based on an analytical approach, Bretherton [220] showed that m was correlated to Ca as m = $1.29 \cdot (3\text{Ca}_d)^{2/3}$ for inviscid bubbles in circular capillaries under a Ca number smaller than 0.01. However, in rectangular microchannels, thin film is very different from in capillaries (see Figure 2.10 (D)a). A gutter region other than the wall film region does contribute to the flow of the carrier fluid, especially when Ca number is over 0.01 the gutter region is featured by a fraction of the liquid flow [203]. Wong et al. [226,227] showed that the liquid flux in the gutter region was in the same direction as the bubble flowing in the rectangular channel and was higher than that of the wall film region by an order of Ca_d. Thus, the dimensionless bubble speed in terms of m can be formulated as m $\propto$ (-$\text{Ca}_d^{1/3}$), which indicates that the bubble flows slower than the carrier fluid. A similar result was reported by Sarrazin et al. [228] that m = $(0.52\text{Ca}_d^{0.32})$ for $10^{-4} < \text{Ca} < 1$.

The droplet speeds determined by being correlated with $Ca_d^{2/3}$ and $(-Ca_d^{1/3})$ are only different within 6% for $10^{-6} < Ca < 1$ [229]. Moreover, an addition of surfactants may slow down the bubble speed compared to without using surfactants [230], which was attributed to a retardation effect caused by the Marangoni stresses. A comprehensive experimental study on the effects of capillary number, droplet size and viscosity contrast on dimensionless droplet speed (v_d/v_s) was done by Jakiela et al. [231]. Shown by figure 4 in their work, v_d/v_s is generally lower than 1 for droplet size $L/W > 2$ at a viscosity contrast (of drop phase over carrier fluid) of 0.3.

In a short summary, a series of factors including geometries, capillary numbers, bubble/droplet sizes, viscosities of involved fluids and with or without surfactants can influence the relative bubble/droplet speed, which may be slightly faster or slower comparatively.

2.5.4 Flow Fields

Interfacial effects and the presence of a thin film for gas-liquid and liquid-liquid two phase flows in microscale devices highlight the roles of viscous forces and interfacial tension. These two factors further lead to the circulating motion within both the liquid slugs and the droplets. The internal circulations are of enormous significance to the mass and heat transfer within the individual segments as well as across the interface where the diffusion could be enhanced by the convective circulations.

Taylor made qualitative sketches of the flow streamlines in liquid slugs that were ahead of long bubbles [200]. Three different streamlines were suggested depending on the m (see equation (2.19)) values, as shown in Figure 2.12. When m > 0.5 at a high Ca number, a complete bypass flow of the liquid surrounding the bubble was formed and a stagnation point emerged at the front head of the bubble, as shown in Figure 2.12 (A)a; when m < 0.05 at a low Ca number, due to a much thinned film, two possible flow streamlines in a reverse direction might be possible, one featured with a stagnation ring at the front head of the bubble (shown by Figure 2.12 (A)b) and the other one featured with two stagnation points that were on the head of the bubble and on the back cap of the slug (shown by Figure 2.12 (A)c). Cox [232] obtained the streamlines shown by Figure 2.12 (A)a and (A)b in experiments; Martinez and Udell [233] as well as Westborg and Hassager [234] computed the same streamlines in numerical simulations. However, the third streamline pattern (Figure 2.12 (A)c) was never confirmed by experiments [235]. Despite of the experimental void, Giavedoni and Saita [236] obtained not only the first two but also the third streamline pattern in a numerical study, as shown in Figure 2.12 (B). Heil [237] numerically studied the effects of inertia on the streamlines in the liquid slugs and showed that they were changed to a closed vortex when Re number reached 20 and the

34
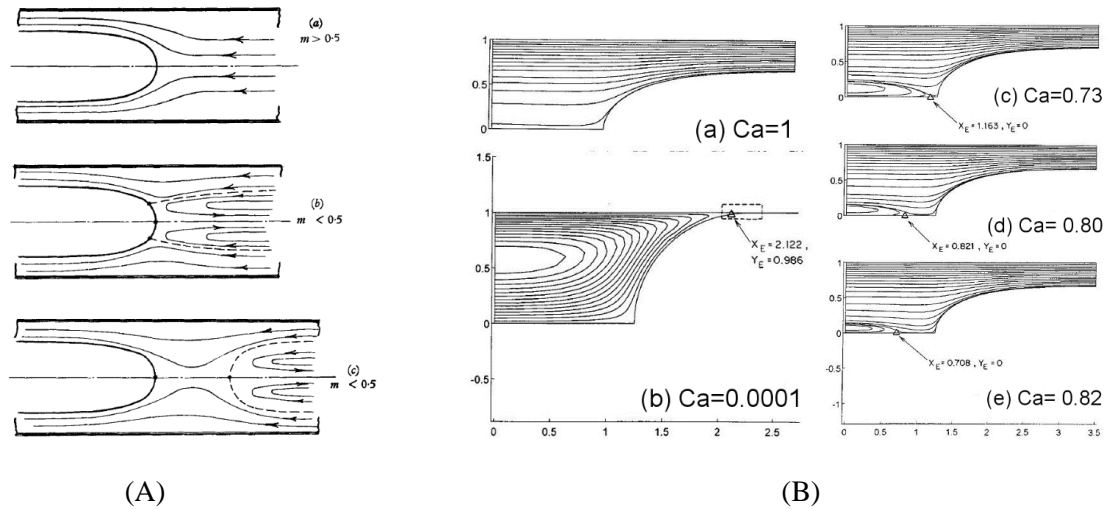
Figure 2.12 Streamline patterns in the liquid slug displaced by a long bubble: (A) qualitative sketches by Taylor [200]; (B) computed streamlines at various Ca numbers (Giavedoni and Saita [236]).

vortex size was smaller as distance was larger from the bubble head. Thulasidas et al. [235] provided an analytical model of the velocity in the liquid slug and experimentally showed the velocity profile of the Taylor flow in liquid slugs in circular capillaries and square cross sectional ones. A complete bypass flow for horizontal flow occurred at Ca = 0.7. For long liquid slugs, the velocity profile was found to be one of Poiseuille flow; but for short slugs the streamlines were curved. These findings had been verified by Taha and Cui [207] who numerically investigated the flow field in the liquid slug ahead of a gas bubble in a Ca range of 0.03 to 1.34. In a follow-up study, Taha and Cui [238] focused on the slug flow in square microchannels and showed the influence of Ca numbers on the bubble profiles on in-plane direction and on diagonal direction as well as the flow fields in the slugs. Increasing Ca numbers from 0.04 to 0.4 and up to 1.35 resulted in a similar streamline transition as that shown in Figure 2.12 (B), and a cross sectional shape transition from an octagon-like to a circular was found as well.

Different from the conventional semi-infinite analysis of the flow field in slugs, liquid slugs enclosed by two bubble meniscuses (one is the front meniscus of the back drop and the other is the back meniscus of the front drop in the flow direction) as well as the inner flow field are of great interests to those who focus on the bubble-train flows (i.e., Taylor flow). Günther et al. [239] quantified the instantaneous recirculation motions in the liquid slugs in straight microchannels and meandering ones using microscopic particle imaging velocimetry (μPIV), as shown in Figure 2.13.

35

Their findings, on the other hand, quantified Thulasidas et al.'s claim about the curved streamlines in short liquid slugs.

However, for liquid-liquid micro segmented flows, there are limited studies dedicated to the internal flow fields of the droplets (liquid), which has been improved only from the last decade and driven by the applications of µPIV or even confocal µPIV. PIV (particle imaging velocimetry) is a non-instructive optical method in which particle (also called 'tracer') distributions are recorded between two consecutive time frames and flow velocity can be determined by calculating the displacements of particles over the time period [240]. Kashid et al. [241] visualized the internal circulations in both water and oil slugs using PIV combined with CFD simulations under different velocities. They reported two zones in both slugs, i.e., a recirculation zone in the centers of the slugs and a stagnant zone (zero velocity). Similarly, Sarrazin et al. [242] reported the internal circulations in water droplets by using both µPIV and numerical simulations; their 2D simulations results were

(A)

(B)
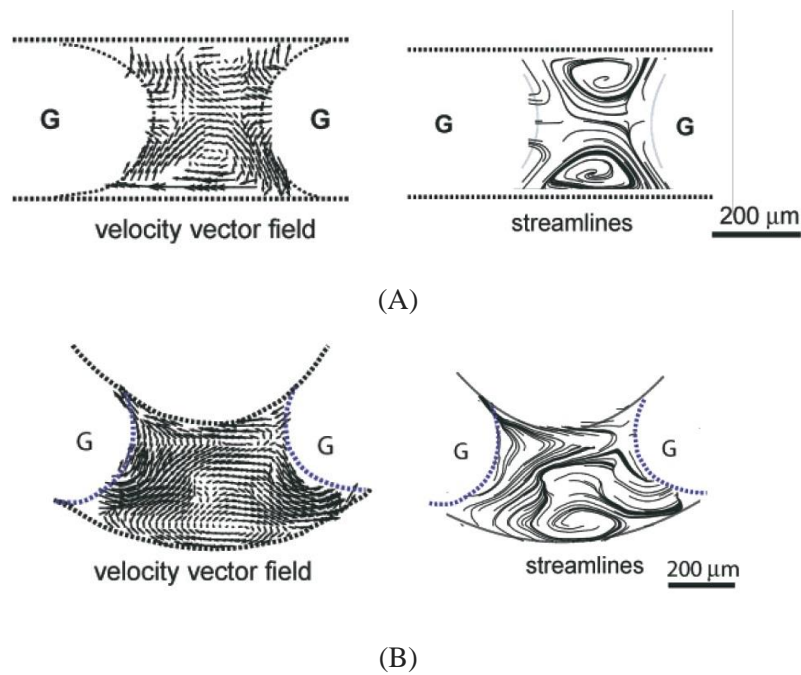
Figure 2.13 Velocity fields in a liquid slug in (A) a straight square microchannel and (B) a meandering square microchannel. Channel width and depth are 400 µm and 280 µm, respectively. (after Günther et al. [239]).

approximately in accordance with Kashid et al.'s results. They also showed the velocity fields in a 3D scenario, i.e., on the cross sectional profile as well as at different depth values. By using a confocal µPIV system, Kinoshita et al. [243] conducted 3D measurement and visualization of the flow field of

a moving droplet in a rectangular microchannel. This was a comprehensive (probably also the first) study on the flow profile of a hydrodynamic droplet in microchannel. Figure 2.14 shows the velocity streamlines depicted by Kinoshita et al. in multiple cross-sections ('x-y' plane) of a droplet at four different focal depths ('z' positions). van Steijn et al. [244] showed transient velocity fields in the continuous fluid when it was pinching off the dispersed phase into droplets using µPIV, which assisted in elucidating the mechanisms of droplet/bubble generations. Malsch et al. [245] used µPIV and studied the internal flows in long water segments flanked either by smaller air segments or long
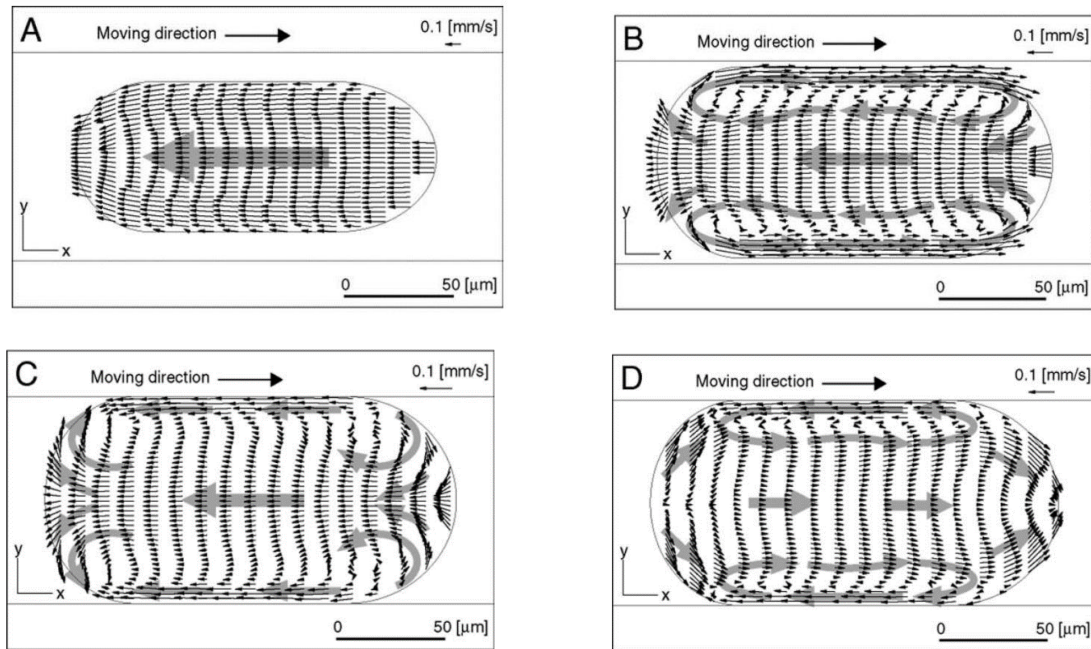
Figure 2.14 Velocity streamlines of a moving droplet at (A) 2µm above the channel bottom wall, (B) 12µm above the bottom wall, (C) 22µm above the bottom wall, and (D) the middle cross section of the droplet, respectively, where channel depth is 58µm (perpendicular into paper). The arrow on the top right of each graph indicates a reference vector. (after Kinoshita et al. [243]).

oil segments, and dedicated the internal flows in water segments to liquid/wall frictions and liquid/liquid frictions, respectively. They also revealed and quantified the internal flows in small water segments during transports in a straight and a meandering microchannel, as shown in Figure 2.15. However, as discussed in Figure 2.14, a focus on an unspecified plane may render a slightly different velocity profile, which may be a drawback of conventional PIV.

More specially, separate and simultaneous measurements of the internal flows in both droplets and

liquid slugs for liquid-liquid two phase microflows have also been achieved by using different tracers in both liquid segments. However, special attention should be paid on differentiating the fluorescent signals from the different tracer particles in order to obtain undistorted flow profile in the interfacial regions. Such simultaneous measurements of flow fields in both segments will not be discussed in details here, but are referred to the work performed by other researchers, such as Miessner et al. [246] and Oishi et al. [247].

(A)   (B)
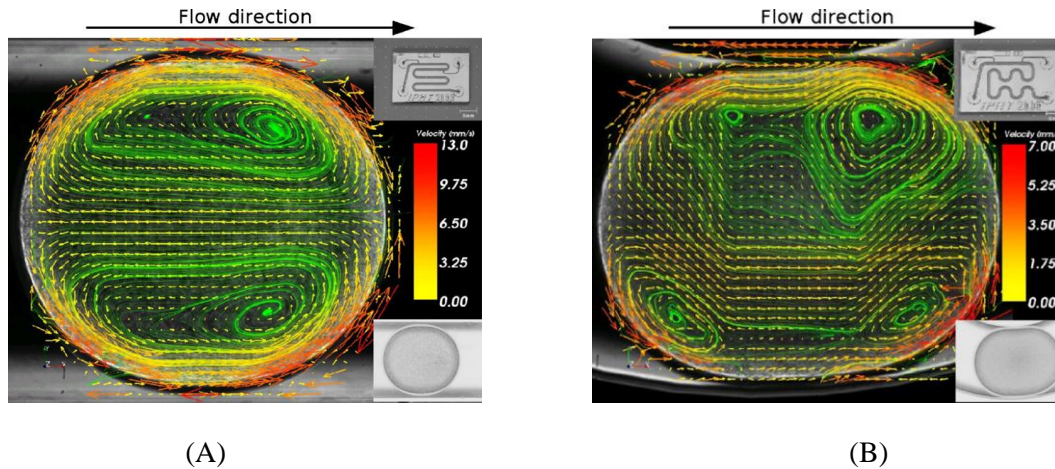
Figure 2.15 Flow fields inside small water segments when they transport in a straight microchannel and a meandering one, respectively. (after Malsch et al.[245]).

2.6 Equation of State (Eos) for Taylor Droplets/Bubbles

In the scope of thermo-physics, an equation of state (Eos) formulates the relations among pressure, temperature and density of substances. Following the themes in previous parts, the discussions here are limited to pure fluids that are normally encountered in the field of two-phase microfluidics and that have been used as either a gas phase or a liquid one.

When a very general dispersed fluid is considered, it might be either a bubble or a droplet surrounded by a continuous liquid in the Taylor flow. Thus it is necessary to use a more applicable equation of state (Eos) to describe the dispersed fluid rather than using the classical ideal gas law. Cubic equations, among other equations, of state in a form of a cubic function of molar volume (the volume of a mole gas or liquid) have been proposed and developed in the past 140 years to correlate pressure, volume and temperature together for a given quantity of substance within a system, to name a few, the Van der Waals Eos [248], the Redlich-Kwong Eos [249], the Soave-Redlich-Kwong Eos [250], Peng-Robinson Eos [251], volume-translated Eos [252,253] and Patel-Teja Eos [254]. Despite

such many cubic Eos, as discussed by a review work [255], a generic cubic equation of state may be written as

$$P = \frac{RT}{V_m - b} - \frac{c}{V_m(V_m + d) + e(V_m - d)}, \tag{2.20}$$

in which b, c, d, and e are constants or functions of the temperature as well as fluid properties (e.g., acentric factors, critical compressibility factors, etc.); P, V and T are pressure, volume and temperature, respectively; R is the universal gas constant. The first term and the second term on the right-hand side of the above equation indicate a repulsion pressure and an attraction pressure, respectively. Among the numerous cubic Eos, but are not limited to the above-mentioned ones, the Soave modified Redlich-Kwong Eos (also called Soave-Redlich-Kwong Eos) and the Peng-Robinson Eos are the most frequently applied cubic equations in research related to the thermo-physical and vapor-liquid equilibrium (VLE) properties. Moreover, as compared by Peng and Robinson [251] between their calculated vapor pressures of pure substances and equilibrium ratios of mixtures and those calculated by Soave-Redlich-Kwong Eos, Peng-Robinson Eos provided slightly more accurate agreements with the experimental data. Therefore, the equation of state proposed by Peng and Robinson is going to be applied in this thesis to correlate the volume change (viz., drop length change) with the pressure drop over the micro channel. Peng and Robinson's equation is provided below

$$P = \frac{RT}{V_m - b(T_c)} - \frac{c(T_c)\beta(T_r,\omega)}{V_m[V_m + b(T_c)] + b(T_c)[V_m - b(T_c)]}, \tag{2.21}$$

in which

$$b(T_c) = 0.07780 \frac{RT_c}{P_c}, \qquad c(T_c) = 0.45724 \frac{R^2 T_c^2}{P_c},$$

$$\beta(T_r, \omega) = [1 + (0.37464 + 1.54226\omega - 0.26992\omega^2)(1 - T_r^{0.5})]^2, \tag{2.22}$$

where P_c, T_c and V_m are the critical pressure, the critical temperature and the molar volume (V_m: volume/moles), respectively; $\beta(T_r, \omega)$ is a non-dimensional function of temperature ratio T_r ($T_r = T/T_c$) and an acentric factor 'ω' of the specific substance ('ω' for common hydrocarbons and N_2, CO_2, H_2S are referred to the figure 2 in Peng and Robinson's original paper.). Assuming the temperature (T) is a constant, equation (2.21) for a known fluid becomes an equation with two unknown variables, i.e., P and V_m. Furthermore, two such equations may be available at the starting point and the ending point of the straight channel.

2.7 Mass Transfer: Dimensionless Number and Models

Mass transfer, as one of the three main subjects of transport phenomena, describes the mass transport from one position (or region) to another that may be driven by gradients of concentration, electrical potential, pressure and/or temperature, and may occur in one single phase (e.g., gas, liquid, or even solid) or across the phase boundaries in multicomponent systems [256]. Mass transfer can be found broadly in various physical and chemical processes, such as gas absorption [257] (mostly in liquids), liquid evaporation [258], liquid-liquid extraction [259] and, for many cases, chemical reactions [260,261]. Revealed by two prevalent models of mass transfer, namely, the film model [262] and the penetration model [257] developed on gas-liquid absorptions, molecular diffusions of the (gas) solute across the interface and exposure time of the liquid to the solute at the interface are two controlling mechanisms of the mass transfer performance when diffusion is a key process in the mass transfer, especially in microscale devices. These findings indicate that a controlling of the mass transfer in two phase microfluidics can be achieved by regulating the molecular diffusion and contacting time from the aspect of either the geometry, the fluid property or the operation conditions [263].

Generally, mass transfer is coupled with hydrodynamic processes and heat transfer. In order to characterize the mass transfer, dimensionless numbers are usually applied, which are analogous to those introduced in 2.2.1 about the forces in fluidics. Two prevalent models, namely, thin film model and penetration model of the interfacial mass transfer have been proposed by Whitman [262] and Higbie [257], respectively. In this section, common dimensionless numbers and models related with mass transfer are introduced. Note that, although most of the dimensionless numbers relevant to mass transfer are introduced, discussions of the mass transfer here are focused on fluids with a presence of interface, or more specifically, for gas-liquid and liquid-liquid systems without chemical reactions.

2.7.1 Dimensionless Numbers

As discussed by Kashid et al. [264], the definitions of the dimensionless numbers used for mass transfer in two phase coexisting cases are generally adapted from the single phase system, which may be dependent on the physical properties of either the gas, the liquid or the averaged properties of both.

In the context of mass transfer, Péclet number (Pe) is defined as a ratio of the transport rate driven by advection via fluid flow over that driven by diffusion. It is formulated as below

$$Pe = \frac{vd}{D_{diff}},$$
(2.23)

in which v is the local flow velocity, m/s; d is the characteristic length, m; and D_{diff} is the diffusion coefficient (or called 'diffusivity') of the diffused species (e.g., gas or liquid molecules) in the liquids, m^2/s. According to Fick's first law [265], diffusion coefficient is defined as a ratio of the diffusion flux (an amount of the substance transported though a unit area during a unit period of time) under a concentration gradient driving the diffusion. Based on the Re and the Pe number, a third dimensionless number, namely, Schmidt number (Sc) can be introduced as follows

$$Sc = \frac{Pe}{Re} = \frac{\eta/\rho}{D_{diff}},$$
(2.24)

which is a ratio of the kinematic viscosity (also called 'momentum diffusivity', η/ρ, m^2/s) and mass diffusivity D_{diff}. It characterizes a relative strength between the diffusivity of the momentum and that of the mass. For a general two phase coexisting case, Sherwood number (Sh) is often applied to evaluate the competition between the convective mass transfer and the molecular diffusion, which are along and across the interface, respectively. It is an equivalent in mass transfer of Nusselt number. Sherwood number is defined as a ratio below

$$Sh = \frac{k}{D_{diff}/d},$$
(2.25)

where k is a convective mass transfer coefficient, m/s. According to the theoretical work and the experimental data from Ranz and Marshall [266], Sherwood number (Sh) can be related to Re and Sc as follows

$$Sh = 2 + 0.6(Re)^{1/2}(Sc)^{1/3}.$$
(2.26)

Based on an analogy to those dimensionless numbers in heat transfer, mass transfer Fourier number (Fo_m), mass transfer Biot number (Bi_m) and Lewis number (Le) are introduced and defined as follows

$$Fo_m = \frac{D_{diff}t}{d^2},$$
(2.27)

$$Bi_m = \frac{k_{bl}}{D_{diff}/d_{in}},$$
(2.28)

$$Le = \frac{\alpha}{D_{diff}},$$
(2.29)

in which k_{bl} and d_{in} are the mass transfer coefficient in a boundary layer and an internal characteristic length in the mixture; α indicates the thermal diffusivity (m^2/s). The above three dimensionless numbers are indicators of: (1) relative rate of species diffusion over species storage, i.e., Fo_m; (2) relative resistance of internal species transfer over that in the boundary layer, i.e., Bi_m;

and (3) relative strength of thermal diffusivity over mass diffusivity, i.e., Le. However, they are usually of interest when both mass and heat transfer are considered, and mostly, in a mixture composed of various species.

In addition, mass transfer may proceed simultaneously with chemical reactions when chemical reactions are involved. A dimensionless number, i.e., Hatta number (Ha), is generally used to compare the reaction rate with the diffusion rate, as shown below,

$$Ha = \frac{\sqrt{k_r D_{diff}}}{k},$$ (2.30)

where k_r is a constant which quantifies the reaction rate. Note that the above definition is dedicated to the first order reaction kinetics, thus k_r has a unit of s^{-1}. A similar dimensionless number comparing the reaction rate with the diffusion rate is the second Damköhler numbers, Da_{II}, which is defined below

$$Da_{II} = \frac{k_r C_0^{n-1}}{k},$$ (2.31)

in which C_0 is an initial concentration and n is the order of the reaction.

2.7.2 Mass Transfer Models

For interphase mass transfer in gas-liquid and liquid-liquid systems, diffusion plays a key role in mass and species transport across the interface. The descriptions of diffusion can be carried out based on Fick's law of diffusion using diffusion coefficients or based on an approach using mass transfer coefficients. Using the former and the latter approach, however, usually yield more distributed parameters (e.g., concentrations at specific positions and time) and lumped parameters (e.g., averaged concentrations of solute in solvent), respectively [267]. Nevertheless, for engineering problems, mass transfer coefficient oriented approaches seem to be reliable enough to provide quantitative insights, particularly in a complex multiphase system. In this section, the definition of mass transfer coefficient is introduced first. Three commonly applied models of interfacial mass transfer are briefly introduced and discussed.

2.7.2.1 Mass transfer coefficient

Given with an interface, the mass transfer proceeds from one side and further into the other side of the interface which might be a well-mixed solution. The transfer amount of the mass or species per unit time is proportional to the interfacial area and a concentration difference, as shown below

$$\dot{N}_{0-1} = kA_i(c_0 - c_1), \tag{2.32}$$

where $\dot{N}_{0-1}$ is the mass transfer rate, mol/s; A_i is the interfacial area, m^2; c_0 and c_1 are the concentration at the interface and the bulk solution, respectively, mol/L. The proportionality k is called a mass transfer coefficient, m/s. Note that k here is subjected to both diffusion and convection which collaboratively contribute to the mass transfer. The definition of mass transfer coefficient in equation (2.32) is correlated with concentration difference and is a simple way to characterize the transfer performance, along with other common definitions of mass transfer coefficients based on partial pressure, molar fractions etc. However, it may be ambiguous due to inappropriately defined or selected concentration difference, interface area and even diffusion induced convection normal to the interface that may distort the concentration profile, as argued by Crussler in his book [267].

2.7.2.2 Thin film model

Thin film model (maybe also called 'stagnant film' model) is one of the two micro-models for describing the interphase mass transfer [262,264]. In this model, a hypothetical stagnant film exists at the interface which facilitates the diffusion of the solute from the gas phase to the bulk liquid, see Figure 2.16 (A). The interface is characterized with a concentration c_0 (which is high enough to neglect any diffusion induced convection that is normal to the interface), and the bulk liquid has a concentration of the gas solute of c_1 where a well mixing exists. Thus a diffusion dominated mass transfer through the film can be described by equation (2.32). However, it may also be described by Fick's first law, as shown in equation (2.33),

(A)   (B)
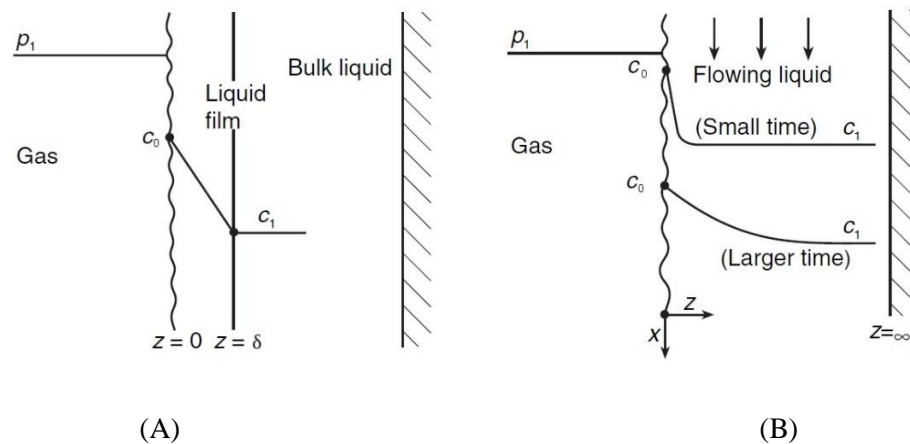
Figure 2.16 Schematics of two models for interphase mass transfer: (A) a thin film model and (B) a penetration model. (after Crussler [267]).

43

$$\dot{N}_{0-1} = \frac{D_{diff}}{\delta} A_i (c_0 - c_1), \tag{2.33}$$

where δ is the film thickness. Therefore, the mass transfer coefficient k can be determined by $D_{diff}/$ δ. Despite its simplicity and straightforwardness, this model is difficult for use since the film thickness δ is difficult to be predicted since δ is subjected to multiple factors, such as geometry, physical properties of both fluids and operation conditions.

2.7.2.3 Penetration model

The second micro-model is called penetration model, which was proposed by Higbie [257], as shown in Figure 2.16 (B). The film is assumed thick and a semi-infinite liquid; additionally, diffusion across the interface dominates over convection in the z direction (i.e., perpendicular to the interface) while convection is a dominant mass transfer mechanism in comparison to diffusion in the x direction (i.e., the flow direction). At the interface, the overall mass transfer can still be characterized by equation (2.32). Besides, according to Crussler [267], an averaged interfacial flux over x can be calculated from below

$$\dot{N}_{0-1} = 2\sqrt{D_{diff}/[\pi \left(\frac{L}{v_{x=0}}\right)]} A_i (c_0 - c_1), \tag{2.34}$$

in which L is the film length of interest in the x direction, and $v_{x=0}$ is a liquid velocity at the interface. Thus the term $(L/v_{x=0})$ quantifies the contact time of the liquid with the gas. Therefore, the mass transfer coefficient k is determined by $2\sqrt{D_{diff}/[\pi(L/v_{x=0})]}$. It is clear that the contact time of the two fluids are a key parameter to deduce the mass transfer coefficient, which is related with the hydrodynamic properties, such as interface length and velocity.

When a dynamic system is considered, the penetration model may be more realistic than the thin film model since it considers the effect of the hydrodynamics. A film-penetration model combining the two models has been proposed and applied, and has been proved mutually complementary with each other [268].

2.7.2.4 Two film model

In the thin film model, only the diffusion process in the liquid film is considered. However, when the diffusion at the gas side is required to be considered (e.g., in a much diluted gas phase), a second layer other than the thin liquid film on the other side of the interface is formed, which was exactly introduced in Whitman's original paper [269]. The two films separated by the interface lead to the

two film model, as schematically shown in Figure 2.17. Here, phase 1 and phase 2 are by default a gas phase and a liquid phase, respectively. Film 1 and film 2 are characterized by the thickness of δ_1 and δ_2, respectively. The mass transfer from the gas phase to the liquid phase is driven by the diffusion through the two films in sequence. In film 1, diffusion of the gas solute is achieved due to a partial pressure gradient from p_1 to $p_{1,0}$, and a concentration $c_{2,0}$ at the interface results from the interfacial partial pressure $p_{1,0}$. In film 2, diffusion is propelled by a concentration gradient from $c_{2,0}$ to c_2.
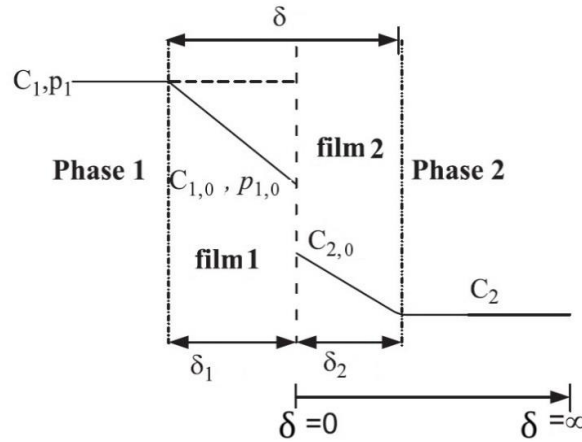
Figure 2.17 Schematic of the two film model for mass transfer (adopted and revised from Kashid et al. [264]).

The overall diffusion process can be described as follows

$$\dot{N}_{1-2} = k_1 A_i (p_1 - p_{1,0}) = k_2 A_i (c_{2,0} - c_2) = k_2 A_i (\frac{p_{1,0}}{H} - c_2), \tag{2.35}$$

in which k_1 and k_2 are the gas phase and the liquid phase mass transfer coefficient, respectively. Note that the interfacial concentration $c_{2,0}$ has been specified as a ratio of the interfacial partial pressure $p_{1,0}$ and a constant H (Henry's constant) according to Henry's Law. On the other hand, the total process can also be analyzed based on equation (2.32), i.e.,

$$\dot{N}_{1-2} = k_{1-2} A_i (c_1 - c_2), \tag{2.36}$$

Integrate the above two equations provides

$$k_{1-2} = \frac{1}{\frac{1}{k_1 H} + \frac{1}{k_2}}, \tag{2.37}$$

where k_{1-2} is an overall mass transfer coefficient. In a similar way, when liquid-liquid systems are considered, the overall mass transfer coefficient may be determined in such a way

45

$$k_{1-2} = \frac{1}{\frac{1}{k_1 K} + \frac{1}{k_2}}, \tag{2.38}$$

in which K is a partition coefficient that is defined by a ratio of the solute concentration in liquid 1 over that in liquid 2.

2.8 Summary

Working with two phase microfluidics is always complicated in comparison to working with a single phase flow, which is mainly due to the interface between phases. An overview of the involved forces and interfacial effects is provided first. Some common geometries which have been frequently applied to facilitate two phase immediate interactions and flows are introduced; some typical flow regimes of gas-liquid and liquid-liquid flows are reviewed; and the underlying mechanisms of the common regimes, particularly of the bubbly/droplet flows, are simply summarized. As a further step, several key hydrodynamic properties of Taylor-type bubbles and droplets in microchannels are discussed, including the thin film isolating those segments from contact with the solid wall, the pressure drop in microchannel under presences of thin film and segments, the flow velocity of the segments, and lastly, the internal circulating motions within slugs and droplets. In order to describe the disperse phase – either gas or liquid, a more general and appropriate equation of state is briefly introduced. Last but not the least, mass transfer which has been focused in microfluidics in recent ten years, is introduced. Instead of reviewing the extensive examples, the discussions in this section of this chapter were on the fundamental aspects of the interphase mass transfer, including some typical dimensionless parameters and three classical models of the mechanisms.

Chapter 3

Experimental System: Building and Optimization

This chapter details an experimental system building which is dedicated to two phase microfluidic studies, especially to those related to extreme pressure/temperature conditions. The unique requirements of this experimental system pose great technical challenges from two aspects, i.e., (1) extreme-pressure-temperature resistant and (2) leakage-free over the total flow paths of the fluids. Moreover, these two requirements ought to be simultaneously met. On the premise of these two requirements, reliability (i.e., no clogging of the micro-device in particular), flexibility (i.e., modulation in order for readily manipulating, such as a change of a component) and coordinability (especially between two connected modulations) are several main goals at the end of the experimental system building. Accordingly, relevant optimizations are carried out after the initial building efforts.

3.1 Common Materials for Microfluidic Devices

Microfluidic devices have been increasingly used in the research fields of biology, chemistry, biochemistry and biomedical as analytical systems and production tools. Multiple materials including silicon, glass, stainless steel, ceramics, and polymers can be used to fabricate the microsystems [270]. In order to choose a suitable material, several factors should be considered, such as mechanical strength, surface chemistry, optical properties, biocompatibilities, temperature or pressure characteristics, costs and the amenabilities to production of the candidate materials. There is no versatile material for all the microfluidic applications. Generally, for particular requirements of an application, one type of material may be preferential over others because of one or more preferred properties. In this section, the pros and cons of several commonly used microfluidic materials, such as silicon, glass and polymers (e.g., poly (dimethyl siloxane) (PDMS), poly(methyl methacrylate) (PMMA) and polycarbonate (PC)) are introduced, which may be referred to for choosing proper materials to fabricate microfluidic devices.

3.1.1 Silicon

In the past several decades, silicon has been used to produce sensors, actuators and microsystems, which promoted the development of electronics, especially the microelectromechanical systems (MEMS). Typical physical properties silicon are shown in Table 3-1 [271]. As can be seen, silicon has a high ratio of mechanical strength over density and excellent temperature characteristics

[270,271]. It is mechanically stable when the temperature in application is below 600°C. Even the deformation of silicon occurs, it either returns to the original form or breaks. The mostly used silicon for microsystems is a monocrystal type. Monocrystalline silicon offers some advantages in terms of mechanical properties, such as simple structure, anisotropic piezoresistivity and etching behaviors [271]. Moreover, silicon, compared with polymers, has excellent chemical resistance and low permeability because of the constituent element carbon and a cubic molecular structure. On the other hand, there are some drawbacks of silicon. A small scratch on the surface of the monocrystalline silicon may cause a crack of the whole silicon body due to mechanical strains. Even worse, there is no grain boundaries to cease the break [271]. Therefore, the surface quality of silicon determines a maximum load. Despite a piezoresistive effect, silicon is not piezoelectric. Generally, a piezoelectric thin film is deposited on silicon for piezoelectricity required on silicon sensors or actuators. Silicon is generally an expensive material compared with polymers. Moreover, it is non-transparent in the visible/UV spectral region, which disables an optical detection or visualization [272]. Other disadvantages lie in etching and sealing issues. The micromachining techniques of silicon are mainly wet chemical anisotropic etching, dry gas phase etching (e.g., reactive ion etching (RIE)) and surface micromachining using a sacrificial layer.

Table 3-1 Physical properties of silicon (adopted from Lang [271]).

Crystal structure	Cubic, diamond lattice
Density	2.3 g/cm^3
Atomic density	5×10^{22} cm^{-3}
Yield strength (Breaking)	1000 MPa
Yield strength (Recommended value for Layout)	100 ~ 200 MPa
Piezo-resistive coefficient k	l60 GPa
Elastic modulus	-120 ~ +120
Thermal conductivity	150 W/m·K
Thermal expansion	2.5×10^{-6} K^{-1}
Thermoelectric coefficient c-Si	800 - 1100 µV/K

Table 3-2 Pros and cons of silicon for microfluidic devices.

	Silicon as a material for microfluidic devices	
Pros	Excellent mechanical rigidity and temperature stability; Anisotropic piezoresistivity and etching behaviors; Excellent chemical resistance; Low permeability; Easy assembly.	
Cons	Mechanically fragile; No piezoelectric effects; High costs; No optical transparency; Wet and dry etching are expensive and time consuming; Sealing process requires clean room, high voltages and temperatures; Only two dimensional geometries.	

However, these etching methods are relatively expensive and time consuming as well. Mostly, sealing silicon-based devices requires a cleanroom environment, during which high voltages and high temperatures are applied [272]. The pros and cons of silicon as a material for microsystems are summarized in Table 3-2.

3.1.2 Glass

Glass is another popular material for fabrication of microfluidic devices. Some reported types of glass include soda lime glass, borosilicate glass (or in a commercial name 'Pyrex') and magneto-optical glasses [273]. Glass shares many similarities with silicon in terms of material properties, such as excellent mechanical rigidity, temperature stability, chemical resistance and low permeability. According to Becker et al. [274], fused quartz has a relatively high thermal conductivity and a high melting point (1665℃). One advantage of glass over silicon is optical transparency, especially when optical detection of particles or visualization of the flow field are required. Some reported glass based microfluidic devices have a certain number of microchannels and compartments at the inlet and outlet which are used to facilitate the feeding of samples and buffer solutions [275]. Glass is biocompatible and is inert to most chemicals employed in biochemical analyses. It has also been proved that glass systems are particularly suitable for separating and sequencing DNA [276,277]. However, glass has some disadvantages. Because of an amorphous molecular structure of glass, the vertical sidewalls in

glass are more difficult to be etched than in silicon [272]. As suggested by McCreedy [278], non-parallel walls may result from glass etching. As the microchannel is etched deeper, the sidewalls are etched as well. A channel with a wider top than the base will be obtained. If wet etching is used, it has the same disadvantages as silicon etching in terms of a high cost and a slow speed. Alternatively, glass can be fabricated by photolithography. However, the fabrication of glass compared with PDMS is still expensive and slow. A pattern transfer based on photolithography is typically composed of several time consuming steps including, chronologically, a complete cleaning of the substrate, a spin coating of photoresist, a pre-exposure baking of the photoresist, photolithographic exposure, a post-exposure baking, and a development of the already exposed resist [279]. During applications, adsorption may occur when a glass system is used with proteins. The pros and cons of glass as a material for microfluidic devices are tabulated in Table 3-3.

Table 3-3 Pros and cons of glass for microfluidic devices.

Glass as a material for microfluidic devices	
Pros	Excellent mechanical rigidity and temperature stability; Excellent chemical resistances; Low permeability; Optically transparent; Favorable biocompatibility.
Cons	Mechanically fragile; High cost; Vertical sidewalls are difficult to etch than silicon; Possible non-parallel walls after etching; Wet etching and photo-structuring are expensive and time-consuming; Sealing process needs clean room, high voltages and temperatures; Only 2D geometries; Possible adsorptions when used with proteins.

3.1.3 Polymers

Polymers have been extensively applied for producing microfluidic devices in the past 20 years. Polymers, according to Becker and Gärtner [280], have a 'Jekyll and Hide' character compared with other materials such as the aforementioned silicon and glass. This character has been reflected by, on one hand, there are many choices in polymers when considering both material properties and micromachining methods; and on the other hand, it is difficult to determine the optimal one among diverse polymers.

3.1.3.1 A classification of polymers

Based on the physical parameters and fabrication techniques, polymers are divided into three categories, i.e., thermosets (e.g., commonly used photoresists), thermoplastics (e.g., PMMA and PC), and elastomers (PDMS). In this classification method, a glass transition temperature (T_g) as a function of chain flexibility is the main parameter [281,282]. A second and a third important parameter in practical applications are heat distortion temperature and decomposition temperature [282], at which the polymers will not support any mechanical stresses as it will collapse and decompose as the polymer chains are broken, respectively. The T_g of thermoset are typically high and comparable to the decomposition temperature. Resist materials applied in lithography, e.g., the photoresist SU-8 in microfluidic applications and polyimides (durable and high-temperature stable) used for microelectronics are two common examples of thermosets. Epoxy and acrylic also belong to this category [280]. In general, thermoplastics can be micromachined using replication methods, such as injection molding or hot embossing. Typical examples of thermoplastics are poly (methyl methacrylate) (PMMA) and polycarbonate (PC), which are among the first materials used in polymer microfabrication. Later, cyclo-olefin polymers and copolymers become popular as well due to favorable optical properties, moldability and low water uptakes [283-285]. In elastomers, molecular chains are longer than those in the above two polymers and do not show any chemical interactions but are physically entangled. As an external force is exerted, the chains will not be entangled anymore but cause the elastomer to stretch. If the external force is removed, the elastomer returns to its original shape instantaneously. Due to its low cost and easy manipulations, elastomers, such as PDMS, have become a popular material in productions of microfluidic devices [286].

3.1.3.2 Pros and Cons of polymers

Becker and Gärtner provides a comprehensive summary of the main mechanical properties (e.g., density, glass transition temperature Young's modulus, resistivity, thermal expansion coefficient.) of the commonly used polymers in microfluidic applications [280]. According to their summaries, polymer materials are superior in terms of easy and precise micromachining, biocompatibility and optical transparency. Polymers, compared with silicon and glass, are very low-cost [287]. Polymers based channels can be structured through molding or hot embossing instead of etching, which accelerates the overall fabrication and enables a mass production of microfluidic devices. Microscale features can be reproduced at a high accuracy in PDMS using replica molding. The polymers based devices can be thermally sealed or be sealed by using adhesives. Generally, polymers are

51

biocompatible and optically transparent. PDMS can be optically transparent down to a wavelength of 280 nm for the light, which thus enables detection schemes. Due to its permeability to oxygen and carbon dioxide, PDMS is especially suitable for cell-based systems. Moreover, the material of PDMS is of no toxicity. PDMS is usually cured under low temperatures relative to silicon and glass. Reversible deformations of PDMS can be feasible. Based on a molecular (van der Waals) contact with the surface, it is capable of be reversibly sealed with itself and a number of other materials. On the other hand, polymers have disadvantages. Surface chemistry control of polymers needs much more care than that of glass or silicon due to possible exchanges between PDMS on the surface and that in the bulk surroundings, especially when the applications last for hours to days. Polymers are generally incompatible with organic solvents and have low stabilities subjected to varied temperatures. In particular, PDMS are not appropriate for certain applications that involving hydrophobic molecules due to potential dissolution in PDMS and a subsequent swelling. Lastly, PDMS may not be appropriate for gas applications, let alone those operate at extreme pressure/temperature conditions. The pros and cons of polymer materials have been simply summarized in Table 3-4.

Table 3-4 Pros and cons of polymers for microfluidic devices (mainly after Becker and Locascio [274]).

	Thermoplastics (e.g., PMMA, PC)	Thermosets (e.g., SU-8)	Elastomers (e.g., PDMS)
Pros	High acid stability; High optical transparency; Low price; Biocompatible; Rapid fabrication; 2D, 3D geometries; Easy assembly.	High mechanical stability; High acid stability; Medium organic solvent stability; Partially optical transparency; Biocompatible; Rapid fabrication; Mostly 2D, 3D possible; Easy assembly.	High acid stability; High optical transparency; Low price; Biocompatible; Rapid fabrication; Mostly 2D, 3D possible; Easy assembly.
Cons	Low mechanical stability; Low temperature stability; Low organic solvent stability.	Medium temperature stability; Medium price.	Very low mechanical stability; Low temperature stability; Low organic solvent stability.

3.2 Experimental System: Building

In this section, the building of an experimental system for two phase microfluidic studies, especially for the ones at extreme pressure/temperature conditions is introduced. An overview of the system is provided first, and then the details of the design and the fabrication of a non-permanent connector and a silicon/glass microchip are given. The connector bridges the connection between macroscale tubing and the microchip, and the microchip facilitates the two phase microfluidic phenomenon.

3.2.1 An Overview of Experimental System

Figure 3.1 and 3.2 show a schematic and a real photo of the experimental system, respectively. The experimental system (see Figure 3.1) consists of a reactant feeding system (tanks and syringe pumps), a microfluidic system (a non-permanent connector and microfluidic chips), an imaging system (a microscope and a high speed camera), pressure\temperature control systems (a back pressure regulator and a transducer, a water circulator, a miniature hotplate, a needle valve) and stainless steel tubing (external diameter are 1/8 or 1/16 inches) as well as control valves (model SS-41GS2, Swagelok) for fluidic connections. Replenished by purpose-oriented fabricated silicon/glass microfluidic chips, this experimental system has been dedicated to studies related to the experimental aspects of two-phase microfluidics especially those under extreme conditions (i.e., high pressures (~10 MPa) and/or high temperatures (up to 200 ~ 300 °C)).

Two syringe pumps (model 260D and 100DM, Teledyne Isco) are utilized to regulate the flow rates and pressures of the two pre-loaded fluids, namely, liquid CO_2 (purity 99.9%, Praxair Canada) and deionized (DI) water. The CO_2 syringe pump (260D, Teledyne Isco) is connected to a liquid CO_2 tank and this tank is equipped with a manual control valve (model 535-2031CGA, CONCOA). This valve rather than a common gas pressure regulator has to be used since it does not result in any pressure decay, which otherwise may cause a CO_2 freezing problem using a typical pressure regulator. The back pressure of the flow in the microfluidic channels and the related tubing is managed by a back pressure regulator (BPR, model EB1ULF1, Equilibar) together with a setting pressure provided from a gaseous N_2 tank (Praxair Canada). As a reference pressure, the setting pressure is applied to the BPR through regulating the N_2 gas by a gas regulator (model PRS 40924801000, Pro-star) right at the outlet of the tank. Technically, only when the back pressure of the outflow (also as an inflow pressure of the BPR itself) from the microchip surpasses the setting pressure can the fluids flow through and maintain a constant flow thereafter. During the experiment, the practical back pressure is measured by an industrial pressure transducer (s model, PTI-S-NG10K-12AQ, Swagelok) installed upstream of the

BPR. Prior to entering to the microfluidic system, liquid CO_2 and water are filtered by two in-line two-micron particulate filters (SS-2F-T7-2, Swagelok) installed at the inlets of the chip connector in order to prevent potential clogging-caused failures of the microchannels. Besides, a circulating water bath (SC150-S45, Thermo Fisher Scientific) and a miniature hotplate (model ph-121s, MSA Factory Co., Ltd, Japan) are available, respectively, for controlling the temperature of the CO_2 not only in the pump but also in the tubing and the temperature of the micromodel as well as the fluids therein. The flow phenomenon on the silicon/glass microchip are visualized using a microscope (including 5x, 10x, 20x, 40x objectives) (model BX51, Olympus) mounted with a high speed camera (model v210, Phantom). This camera is capable of capturing images at 2000 frames per second (fps) at the full 1280×800 resolution, and faster frame rates can be achieved at reduced resolutions. Compared with a halogen lamp, the mercury lamp of the microscope together with an exterior power supply (model BH2-RFL-T3, Olympus) can provide a better illumination with a higher intensity and is thus going to be used. Basically, the operation parameters of the experimental system including the flow rates and pressures of the fluids, the back pressure at the end of the fluidic unit can be recorded in real time. And the flow phenomenon of the two phase microflows are visualized and captured by the camera built-in software in a computer. After the experiments, the videos and images captured can be further exported in other formats (e.g., '.tiff' or '.avi'), processed in the software ImageJ (National Institute of Health, the US) and analyzed using the software Matlab (R2014a, Mathworks Inc.) for extracting the parameters of interests.

Most of the components of the experimental system can be available from market. The only two parts which call for self-production are a non-permanent connector bridging the macroscale stainless steel tubing with the microchip and the more key component – silicon/glass microchip. In the next, the designs and the fabrications of these two components are discussed.

3.2.2 Non-permanent Connector: Design and Fabrication

A non-permanent connector which is rooted in an idea of 'plug-and-play' for a packaging of micromodels [288], has been designed and machined in lab for bridging fluid connections from macro tubing to microchannels, as shown in Figure 3.3. It is composed of (1) a robust compression upper part (316 stainless steel), (2) a bottom part (316 stainless steel) with flow ports, (3) a borosilicate glass cuboid (49.8 mm $\times$ 25 mm $\times$ 10.2 mm) ensuring a uniform compression between the upper and bottom parts.

The bottom part is specifically designed with three grooves (each is of a inner diameter of 1.78 $\pm$
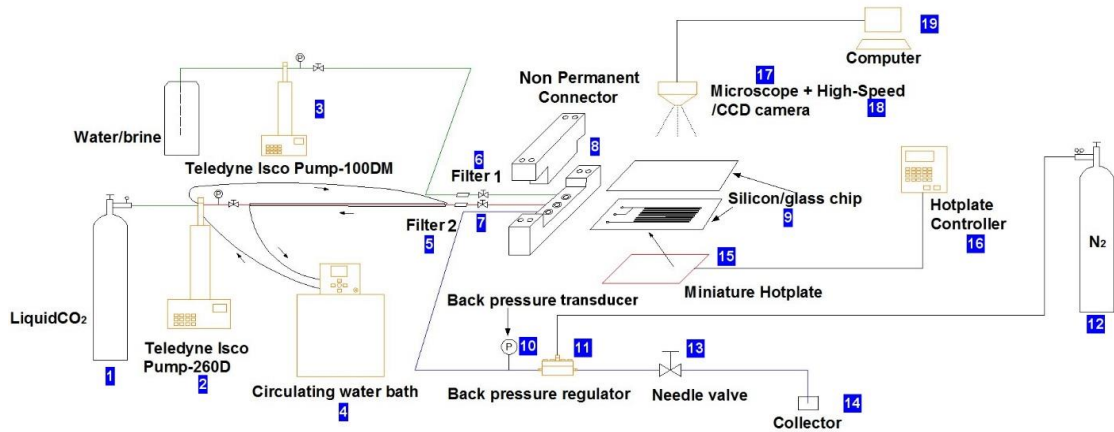
Figure 3.1 Schematic of the experimental system. Noted devices in this schematic are: 1. liquid CO_2 tank; 2. CO_2 syringe pump; 3. water pump; 4. circulating water bath; 5 & 6. two-micron filters; 7. fluid entry valves; 8. non-permanent connector; 9. silicon/glass chip; 10. back pressure transducer; 11. back pressure regulator; 12. nitrogen (N_2) gas tank; 13. needle valve; 14. fluids collector; 15. miniature hotplate; 16. hotplate controller; 17. microscope; 18. camera; 19. computer.
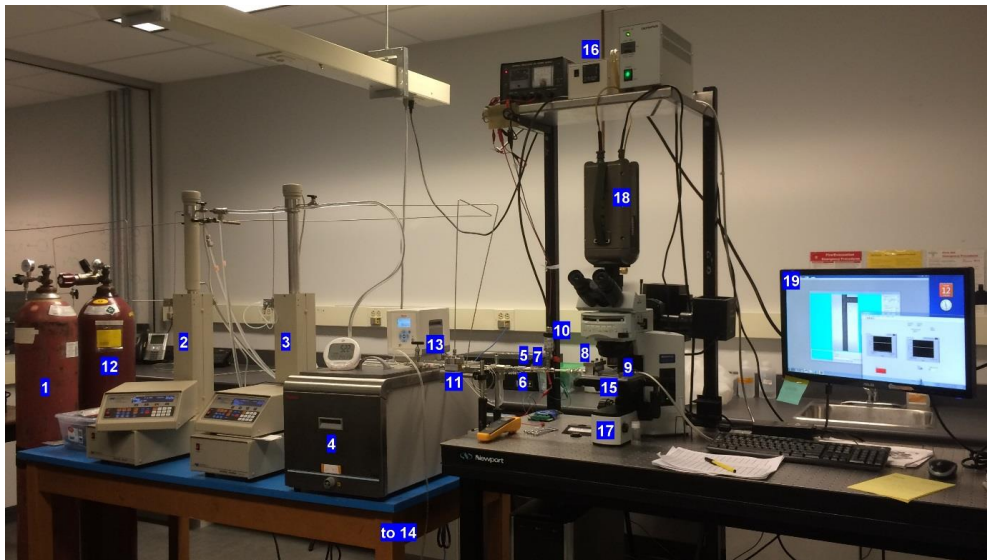
Figure 3.2 A real photo of the experimental systems. Noted items in the photo are referenced to Figure 3.1.

0.13 mm, an outer diameter of 5.72 ± 0.13 mm and a depth of 1.32 ± 0.05 mm) on the top central surface, and three Viton fluoroelastomer O-rings (size number: AS568-004, hardness: Duro 90A; Marco Rubber) are placed in the grooves to be used for sealing thanks to their deformations under

55
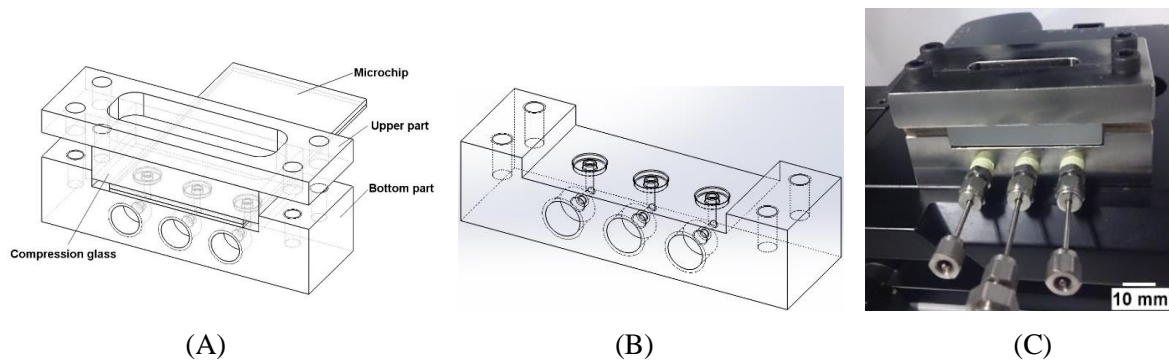
Figure 3.3 Schematics of a non-permanent connector for microchips: (A) an assembly of the connector and a microchip; (B) the bottom part of the connector (length $\times$ width $\times$ height = 80 $\times$ 25 $\times$ 20 mm). (C) A real photo of the connector in an assembled way.

compressions. The central openness (diameter: 0.76 mm) of each groove element is connected to a 1/16'' female NPT (National Pipe (Tapered) Thread) featured hole on the front side of the connector facing to the incoming fluids. Three straight fittings for housing 1/16'' (OD) stainless steel tubing are employed to interlink the tubing with this connector by their threads matching eventually. Even so, thread seal tape (yellow color) is also necessary for use in practice.

The upper part (7 mm thick) is designed and produced with four identical holes for placing socket head cap screws (size: M5, Swagelok), and these screws are able to reach the other four holes but with threads on the bottom part and to be appropriately tightened for compressions. A central region of the upper part is lathed through to provide an alternative observation of the O-ring sealing areas.

The sealing compression is eventually fulfilled by using a glass cuboid which is placed between the upper part and the microchip top surface. It delivers and exerts the compression forces on the microchip against the O-rings at the bottom of the microchip, resulting in the sealing of the two inlets and an outlet of the microchip relative to the incoming fluids based on the deformation of the O-rings. In essence, the sealing are the type of face sealing which lies both at the bottom face of the groove as well as of the O-ring itself and at the top face of the O-ring in contact with the bottom face of the microchip. In addition, the excellent surface quality of the glass cuboid ensures uniformly distributed forces onto the microchip top surface.

Other than the O-rings, the compression screws, the stainless steel straight fittings and the glass cuboid are available from market, the upper and the bottom part have to be machined. The machining work of these two parts have been carried out on a CNC (computer numerical control) machine in the Engineering Machine Shop in the University of Waterloo.

3.2.3 Silicon/Glass Microchip: Design and Fabrication

Based on previous survey of the materials for microfluidic devices as well as a requirement of high pressure resistant, a silicon/glass microchip is chosen as in this thesis, given that they can offer excellent gas impermeability, durability under extreme conditions and inert chemical property etc. Moreover, silicon is chosen as a base slide because of its thermal conductivity in case a temperature control of the microchip is required. It is worth noting that the fabrication of silicon/glass microchip in this thesis is the very first in the Microfluidics Laboratory, University of Waterloo, according to the best knowledge of the author. Here, a dimensional design of the microchannel as well as selection criteria of wafer thicknesses are proposed and discussed first. The fabrication procedures (also called 'recipe') of a silicon/glass microchip are detailed.

3.2.3.1 Dimensional design: cross-sectional force balance and wafer selection

Deep reactive ion etching (DRIE) is chosen as an etching method of silicon wafer, which can produce rather perfect vertical sidewalls compared with wet etching methods (e.g., anisotropic KOH or TMAH (tetramethylammonium hydroxide) etching, isotropic HNA (HF acid + nitric acid + acetic acid) etching). Hence, the cross section of the etched channel will be resulted in a rectangular shape. Figure 3.4 shows a structural model of the etched structure in the silicon slide after bonding with a glass slide. Within the structure, there is a constant pressure P ($0 < P < P_{max}$). Focusing on the etched rectangular channel region, there must be a force balance scenario on both the silicon beam (at the bottom) and the glass beam (on the top), which can be analyzed based on a model of 'beam fixed at both ends with uniformly distributed load'. The shear force at shear plane A and B, as a result of the loaded pressure, have a magnitude of (PW_sL_0)/2, where W_s is the channel width at the silicon side and L_0 is a unit length on the stressed surface (perpendicular into the paper). At shear plane A, the shear force is required to be no larger than the ultimate tensile stress on this plane of the material (silicon here), i.e.,

$$\frac{PW_sL_0}{2} \leq \sigma_u\ (t_s - d)L_0, \tag{3.1}$$

in which σ_u is the ultimate tensile stress of the material; t_s is the thickness of silicon wafer; d is the channel depth. Therefore,

$$P \leq \frac{2\sigma_u(t_s-d)}{W_s}, \tag{3.2}$$

Accounting for stress concentration at the channel edges, a first safety coefficient k_1 ($5 \leq k_1 \leq 10$) is

57
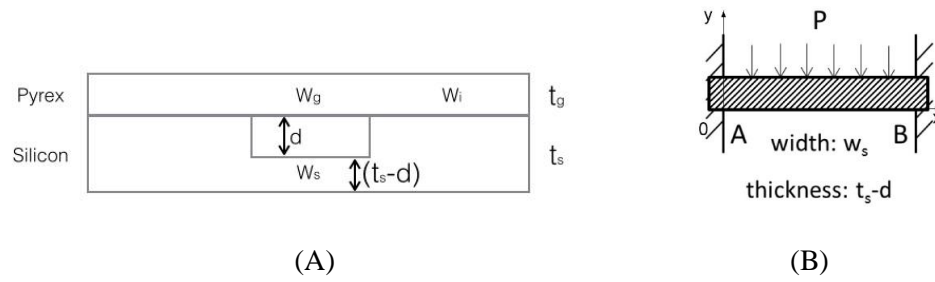
Figure 3.4 (A) Structural model of the cross section of a silicon/glass microchip and (B) a problem description of the silicon and glass layer (channel part) as a beam fixed at both ends with uniformly distributed load P (pressure, i.e., newton per unit area).

induced [289]. Other stresses, e.g., shear stress in other planes, stress concentration in possible imperfections etc. call for a second safety coefficient k_2 ($k_2 = 10$ is suggested by Marre et al. [288]). For a maximum safety of the silicon side, $k_1 = 10$ and $k_2 = 10$ are adopted in our calculations, thus

$$P \le \frac{2\sigma_u(t_s-d)}{k_1 k_2 W_s},$$
(3.3)

Similarly, an equation of force balance of glass side:

$$P \le \frac{2\sigma_u{'}t_g}{k_1 k_2 W_g},$$
(3.4)

in which $\sigma_u{'}$ is the ultimate tensile stress of the borosilicate glass; t_g and W_g are the thickness of the glass slide and the width of the channel at glass side, respectively. The rectangular cross section of the channel leads to $W_s = W_g$. Equation (3.3) and (3.4) correlate the maximum applied pressure with the material properties and the dimensional parameters of the microchannel. Table 3-5 lists the allowed maximum applied pressures in specifically configured channels with a constant depth of 100 µm (i.e., d = 100 µm) as a consequence of various channel width (100 ~ 350 µm). Other conditions are as follows: $\sigma_u = 1$ GPa at 25 °C (for comparison, $\sigma_u = 300$ MPa at 500 °C) [288], $\sigma_u{'} = 200$ MPa (typical range is 20 ~ 5000 MPa) [290], $t_g = 700$ µm, $t_s = 525$ µm.

Table 3-5 Allowed applied pressures in a constant-depth channel (d = 100 µm) subjected to various channel width.

$W_s = W_g$ (µm)	100	150	200	250	300	350
P (MPa)	≤ 28	≤ 18.67	≤ 14	≤ 11.2	≤ 9.33	≤ 8

Besides, a second criterion has been proposed by Marre et al. [288] for selecting suitable silicon wafer and glass wafer in terms of their thickness, i.e., the relative deformation of the silicon slide is preferred to be comparable to that of the glass slide. In Figure 3.4, according to Gere and Goodno [291], the deformations of the silicon (ε_s) and the glass (ε_g) beam can be determined from below

$$\varepsilon_s(x) = \frac{PL_0x}{24E_sI_s}(W_s{}^3 - 2W_sx^2 + x^3), \tag{3.5}$$

$$\varepsilon_g(x) = \frac{PL_0x}{24E_gI_g}(W_g{}^3 - 2W_gx^2 + x^3), \tag{3.6}$$

in which x indicates the distance of the beam cross section from plane A. E_s and E_g are the Young's modulus of silicon and glass, respectively; I_s and I_g are the area moment of inertia of the beam cross section for silicon and glass, which can be determined by $(t_s\text{-}d)L_0{}^3/12$ and $t_gL_0{}^3/12$ based on a rectangular cross section of each beam, respectively. At each x position, the tensile strain of each beam relative to its thickness should be the same in order for the two sides to collaboratively absorb the tensile force outwards from the interior channel, which can be formulated as

$$\frac{\varepsilon_s(x)}{t_s} = \frac{\varepsilon_g(x)}{t_g}, \tag{3.7}$$

Given that $W_s = W_g$, integrate (3.5), (3.6) and (3.7) we have

$$\frac{E_s}{E_g} = \frac{t_g{}^2}{t_s(t_s-d)}. \tag{3.8}$$

Given a constant channel depth (100 µm) and Young's modulus ($E_s = 130$ GPa for silicon of a <100> plane configuration [292]; $E_g = 64$ GPa [290]), there is a relation between the thickness of the silicon wafer and that of the glass wafer, based on which the selections are made. Table 3-6 lists the thickness ratio and the Young's modulus ratio of the candidate silicon and glass wafer. $t_s\,(t_s\,\text{-}100)\,/t_g{}^2$ is always smaller than the ratio of the glass modulus over that of silicon. In practice, since $E_g\,/\,E_s$ is essentially much lower than 1, $t_s\,(t_s\,\text{-}100)\,/t_g{}^2$ can be close to $E_g\,/\,E_s$ as long as it is smaller than 1, i.e., the silicon wafer can be thinner than the glass wafer.

Table 3-6 Thickness of the silicon and glass wafer versus their modulus.

Designs	$t_s\,(t_s\,\text{-}100)\,/t_g{}^2$ (µm^2/µm^2)	E_g/E_s
Design 1	=525×(525-100)/700^2 = 0.455	0.49
Design 2	=1000×(1000-100)/2000^2=0.225	

3.2.3.2 Fabrication of silicon/glass microchip

A silicon wafer (4'' diameter, <100>, single side polished (SSP), 525 µm thick) and a glass wafer (4'' diameter, double side polished, 700 µm thick, Borofloat 33 borosilicate glass, Schott) are used to fabricate a silicon/glass microfluidic chip. Prior to the fabrication, a photo mask with an image of two dimensional network patterns is designed using AutoCAD (version 2012, Autodesk Inc.) and commercially printed by on Mylar films with a 20,000 dpi resolution (CAD/Art Services, Inc.). The minimum feature size is 10µm at the highest resolution. Photo mask is available in various sizes. A letter size (11'' x 14'') is used on which 6 masks (outer diameter is 4'') can be aligned. Next, the fabrication proceeds sequentially in several main steps, including: (1) standard photolithography, (2) deep reactive ion etching (DRIE), (3) drilling and wafer cleaning, (4) anodic bonding and (5) dicing. Detailed procedures for fabricating silicon/glass micromodels are detailed below:

(1) Photolithography:

- Dehydrate the silicon wafer at 195 °C for 15 min, and cooling to room temperature;

- Coat the silicon wafer with HMDS (hexamethyldisilazane, a primer for coating photoresist next) for 90 seconds under 3000 rpm (rounds per minute) with a medium acceleration;

- Coat the silicon wafer with a positive photoresist (PR) S1818 for 90 seconds under 3000 rpm;

- Softbake the wafer at 100 °C for 10 minutes, then naturally cool;

- Expose on mask aligner (Karl Suss MA4, Süss MicroTec AG.) for 90 seconds;

- Exposed wafer is developed in MF 312: DI water (1:1, volume ratio) for 2 minutes, then rinse with DI water and air drying;

- Development quality is inspected using a microscope with 5x and/or 20x objectives.

(2) Deep reactive ion etching (DRIE)

DRIE etching is performed on a deep silicon plasma etching system (PlasmaPro Estrelas 100, Oxford Instruments). This system is hosted by the Pratt Microfabrication Facility, Toronto NanoFabrication Centre, which can be used to etch high aspect-ratio anisotropic trenches into silicon-based substrates based on either a Bosch process (etch Rate > 25 µm/min, maximum aspect ratio = 70:1, uniformity < ± 3%, selectivity to PR > 250:1, scallops< 300 nm) or a cryogenic process. The principles of SF_6 and C_4F_8 for etching and passivation of sidewalls, respectively, are presented elsewhere [293].

- Use a general Bosch process (~ 15 µm/minute);

- Etch 68 cycles (each circle consists of passivation and etching) for 6 mins 44s results in a 102 µm depth;

- Or use a fast etch process (~20 µm/min);

- Etch 5 minutes;

- Etched channels are imaged by a microscope with 5x and/or 20x objectives, and the depth and width are measured, as shown in Figure 3.5.

(3) Drilling and wafer cleaning (photoresist removal)

After the DRIE, two inlets and an outlet are drilled for future fluids' inflowing and outflowing at their designed locations by using a driller (drill diameter 0.6 mm, SERVO B-1 driller, Altadena, California). Water droplet cooling is employed to remove substantial heat at drilling place. It is advised that the drilling is done slightly and repeatedly, avoiding excessive shear forces destroy the wafer. After drilling, the silicon wafer is cleaned using acetone and Piranha (hydrogen peroxide

(A)   (B)   (C)
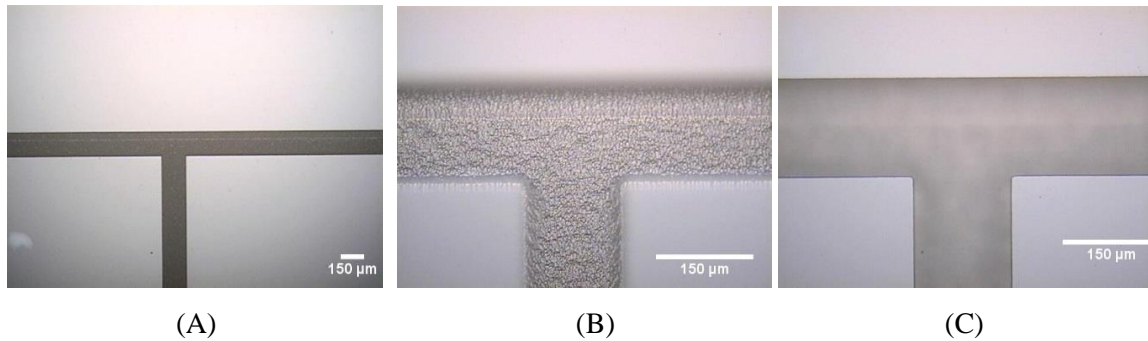
Figure 3.5 Images of a T-junction (channel width: 200 µm, depth: 102 µm) etched in a silicon wafer by DRIE, which are captured by a microscope with a 5x objective and a 20x objective, respectively. (A) T-junction imaged by a 5x objective, (B) the bottom plane and (C) the top plane of T-junction imaged by a 20x objective. Scaled bar in each graph: 150 µm.

(H_2O_2): sulfuric acid (H_2SO_4), 1:3 (volume ratio)) solution to remove the residual photoresist. All the following procedures are required to be done on a wet bench.

- Clean wafer using acetone for 1min, then rinse wafer using water, air drying;

- Prepare Piranha solution, where H_2O_2 (350 mL) is added into H_2SO_4 (1050 mL) slowly and uniformly (personnel should wear a goggle, double-layer rubber gloves);

- Slowly immerse the wafer (together with its clip) in Piranha and leave it there for more than 10 mins (10 ~ 40 minutes);

- Wafer is removed out from Piranha (with no obvious acid droplet) and immersed in water for more than 10 mins;

- Dry wafers using N_2, wafer cleaning is completed.

- Leave Piranha for cooling over a period of more than 12 hours, and carefully pour it into a specific waste barrel after the cooling.

4) Anodic bonding

The patterned and cleaned silicon wafer is going to be covered by a borosilicate glass wafer (Borofloat 33, SCHOTT) to form enclosed microchannels, which is achieved by anodic bonding. Here, anodic bonding is performed in a wafer bonder (AWB-04, Aligner Wafer Bonder, AML).

- Load silicon and glass wafers, close the lid;

- Start the pump and wait the vacuum reaches 10^{-4} mbar, then start the heating and set the temperature between the upper and lower wafer to be 400 °C, when temperature is 400 °C, apply force 100 N;

- Set target voltage to be 600 V and current limit 4 mA, turn on 'HV (high voltage) supply' and wait for 10 minutes;

- After 10 minutes, turn off 'HV supply';

- Rely on a slow natural cooling and wait the temperature drops from 400 °C to below 100 °C. Bonded wafers can only be taken out when the temperature is below 100 °C, otherwise forced cooling may crack the wafers thanks to rapid thermal stress variations;

- Prior to wafers' moving out, turn off the pump and wait until its rotation speed is 0, then purge with N_2 until atmospheric pressure is reached, stop the purging and remove the bolts;

- Moving the bonded wafers out.

(5) Dicing (of bonded wafers)

The bonded wafers (4'' diameter) need to be diced into a rectangular microchip (74 mm × 44 mm) for being assembled with the nonpermanent connector. The dicing is achieved by an automatic wafer dicer (Automatic Dicing Saw, DAD 3220, Disco Corporation) by a blade, in which the dicing process can be programmed in terms of dicing direction and step dicing depth and can be cooled by an

external water flowing. Figure 3.6 shows two photos of a microchip just after anodic bonding (or before dicing) and after dicing, respectively.

(A)   (B)
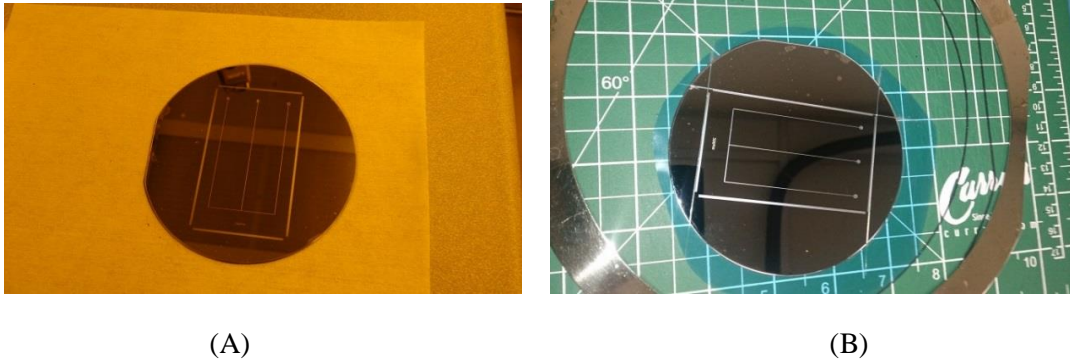
Figure 3.6 Photos of a silicon/glass microchip: (A) before dicing (or say, after bonding) and (B) after dicing, the rectangular microchip is the central piece of the diced wafers.

3.3 Experimental System: Optimization

After a general building of the experimental system by connecting the various functional modulations, the system is still a distance away from a complete form for experiments, let alone for those goals proposed at the beginning of this chapter. There are a few key improvements having been made during the building stage but not introduced further in this thesis, such as:

◆ A temperature control strategy is proposed and implemented for not only the CO_2 in the pump cylinder but also for when flowing from the pump to the microchip. A 'tube in tube' solution is applied in which the stainless steel tubing (CO_2 flows) are inserted into vinyl tubing holding the circulation water. Thus a closed circulating water temperature control circuit is formed and a continuous counter flow between the water in the vinyl tubing and the CO_2 in the stainless tubing ensures the temperature of CO_2 flow.

◆ A self-made aluminum stage for the microfluidic modulation (including the connector and the microchip) is manufactured which facilitates the connector and maintains a void space between the microchip after its assembly with the connector and the stage surface. A miniature hotplate whose total thickness is slightly less than the space height can be installed in the void space. Its edges are steadily compressed by four small blocks against the stage itself and the remaining thin gap (between the hotplate and the microchip) being filled by a thermal interface material (silicone, 10405K83, Dow Corning).

◆ A three-way valve is installed at the immediate downstream of the pressure regulator of the nitrogen tank that has been used to provide the back pressure. The valve allows not only the filling of nitrogen gas for setting up a back pressure but also the releasing of this gas when either adjusting or removing the back pressure is required.

As concluded, although there are not any specific parameters to evaluate how much such efforts have improved the performance of the system, the improvements introduced here indeed add more manipulability for operators working with the system in future.

Other than the above technical improvements, there are mainly four other key optimizations having been made toward the experimental system, including: (1) connector/microchip assembling optimizations; (2) two-micron filter installation; (3) calibration of an industrial pressure transducer; and (4) a DI water refilling solution. These optimizations are detailed in the following.

3.3.1 Connector/Microchip Assembling

A successful assembling of the microchip with the non-permanent connector is important for both a leakage-free configuration of the entire system and a safe condition for the microchip itself. Since the silicon/glass microchip is much more fragile relative to the stainless steel bodied connector due to the materials and the very thin thickness (1.2 mm or so), it is a challenge to account for these issues technically. In order to enable a leakage-free scenario at the O-ring places, a tightened compression thanks to the screw compressions is preferred; however, it may crack the microchip due to an over-tightening. On the other hand, without a sufficient compression leakage may occur under extreme pressures.

Accounting for a leakage-free operation as well as the safety of the microchip, the author has conducted a series of assembling tests over multiple factors, such as (1) two differently sized upper part (an original one: 80 mm $\times$ 25 mm $\times$7 mm; a new one: 80 mm $\times$ 37 mm $\times$12 mm) of the connector; (2) three different glass compression blocks (borosilicate glass cuboid: 49.8 mm $\times$ 25 mm $\times$10.2 mm; PMMA plastic glass cuboid 1: 49.6 mm $\times$ 20 mm $\times$11.7 mm; PMMA plastic glass cuboid 2: 49.3 mm $\times$ 23.9 mm $\times$12.1 mm); (3) O-rings or X-rings (O-rings: AS568-004, hardness is 75A or 90A; X-rings: AS568-004, hardness is 75A); and (4) compression screws (M5) tightening using a screw driver or hands.

The method of an assembling test can be elucidated as follows: once an assembled strategy is applied to the microfluidic modulation, first fill the central tubing with pressurized CO_2, and when a

microchip is indeed assembled, the pressure measured by the back pressure regulator can be read from computer; then close the two valves (item 7 in Figure 3.1) in front of the connector, and leave the microfluidic modulation in a closed status for a period of the total testing time (e.g., 1 day or a certain hours), during when the end needle valve (item 13 in Figure 3.1) is kept totally closed; after the test is over, to check the back pressure history to see if it is overall a constant or decline over the time, and then slowly open the needle valve to release the CO_2, as long as the pressure goes back to almost 0 (relative to atmospheric pressure), loose the screws slowly and gently to check the statuses of the microchip, compression block, and O-rings (or X-rings).

Whether there is a leakage or not is determined by the pressure history as measured by the pressure transducer. If there is no significant decline of the CO_2 pressure over the time, it can be deemed as a leakage-free result. And besides, the safety of the microchip can be visually identified by the completeness of the chip itself.

Five tests of the assembling strategies have been carried out, and the details including the failures, the successes and some expertise are provided in the Appendix A. Generally, it is found that a leakage-free assembly of connector/microchip with a guaranteed safety of the microchip can be resulted from: (1) applying a robust upper part (the new one instead of the original one), and (2) a uniform hand-tightening of the compression screws (which is sufficiently tight for working with up to 80bar). Moreover, it is found that both the O-rings and X-rings have suffered from an inflation of the high pressurized CO_2 and as a consequence, these rubber rings are always inflated but simultaneously suppressed by the compressions. It is also suggested that, for the safety of the devices, actions during filling and releasing the medium should always be slowly and gently; and always keep in mind that the medium after the tests or experiments should be released off from inside the device.

3.3.2 Two Two-Micron Filter Installation

Liquid CO_2 and DI water are the two main fluids contained in respective syringe pumps, however, the exact purities of the two fluids in the pump cylinders are not very clear (liquid CO_2 in the tank has a 99.7% purity but that of DI water is unknown). In order to prevent any clogging caused microchip failures, the author has proposed to install two two-micron filters prior to the entries of fluids into the connector as well as the microchip. These two filters (model SS-2F-T7-2, Swagelok) are an in-line type with two tube adapters on two ends for 1/8'' stainless steel tubing which can filter the impurities with sizes over 2 µm. Nevertheless, another issue may arise due to the installation of a filter on the fluid path in the tubing, i.e., a pressure decline as a result of the flow resistance thanks to the filtering

materials in the filter. Therefore, a comparative study of the pressures upstream and downstream of the filter is carried out. The setup can be illustrated in Figure 3.7(A).

| (A) | (B) |
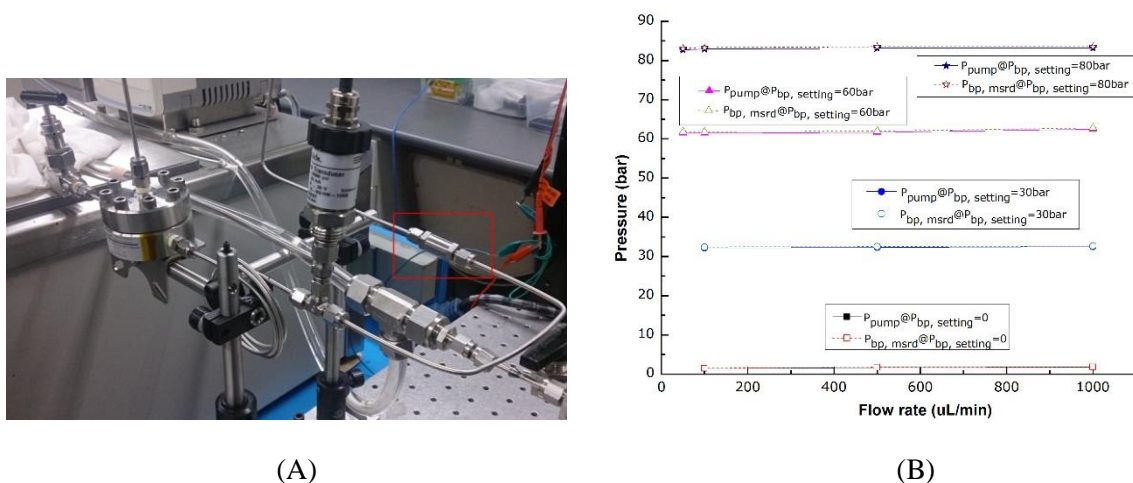
Figure 3.7 A comparative study of the pressures upstream and downstream of a two-micron filter at various flow rates of water (50, 100, 500, 1000, unit: µL/min): (A) setup; (B) upstream pressure P_{pump} (solid lines) versus downstream pressure $P_{bp,msrd}$ (dash lines) at four pre-set back pressures (0 bar-squares, 30 bar-circles, 60 bar-triangles, 80 bar-stars).
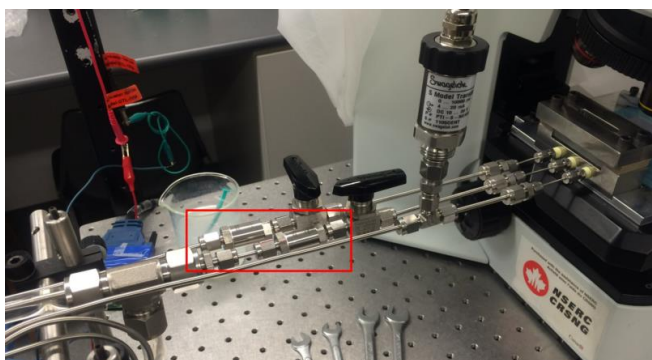
Figure 3.8 A photo showing the installations of two two-micron filters at upstream of two valves, respectively, for CO_2 and DI water stream.

The water pump operates at four constant flows, i.e., 50 µL/min, 100 µL/min, 500 µL/min, 1000 µL/min; and four different back pressures (0, 30 bar, 60 bar, 80 bar) provided by the back pressure regulator (connected with a nitrogen tank) are studied. The upstream pressure P_{pump} and the downstream pressure $P_{bp,msrd}$ are measured by the syringe pump and the back pressure transducer (installed between the filter and the back pressure regulator), respectively. The results are shown in Figure 3.7(B). By compare P_{pump} with $P_{bp,msrd}$, there are always very slight deviations; however, the

deviations are never much over 0.4bar. Moreover, both P_{pump} and $P_{bp,msrd}$ are 1 ~ 2 bar higher than the pre-set back pressure, which is rational and in this way can the water flow occurs. Note that the pre-set back pressures are read from the pressure gage at the gas pressure regulator at the outlet of the nitrogen tank, they may be not very accurate, but it does not influence much since the back pressure will always be referred to that measured by the back pressure transduce in future. The comparison between the upstream pressures and downstream pressures indicates that the two-micron filter does not render a significant pressure decline. Figure 3.8 shows a photo of the two two-micron filters installed upstream of two valves for both the CO_2 stream and the DI water stream.

3.3.3 Back Pressure Transducer Calibration

The back pressure transducer is a standard industrial one (s-model, PTI-S-NG10K-12AQ, Swagelok). However, it is not a ready-to-use transducer. Therefore, a direct-current circuit has to be built where the pressure transducer behaves as an electrical resistance, as shown in Figure 3.9(A). Its signals (e.g., voltage or current) can be measured and transferred to digital signals in the computer for pressure measurements. Prior to its applications in measuring pressures, it has to be calibrated first, which can be done by correlating the measured pressures with the voltage signals. And the calibration circuit will be the exact one for practical uses as well. Some properties of the pressure transducer have been listed in Table 3-7.

Table 3-7. Properties of the pressure transducer.

Properties	Back pressure transducer (PTI-S-NG10K-12AQ, Swagelok)
Input (DC)	10 ~ 30 V
Output	4 ~ 20 mA
Wiring type	Direct 2-wire
Connection	1/4 inch tube connector
Sensor type	Piezo-resistive
Maximum load	R_L (Ω) = (U_{PT} -10)/0.02

Since the pressure transducer sensor (88.3 kΩ) is a piezo-resistive one, its response to a pressure effect will be a resistance change immediately, which further changes the electrical current that is also reflected at a resistance load. Because of a constant value of the load (178 Ω), the voltage will be linearly changing with the current. The voltage signal (V) is then transferred to the computer where they are correlated with the measured pressures. The referenced pressures are those read from the

pump, and a similar setup as that shown in Figure 3.7(A) has been used to conduct the calibration. Figure 3.9(B) shows a linear calibration line of the measured pressures as a function of the voltages.

(A)   (B)
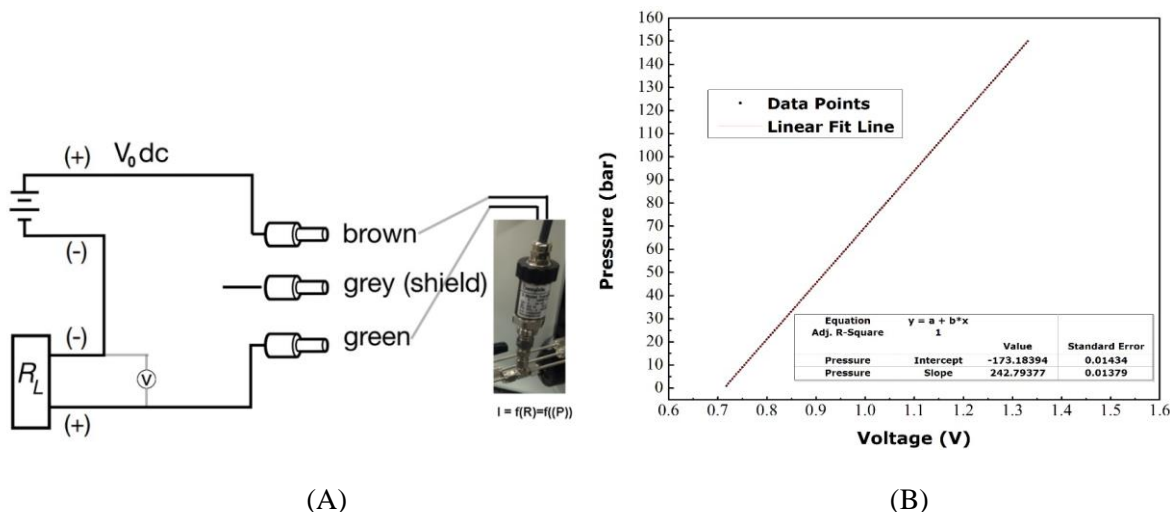
Figure 3.9 (A) A calibration as well as an application circuit for the back pressure transducer. A direct-current source of a constant voltage 15V is applied. (B) A linear calibration line of pressures against voltages.

The pressures applied at the CO_2 pump ranges from 1 to 150 bar. Resulted voltage measured at the load has a range from 0.7178 V to 1.3312 V. The data points of the pressures (P_{bp}) have been linearly fitted to the corresponding voltages (V), and the calibration line is formulated as

$$P_{bp}(bar) = 242.794 \cdot V - 173.184 \tag{3.9}$$

and the two factors on the right hand side have a standard error of 0.01379 and 0.01434, respectively. This calibration is going to be used to process the measured voltages in order to deduce the measured back pressures, which is realized by a LabView (National Instruments) program on the computer.

3.3.4 Water Refilling Solution

Unlike the CO_2 which can be refilled in the syringe pump relying on the tank pressure and a back motion of the cylinder piston, there is no high pressure source on which the DI water can rely to refill the cylinder of the water syringe pump. Therefore, a refilling solution has to be proposed. Figure 3.10 shows a schematic of the water refilling solution based on a peristaltic pump as well as the connection tubing. When this pump operates, DI water in the container can be pumped into the tubing, and when the refilling starts at the pump side, the DI water will be drawn into the pump cylinder. Depending on
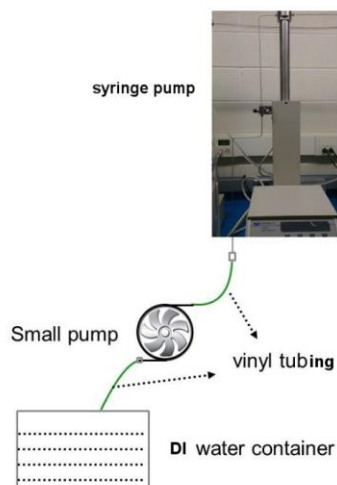
Figure 3.10 Water refilling assisted by using a peristaltic pump.

a relative magnitude between the pumping rate at the small pump and the refilling rate into the cylinder, pure DI water or DI water plus a fraction of air may be refilled. In practice, a slightly lower refilling rate at the syringe pump than that at the peristaltic pump is advised, preventing air from entering into the pump cylinder. Once the refilling is done, the ball valve installed between these two pumps (and on the syringe pump) should be kept closed. The above setup can be disconnected and stored at a dry place.

3.4 Summary

This chapter shows an experimental system built from scratch. The system is dedicated to two phase microfluidic studies, especially those operate at extreme pressure/temperature conditions. Common materials including silicon, glass and polymers for fabricating microfluidic devices are briefly discussed first. By comparisons, silicon/glass are chosen as the microchip materials in this thesis. An overview of the overall experimental system is provided. As the core part of the system, the microfluidic modulation including a non-permanent connector and a microchip is focused. The designs and the fabrications of these two devices are detailed. Besides, the experimental system after initial building efforts has been optimized from several aspects, such as the connector/microchip assembling, two two-micron filter installations, a back pressure transducer calibration, and a water refilling solution.

Chapter 4

Highly Pressurized Partially Miscible Liquid-Liquid Flow in a Micro T-junction

The experimental work in this chapter have been published on the journal Physical Review E as a two-part study:

Ning Qin, John Z. Wen, and Carolyn L. Ren. "Highly Pressurized Partially Miscible Liquid-liquid Flow in a Micro T-junction. I. Experimental observations". **Physical Review E**, 95, 043110, 2017.

Ning Qin, John Z. Wen, and Carolyn L. Ren. "Highly Pressurized Partially Miscible Liquid-Liquid Flow in a Micro T-junction. II. Theoretical justifications and modeling". **Physical Review E**, 95, 043111, 2017.

Abstract:

The results of an experimental study of a partially miscible liquid-liquid flow which is highly pressurized and confined in a microfluidic T-junction are reported here. Two main flow patterns, i.e., drop flow and co-flow, are identified for Ca_c: $10^{-3} \sim 10^{-2}$ and 10^{-4}, respectively. The characteristics of the drop flow are quantitatively investigated. Drop flow is characterized by an elongating-squeezing stage through which the common 'necking' time (see Garstecki et al. [122]) for truncating the dispersed liquid stream is extended and the truncation point is subsequently shifted downstream from the corner of the T-junction. This effect modifies the scaling function proposed by Garstecki et al. [122]. Experimental measurements further demonstrate the speeds of the drops immediately following their generations can be approximated by the mean velocities from averaging the total flow rates over the channel cross section. In addition, the development of spacing between an emerging drop and the newly produced one within one period of drop generation is visualized and analyzed. A linear model based on drop speed difference is developed to predict the spacing development over time for, respectively, during the filling and the elongating-squeezing stage of the emerging drop. Theoretical justifications to the quantitative studies on drop flow cover various mass transfer mechanisms. The effects and the magnitudes of these mechanisms are evaluated.

4.1 Introduction

Two-phase flows (specifically, liquid-liquid and gas-liquid) within confined microscale (<1mm) planar (a uniform depth) geometries, e.g., cross-flowing junctions and flow focusing and co-flowing

devices, are generally characterized by a laminar flow without turbulent mixing [294] and by certain nonlinearities (referring to the motion equation) resulted from the interfacial effects [123,125,295]. Following a few pioneering experimental studies specifically on two-phase microflows in early 2000s [104,123,169], numerous studies have been performed upon liquid-liquid and gas-liquid flows in microfluidic geometries. Most of them focused on the fluid-fluid (hydrodynamic) interactions and the characterization and analysis of the following functions such as the breakup of one flow stream into fluid segments as well as its mechanics [122,185,191,244,296-299], the development of various flow patterns [122,125,126,131,184,300,301], and the scaling characteristics (e.g., length or volume) of the emulsified monodispersed droplets or bubbles [122,183,184,187,192,193,302]. One of the mostly examined geometries among these studies on generating and manipulating fluid segments is T-junction (the main type of cross-flowing junctions, others including Y- and H-junctions etc.), which gains popularity thanks to its simple design and capability of producing uniform droplets [101,303]. Due to physical merits (e.g., no axial dispersion and enhanced mixing within flowing segments) over continuous microfluidics and the attempted applications in fabricating special materials or in screening and analyzing (bio-)chemical reaction products, drop flows in microfluidics have received excessive attention over the past 15 years or so, in particular, on the fundamental physical aspects of drop generation [304]. Droplet production is usually driven by the instability as a result of shear stresses competing with surface tension, which had been revealed by Taylor [305]. According to several early models[177,306,307], forces including cross-flowing drag force imposed by the continuous fluid, interfacial tension, pressure difference across the interface, and inertial forces due to the relative motion have been considered. The other type of droplet breakup distinct from the unconfined one is exactly the confined droplet generation, in which the dispersed emerging drop is capable of filling the whole main channel obstructing the continuous phase before the breakup occurs. Moreover, there exists a thin film of the continuous fluid separating the drop and channel wall. As a result, the upstream pressure within the continuous fluid increases [122,308] and drives the interface toward a pinch-off position which may locate near the inner corner of the T-junction (a more common scenario, especially for studies of scaling droplet sizes) or a certain distance downstream away from it [125,177,309]. When the neck reaches a critical value, the dispersed (emerging) fluid is then squeezed into a droplet (or, a segment whose length is several times larger than the channel width). Various models have been developed for the droplets under different generation regimes [122,310-312] including: (1) pressure-dominated squeezing regime, (2) shear-driven dripping and jetting regime, and (3) a transitional regime.

However, limited studies are dedicated to the hydrodynamics of miscible (even partially miscible) fluids in micro-scale geometries [313-318]. CO_2 ranging from gas, liquid to supercritical state has been employed as one of the phases in two-phase microfluidic flows for multiple applications in green chemistry, nano-material syntheses and environmental science (see Table 4-1) over the past decade, where the other phase is often an aqueous fluid. CO_2-water pair is one of the most studied fluid pairs in physical chemistry [319]. In view of Gibbs energy change (ΔG) at room temperature, the CO_2-water system at room temperature is very likely a non-mixed two-component one which is featured with an albeit-hypothetical positive ΔG [320] by accounting for the solubility of CO_2 in water (molar fraction ≤ 0.03 mole/mole for pressures and temperatures ranging from 0 to 200bar and 0 to 110°C, respectively) [321,322]. On the other hand, the addition of CO_2 in an aqueous liquid indeed increases the effective viscosity of the bulk fluid under equilibrium conditions, and the bubbly CO_2 results in certain visco-elasticities of the multi-phased suspension with varying rheology [323]. Despite the CO_2/water system confined in micro geometries has been treated as one sharp-interface model [324], it is still unclear whether the dissolved CO_2-in-water (in particular on a molecular level) interface exhibits analogous interfacial effects as their immiscible counterparts do.

Table 4-1 Application examples of CO_2 as a phase in microfluidic systems.

Application	Reference
Chemical reaction	
As solvent or co-solvent	Kobayashi, Mori & Kobayashi [68]; Benito-Lopez et al. [70]; Trachsel et al.[73].
As solvent for extraction	Luther & Braeuer [325]; Assman, Kaiser & von Rohr [74]; Assman et al. [75].
Chemical properties	
Solubility	Tumarkin et al. [88]; Abolhasani et al. [81]; Liu et al. [80]; Cubaud, Sauzade & Sun [87].
Diffusivity	Fadaei, Scarff & Sinton et al. [326]; Sell et al. [327].
Material synthesis	
As a solvent	Marre et al. [328]; Gendrineau et al. [79].
Transport & distribution	
In microchannels	Marre et al. [329]; Ohashi et al. [71]; Blanch-Ojea et al. [330]; Guillaument et al. [331]; Luther et al. [332]; Ogden et al. [333]; Knaust et al. [334].
In micro-scale porous media	Zhang et al. [60]; Kim et al. [57]; Wang et al. [61]; Kim, Sell & Sinton [335]; Kazemifar et al. [336].
Review articles	Marre et al. [67]; Abolhasani et al. [83].

This study experimentally investigates the fluid dynamics of CO_2/water confined in a micro T-junction where the denser and viscous water is the continuous phase and the comparably dense but much less viscous liquid CO_2 is the dispersed phase. This chapter proceeds as follows. Section 4.2 presents the experimental system and the micromodel that are utilized for studying, in particular, high-pressured two-phase microfluidics as well as how the experimental data are processed. In section 4.3, we describe the procedures of our experimental work and detail the different stages of one period of the drop generation based on our observations of the flow regimes under the flow conditions investigated. In section 4.4, we first discuss the effects of the dissolution of CO_2 molecules in the continuous fluid-water and compare the relative strengths of the involved convection and diffusion processes. Then we show the experimental results and our discussions from the point of view of the related hydrodynamics. Finally, section 4.5 summarizes our experimental observations and provides a conclusion of this work.

4.2 Experimental Setup

The experimental system introduced in Chapter 3 has been utilized to conduct the experimental study in this chapter. In this section, the discussions are focused on the specific devices and methods required by the experimental study.

A micro T-junction is fabricated in a silicon/glass microchip. Prior to the fabrication, a photo mask with an image of 2D network patterns (figure 4.1 (A)) is designed using AutoCAD (version 2012, Autodesk Inc.) and commercially printed. The fabrication proceeds in the sequence of (1) standard photolithography, (2) deep reactive ion etching (DRIE), (3) inlet & outlet drilling and wafer cleaning, (4) anodic bonding of silicon and glass wafer, and (5) dicing of the bonded wafers (figure 4.1 (B)) into a final size (74mm×44mm×1.2mm). Detailed procedures of the fabrication can be found in Chapter 3. After the DRIE but prior to wafers bonding, the channel size of the T-junction is examined under a microscope (a 20x objective applied, Nikon Eclipse) mounted with a camera (model KP-D50, Hitachi). Figure 3.5(B) is a bottom view of the T-junction where the channel width is measured using ImageJ (version 1.48, NIH, USA), and Figure 3.5(C) shows the top of the channels. Based on a focusing shift from the top to the bottom of the channel through turning the fine focus knob of the microscope, channel depth (D) can be estimated. The width (W) and the depth (D) of both the main channel and the side channel are (150 ± 2.5) µm and (100 ± 2) µm, respectively.

Liquid CO_2 and DI water are used as the dispersed phase flowing in the side channel and the continuous phase flowing in the main channel, respectively, and they encounter at the T-junction

(figure 4.2 (A)). The flow phenomenon at the T-junction are visualized using a microscope (includes a 5x and a 10x objective) (model BX51, Olympus) mounted with a high speed camera (model v210, Phantom). This camera is capable of capturing images at 2000 frames per second (fps) at the full 1280×800 resolution, and faster frame rates can be achieved at reduced resolutions. Over all the flow conditions in this study, the 10x objective together with a frame rate of no lower than 5000fps that resulted in a 304×800 resolution is applied; and only when the drop length or drops spacing is oversized (larger than 5W) do we additionally employ the 5x objective as well as a 3000 fps and a

(A)   (B)
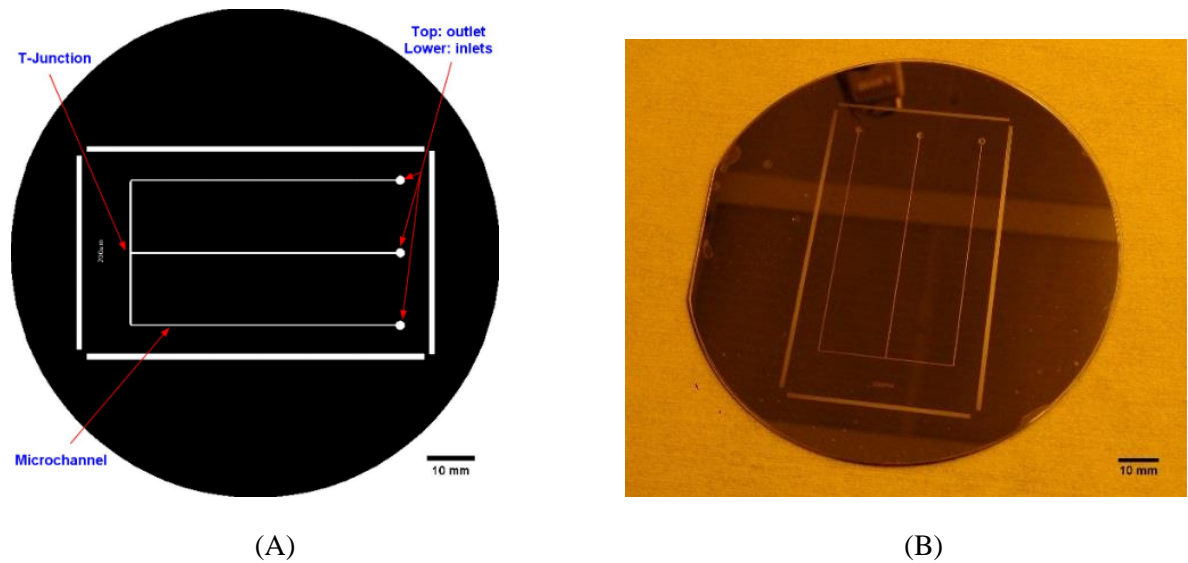
Figure 4.1 A silicon/glass microchip featured by a micro T-junction. (A) Schematic of the photo
mask showing the T-junction, microchannels and one outlet as well as two inlets; (B) a
photo of the to-be-diced silicon/glass microchip after the anodic bonding of the two
wafers. The rectangles enclosing the microchannel region outline an after-dicing size of
74 mm $\times$ 44 mm of the microchip.

a 560×800 resolution. Compared with a halogen lamp, the mercury lamp of the microscope together with an exterior power supply (model BH2-RFL-T3, Olympus) can provide a better illumination with a higher intensity and is thus applied. Based on frames-stacked videos showing the flows at the T-junction, descriptive parameters (e.g., drop length, drops spacing, and drop speed), as shown in figure 4.2 (A), of the liquid CO_2 drops become measurable. Raw videos from the experiment are first adjusted to their best qualities (in terms of brightness, contrast or color balance) and are then cropped to the sizes (185×800 and 95×800 from using 10x objective and 5x objective, respectively) of interest for the following processing, both of which are done using the software ImageJ. Afterwards, the

videos are imported to Matlab (version R2014a, Mathworks) and the above parameters are measured by using a series of self-developed Matlab codes based on identification of drops (figure 4.2 (B)).
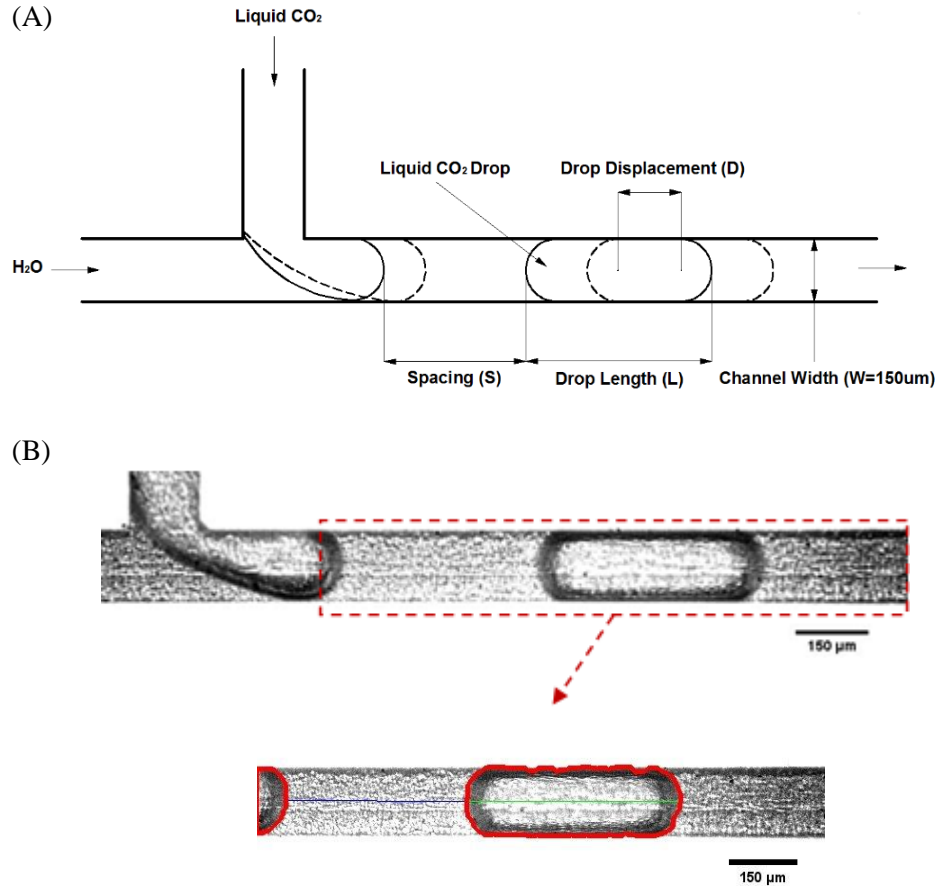
Figure 4.2 An example of liquid CO_2 and water two-phase flow in a micro T-junction where liquid CO_2 drops are being produced. (A) Schematic of a newly generated liquid CO_2 drop and a second one starts formation: solid lines and dash lines depict the drops at the ith and the $(i+1)^{th}$ frame, respectively, during one period of drop generation. Parameters to be measured include: (I) drop length L, (II) drop spacing S between the emerging drop and the adjacent formed one within one period, and (III) drop speed V determined by the drop displacement Δd (centroid to centroid) during one time interval Δt of the frames. (B) A sample of frame selected from the experiment video. Image below shows an identification of a formed drop and the measurements of drop length L and drop spacing S using the same frame in Matlab.

4.3 Experimental Procedures And Observations

Prior to experiments, water bath at a temperature of (25 ± 0.4) °C is circulated within the vinyl tubing (enclosing the circulating water as well as the stainless steel tubing) and a temperature control jacket (for CO_2 cylinder) of the CO_2 pump for 30 minutes in order to maintain the CO_2 temperature at 25°C. With a setting pressure of (64 ± 1) bar (shown by the N_2 tank regulator, see Figure 3.1) applied at the BPR, liquid CO_2 from its pump infuses into the stainless tubing and the microchannels in a controlled way by slowly opening two CO_2-side valves (installed upstream of the connector). During this process, two water-side valves are kept closed to prevent the infused CO_2 from entering the water pump. Due to a lower pressure (~60 bar) than 64 bar, infused CO_2 will not rush through the BPR but stays within the microchannels and the tubing. Afterwards, a constant flow rate of 50 µL/min is applied to CO_2, and the pump piston's continuous compression results in an increase of CO_2 pressure. Only until the pressure reaches the setting pressure will the BPR diaphragm be jacked up to allow CO_2 flows through at that flow rate. The real back pressure measured by the pressure transducer at present is 65 bar. Using the water pump the pressure of DI water is raised to 65 bar in advance and a constant flow rate of 50 µL/min is given, and then the two water-side valves are slowly opened to let the water enter into its tubing and the microchannels. The two liquids are very likely to meet between the close-to-connector valve (Figure 3.1) and the T-junction on-chip. Within 1 minute or so, liquid CO_2 and water can be observed and start to interact constantly at the T-junction.

Figure 4.3 shows that a drop flow results from this set of flow conditions ($Q_{LCO2} = 50$ µL/min; $Q_{H2O} = 50$ µL/min) which is characterized by a periodic generation of liquid CO_2 drops. The period is mainly composed of: (A) a stagnating & filling stage, (B) an elongating & squeezing stage and (C) a truncating stage in a chronological order.

(A) Stagnating & filling: immediately after a drop is produced, there is an instant retraction of the ends of the drops (one is the back end of the newly produced drop and the other is the front end of the emerging drop) from the truncation point due to interfacial tension and a transient recovery (or stabilization) of the new interface. This interfacial preparation-like transience does not contribute too much to the advancing of the CO_2 front which earns the name of "stagnating". From this ready-to-go moment until the CO_2 portion touches the far-end channel wall, CO_2 gradually blocks the cross section of the microchannel as well as the water flow, which is termed as "filling". Stagnating versus filling in Figure 4.3 is 0.2/1.4 (ms/ ms). During this stage, the pressure difference between CO_2 (P_c) and water (P_d) facilitating the CO_2 filling dominates the

interfacial variations relative to the Laplace pressure (ΔP_L, determined by the interfacial tension (γ) and the radii of curvatures according to Young-Laplace equation).
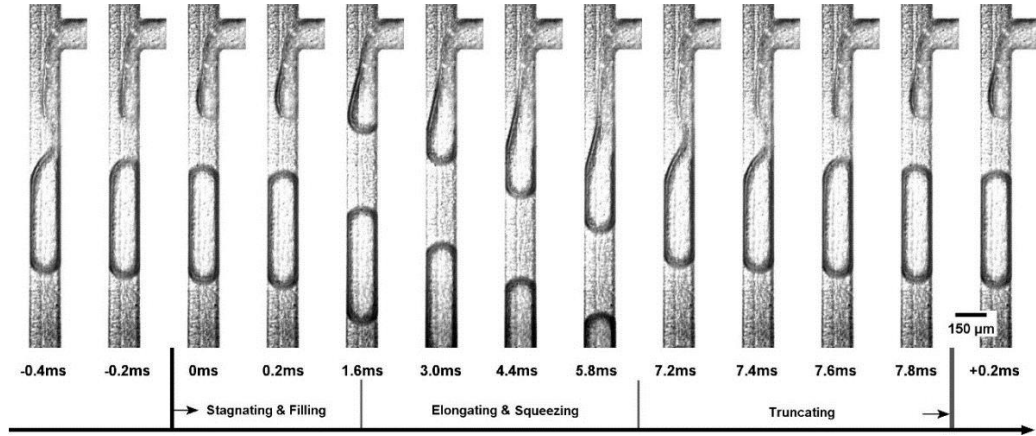
Figure 4.3 A quick overview of one period ($t_0 = 7.8$ ms) of liquid CO_2 drop generation during the flow condition where both CO_2 and water flow at 50 µL/min. Note that the images are rotated 90° clockwise as compared to figure 4.2 for ease of alignments. The period t_0 is generally divided into three stages: (a) a stagnating and filling stage t_{sf}, (b) an elongating and squeezing stage t_{es}, and (c) a truncating stage t_{tr}. And each stage is characterized by a specific time length. Here within one period $t_0 = 7.8$ ms, t_{sf}, t_{es} and t_{tr} are approximately 1.6 ms, (6.6 - 1.6) = 5 ms and (7.8 - 6.6) = 1.2 ms, respectively.

(B) Elongating & squeezing: once the water, as the continuous phase, is blocked, a notable pressure is built up in the proximity of the interface on water side which leads to a resisting effect towards the incursion of the CO_2 portion particularly on the upper section (see Figure 4.3) of their interface. As the CO_2 portion elongates further downstream, its clear upper section is also elongated and simultaneously squeezed almost parallel to the water flow. On the other hand, the shading section starting from the juncture with the clear section to the upper contact point with the far-end wall is pushed downstream as well, which is driven by the continuous phase pressure (P_c) plus the Laplace pressure (more specifically, its component on the flowing direction of water) competing with the within drop pressure. Note that the conjuncture identifying the clear upper section from the shading section also migrates hydrodynamically accompanying the clear section. Once the sum of the continuous phase pressure (P_c) and the Laplace pressure (more specifically, its component perpendicular to the CO_2 flow direction) approaches to the within drop pressure at the conjuncture, it indicates the end of the second stage and an onset of the next one.

(C) Truncating: as long as the pressure conditions are reached, water starts to truncate the emerging drop of liquid CO_2. Generally, the truncating commences from the above conjuncture where the Laplace pressure can effectively cope with water to resist the liquid CO_2 drop side. During this stage, a concave is formed first at the conjuncture and expands to touch the wall within a very short time (1 ms or so). By this moment, the emerging drop splits into two segments: the front one forming as a complete drop and the back one becoming another emerging drop.

Following the first flow condition ($Q_{H2O}/Q_{LCO2} = 50$ (μL/min)/50 (μL/min)), more flow cases in terms of different combined flow rates of liquid CO_2 and water have been investigated. These cases (Table 4-2) numbered from 1 to 28 can be categorized into two groups: the first group (case 1-21 with case 12 as an exception) has a constant total flow rate ($Q_{LCO2} + Q_{H2O} = 100$ μL/min) while the flow rate of CO_2 is first increased and then decreased and the flow rate of water is first decreased and then increased; the second group (case 22-28) is featured by a constant flow rate of liquid CO_2 ($Q_{LCO2} = 50$ μL/min) as well as stepwise ascending flow rates of water from 100 μL/min up to 500 μL/min. Case 12 was designed to test the minimum flow rate ratio that still results in co-flow. Sequentially, when a new pair of flow rates are applied, the videos of this case are recorded after a waiting time of 30 minutes when the flow regime is deemed as stabilized. Table 4-2 provides two parameters that are derivable from the two flow rates, namely, flow rate ratio (Q_{H2O}/Q_{LCO2}) and capillary number Ca_c ($Ca_c = \eta_c u_c/\gamma$) of the continuous phase-water. Here, η_c, u_c and γ are the dynamic viscosity ($\eta_c = 890$ μPa·S at $T = 298$ K and $P_c = 65$ bar [337] of water, the mean velocity ($u_c = Q_{H2O}/(D·W)$) of the water phase through the entire cross section of the channel and the quasi- equilibrium interfacial tension ($\gamma = (31.7\pm0.3)$ mN·m^{-1}, see Hebach et al. [338] and Georgiadis et al. [339]) of water with liquid CO_2, respectively.

Flow regimes of the 28 cases are shown as a function of Q_{H2O}/Q_{LCO2} and Ca_c number (see Figure 4.4) by selecting either the frames at the end of their truncating stages (for drop flows) or representative frames of the co-flows. As Q_{H2O}/Q_{LCO2} is reduced from 50/50 down to 15/85, Ca_c (calculated by water) has a reduction from O (10^{-3}) to O (10^{-4}). As a result, a transition of flow regime from drop flow to co-flow occurs (Figure 4.4(A)). As Q_{H2O}/Q_{LCO2} further reduces, there is no more regime transition where co-flow becomes a dominant flow regime. The minimum Q_{H2O}/Q_{LCO2} being applied is 5/220 (case 12) and it still results in a co-flow regime. However, CO_2 stream occupies a larger area than water compared with in case 11. Despite lower Q_{H2O}/Q_{LCO2} and/or Ca_c are not studied, the extreme case assuming Q_{H2O} approaches 0 ($Q_{H2O}/Q_{LCO2} \approx 0$, $Ca_c \approx 0$) can lead to a pure CO_2 flow.

Table 4-2a Investigated cases in this experimental study: case 1 to 13.

Case #	1	2	3	4	5	6	7	8	9	10	11	12	13
Q_{H_2O} (µL/min)	50	40	30	25	20	15	12	10	8	6	5	5	15
Q_{LCO_2} (µL/min)	50	60	70	75	80	85	88	90	92	94	95	220	85
Q_{H_2O}/Q_{LCO_2}	1	0.67	0.43	0.33	0.25	0.18	0.14	0.11	0.09	0.06	0.05	0.02	0.18
Ca_c	1.6×10^{-3}	1.2×10^{-3}	1.0×10^{-3}	0.8×10^{-3}	0.6×10^{-3}	4.7×10^{-4}	3.7×10^{-4}	3.0×10^{-4}	2.5×10^{-4}	1.9×10^{-4}	1.6×10^{-4}	1.6×10^{-4}	4.7×10^{-4}
t_0 (ms)	7.8	9	11.4	13.6	16.4								23.2
f (Hz)	128	111	88	74	61								43

Table 4-2b Investigated cases in this experimental study: case 14 to 28.

Case #	14	15	16	17	18	19	20	21	22	23	24	25	26	27	28
Q_{H_2O} (µL/min)	55	60	65	70	75	80	85	90	100	125	150	175	200	350	500
Q_{LCO_2} (µL/min)	45	40	35	30	25	20	15	10	50	50	50	50	50	50	50
Q_{H_2O}/Q_{LCO_2}	1.22	1.5	1.86	2.33	3	4	5.67	9	2	2.5	3	3.5	4	7	10
Ca_c	1.7×10^{-3}	1.9×10^{-3}	2.0×10^{-3}	2.2×10^{-3}	2.3×10^{-3}	2.5×10^{-3}	2.7×10^{-3}	2.8×10^{-3}	3.0×10^{-3}	3.9×10^{-3}	4.7×10^{-3}	5.5×10^{-3}	6.2×10^{-3}	1.1×10^{-2}	1.6×10^{-2}
t_0 (ms)	8.4	8.6	8.2	10.4	10.8	14.2	19.6	128.6	6.3	4.7	3.8	3.2	2.8	1.7	1.1
f (Hz)	119	116	122	96	92	70	51	5~7	157	214	260	315	352	600	888

(A)
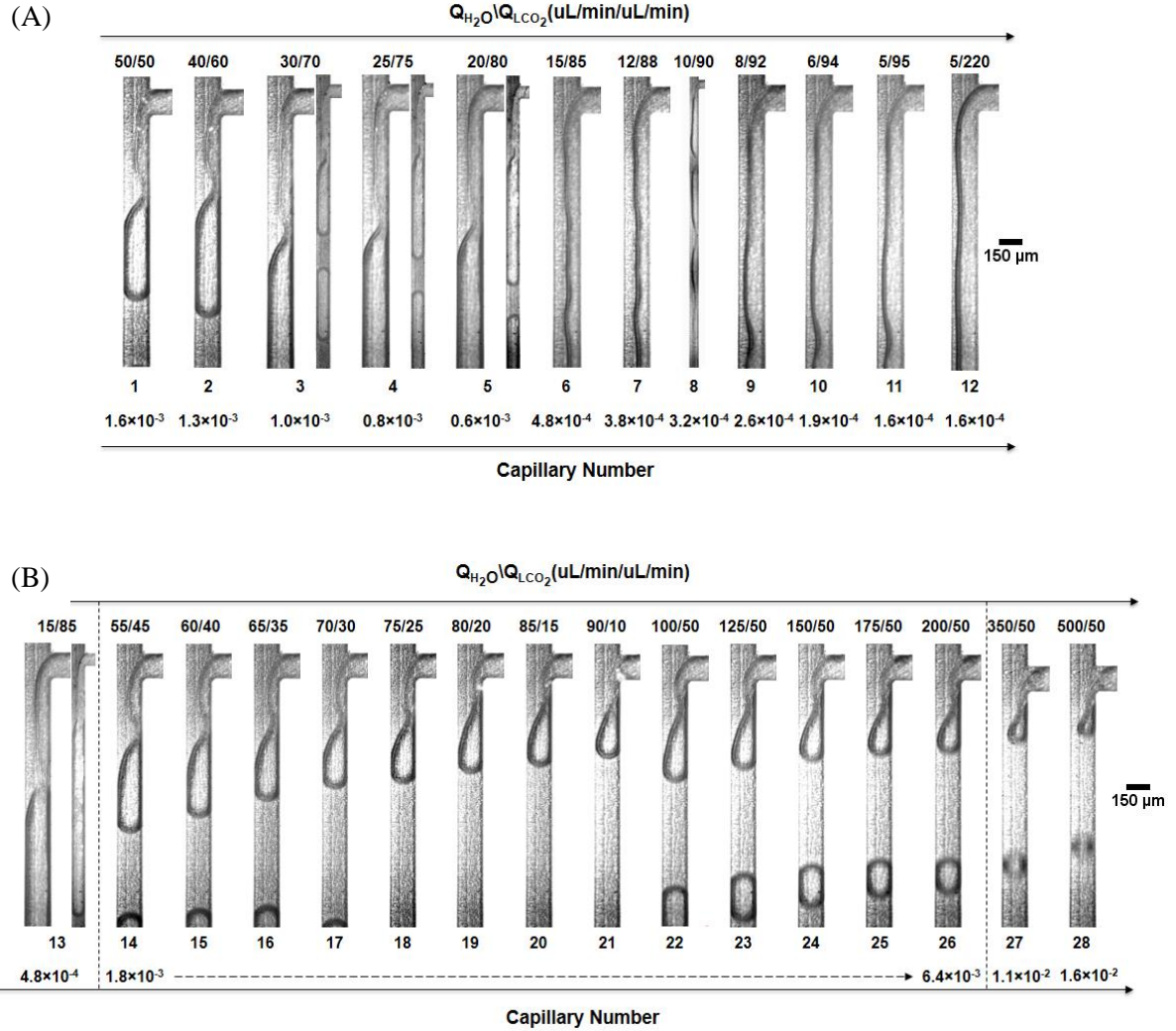
Figure 4.4 Flow regimes of liquid CO_2 and water two-phase flow at a T-junction as a function of Q_{H2O}/Q_{LCO2} and Ca_c number: liquid CO_2 enters from the side channel as the dispersed phase and water flows in the main channel as the continuous phase of the T-junction. (A) Q_{H2O}/Q_{LCO2} and Ca_c number are decreased from 50/50 to 5/220 and 1.6×10^{-3} to 1.6×10^{-4}, respectively. Case 3 to 5 are shown by two frames captured using a 10x (left) and a 5x objective (right). Case 8 is shown by an end-to-end combination of three frames from using the 5x objective. (B) From case 13 to 21, Q_{H2O}/Q_{LCO2} and Ca_c number are both increased due to the flow rate increase of water; from case 22 to 28, water flow accelerates from 100 to 500 μL/min while the liquid CO_2 is maintained as a constant flow. As Ca_c reaches $O(10^{-2})$, it leads to a dripping regime (case 27 and 28) of the drop flow.

80

Next the cases featured by $Q_{H2O}/Q_{LCO2}>1$ are to be investigated. First, Q_{LCO2} is reduced from 220 to 85 µL/min, and meanwhile Q_{H2O} speeds up from 5 to 15 µL/min (case 13, Figure 4.4(B)). The conditions of case 6 are re-applied here but the flow regime (even after 30 minutes) seemingly 'oversteps' into drop flows rather than recurring as a co-flow. Instead of using a hysteresis mechanism in terms of the history of the applied flow rates in a comparable study [340], a memory of interfacial force relative to viscous one represented by Ca number may account for the flow regime drift in a better way. Corresponding to the flow rate variations from case 12 to 13, local P_c and P_d may have increased and decreased by a certain extent (although the two pressures are impossible to be measured locally right now, their upstream pressures shown by the pumps have an increase of 6 kPa and a decrease of 2 kPa, respectively, while the measured back pressures have no change.) than that in case 12, respectively. If additionally assisted by the interfacial force in memory (much superior over viscous force in case 12 than in case 13), water phase is very likely to truncate the liquid CO_2 stream and thus leads to a drop flow. However, more detailed studies are required to validate our deduction about the inherited effect of interfacial force (variable interfacial tension and/or contact angle might contribute in this), which is beyond the scope of this study. After this case, Q_{LCO2} is gradually reduced from 45 to 10 µL/min and Q_{H2O} keeps increasing from 55 up to 90 µl/min simultaneously (case 14 to 21, Figure 4.4(B)), both of which are performed every 5 µl/min at the pumps. Note that beyond $Q_{H2O}/Q_{LCO2} = 90/10$ (when $Ca_c = 2.8\times10^{-3}$), there is no more two phase flows and water occupies the whole channel. Drop generations of case 14 to 21 are basically capable of being described and analyzed taking advantage of the above three stages. As both Q_{H2O}/Q_{LCO2} and Ca_c increase in this range, drop sizes (L) become smaller at least by observations qualitatively. In addition, the truncation points are getting closer to the corner of the T-junction as well; however, it does not imply the drop generation is faster (Table 4-2(B)).

The constant total flow rate of 100 µL/min limits the range of Ca_c ($10^{-4} \sim 10^{-3}$) for the study of the effect of Ca number. Thus, by controlling the liquid CO_2 as a constant flow ($Q_{LCO2} = 50$ µL/min), the flow rates of water have been increased from 100 up to 500 µL/min in order to provide higher Ca_c. Ranging from case 22 to 26, the drop flows evolves consistently with the trend of previous cases. Given with the cross section area (150 µm $\times$ 100 µm) of the microchannel, only when Q_{H2O} exceeds approximately 320 µL/min will the resulted Ca_c be $O(10^{-2})$. Case 27 and 28 are characterized by $Ca_c = 1.1\times10^{-2}$ and $Ca_c = 1.6\times10^{-2}$, respectively, and consequently, a distinct flow regime-dripping regime-occurs where the emerging drop during the period of generation is unable to block the channel. Besides, the drop generations are much faster (Table 4-2(B)) and the ratio (L/W) of drop

length (L) over channel width (W) approaches to 1 or maybe smaller than 1 (seem as suspended drops, Figure 4.4(B)). Other than Q_{H2O}/Q_{LCO2} and Ca_c, Table 4-2 also lists the periods (t_0, ms) and the frequencies ($f = 1/t_0$, Hz) of all the drop generations of the relevant cases. For case 1 to 21, high frequencies (>100 Hz) are achieved in the vicinity of $Q_{H2O}/Q_{LCO2} = 1$ (specifically, $Q_{H2O}/Q_{LCO2} = 0.67$ ~ 1.86); for the cases with a constant liquid CO_2 flow (case 22 to 28), the frequencies of drop generations are positively correlated with Ca_c, and those of the two dripping regimes are so high that although a faster frame rate (8000 fps, compared with 5000 fps for cases 1 to 21 and 6000 fps for cases 22 to 26) of the camera is applied, it does not improve much in providing quality captures of the drops especially after the generation (Table 4-2(B)).

4.4 Theoretical Discussions

4.4.1 Interfacial Dissolution of CO_2 in Water within the T-junction

4.4.1.1 Hydration of the dissolved CO_2 molecules

The hydration of CO_2 when it dissolves in water (pH $\approx$ 5.93), as formulated by the reaction at chemical equilibrium below, can produce carbonic acid:

$$CO_2(aq) + H_2O \rightleftharpoons H_2CO_3(aq). \tag{4.1}$$
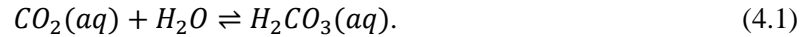
The equilibrium constant K_{CO2}, as defined by the ratio of the reaction rate constant (k_f) of the forward reaction over that (k_r) of the reverse reaction under equilibrium (k_f/k_r, which also equals to the concentration ratio [H_2CO_3]/([CO_2]×[H_2O]) at equilibrium, where square bracket denotes the concentration in the unit of mole/L (or mol/L); however, the above reaction is generally a pseudo-first-order reaction because of a constant [H_2O] and [H_2O] can thus be omitted out of the denominator, i.e., k_f/k_r = [H_2CO_3]/[CO_2].), indicates how much CO_2 can be hydrated into carbonic acid. At 25°C, $K_{CO2} \approx 1.7 \times 10^{-3}$ (unit:1) for the above reaction indicates the vast majority of CO_2 exists as molecular CO_2 rather than H_2CO_3 in water [341]. The other fact is that the forward process is much slower than the reverse to reach equilibrium at room temperature ($k_f \approx 0.035$ s^{-1} versus $k_r \approx 20.6$ s^{-1} for the first-order reaction with respect to CO_2 and H_2CO_3 [342,343]; given by the time scale of the CO_2 drop generations at T-junction (Table 4-2, but without considering case 13 and 21), it is even not long enough for the above reaction to reach equilibrium. When the concentration of H_2CO_3 is relatively low in the aqueous solution, an overall reaction including the dissociation of H_2CO_3 for producing bicarbonate HCO_3^- is usually introduced to replace equation (4.1) by the following

$$CO_2 + H_2O \rightleftharpoons HCO_3^- + H^+. \tag{4.2}$$

Note that the CO_2 in the above overall reaction includes both aqueous CO_2 and hydrated ones (H_2CO_3). The equilibrium constant (K'_{CO2}) of the overall reaction can be expressed as

$$K'_{CO2} = k'_f/k'_r = [HCO_3^-][H^+]/([CO_2] \cdot [H_2O]). \tag{4.3}$$

The value of K'_{CO2} at 25 °C and very low ionic strength (~0) is 4.45×10^{-7} [344]; or pK_a ($pK_a = -\log_{10}K_a$) is 6.35 as an apparent dissociation constant of nominal H_2CO_3 (including CO_2 (aq) and the rare carbonic acid) here [341]. In fact, the pK_a of carbonic acid (purely H_2CO_3) is around 3.6 at 25 °C [341]. Furthermore, bicarbonate may dissociate into hydrogen ion (H^+) and carbonate ions (CO_3^-) by the reaction

$$HCO_3^- \rightleftharpoons CO_3^{2-} + H^+, \tag{4.4}$$

which is characterized by a second equilibrium constant K_{HCO3^-} defined as

$$K_{HCO_3^-} = [CO_3^{2-}][H^+]/[HCO_3^-]. \tag{4.5}$$

Comparatively, K_{HCO3^-} has a value of 4.84×10^{-11} (mol/L), or the dissociation constant pK_a of HCO_3^- is 10.3 [344]. Due to its much lower dissociation constant ($pK_a \approx 14$ at 25 °C [345]), water's ionization equilibrium by itself is beyond the scope of our discussion. In a nutshell, the hydration of dissolved CO_2 at the interface shows an overall negligible effect to the total dissolved CO_2 molecules, and they are still vastly present as CO_2 molecules in the aqueous solution, given the time scale in the micro T-junction.

4.4.1.2 Theoretical estimate of diffusion-controlled dissolution

CO_2 molecules, after their dissolution in water (i.e., dissolved CO_2(aq) molecules), can be transported from the bulk CO_2 to water driven by the diffusion of the CO_2(aq) molecules under a certain concentration gradient. In general, several mechanisms should be considered when discussing mass transfer, which mainly include hydrodynamic dispersion, convection and diffusion. Considering a mixing zone with a concentration gradient of the sample of interest in a pressure driven microchannel flow, velocity profile is parabolic type which causes distortion to the mixing zone and must be considered in evaluating the mass transfer in this region. However, for the mixing zone shown in Figure 4.5, which is a small region of the entire interface between the dispersed and continuous phase in the x-y plane, hydrodynamic dispersion is negligible. The curved interface is meant to illustrate the impact of the interfacial tension between the CO_2 drop and the thin water film that exists between the

CO_2 drop and channel walls in the z-direction (top and bottom channel walls). First, the velocity component in y-direction (channel height direction) is small which is mainly induced by the vortices inside the droplets. Therefore, the hydrodynamic distortion to the mixing zone caused by the velocity component in the y-direction is negligible. Second, the velocity component in the x-direction is also small. During the filling and stagnation stage, there exists a velocity component in the x-direction which is much smaller than that in the z-direction. When the drop formation evolves from the filling to the elongating and squeezing stage which is the longest stage among the three stages, the velocity component in the x-direction is approaching zero because the interface is almost parallel to the vertical channel walls. Therefore, its overall impact on hydrodynamic dispersion is negligible. Third, the possible distortion to the mixing zone could be caused by the shear motion over the interface, which is induced by the difference of the velocity component in the z-direction between the continuous and dispersed phases. However, this hydrodynamic distortion is also negligible if considering the entire drop formation period. This study operates in the squeezing regime and in the longest stage, elongating and squeezing stage, the continuous phase upstream is almost completely blocked by the CO_2 drop which almost touches the channel walls. This results in a negligible shear motion over the interface and thus negligible hydrodynamic distortion. During the first short filling stage, the shear motion is appreciable. However its effect in distorting the mixing zone is reduced to a certain extent by the interfacial tension that tends to hold the interface in shape. Therefore, overall the hydrodynamic dispersion caused by the shear motion can be neglected.

The CO_2 transport over the mixing zone region due to convection is mainly influenced by the velocity component in the x-direction because the velocity in the z-direction is tangential to the interface. As discussed above, the velocity component in the x-direction is very small during the filling stage and almost approaches to zero during the long elongating and squeezing stage. Therefore the mass transfer of CO_2 over the mixing zone is mainly dominant by diffusion.

The dissolution and diffusion of the CO_2 molecules is schematically described in Figure 4.5. Due to the unsteady interface in terms of its location and shape, it is assumed that

(1) water is an isotropic and homogeneous solvent;

(2) the diffusion coefficient of CO_2 molecules into water, D_{CD}, is a constant;

(3) the effect of the finite water film (thickness $\approx$ 2%×hydraulic diameter [81]), which exists between CO_2 and the channel walls due to wettability, on CO_2 dissolution and diffusion is negligible and thus we only consider the transport process across the diffusive film (shown in Figure 4.5);

84

(4) mass transport is one-dimensional in the direction perpendicular to the interface (x-direction in the revised Figure 4.5), in other words, we focus on the x-y plane;

(5) quasi-steady state is achieved, which is rational especially in the 'elongating & squeezing' stage, the generally longest stage compared to the other two stages. Therefore the location of the interface is constant relative to the channel wall; and the hydrodynamic dispersion on x-axis may approach zero.

For this one dimensional model under a quasi-steady state (on the negative 'x' direction), the dissolution of CO_2 molecules at the interface (solid line in Figure 4.5) and the diffusion of the dissolved $CO_2(aq)$ molecules in water can be described by the following two equations:

$$\left.\frac{dC}{dt}\right|_{x\sim0} = K_{CD}A(C_s - C),$$

(4.6)

$$J_x = -D_{CD}\frac{dC}{dx}.$$

(4.7)

where C is the concentration of the dissolved CO_2 in water at time t $(0 < t < t_0)$, C_s is the solubility of CO_2 in water at a given pressure and temperature, K_{CD} is a constant with a unit of $1/(m^2 \cdot s)$ and A is the effective dissolution area (i.e., the area of the concave interface). Equation (4.7) is the Fick's first law of diffusion, where J_x $(mol/(m^2 \times s))$ is the diffusion molar flux of the dissolved CO_2 molecules per square meter per second and it is related to the concentration gradient. Note that we omit the convective molar flux in this binary mixture caused by molar average velocity in view of the very small molar fraction $(C/(C+C_{H2O}) \leq 2 \times 10^{-3})$ of CO_2 in the mixture.

Integrate equation (4.6) and (4.7) at $x=0$ with time approaching infinite $(t \sim \infty, X_D \sim W/2)$ leads to

$$\left.\frac{dC}{dt}\right|_{x\sim0} = K_{CD}A\frac{W}{2}\frac{J_0}{D_{CD}},$$

(4.8)

if V as the final dissolution volume is introduced, , equation (4.8) can be revised to

$$\frac{1}{V}\left.\frac{d(VC)}{dt}\right|_{x\sim0} = K_{CD}A\frac{W}{2}\frac{J_0}{D_{CD}},$$

(4.9)

in which $d(VC)/dt$ at $x = 0$ offsets $J_o \times A$ (mol/s) and yields the factor K_{CD}

$$K_{CD} = \frac{D_{CD}}{VW/2}.$$

(4.10)

Thus equation (4.6) can be rewritten as

$$\frac{dC}{dt}\bigg|_{x\sim0} = \frac{D_{CD}A}{VW/2}(C_s - C). \qquad (4.11)$$

Equation (4.11) describes the dissolution of CO_2 molecules at the interface in terms of the concentration variations over a sufficiently long period of time, which is dominated by diffusion as well. The integration of this equation leads to

$$C_{x\sim0} = C_s(1 - e^{-\frac{D_{CD}A}{VW/2}t}). \qquad (4.12)$$

(A)   (B)
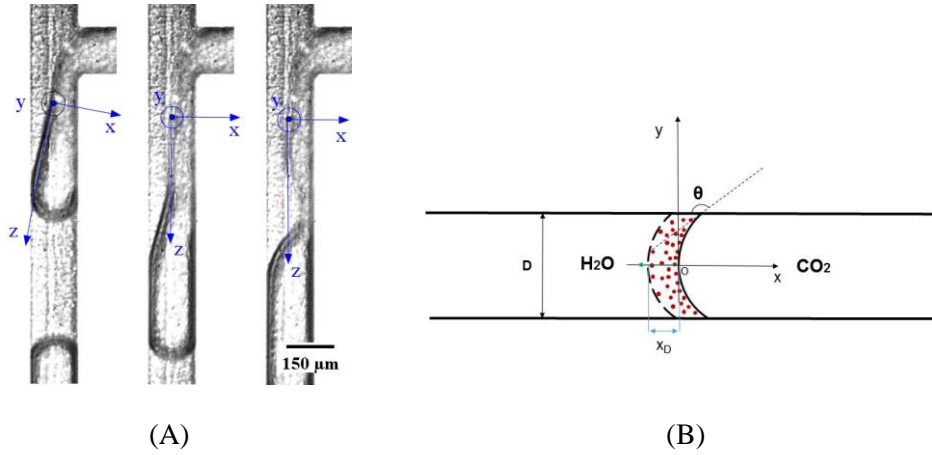
Figure 4.5 (A) Indications of the Cartesian coordinates (x: perpendicular to the liquid CO_2 stream; y: tangential to the interface and in the channel depth direction; z: tangential to the interface and in the flow direction; origin: one point-of-interest on interface at a half channel depth), scale bar: 150µm. (B) Schematic of the transport of the dissolved CO_2 molecules from the interface (solid line) into water driven by dissolution and diffusion (in x-y plane). The region outlined by a solid line and a dash line represents a diffusive film of the CO_2 molecules. Note that this diffusive film is enlarged for easy viewing and is actually very thin compared to the channel depth D ($X_D/D \sim 10^{-2}$, where X_D is the thickness of the diffusion film.). The schematic shows a cross-sectional view of the two phases separated by two interfaces, one (the solid line) is between CO_2 and the CO_2 aqueous solution and the other (the dash line) is a hypothetical one between pure water and the CO_2 aqueous solution where CO_2 concentration is non-zero but approaching zero.

Based on an approximation of $V\sim A\times W/2$, equation (4.12) may be simplified as

$$C_{x\sim0} = C_s(1 - e^{-\frac{4D_{CD}}{W^2}t}). \qquad (4.13)$$

86

The diffusion coefficient of CO_2 molecules into water, D_{CD}, at $T = 298$ K can be estimated by the Stokes-Einstein relation [346] as

$$D_{CD} = \frac{k_B T}{6\pi\eta r},$$ (4.14)

where k_B, η and r are the Boltzmann constant ($k_B = 1.38\times10^{-23}$ J/K), the dynamic viscosity ($\eta = 890$ µPa·s at 298 K) of water and the kinetic radius of the hypothetical sphere-shaped CO_2 molecules ($r = 1.65$ Å $= 1.65\times10^{-10}$ m, see Li et al. [347]), respectively. Therefore, D_{CD} is approximately 1.5×10^{-9} m^2/s and equation (4.13) can be specifically written as follows,

$$C_{x\sim0} = C_s(1 - e^{-\frac{4}{15}t}).$$ (4.15)

Moreover, C_s at the applied pressure and temperature condition in this study has a value of 1.267 mol/L or so based on the literature [321,322] where the molar fraction of CO_2 is approximately 0.0247 mole per 1 mole water. As a result, equation (4.15) can be further specified as

$$C_{x\sim0} \ (mol/L) = 1.267(1 - e^{-\frac{4}{15}t}).$$ (4.16)

In view of the time durations in Table 4-2, they are too short to render a saturation scenario of the dissolved CO_2 at the interface, though a large number ($10^{-4}N_A$, N_A: Avogadro number) of CO_2 molecules at least conceptually arise in the aqueous solution near the interface.

4.4.2 Diffusion of CO_2 in Water within the T-junction

4.4.2.1 Molecular diffusion of the dissolved CO_2 molecules

As discussed in section 4.3, the interface between liquid CO_2 and water within the T-junction during the second and the third stage of one period has a clear upper section and a shading lower section. The former, as observed, barely moves relative to the shading section due to a compromise of the capillary pressure in squeezing CO_2 stream. This section of the interface is considered quasi-hydrostatic and diffusion becomes the only transport mechanism of the dissolved CO_2 molecules. To evaluate how far the CO_2 molecules can be transported into water, namely, the diffusion distance, an appropriate solution of Fick's second law may be required [348]. The diffusion equation for one dimensional model at a non-steady state has been defined by Fick's second law [265], i.e.,

$$\frac{\partial C}{\partial t} = D_{CD}\frac{\partial^2 C}{\partial x^2}.$$ (4.17)

The above partial differential equation can be solved by inducing a constructed function $y = \dfrac{x}{\sqrt{4D_{CD}t}}$ and being rearranged as a total differential equation of C with respect to y. Here, a final solution is provided (see equation 4.18) and the detailed deductions can be found in literature [349,350].

$$\int dC = \int Be^{-y^2}\,dy,\tag{4.18}$$

where B is a constant resulting from the integration. In order to solve the above integrals, the following boundary conditions are used

$$C = \begin{cases} C_x = C_0, \ at \ y = 0 \ (x = 0, t > 0) \\ C_x = C_b = 0, \ at \ y = \infty \ (x = \infty, \ t = 0). \end{cases}\tag{4.19}$$

Therefore, we have

$$\int_{c_0}^{0} dc = B\int_{0}^{\infty} e^{-y^2}\,dy.\tag{4.20}$$

Based on the properties of error function erf(y) and complementary error function erfc(y), we have

$$\mathrm{erf}(y) = \frac{2}{\sqrt{\pi}}\int_{0}^{y} e^{-\xi^2}\,d\xi,$$

$$\mathrm{erfc}(y) = 1 - \mathrm{erf}(y) = \frac{2}{\sqrt{\pi}}\int_{y}^{\infty} e^{-\xi^2}\,d\xi.\tag{4.21}$$

Let $y = 0$ in equation (4.21),

$$\int_{0}^{\infty} e^{-y^2}\,dy = \frac{\sqrt{\pi}}{2}.\tag{4.22}$$

Substitute (4.22) into (4.20) gives

$$B = \frac{-2c_0}{\sqrt{\pi}}.\tag{4.23}$$

Substitute B back to equation (4.18) yields

$$\int dC = \frac{-2c_0}{\sqrt{\pi}}\int e^{-y^2}\,dy.\tag{4.24}$$

Solving the integrals from $y = 0$ to $y = \dfrac{x}{\sqrt{4D_{CD}t}}$ on the two sides of equation (4.24),

$$\int_{c_0}^{c_x} dc = \frac{-2c_0}{\sqrt{\pi}}\int_{0}^{y=\frac{x}{\sqrt{4D_{CD}t}}} e^{-\xi^2}\,d\xi,$$

$$c_x - c_0 = (-c_0)\,\mathrm{erf}(y).\tag{4.25}$$

The error function $\text{erf}(y)$ can be expanded using Taylor series as

$$\text{erf}(y) = \frac{2}{\sqrt{\pi}}\sum_{n=0}^{\infty}\frac{(-1)^n(y)^{2n+1}}{n!(2n+1)} = \frac{2}{\sqrt{\pi}}\left(y - \frac{y^3}{3} + \frac{y^5}{10} - \frac{y^7}{42} + \cdots\right). \qquad (4.26)$$

The first term on the right side of equation (4.26) is applied to approximate the error function, and hence,

$$\text{erf}(y) \sim \frac{2}{\sqrt{\pi}}y = \frac{2}{\sqrt{\pi}}\frac{x}{\sqrt{4D_{CD}t}} = \frac{x}{\sqrt{\pi D_{CD}t}}. \qquad (4.27)$$

Substitute (4.27) into (4.25) yields

$$c_x = c_0\left(1 - \frac{x}{\sqrt{\pi D_{CD}t}}\right). \qquad (4.28)$$

C_x is the concentration of the dissolved CO_2 molecules at a diffusion distance x from the interface (Figure 4.5) and let $c_x \approx 0$ be a critical concentration, then we have

$$|x| \approx \sqrt{\pi D_{CD}t}, \qquad (4.29)$$

where t is the diffusion time. It is obvious that the absolute value of the diffusion distance x mainly depends on the diffusion time t since diffusion coefficient is a constant which is on the order of 10^{-9}. However, t is uneasy to be exactly quantified because the hydrostatic state of one specific point on the clear section only lasts for limited time (t) out of one period t_0. Diffusion time t can be written as

$$t = at_0 \quad \text{for} \quad 0 < a < 1, \qquad (4.30)$$

where a is a fractional number. 'a' varies among different cases with different Q_{H2O}/Q_{LCO2}; even under the same case, it also varies among various locations at the clear section. Generally, 'a' is larger at a location closer to the front corner of the T-junction than the one at a further downstream location. Consequently, equation (4.29) may be rewritten as

$$|x| \approx \sqrt{\pi D_{CD}at_0} \quad \text{for} \quad 0 < a < 1. \qquad (4.31)$$

Case 1, for example, has a period of $t_0 = 7.8$ ms, and the maximum value of 'a' is approximated as $(7.8-1.6)/7.8=0.795$. Thus the maximum diffusion distance on the clear section under case 1 is about 5.4 µm based on equation (4.31). It means that diffusion effect maximally covers a distance range from 0 to 5.4 µm from the clear section of the interface under case 1. This estimation results from the critical concentration $c_x \approx 0$; if $c_x = c_0/2$ is applied, the corresponding distance range will be 0 to 2.7 µm. Regardless of the applied critical concentration, the diffusion distance x compared with the channel width W is a small value ($\leq 3.6\%$).

4.4.2.2 Relative importance of the 'transverse advection' over molecular diffusion

Although the diffusion is more like a transverse process relative to the flow direction, it has a 'transverse' effect, however, from the advection of the continuous fluid-water when focusing on the mass transport of the dissolve CO_2 molecules in sequence. It always occurs in the sequence from dissolution to diffusion and advection. Peclet number, defined as $Pe = \dot{\gamma}/(D_{CD}/D \cdot X)$, is a dimensionless number that compares the transport rate caused by advection to that caused by diffusion, where $\dot{\gamma}$ is the shear rate on the interface, D is the channel depth and X is a characteristic distance on the dimension of the diffusion. Within the T-junction in our study, the shear rate $\dot{\gamma}$ is estimated as $\dot{\gamma} \sim <v>/D \sim Q_{H2O}/(D \times W)/D$ [90], where D is 100 µm in our study; X is designated as half of the channel width W, i.e., $X \sim W/2 = 75$ µm. Therefore, Pe can be expressed as follows.

$$Pe \sim Q_{H_2O}/(2D \times D_{CD}). \tag{4.32}$$

Substituting the values of D and D_{CD} in equation (4.28), Pe can be calculated by

$$Pe \sim \frac{1}{3} \times 10^{13} Q_{H_2O}. \tag{4.33}$$

Note that the volumetric flow rates Q_{H2O} shown in (4.33) are in m^3/s rather than in µL/min (Table 4-2). Pe then can be approximated by $(10^4 \times Q_{H2O}/180)$. Based on the investigated flow rates (Table 4-2), Pe ranges from $O(10^2)$ to $O(10^4)$, which indicates the dominance of advection over diffusion in the transport of CO_2 molecule into water. Nevertheless, it is noted that this relative importance between advection and diffusion depends on the local shear rates near the interface.

4.5 Experimental Results and Modeling

Our study has investigated the flow regimes (Figure 4.3) resulted from various flow rate ratios (Q_{H2O}/Q_{LCO2}) as well as Ca numbers of the continuous phase-water. Within the ranges of these two dimensionless parameters, drop flows (including the dripping regime in case 27 and 28) and co-flows are the two main flow regimes. Regarding the drop flows, the length (L) and speed (V) of the generated liquid CO_2 drops, and the spacing (S) between an emerging drop and the adjacent generated one during one period are measured, respectively.

4.5.1 Drop Length as a Function of Q_{H2O}/Q_{LCO2}

Shown by Figure 4.2, the length of the generated liquid CO_2 drop is measured from the front end to the back end of the drop. For each drop flow case in Table 4-2, the length measurement is performed

over multiple drops and the mean value $\bar{L}$ calculated from the sample lengths (L_i, i=1, 2, 3,···, N) is considered as the drop length for this case, i.e.,

$$\bar{L} = \frac{1}{N}\sum_{i=1}^{N} L_i,$$
(4.34)

or $\quad \frac{\bar{L}}{W} = \frac{1}{N}\sum_{i=1}^{N}\left(\frac{L_i}{W}\right).$
(4.35)

In addition, the standard deviation, s, is determined using Bessel's correction, which is written as

$$s = \sqrt{\frac{1}{N-1}\sum_{i=1}^{N}\frac{(L_i-\bar{L})^2}{W^2}}.$$
(4.36)

Based on the above equations, normalized liquid CO_2 drop length (L/W) is plotted against the Q_{H2O}/Q_{LCO2}, as shown in Figure 4.6. An error bar representing the standard deviation is also added. When the total flow rate of liquid CO_2 and water is 100μL/min (Figure 4.6 (A)), the length of the liquid CO_2 drop decreases rapidly as Q_{H2O}/QL_{CO2} rises from around 0.2 to 1; however, this decrease tends to reach a plateau as Q_{H2O}/QL_{CO2} further increases from 1 up to 9. When the flow rate of liquid CO_2 is maintained as 50 μL/min (Figure 4.6(B)), the variation of the drop length subjected to Q_{H2O}/QL_{CO2} is analogous to that in Figure 4.6(A). Overall, the normalized liquid CO_2 drop length L/W versus the flow rate ratio Q_{H2O}/QL_{CO2} can be approximated by a power function

$$\frac{L}{W} \sim 1 + A(Q_{H2O}/Q_{LCO2})^B,$$
(4.37)

where the exponent B is negative ($B < 0$). Specifically, the fitted curves in Figure 4.6 (A) and Figure 4.6 (B) are formulated as L/W=1+2.83$(Q_{H2O}/Q_{LCO2})^{-0.768}$ and L/W=1+2.86$(Q_{H2O}/Q_{LCO2})^{-1.274}$, respectively. These results are different from the long-held claim that the drop (or droplet) size is approximately linear with the flow rate ratio of the dispersed to the continuous phase (Q_{H2O}/Q_{LCO2}) at T-junctions under the squeezing (and/or transition) regime, where the factor A is estimated as $d_{neck}/v_{squeeze}$, i.e., the time of the drop's neck being squeezed off [122]. It is noteworthy that, although an inverse flow rate ratio (Q_c/Q_d instead of Q_d/Q_c) is applied in our study, it does not alter the intention of correlating drop sizes to comparative flow rates. Although the exponent B here does not agree with the prediction by Garstecki et al., it is still within the vicinity of (-1). However, the determination of A in our study requires taking account of not only the "squeezing" (i.e., truncating) time but also the "elongating" time (Figure 4.3) when the liquid CO_2 keeps entering and thus increases the length of the emerging drop, which is attributed to the elongating-squeezing regime distinguished from the general "squeezing" regime. The final length L is generally determined by how much CO_2 has entered in terms of length during the aforementioned three stages (Figure 4.3),

91
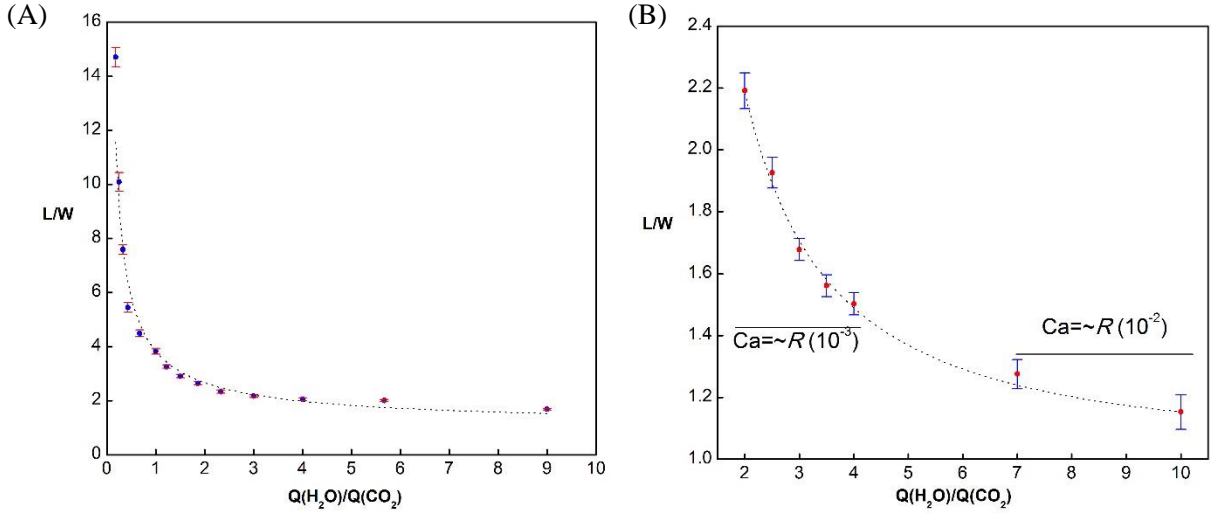
Figure 4.6 Liquid CO_2 drop size as a function of flow rate ratio (Q_{H2O}/QL_{CO2}): the drop length (L) is normalized by the width ($W = 150$ µm) of the microchannel. (A) $Q_{H2O} + Q_{LCO2} = 100$ µL/min); (B) $Q_{LCO2} = 50$ µL/min, Ca_c steps towards $O(10^{-2})$ from $O(10^{-3})$ when Q_{H2O}/QL_{CO2} reaches to 7. Error bar: the standard deviation (s) of the mean normalized drop length ($\bar{L}/W$).

i.e., $L \sim (\Delta L_{sf} + \Delta L_{es} + \Delta L_{tr})$, where ΔL_{sf}, ΔL_{es} and ΔL_{tr} are the length increases during the filling, elongating and squeezing, and truncating of the emerging drop, respectively. It is adopted here that the length increase ΔL_{sf} (Figure 4.7(A)) as a result of CO_2 filling (i.e., the length of the tip of the emerging drop) at the end of the first stage is on the order of channel width W [122]. Therefore,

$$\Delta L_{sf} \sim W. \tag{4.38}$$

In order to determine ΔL_{es}, the time duration t_{es} of the elongating and squeezing stage needs to be estimated, which can be achieved by dividing the advancing distance of the continuous fluid (water) by its mean flow speed $Q_{H2O}/(D \times W)$. It is observed that at the end of the elongating & squeezing stage (Figure 4.7(B), right frame), for most of the investigated drop flow cases, the conjuncture between the clear section and inclined shading section at the interface is located nearby the centerline of the main channel; in addition, the two sectional interfacial lines approximate to straight lines and the shading section line intersects the sideline of the channel forming an angle θ ($\theta = (12\pm1)°$). The advancing distance Y of water during this second stage can be calculated by

$$Y = \frac{W/2}{\tan\theta}, \tag{4.39}$$

and hence

92

$$t_{es} \sim \frac{Y}{QH_2O/(D \times W)}. \tag{4.40}$$

During the time, t_{es}, liquid CO_2 from the side channel keeps entering the emerging drop at a mean speed of $Q_{LCO2}/(D \times W)$. Based on these two parameters, the drop length increase, ΔL_{es}, can be estimated as

$$\Delta L_{es} \sim \frac{Y}{QH_2O/(D \times W)} \frac{Q_{LCO_2}}{DW} = Y(Q_{H2O}/Q_{LCO2})^{-1} \tag{4.41}$$

(A)   (B)   (C)
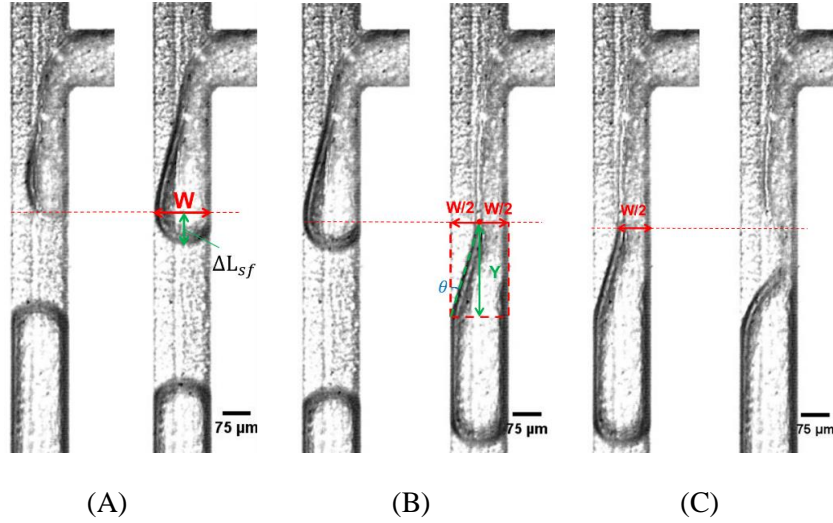
Figure 4.7 Liquid CO_2 drop length increases during the main three stages, namely, the stagnating & filling stage, the elongating & squeezing stage and the truncating stage of one period of drop generation. (A) Drop length increase ΔL_{sf} from the beginning to the end of the filling; (B) the time estimate of the elongating & squeezing stage by observing the advancing distance (Y) of the water front from the filling end to the end of elongating & squeezing, the right frame shows that (I) the conjuncture between the clear and the shading section is located in the vicinity of the midpoint of the channel width and (II) the shading sectional line intersects the channel sideline with a characteristic angle θ (12±1°); (C) the truncating time estimate by considering the pinching off of the rest $W/2$ thick CO_2.

Following the above strategy for ΔL_{es}, the drop length increase, ΔL_{tr}, during the truncating stage can be estimated as follows

$$\Delta L_{tr} \sim \frac{W/2}{QH_2O/(D \times W)} \frac{Q_{LCO_2}}{DW} = \frac{W}{2}(Q_{H_2O}/Q_{LCO_2})^{-1}. \tag{4.42}$$

Combining equations (4.38), (4.41) and (4.42), the length L of the generated liquid CO_2 drop can be approximated as

$$L \sim \Delta L_{sf} + \Delta L_{es} + \Delta L_{tr} = W + Y(Q_{H_2O}/Q_{LCO_2})^{-1} + \frac{W}{2}(Q_{H_2O}/Q_{LCO_2})^{-1}, \qquad (4.43)$$

if the above equation is further divided by W and rearranged,

$$\frac{L}{W} \sim 1 + (\frac{Y}{W} + \frac{1}{2})\,(Q_{H_2O}/Q_{LCO_2})^{-1}. \qquad (4.44)$$

Substitute equation (4.39) to (4.44),

$$\frac{L}{W} \sim 1 + (\frac{1}{2\tan\theta} + \frac{1}{2})\,(Q_{H_2O}/Q_{LCO_2})^{-1}. \qquad (4.45)$$

By comparing equation (4.37) with (4.45), the factor A corresponds to $\frac{1}{2}(\frac{1}{\tan\theta} + 1)$. Given the value of θ (12°±1°), A has a value of (2.85±0.2) from the theoretical estimation, which approximates to the fitted values from the experimental data (Figure 4.6 (A) and (B)).

4.5.2 After-Generation Speeds of the Drop under Various Q_{H2O}/Q_{LCO2}

The measurement of the drop speed, V, after its generation has been briefly discussed in Figure 4.2. More specifically, one liquid CO_2 drop immediately after its generation starts to be identified and its centroid can be located by the Matlab code. Based on the frame rate applied to imaging, the time interval, Δt, between two consecutive frames should be 1/(fps-1). Since very high frames (fps $\sim 10^3$) are used in experiments, the time interval can be approximated as $\Delta t \approx 1/fps$. Moreover, the drop displacement (centroid to centroid), Δd, during this time interval can also be measured depending on the centroid location shift. Therefore, the speed V_i of this specific drop from the ith to the $(i+1)^{th}$ frame can be calculated as

$$V_i = \frac{\Delta d|_{i \to (i+1)}}{1/fps}. \qquad (4.46)$$

Assume the $(N+1)^{th}$ frame is the last one which can present a complete profile of this drop within the field of view of this video, the mean speed can be calculated from the equation below

$$V_j = \frac{1}{N}\sum_{i=1}^{N} V_i = \frac{1}{N}\sum_{i=1}^{N}\frac{\Delta d|_{i \to (i+1)}}{1/fps}, \qquad (4.47)$$

where V_j is deemed as the speed of this drop, j denotes the jth (j=1, 2, 3… M) liquid CO_2 drop whose speed has been measured from the video. Accordingly, the drop speed as a characteristic speed of one drop flow case (Table 4-2) can be determined by

$$\bar{V} = \frac{1}{M}\sum_{j=1}^{M} V_j. \tag{4.48}$$

Analogous to the drop length, the standard deviation of the drop speed for each drop flow case is also provided as follows

$$s' = \sqrt{\frac{1}{M-1}\sum_{j=1}^{M}(V_j - \bar{V})^2}. \tag{4.49}$$
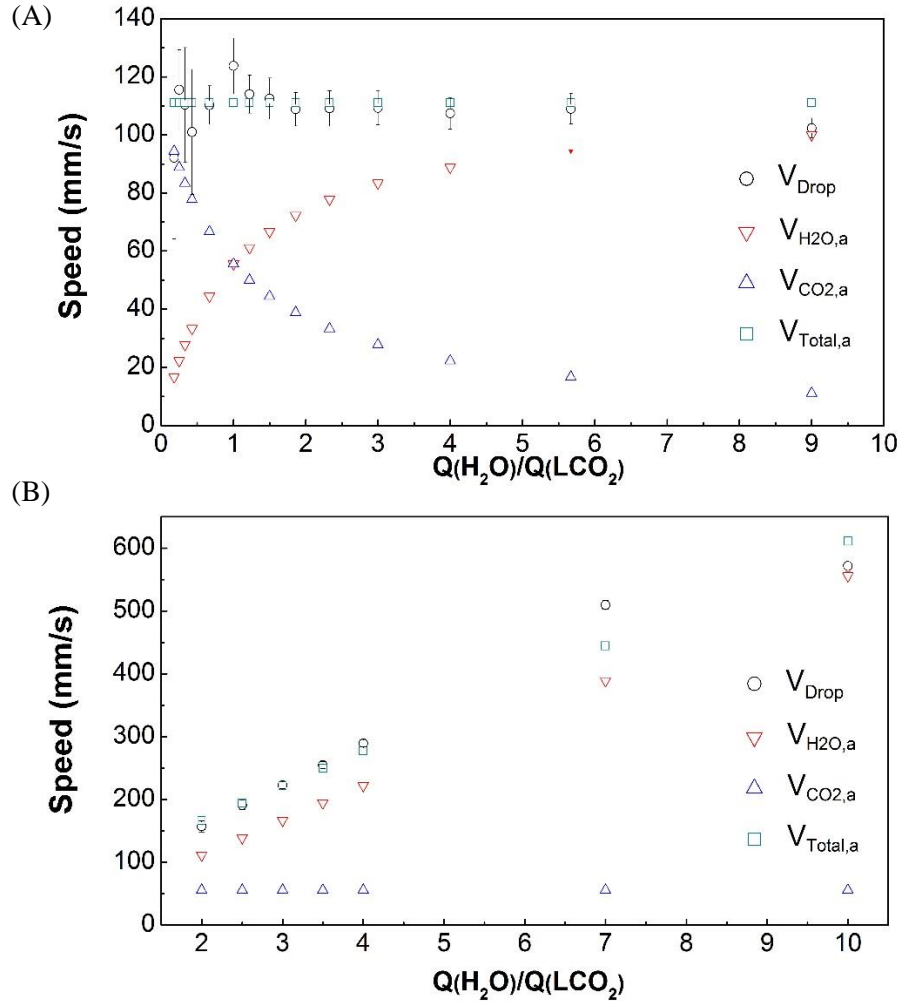
Figure 4.8 Comparison of the speeds of the liquid CO_2 drops (round dots) after generation to the average flow velocities of water (downward triangles) and liquid CO_2 (upward triangles) as well as the averaged total velocity (squares) of the two fluids under drop flow cases for (A) $Q_{H_2O} + Q_{LCO_2} = 100$ µL/min and (B) $Q_{LCO_2} = 50$ µL/min, respectively. Average velocities are defined as $V_{H_2O,a} = Q_{H_2O}/(D{\times}W)$, $V_{CO_2,a} = Q_{CO_2}/(D{\times}W)$ and $V_{Total,a} = (Q_{H_2O}+Q_{LCO_2})/(D{\times}W)$. Error bar: the standard deviation (s') of the drop speed V_{Drop}.

Figure 4.8 plots the after-generation drop speeds for all drop flow cases against their specific values of Q_{H_2O}/Q_{LCO_2} ranging from around 0.2 to 9 for $Q_{H_2O} + Q_{LCO_2} = 100$ µL/min (Figure 4.8(A)) and from 2 to 10 for Q_{LCO_2}=50µL/min (Figure 4.8 (B)), respectively. In addition, three average velocities, i.e., $V_{H_2O,a}$, $V_{CO_2,a}$ and $V_{Total,a}$ that are derived from the flow rates of water and liquid CO_2 are introduced as the reference velocities. For the drop flows under a condition of $Q_{H_2O} + Q_{LCO_2} = 100$ µL/min (Figure 4.8(A)), there exists a waxing and waning relation between $V_{H_2O,a}$ and $V_{CO_2,a}$ as Q_{H_2O}/Q_{LCO2} monotonically increases or decreases in the studied range; however, the hypothetical average velocity $V_{Total,a}$ derived from the total flow rates is a constant (111 mm/s). Comparatively, the speed of the drop after generation is much closer to their corresponding $V_{Total,a}$ under the same Q_{H_2O}/Q_{LCO_2} for almost all drop flow cases; the only two exceptions are under the two extreme conditions of Q_{H_2O}/Q_{LCO_2} (0.18 and 9) when either liquid CO_2 or water has dominated over the other resulting in the final drop speed. Overall, the drop speed values agree well with the averaged total velocity $V_{Total,a}$ especially when $Q_{H_2O}/Q_{LCO_2} > 1$; although there is less conformity when $Q_{H_2O}/Q_{LCO_2} \leq 1$, V_{Drop} are numerically proximal to $V_{Total,a}$ rather than $V_{H2O,a}$ or $V_{CO2,a}$ particularly accounting for their error bars. For the drop flows under the condition $Q_{LCO2} = 50$ µL/min (Figure 4.8(B)), $V_{CO2,a}$ becomes a constant (55.6 mm/s) and the drop speed keeps increasing linearly as a result of the increasing Q_{H2O} from 100 µL/min to 200 µL/min per 25 µL/min. Similar to that when $Q_{H_2O} + Q_{LCO_2} = 100$ µL/min, V_{Drop} agrees very well with $V_{Total,a}$. However, as the flow rate of water strides to 350 µL/min and 500 µL/min (accordingly, Ca_c increases to $O(10^{-2})$ from $O(10^{-3})$.) the dripping regime of drop generation emerges where the emerging drop can never touch the far-end channel wall and the period of generation is extremely short ($t_0 < 2$ ms). By observing the drop generations within case 27, we believe that at the very end of the generation the tip of the emerging drop has a speed ($V'_{CO2,a}$) faster than that inherits from the flow of liquid CO_2 through the entire cross section of the channel, which may be due to the actually narrowed cross section (Figure 4.4(B), case 27) for the same flow rate Q_{LCO2}. Thus, a revised $V'_{Total,a}$ instead of the one in Figure 4.8(B) needs to be used for comparison, which can be formulated as

$$V'_{Total,a} = \frac{Q_{H_2O}}{D \times W} + \frac{Q_{CO_2}}{D \times (bW)},$$

(4.50)

in which the second term on the right-hand side is $V'_{CO2,a}$, i.e.,

$$V'_{CO_2,a} = \frac{Q_{CO_2}}{D \times (bW)},$$

(4.51)

where factor a in denominator is smaller than 1 and bW indicates the actual channel width occupied by the liquid CO_2 in the T-junction region but below its corner. Note that bW ought to be location-dependent along the interface, however, for simplification an estimated median value ($a \sim 1/2$) will be applied. Based on the above assumption, we have

$$V'_{Total,a} - V_{Total,a} = \frac{1-b}{b} \frac{Q_{CO_2}}{D \times W},$$ (4.52)

Substituting b $\sim$ 1/2 into equation (4.52) yields ($V'_{Total,a}$ - $V_{Total,a}$) = Q_{CO_2}/($D \times W$), i.e., $V'_{Total,a} = V_{Total,a} + V_{CO_2,a}$. When $Q_{H_2O}/Q_{LCO_2} = 7$ (Figure 4.8(B)), V_{Drop} is measured as 509.7 mm/s and $V_{Total,a}$ is 444.4 mm/s; if the revised averaged total velocity $V'_{Total,a}$ (500 mm/s) is used to compare with V_{Drop}, it still justifies that V_{Drop} correlates with the averaged total velocity. As Q_{H_2O}/Q_{LCO_2} reaches 10, Q_{H_2O} becomes a dominant role in determining the final drop speed; even without accounting for the difference of the averaged total velocity caused by the liquid CO_2, the estimation of V_{Drop} using $V_{Total,a}$ can still be of a 93% confidence, which is calculated as follows

$$\left(1 - \frac{V_{Total,a} - V_{Drop}}{V_{Drop}}\right)\% = \left(1 - \frac{611.1mm/s - 571.9mm/s}{571.9mm/s}\right)\% \approx 93\%.$$ (4.53)

4.5.3 Periodic Development of Spacing Between Emerging Drop and the Adjacent Formed one

Spacing between two consecutive drops in the flow channel represents how closely the chasing drop follows with the precede one. This spacing actually originates from that between the emerging drop and the adjacent already-formed drop at the very end of one period of drop generation as well as its development during the period. Different from the drop length and the drop speed as characteristic parameters of the formed drop, the spacing between the emerging drop and the formed one correlates drops and is time-dependent within one period. The periodic spacing development can be analyzed based on the drop length increase during the filling stage and the speed of the emerging drop and the formed one as discussed above. The spacing always evolves from an initial value S_0 (Figure 4.9(A)) that stems from the pinch-off and the retractions at the interface for producing the formed liquid CO_2 drop.

During the filling stage prior to the emerging drop blocking the main channel, the formed drop moves downstream at a speed $\sim$ ($V_{H_2O,a} + V_{CO_2,a}$) as discussed in (4.5.2). On the other hand, the emerging drop has a secondary effect besides filling, i.e., flowing downstream. Its effective displacement is exactly the drop length increase ΔL_{sf} ($\sim W$) during the filling time t_{sf}. As a result, the

97
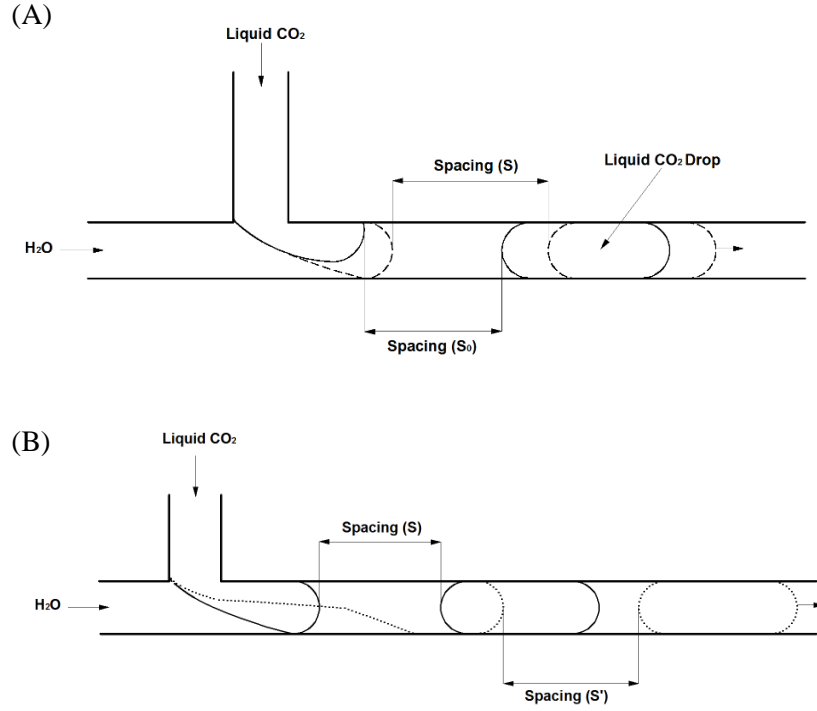
Figure 4.9 Schematics of the development of spacing between an emerging drop and the adjacent formed one within one period of drop generation: (A) spacing increases from S_0 (at the beginning, solid lines) to S (at the end, dash lines) during the filling stage and (B) spacing increases from S (at the beginning, solid lines) to S' (at the end, dot lines) during the elongating & squeezing and the truncating stage.

effective mean speed of the emerging drop within the filling stage can be estimated as

$$V_{sf,eff} = \frac{\Delta L_{sf}}{t_{sf}} \sim \frac{W}{t_{sf}}. \tag{4.54}$$

Based on the speeds of the emerging drop and the already formed one together with the initial spacing S_0, the spacing in the filling stage increases linearly as a function of time, which can be formulated as

$$S(t) = S_0 + \left[\left(V_{CO_2,a} + V_{H_2O,a}\right) - \frac{W}{t_{sf}}\right] \cdot (t - 0), 0 < t \leq t_{sf}, \tag{4.55}$$

or

$$S(t) = S_0 + \left(\frac{Q_{CO_2} + Q_{H_2O}}{DW} - \frac{W}{t_{sf}}\right) \cdot t, 0 < t \leq t_{sf}. \tag{4.56}$$

98

Note that the spacing estimate may only be applicable to the drop flow cases excluding the dripping flows (case 27 and 28) because either the speed of the emerging drop or that of the already formed drop needs to be amended since the emerging drop, during dripping regime, does not reach the far-end channel and $V_{Total,a}$ does not represent the actual averaged total velocity. However, the strategy for estimating spacing can be analogous to the dripping regime where the continuous fluid may dominate the increasing rate of spacing $((S - S_0)/t)$.

As soon as the emerging drop blocks the main channel, it commences the following stages and its mean speed at the front tip is supposed to be consisted of two components: one speed component is contributed by the filling of liquid CO_2 at a rate of Q_{CO_2} (i.e., $V_{CO_2,a}$), and the other by the continuous fluid via the contact upon the interface (more specifically, the shading section). As observed from the drop flows (excluding case 27 and 28), this latter speed component approximates to the moving speed of the inclined shading section of the interface (Figure 4.7(B)), which is reasonable given that the shading section is mainly propelled downstream by water especially under the drop flow cases. It is discovered that during the elongating & squeezing stage the water front in contact with the shading section advances downstream by a distance of Y (Figure 4.7(B)), and Y can be approximated by $W/(2\tan\theta)$. As a consequence, the mean speed of the shading section, V_{sh}, over the time of the elongating & squeezing stage (t_{es}) plus that of the truncating stage (t_{tr}) can be determined as follows

$$V_{sh} \sim \frac{Y}{t_{es}+t_{tr}}. \tag{4.57}$$

Based on $W = 150$ μm and $\theta \approx 12°$, Y is calculated as 353 μm or so. Therefore, the mean speed V_{sh} becomes dependent on the total time (i.e., $t_{es} + t_{tr}$) of the elongating & squeezing and the truncating stage. Moreover, the speed of the front tip of the emerging drop, $V_{CO2,\,tip}$, can be estimated by summing up $V_{CO_2,a}$ and V_{sh}, such that

$$V_{CO_2,tip} = V_{CO_2,a} + V_{sh}. \tag{4.58}$$

or,

$$V_{CO_2,tip} = \frac{Q_{CO_2}}{D \times W} + \frac{Y}{t_{es}+t_{tr}}. \tag{4.59}$$

Thus, the spacing increase $[S'(t) - S(t_{sf})]$ during the elongating & squeezing and the truncating stage at the moment, t, can be calculated by

$$S'(t) - S(t_{sf}) = [\left(\frac{Q_{CO_2}+Q_{H_2O}}{D \times W}\right) - (\frac{Q_{CO_2}}{D \times W} + \frac{Y}{t_{es}+t_{tr}})] \cdot (t - t_{sf}), \ t_{sf} < t \leq t_0, \tag{4.60}$$
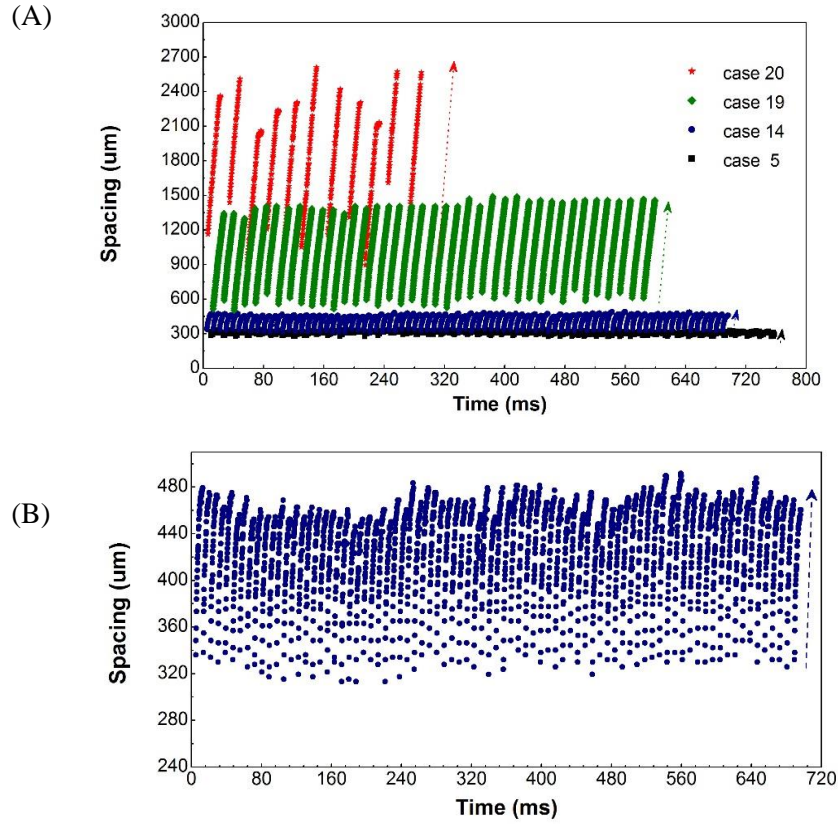
Figure 4.10 (A) The development of spacing between the emerging drop and the adjacent formed one as observed for the drop flow case 5 (■), case 14 (●), case 19 (♦) and case 20 (★), respectively; (B) the detailed spacing development as observed continuously from 86 pairs of those two drops for case 14 ($Q_{H_2O} = 55$ µL/min, $Q_{CO_2} = 45$ µL/min). Each upright dot line (indicated by the arrow) in the same row depicts an elemental spacing development during one period of the (emerging) drop generation.

Substitute equation (4.56) at $t = t_{sf}$ into equation (4.60) and rearrange,

$$S'(t) = S_0 + \left(\frac{Q_{CO_2}+Q_{H_2O}}{D \times W} - \frac{W}{t_{sf}}\right) \cdot t_{sf} + \left(\frac{Q_{H_2O}}{D \times W} - \frac{Y}{t_{es}+t_{tr}}\right)(t - t_{sf}), t_{sf} < t \leq t_0. \qquad (4.61)$$

Combine equations (4.56) with (4.61), the spacing development over time within one period t_0 ($t_0 = t_{sf} + t_{es} + t_{tr}$) of drop generation can be described as follows

$$spacing = \begin{cases} S_0 + \left(\frac{Q_{CO_2}+Q_{H_2O}}{D \times W} - \frac{W}{t_{sf}}\right) \cdot t, 0 < t \leq t_{sf} \\ S_0 + \left(\frac{Q_{CO_2}+Q_{H_2O}}{D \times W} - \frac{W}{t_{sf}}\right) \cdot t_{sf} + \left(\frac{Q_{H_2O}}{D \times W} - \frac{Y}{t_{es}+t_{tr}}\right)(t - t_{sf}), t_{sf} < t \leq t_0. \end{cases} \qquad (4.62)$$

100

The spacing development between emerging drops and their adjacent already formed ones have been investigated through imaging for almost all the drop flow cases except case 21 in our experiments; the exception of case 21 is because that the resulted spacing therein has been so long that it is beyond the maximum observable field of view. Figure 4.10(A) shows the spacing development between emerging drops and their adjacent already formed ones as observed for the drop flow case 5, case 14, case 19 and case 20, respectively; Figure 4.10(B) focuses on case 14 and shows more details on the spacing increases within one period of the drop generation. For case 5 ($Q_{H_2O} = 20$ µL/min, $Q_{CO_2} = 80$ µL/min), t_{sf}, t_{es} and t_{tr} comprising one period of drop generation are around 1.3 ms, 13.6 ms and 2 ms, respectively. As a result, W/t_{sf} becomes equivalent to ($Q_{H_2O} + Q_{LCO_2}$)/($D \times W$) numerically during the stagnating & filling stage, so does $Y/(t_{es}+t_{tr})$ relative to $Q_{H_2O}/(D \times W)$ during the elongating & squeezing and the truncating stage. Therefore, the spacing during the overall period becomes a constant estimated by S_0. This result is verified by experimental measurements (Figure 4.10(A), case 5) as well where the spacing is (307.2±11.2) um. For case 19 ($Q_{H_2O} = 80$ µL/min, $Q_{CO_2} = 20$ µL/min), t_{sf} and ($t_{es}+t_{tr}$) are about 4.4 ms and 9.8 ms, respectively; if substituted into equation (4.62), the time factor in equation (4.62) is calculated as 77 mm/s for $0 < t \leq 4.4$ ms and 52.89 mm/s for 4.4 ms $< t \leq 14.2$ ms. These values are consistent with the experimental results as shown in Figure 4.10(A). However, the experimental data of spacing for case 20 among different periods (or say, different pairs of those two drops) are not so uniform as that for other cases, though the spacing development within one specific period is still linear and may be predicted by equation (4.62). The overall oscillating spacing under case 20 results from the very low flow rate of liquid CO_2, Q_{CO_2} (15µL/min which might not be very reliable as provided by the pump) as well as the resulted high Q_{H_2O}/Q_{CO_2}. Moreover, a 5x instead of 10x objective is applied for imaging the long spacing of case 20, which compromises the resolution of the video and induces more errors to the spacing measurements.

The upright dot lines plotted in Figure 4.10(B) show the details of the spacing increases of 86 consecutive pairs of the emerging drops and their adjacent already formed counterparts over a total time of almost 700 ms, and one period of the (emerging) drop generation is $t_0 = 8.4$ ms ($t_{sf} = 2$ ms and ($t_{es} + t_{tr}$) = 6.4 ms). In order to be compared with that from the theoretical calculations based on equation (4.62), the spacing data of the 86 pairs, as a sample of case 14, are averaged at each moment within the one period, t_0, per 0.2 ms time interval derived from $t_0 = 1/f = 1/5000$ to reflect the characteristic spacing development of this drop flow case. This averaging treatment seems as a horizontal squeezing of the sponge-like data shown in Figure 4.10(B) into one single upright line. The

averaged spacing within one period of drop generation are plotted (as the black dots) in Figure 4.11. The error bar indicates a 95% confidence of the spacing within two standard deviations from the mean value (shown by the dots) based on the normal distribution. The experimental spacing versus time, within one period, t_0, are linearly fitted as

$$\text{spacing}_{\text{ex,fit}}(\mu m) = \begin{cases} 331 + 42.6t, & 0 < t \leq 2 \text{ ms} \\ 397 + 9.78t, & 2 < t \leq 8.4 \text{ ms} \end{cases} . \tag{4.63}$$
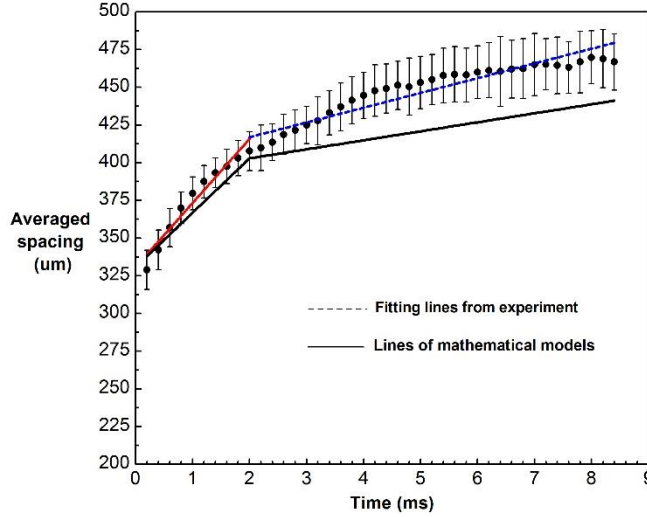
Figure 4.11 Averaged spacing within one period (8.4ms) of drop generation under drop flow case 14. The experimental data herein are averaged from those in figure 12b, and each error bar indicates two standard deviations from the averaged spacing upon the corresponding time moment. Dash lines are the fitting lines from the averaged spacing; and solid lines are the linear functions from the theoretical estimates in equation (4.60).

The total sum of squares (*TSS*) and the residual sum of squares (*RSS*) for the above two fitting functions are 41.25 μm^2 and 2.3 μm^2 within 0 ~ 2 ms and 48.93 μm^2 and 4.95 μm^2 within 2 ~ 8.4 ms, respectively. Instead of *R*-squared, adjusted *R*-squared is introduced as the coefficient of determination below to weigh how well the fittings are relative to the experimental spacing, i.e.,

$$\text{adjusted } R^2 = 1 - \frac{RSS/(n-K-1)}{TSS/(n-1)}, \tag{4.64}$$

where *n* and *K* are the number of points and the number of explanatory variables, respectively. Here, *n* for the two functions are 10 and 33, and *K* is 1 for both functions since there is only one variable time (*t*) in the question. Thus, adjusted R^2 for the two fitting functions can be calculated as 93.72% and 89.56%.

102

On the other hand, according to equation (4.62), the spacing development within one period of the drop flow case 14 can be expressed as equation (4.65),

$$\text{spacing}(\mu m) = \begin{cases} 331 + 36.1t, & 0 < t \le 2\text{ms}; \\ 391 + 5.97t, & 2 < t \le 8.4\text{ms}; \end{cases} \qquad (4.65)$$

which are also plotted in Figure 4.11. Note that the initial spacing, S_0, inherits from the first fitting above when $t = 0$. Qualitatively, the theoretical model (equation (4.62)) is consistent with the experimental fittings, which is a bit better during the first stage (0 ~ 2 ms) of the one period (8.4 ms) but is slightly deviated during the elongating & squeezing and the truncating stage (2 ~ 8.4 ms). Moreover, the slopes in the models are both lower than those in the experimental fitting functions. These differences arise from the estimate of the total flow speed by using the total flow rate as well as a certain overestimate of the speed of the emerging drop.

A quantitative comparison of the spacing between those resulted from the experimental fittings and the theoretical estimates can be conducted as follows

$$\frac{|\text{spacing} - \text{spacing}_{\text{ex,fit}}|}{\text{spacing}_{\text{ex,fit}}} \times 100\% = \begin{cases} \frac{6.45t}{42.6t+331}, & 0 < t \le 2 \text{ ms} \\ \frac{3.81t+6.36}{9.8t+397}, & 2 < t \le 8.4 \text{ ms.} \end{cases} \qquad (4.66)$$

Therefore, the largest relative errors between the experimentally fitted spacing and the model predicted spacing are 3.1% at $t = 2$ ms for the first stage and 8% at $t = 8.4$ ms for the elongating & squeezing stage and the truncating stage, respectively. These errors are acceptable given the uncertainty of the drop speed measurement of case 14 (Figure 4.8(A)) where the mean drop speed is 114 mm/s with a standard deviation of 6.5mm/s.

4.6 Conclusions

This chapter presents an experimental study on a pair of highly pressurized partially immiscible fluids (liquid CO_2 as the dispersed phase and DI water as the continuous phase, respectively) confined in a micro T-junction. Main results are listed as follows:

◆ Over the range of flow conditions (Ca: $O(10^{-4})$ ~ $O(10^{-2})$; Q_c/Q_d: 5/220 ~ 90/10 for a constant total flow rate and 100/50 ~ 500/50 for a constant flow rate of the dispersed phase, respectively), drop flow (Ca: $O(10^{-3})$ ~ $O(10^{-2})$) and co-flow (Ca: $O(10^{-4})$) have been identified.

◆ The drop flow is characterized by an elongating-squeezing regime in which the dispersed liquid CO_2 first fills the main channel and the continuous phase (water) then squeezes the dispersed

103

stream and simultaneously elongates it. As a consequence, the common 'necking' time for the truncation is increased (both squeezing and elongating contribute to this), the truncation point is shifted further downstream from around the corner of the T-junction. This effect explains the role of the factor α in '$L/W=1+\alpha(Q_c/Q_d)^{-1}$'. But in this study, α is much larger than 1. t_{es} corresponds to the elongating-squeezing stage during which the dispersed liquid CO_2 keeps flowing into the emerging drop. The calculated drop length increase ΔL_{es} during this stage justifies the value of α in our study. Although this factor cannot be predicted by the common method ($\alpha \sim d_{necking}/t_{necking}$), it does not challenge the 'flow-rate-controlled' formulation proposed by Garstecki et al. [122]. A transitional capillary number of 1×10^{-2} is also characterized in our study as the dripping regime emerges, which was reported previously by De Menech et al. [125] in numerical simulations. The interface of the emerging drop can never touch the far-end channel wall and the drop generations are characterized by very fast drop generation frequencies ($f \geq 600$ Hz) and smaller drops ($L_{drop} < W$).

- After-generation speed of the drop has been measured. Generally, this transient speed can be approximated to the mean value calculated from the total flow rates of the two fluids divided by the cross section area of the main channel. It is advised that this approximation might be able to be comprehended from the perspective of conservations of momentum and kinetic energy. The produced drop immediately truncated from the dispersed stream is featured by two components of kinetics: one is inherited from the original dispersed fluid flow and the other results from the 'pushing' effect of the continuous fluid under the pressure gradient.

- The development of drop spacing within one period of the drop generation as well as the final spacing values at the end of the one period have been reported. Based on speed difference between the emerging drop and the newly produced complete one, a linear model is developed to predict the spacing as a function of the time during, respectively, the filling stage and the elongating-squeezing stage of the emerging drop. In view of a periodic occurrence of the spacing development, the model agrees well with experimental results.

- Theoretical justifications on the transport mechanisms at the interface between CO_2 and water show that: (1) the CO_2 hydration at the interface is overall negligible, (2) a saturation scenario of the dissolved CO_2 molecules in the vicinity of the interface will not be reached within the contact time between the two fluids, and (3) molecular diffusion does play a role in transporting the dissolved molecules, but the diffusion distance is very limited compared with the channel width.

Chapter 5

Mass Transfer and Hydrodynamic Shrinkage of Liquid CO$_2$ Taylor Drops in a Straight Microchannel

The experimental work in this chapter have been prepared as an article and it will be submitted soon.

Qin, N., Wen J.Z., Ren C.L. "Mass Transfer and Hydrodynamic Shrinkage of Liquid CO$_2$ Taylor Drops in a Straight Microchannel". 2017, prepared.

Abstract:

Hydrodynamics and interfacial mass transfer induced shrinkage of liquid CO$_2$ drops in water under a Taylor flow regime are studied in a straight microchannel (length/width ~100). A general form of a mathematical model of the drop-side mass transfer coefficient (k_d) is provided first. Based on detailed mathematical expressions of surface area (A) and volume (V) of a Taylor drop in a rectangular microchannel, a specific form of k_d is given as a function of the channel geometry (channel width W and channel depth D), concentration difference between the bulk drop and a hypothetical saturated interface, contact angle (θ_c), drop length (L_x) and time (t). In experiments, drop size (i.e., length) and speed at three specified positions of the straight channel, namely, immediately after drop generated from a T-junction (position 1), the midpoint of the channel (position 2), and the end of the channel (position 3) are measured. Drop length reductions from position 1 to 2 and down to 3 quantify the drop shrinkage, which could be related to the drop speed and the flowing time of the drop. Overall drop-side mass transfer coefficients are calculated mainly based on L_x and t. Results show that shorter CO$_2$ drops produced by lower flow rate ratio (Q_{LCO2}/Q_{H2O}) of CO$_2$ and water are usually characterized by higher (nearly three times) k_d than those result from higher Q_{LCO2}/Q_{H2O}, which is mainly attributed to the longer flowing time in the channel, given that the surface-volume ratios (S/V) of all drops are rather unanimous. Based on the reviewed models for predicting the pressure drop of segmented flow in microchannel in Chapter 2 and the Peng-Robinson equation of state (Eos) as well as estimated initial pressures of drops at T-junction from experiments, the overall pressure drops in the long straight channel as well as the resulted drop volume change are quantified. The overall pressure drop from position 1 to 3 is by average 3.175 kPa with a ~1.6% standard error, which, however, results in a relative drop volume change of 0.3‰ to 0.52‰.

5.1 Introduction

Mass transfer can be found broadly in various physical and chemical processes, such as gas absorption [257] (mostly, in liquids), liquid evaporation [258], liquid-liquid extraction [259] and, for many cases, chemical reactions [260,261]. Revealed by two prevalent models of mass transfer, namely, the film model [262] and the penetration model [257] developed on gas-liquid absorptions, molecular diffusions of the (gas) solute across the interface and exposure time of the liquid to the solute at the interface are two key factors for determining the mass transfer performance. This finding indicates that the mass transfer can be controlled by regulating the molecular diffusion and contacting time, which can be achieved from either the apparatus or the fluid side [263]. On the other hand, it elucidates why unique macroscopic apparatus (e.g., bubbling columns and film reactors) and stirring strategies, by either increasing interfacial area or inducing disturbance at the solvent side, have been developed and implemented extensively [351,352]. Nevertheless, mass transfer within those conventional apparatus may still be a bottle-neck for intrinsically rapid kinetics featured reactions [353,354] due to the flow conditions (e.g., superficial velocity, flow regimes) in the apparatus and the surface-volume ratio of the reactants. In addition, particularly for bubbles/drops/films involved macro-scale reactors or contactors, one limitation is the size distribution of those gas or liquid segments may be compromised or difficult to be narrowed given hydrodynamic uncertainties (e.g., eddies) [355-357].

   Microfluidics as well as microTAS (micro total analysis systems) have rapidly progressed over the last twenty years [98,358,359], and have become promising alternatives to above mentioned conventional apparatus. Some merits of microfluidics may include, but are not limited to larger surface-volume ratios, enhanced mass transfer performances, predictable and uniform gas/liquid segments, convenient controls of reaction parameters and increased securities. Besides, kinetics of chemical processes and characterization of the fluid-fluid mass transfer could be revealed and achieved, respectively [360-363]. Analogous to the studies related to conventional apparatus, gas-liquid biphasic systems as well as the interphase mass transfer are also a research focus within the microfluidics sector [364-369]. Liquid-liquid systems, with most interests on interphase mass transfer based extractions, emulsions and reactions have been probed as well in capillary- and microchannel-based reactors [210,223,241,370-372]. As argued in literature [373,374], flow regimes are very likely to influences the mass transfer that mainly occurs at the interface, though the influence might be insignificant [375]. Among all flow regimes, Taylor flow (maybe also referred slug, bubble train,

segmented or intermittent flow) has become a widely studied one [108,173]. Taylor segments are generally characterized with a Bond number (Bo = $\Delta\rho g d^2/\sigma$) smaller than 3.37 and a capsular form whose equivalent diameter is times of the channel (hydrodynamic) diameter. The popularity of Taylor flow in interphase mass transfer studies, as discussed [108,173,376], is due to: (1) the stability and predictability of the flow regimes[108], (2) well-defined drop/slug hydrodynamic characteristics (e.g., morphology, monodispersity, size, speed, thickness of the thin film that encloses the drops and separate the slugs from one another), and (3) the recirculation within both the liquid slugs and drops that could enhance heat and mass transfer [200,243,377]. As reviewed by Kashid et al. [173], gas-liquid and liquid-liquid systems in Taylor flow regime within microscale devices have been massively studied. Among the fluids, carbon dioxide (CO_2) has started to be attempted in the past decade (especially after 2010) with main interests on the microscale fluid dynamics and the chemical processes, as shown by Table 4-1 in Chapter 4. These attempts are usually driven by: (1) the environmental role of CO_2 as one of the major greenhouse gases in climate change, and (2) the physical and chemical properties of CO_2 based on which chemical reactions and material syntheses may be carried out in an efficient as well as a green way.

In this work, highly pressurized liquid CO_2 in a Taylor flow regime is going to be studied in a uniquely fabricated microscale device. De-ionized (DI) water is used as the solvent as well as a continuously flowing liquid. A microscale T-junction is applied to produce the liquid CO_2 Taylor drops. With a long straight microchannel downstream, the hydrodynamics and mass transfer of liquid CO_2 Taylor drops in water are probed. In section 5.2, a general mathematical model of the drop side mass transfer coefficient (k_d) is developed based on drop volume change in a hydrodynamic scenario. Based on a detailed geometrical description of a single drop enclosed by thin films in a rectangular microchannel, a specific form of k_d is derived, which is realized due to meticulous calculations of the surface area and volume of the drop. In section 5.3, based on calculated pressure drop as introduced in the section of 2.5.2 of chapter 2 and estimates of the initial CO_2 pressure in the T-junction, drop volume changes subjected to the pressure drops are analyzed, which is achieved partially thanks to the Peng-Robinson equation of state (Eos) [251]. Section 5.4 introduces the experimental methodologies and procedures and shows an overview of observed liquid CO_2 drops at three specified positions of the channel. In section 5.5, experimental results are shown and discussions are given. Section 5.6 is a summary of this work.

5.2 Mathematical Models of Drop-Side Mass Transfer Coefficient (k_d)

In this section, two mathematical models, namely, a general form and a specific form, of the mass transfer coefficient k_d (m/s) of the drop phase in a continuously flowing fluid situated in a long straight microchannel in Taylor flow regime are developed.

5.2.1 A General Form of k_d in Infinitesimal Time

In order to formulate the mass transfer coefficient k_d of the drop phase, a one-dimensional and unsteady flow problem is considered here. Despite an apparently overall unsteady state, the flow featured with an intermittency could be state when an accompanying reference frame relative to the moving drops is induced that enables an ensemble averaging [378]. Assume a solute drop moves at speed v_1 and is characterized by length L_1, as shown in Figure 5.1, it may exhibit a shrinkage caused size reduction in terms of drop length (as well as the drop volume V) decrease due to the dissolution-diffusion mechanism at the interface. Accordingly, drop length L becomes a function of the position (x) along the straight microchannel. Drop speed together with a certain known distance ($x_{n+1}-x_n$, n is a positive integral) provides the time scale within which an observable size reduction arises. Figure 5.1 shows a schematic of a liquid solute drop characterized by different lengths at different positions. The continuous fluid behaves as a solvent for the drops and presumably maintains a constant flowing speed spanning the overall length of the straight channel. The cross section of the microchannel is rectangular. Its width and depth are denoted by W (see Figure 5.1) and D (not shown but deemed perpendicular into paper in the schematic).

Analogous to heat conductivity in thermal conduction, mass transfer coefficient k_d (m/s) can be defined as follows

$$k_d A \Delta C = \dot{n}_d, \tag{5.1}$$

where A is the effective mass transfer interfacial area, m^2; ΔC is the concentration difference across the interface that drives the mass transfer, mole/L (or mol/L); and $\dot{n}_d$ is the molar flux of the solute into the continuous fluid, mole/s. According to its definition, $\dot{n}_d$ can also be expressed from the viewpoint of mass transfer, such that

$$\dot{n}_d = \frac{dn}{dt} = \frac{1}{M}\frac{dm}{dt} = \frac{1}{M}\frac{d(\rho V)}{dt} = \frac{1}{M}\frac{\rho d(V)+V d(\rho)}{dt}, \tag{5.2}$$

where ρ, V and M are density (kg/m^3), volume (m^3) and molecular weight (kg/kmol) of the solute drop, respectively. Here the solute drop is assumed homogeneous and is characterized as an incompressible flow (i.e., its density is a constant which is independent of time) in the microchannel.

Therefore, d(ρ)/dt equals to 0, and equation (5.2) can be simplified as

$$\dot{n}_d = \frac{1}{M} \frac{\rho d(V)}{dt}.$$

(5.3)
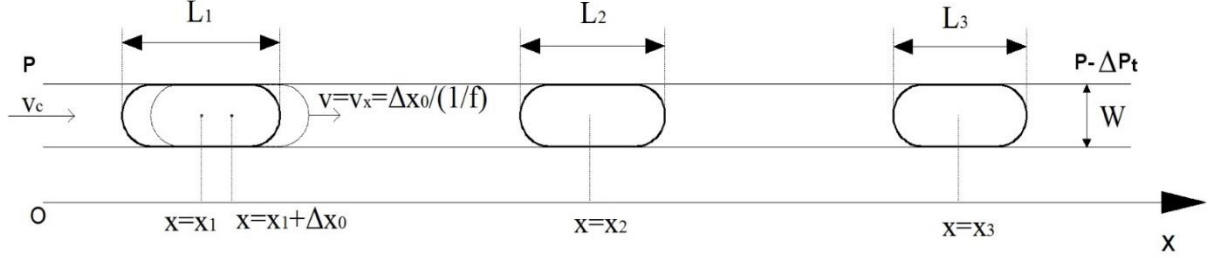
Figure 5.1 Schematic of the dissolution of a liquid drop in the other liquid in Taylor flow regime in a straight microchannel. L_x (x = 1, 2, 3...) and v_x indicate the drop length and drop speed at position x, respectively. v_c is the mean flowing speed of the continuous fluid over the cross-section of the microchannel. v_x can be determined from two consecutive frames in sequence by dividing drop displacement (Δx_0) over the time interval (i.e., 1/f, where f is the frame rate per second (fps)) between these two frames.

Here, a hypothetical 'molar concentration' of the pure solute drop, C_d (mol/L) is introduced. Due to a pure substance composition, the solute drop is not a rational solution and has no physical significance. However, the solute drop is assigned with a nominal 'molar concentration' C_d in order to develop a mathematical model, which is formulated as below

$$C_d = \frac{\rho}{M}.$$

(5.4)

Combine equation (5.3) and (5.4),

$$\dot{n}_d = C_d \frac{d(V)}{dt},$$

(5.5)

by which the mass transfer is correlated with the solute drop shrinkage in terms of volume change over time. Substitute equation (5.5) to (5.1),

$$k_d A = \frac{C_d}{\Delta C} \frac{d(V)}{dt}.$$

(5.6)

One of the main interests in this problem is the solute drop length reduction, or say, the volume reduction due to the diffusion-controlled dissolution in a hydrodynamic circumstance. The sharp interface separating the solute drop phase from the continuously flowing solvent is very likely to be featured with an equilibrium concentration in a saturation scenario, where this equilibrium

concentration is denoted by C_e (mol/L). C_e and C_d form a concentration difference on the solute side that acts as a driving force for the molar flux. Hence, the concentration difference ΔC is formulated as

$$\Delta C = C_d - C_e. \tag{5.7}$$

Substitute equation (5.7) into (5.6),

$$k_d A = \frac{C_d}{C_d - C_e} \frac{d(V)}{dt}. \tag{5.8}$$

Equation (5.8) is a general form of k_d for the drop phase in an infinitesimal time during which the drop maintains a constant surface area.

5.2.2 A Specific Form of k_d Based on Drop Morphology under Taylor Flow (Ca < 10^{-2})

As shown by equation (5.8), only the geometrical parameters, namely, the effective interfacial area A and the drop volume V, of the solute drop are remaining parameters to put forward the mass transfer coefficient. In order to expression A and V using accessible parameters that can be readily measured, a single solute drop in a microchannel under a three dimensional scenario is considered, see Figure 5.2. It shows a solute drop flowing a microchannel that has a width W and a depth D ($D \leq W$). As shown in Figure 5.2b, 5.2c and 5.2d, a thin film (with thickness δ and δ' at the channel wall and the channel corners) of the continuous fluid enclosing the drop exists at between the drop and the channel wall. The thin film prevents the drop from contacting the wall, which is due to the wall wettability preferrence to the continuous fluid. The drop is characterized with an end-to-end length L and two principal radii of curvature (i.e., R_w and R_d) of its meniscues, see Figure 5.2b and 5.2c.

In order to obtain precise areas and volumes of the drop meniscuses so as those of the whole drop, the two radii of curvature R_w and R_d need to be derived by inducing contact angle θ_c between the drop and the wall with a presence of the continuous fluid, see Figure 5.3. Here, R_w is chosen as an example to show how the radii of curvature of the drop meniscus is determined. Focusing on the triangle denoted with a right angle symbol, two geometric formulas can be obtained,

$$R_w \cdot \cos(\pi - \theta_c) = W/2 - \delta, \tag{5.9}$$

$$R_w \cdot \sin(\pi - \theta_c) + L_{c,w} = R_w. \tag{5.10}$$

After rearranging, R_w and $L_{c,w}$ can be obtained as

$$R_w = \frac{W/2 - \delta}{- \cos \theta_c}, \tag{5.11}$$

and

110

$$L_{c,w} = \frac{W/2-\delta}{-\cos\theta_c}(1-\sin\theta_c). \tag{5.12}$$
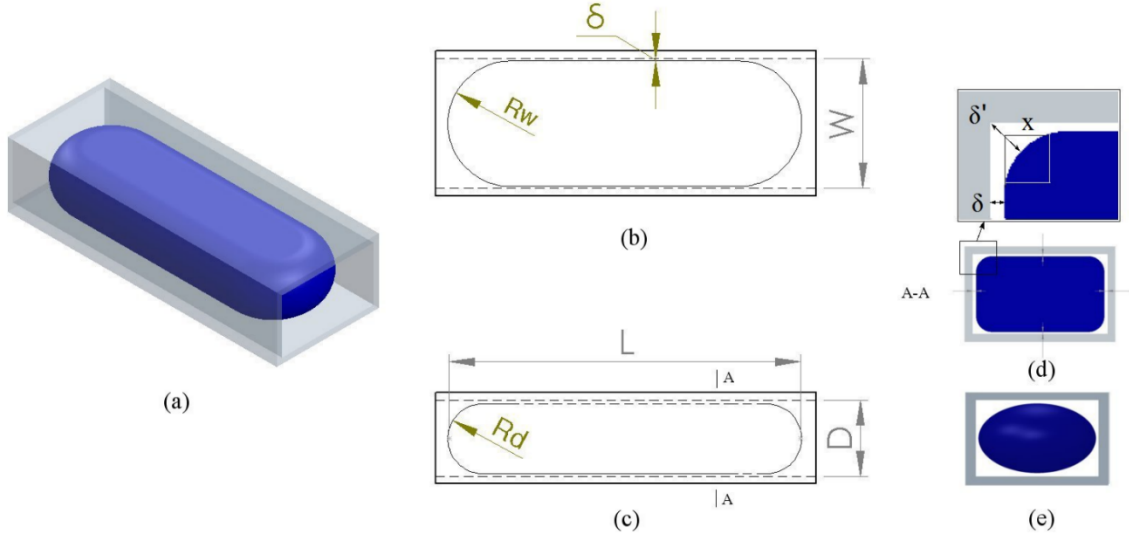
Figure 5.2 Geometrical schematics of one single drop flowing in a rectangular microchannel that has a width W and a depth D. (a) A three dimensional view of the drop confined in the microchannel; (b) a top view of the drop showing the width of the microchannel, the thickness (δ) of the thin film of the continuous fluid, and the radii of curvature (R_w) at a projected plane of the top view; (c) a side view of the drop showing the length (L) of the drop, the depth (D) of the microchannel, and the radii of curvature (R_d) at a projected plane of the side view; (d) a sectional view of the drop where the thin film enclosing the drop is assumed of a uniform thickness (δ) at the channel wall and of a characteristic thickness (δ') at the channel corners; (e) a projected right view of the drop meniscus being approximated a half of a general triaxial ellipsoid.

As a further step, the length of the drop main part, i.e., $L_{m,w}$ can be determined by a deduction of the length of drop meniscus from the total length L, i.e.,

$$L_{m,w} = L - 2L_{c,w} = L - \frac{W-2\delta}{-\cos\theta_c}(1-\sin\theta_c), \tag{5.13}$$

Based on the above parameters, the surface area and the volume of the drop are able to be solved based on a three-component assumption of the drop, i.e., two drop meniscuses and one main central part, see Figure 5.3. Thus, the surface area and the volume of the drop are formulated as

$$A = 2A_{c,w} + A_{m,w}, \tag{5.14}$$

111

and

$$V = 2V_{c,w} + V_{m,w},$$ (5.15)
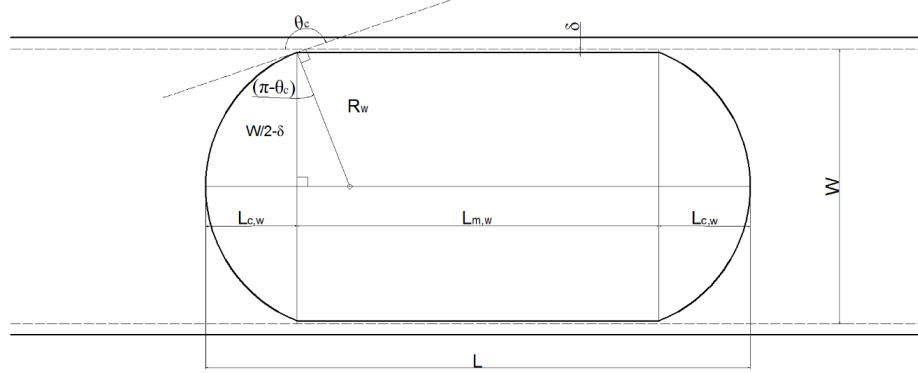
Figure 5.3 Geometrical description of one single drop situated in microchannel. The ellipse shows a symbol of the drop and two horizontal dash lines show the inner channel wall. The drop is considered being composed of two caps at the ends and a main part in the middle.

where $A_{c,w}$ and $V_{c,w}$ are the surface area and volume of the drop meniscus, $A_{m,w}$ and $V_{m,w}$ are the surface area and volume of the central part. The drop meniscus is approximated a half of a general triaxial ellipsoid whose semi-axes are of lengths of $(W/2 - \delta)$, $(D/2 - \delta)$ and $L_{c,w}$, respectively, see Figure 5.2e and Figure 5.3. For $A_{c,w}$, an approximation (Thomsen's formula) proposed by Knud Thomsen [379] is applied for estimation, i.e.,

$$A_{c,w} \approx 2\pi \left\{ \left[\left(\frac{W}{2} - \delta \right)^p \left(\frac{D}{2} - \delta \right)^p + \left(\frac{W}{2} - \delta \right)^p L_{c,w}{}^p + \left(\frac{D}{2} - \delta \right)^p L_{c,w}{}^p \right] / 3 \right\}^{\frac{1}{p}},$$ (5.16)

and the least relative error is within $\pm 1.061\%$ when $p \approx 1.6075$. In addition, the volume of the drop meniscus part $V_{c,w}$ is calculated by,

$$V_{c,w} = \frac{4}{3} \pi \left(\frac{W}{2} - \delta \right) \left(\frac{D}{2} - \delta \right) L_{c,w}.$$ (5.17)

Prior to calculating $A_{m,w}$ and $V_{m,w}$, the perimeter and area of the drop cross-sectional profile of the central portion perpendicular to the flowing direction (see Figure 5.2d) are required to be determined. By referring to the film thickness at the channel wall and at the wall corners, as shown in the detailed drawing in Figure 5.2d, the perimeter and the area of the drop cross section are expressed by $2(\pi x + W + D - 4\delta - 4x)$ and $[WD - 2\delta(W + D) - (4 - \pi)x^2 + 4\delta^2]$, respectively, in which 'x' can be estimated by $x \approx \frac{\delta' - \sqrt{2}\delta}{\sqrt{2} - 1}$. According to reported results of Taylor bubble (or slug) flows in rectangular capillaries

112

with a capillary number (Ca) below 10^{-2} in literature [81,198,199], the thin fim thickness at the channel wall δ and at the channel corners δ' may be approximated by 0.02W and 0.1W, respectively. Thus x can be simplified as 0.17W. The perimeter and the area of the drop cross section are further simplified, respectively, as $2(0.774W + D)$ and $(0.96WD - 0.0632W^2)$. Further, $A_{m,w}$ and $V_{m,w}$ of the main central part of the drop can be written as follows

$$A_{m,w} = 2(0.774W + D) \cdot L_{m,w}, \tag{5.18}$$

and

$$V_{m,w} = (0.96WD - 0.0632W^2) \cdot L_{m,w}, \tag{5.19}$$

Substitute equation (5.13) into the above two equations and rearranging δ by 0.02W,

$$A_{m,w} = 2(0.774W + D) \cdot (L + 0.96\frac{1-sin\theta_c}{cos\theta_c}W), \tag{5.20}$$

and

$$V_{m,w} = (0.96WD - 0.0632W^2) \cdot (L + 0.96\frac{1-sin\theta_c}{cos\theta_c}W), \tag{5.21}$$

Similarly, equation (5.16) and (5.17) are specified as follows

$$A_{c,w} \approx 2\pi \left\{ \frac{(0.24WD - 0.0096W^2)^{1.6075}}{3} + \frac{[(0.48W)^{1.6075} + (0.5D - 0.02W)^{1.6075}] \cdot \left(0.48\frac{1-sin\theta_c}{-cos\theta_c}W\right)^{1.6075}}{3} \right\}^{0.6221}, \tag{5.22}$$

$$V_{c,w} = 0.32\pi W(0.5D - 0.02W) \cdot 0.96\frac{1-sin\theta_c}{-cos\theta_c}W. \tag{5.23}$$

Integrate equations (5.20) ~ (5.23) with (5.14) and (5.15), the surface area A and volume V of a drop are

$$A = 4\pi \left\{ \frac{(0.24WD - 0.0096W^2)^{1.6075}}{3} + \frac{[(0.48W)^{1.6075} + (0.5D - 0.02W)^{1.6075}] \cdot \left(0.48\frac{1-sin\theta_c}{-cos\theta_c}W\right)^{1.6075}}{3} \right\}^{0.6221} +$$

$$(1.548W + 2D) \cdot (L + 0.96\frac{1-sin\theta_c}{cos\theta_c}W), \tag{5.24}$$

and

$$V = (0.96WD - 0.0632W^2) \cdot L + (0.0435WD + 0.0221W^2) \cdot \frac{1-sin\theta_c}{-cos\theta_c}W. \tag{5.25}$$

It is worth noting that a transitional surface section from the drop meniscus to the main central part is not considered here. Instead, it is incorporated to the central part of the drop. Thus, the surface area and the volume determined by equation (5.24) and (5.25) are likely to overestimate slightly. Moreover, the incorporation may only be appropriate when drop length L is relatively larger than the channel width W, thus the transitional area compared with the realistic central part featured by a cross section as shown in Figure 5.2d becomes a small value. The formulation of A and V are generally based on that the volume of the main part is larger than that of the two meniscus parts, i.e., $V_{m,w} > 2V_{c,w}$. Thus, there exists a critical drop length L determined by the channel geometry (W and D) and the contact angle θ_c, below which equation 5.24 and 5.25 may not be applicable.

It can be seen from the expressions of A and V that the surface area and the volume of the flowing drop in a defined geometry (W and D are known) with involved fluids being known (contact angle may be acquired) can be determined as long as drop length L can be measured. Therefore, an overall solute-side mass transfer coefficient k_d, as preliminarily given in equation (5.8), can be specified as follows

$$k_d = \frac{1}{A}\frac{C_d}{C_d - C_e}\frac{d(V)}{dt} = \frac{1}{A}\frac{C_d}{C_d - C_e}(0.96WD - 0.0632W^2)\frac{d(L)}{dt}$$

$$\downarrow$$

$$k_d\frac{C_d - C_e}{C_d}\frac{1}{(0.96WD - 0.0632W^2)}dt = \frac{1}{A}d(L)$$

$$\downarrow$$

$$\int k_d\frac{C_d - C_e}{C_d}\frac{1}{(0.96WD - 0.0632W^2)}dt = \int \frac{1}{A}d(L) = \frac{1}{(1.548W + 2D)}\int \frac{1}{A}d(A)$$

$$\downarrow$$

$$k_d\frac{C_d - C_e}{C_d}\frac{1}{(0.96WD - 0.0632W^2)}t = \frac{1}{(1.548W + 2D)}(\ln A)_{A_x}^{A_0} + B$$

in which B is a constant resulting from the integral. An initial condition that $A_x = A_0$ at $t = 0$ can be applied to determine $B = 0$. Thus,

$$k_d = \frac{(0.96WD - 0.0632W^2)}{(1.548W + 2D)} \cdot \frac{C_d}{C_d - C_e} \cdot$$

$$\ln \frac{4\pi \left\{ \frac{(0.24WD - 0.0096W^2)^{1.6075}}{3} + \frac{[(0.48W)^{1.6075} + (0.5D - 0.02W)^{1.6075}] \cdot \left(0.48\frac{1 - \sin\theta_c}{-\cos\theta_c}W\right)^{1.6075}}{3} \right\}^{0.6221} + (1.548W + 2D) \cdot (L_0 + 0.96\frac{1 - \sin\theta_c}{\cos\theta_c}W)}{4\pi \left\{ \frac{(0.24WD - 0.0096W^2)^{1.6075}}{3} + \frac{[(0.48W)^{1.6075} + (0.5D - 0.02W)^{1.6075}] \cdot \left(0.48\frac{1 - \sin\theta_c}{-\cos\theta_c}W\right)^{1.6075}}{3} \right\}^{0.6221} + (1.548W + 2D) \cdot (L_x + 0.96\frac{1 - \sin\theta_c}{\cos\theta_c}W)} \frac{1}{t},$$

$$(5.26)$$

which is the specific form of k_d based on detailed descriptions of the drop morphology in terms of its surface area and volume in Taylor flow ($Ca < 10^{-2}$) regime. k_d can be determined by the drop lengths at the beginning and the ending point during the time period of interest, given known geometries of the microchannel. Moreover, its applicability is exactly the same as that of the drop surface area and the volume, as shown in equation (5.24) and (5.25), respectively.

5.3 Effect of Pressure Drop in Microchannel on Drop Volume Change

The pressure drop of liquid-liquid and gas-liquid flows in Taylor flow regime in microchannel has been introduced and discussed in section 2.5.2 in Chapter 2. Due to the unique physical properties (e.g., density, viscosity) of liquid CO_2, it is better to use a pressure drop model which may be applicable for both gas-liquid and liquid-liquid Taylor flows to estimate the pressure drop of liquid CO_2 Taylor flow in the straight microchannel. As discussed at the end of the section 2.5.2 in Chapter 2, a modified Warnier's model by Eain et al. [219,221] may be applicable to calculate the pressure drop over the total channel length with a presence of liquid CO_2 Taylor flow. The only difference between the modified Warnier's model and the original one (Warnier's model) lies in a curvature parameter of 8.16 rather than 7.16 (see details in section 2.5.2 in Chapter 2). This modified Warnier's model is shown below

$$\Delta P_t = L_t \frac{32\eta_c \overline{v_c}}{(2R_h)^2} \left[1 + \frac{8.16 \times 3^{\frac{2}{3}}}{32} \frac{1}{L_c^*} \frac{A_c}{A_d} \frac{1}{(Ca_d^{\frac{1}{3}} + 3.34Ca_d)} \right], \quad (5.27)$$

In addition, an appropriate equation of state (Eos) is required as well to obtain a volume change of the liquid CO_2 drops. As introduced previously in section 2.6 in Chapter 2, the Peng-Robinson's equation can be applied to correlate the pressures with the molar volume V_m. According to equations (2.21), two similar equations may be available at the starting point (pressure: P_0) and the ending point

(pressure: P_t) of the straight channel, an equation set including these two equations as well as a pressure drop can be written as follows

$$\begin{cases} P_0 = \dfrac{RT}{V_{m0}-b(T_c)} - \dfrac{c(T_c)\beta(T_r,\omega)}{V_{m0}[V_{m0}+b(T_c)]+b(T_c)[V_{m0}-b(T_c)]}, \\[2mm] P_t = \dfrac{RT}{V_{mt}-b(T_c)} - \dfrac{c(T_c)\beta(T_r,\omega)}{V_{mt}[V_{mt}+b(T_c)]+b(T_c)[V_{mt}-b(T_c)]}, \\[2mm] \text{and } \Delta P_t = (P_0 - \dfrac{\sigma\cos\theta_c}{R_h}) - (P_t - \dfrac{\sigma\cos\theta_c}{R_h}) = P_0 - P_t. \end{cases} \tag{5.28}$$

If P_0 could be measured or estimated from practical situation, given the pressure drop determined by equation (5.27), P_t at the ending point of the microchannel can be predicted and used to solve the two unknowns, i.e., V_{m0} and V_{mt}, where the subscript '0' and 't' indicate the parameters at the starting and the ending point, respectively. Note that the temperature is assumed a constant here, thus the molar volumes are merely related to pressures. Besides, the factors b, c and β are determined by equation set (2.22). Based on the solutions of V_{m0} and V_{mt}, relative volume change $\Delta V_t/V_0$ of the drop due to the pressure decay can be calculated by

$$\Delta V_t/V_0 = N\cdot\Delta V_{mt}/V_0 = N\cdot(V_{mt}-V_{m0})/(N\cdot V_{m0}) = \frac{V_{mt}}{V_{m0}} - 1. \tag{5.29}$$

According to equation (5.27), (5.28) and (5.29), an estimated (or even directly measured) initial pressure and a (quantitative) knowing of Taylor flow in the microchannel are required to obtain the volume change of the drop caused by the specific pressure decrease. However, without experiments and numerical methods, such a clear idea of the drop volume change will not be possible.

5.4 Experimental Methodology

5.4.1 Setup and Measurements

A same experimental system introduced in Chapter 3 is applied here to undertake the hydrodynamic dissolution of pressurized Taylor drops in a straight microchannel. Shown by Figure 5.4, a micro T-junction is used to produce Taylor drops in the microchannel. In particular, liquid carbon dioxide (purity 99.9%, Praxair Canada) is employed as a dispersed fluid which is injected at constant flow rates into the side channel of the T-junction; de-ionized (DI) water is the continuous liquid flowing at varied constant flow rates in the main channel of the T-junction. The side channel, main channel as well as the downstream straight microchannel (total length L_t = 14.7 mm) are all characterized by a uniform width of 150 µm and a uniform width of 100 µm. Although not shown, the further downstream to the end of the straight microchannel features a 90 degree turning and a 55 mm long

116

channel connecting to the outlet of the connector. The back pressure of the flowing system is controlled by a back pressure regulator (model EB1ULF1, Equilibar) together with a needle valve. A nitrogen gas tank provides a reference back pressure at the back pressure regulator. However, the practical back pressure during experiments is measured by a pressure transducer (Swagelok) installed between the connector and the back pressure regulator.
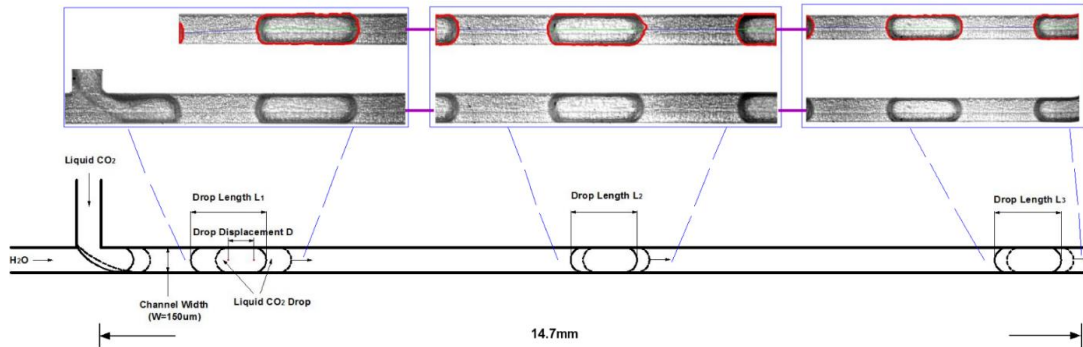
Figure 5.4 Schematic of the experimental methodology for investigating dense CO_2 drops' shrinkage in a straight microchannel ($16 < L_t/L_x < 60$, x = 1, 2, 3; W=150 µm, L_t = 14.7 mm). The drop length L_x is measured at three positions, i.e., immediately after the drop generation (position 1), at the midpoint of the microchannel length (position 2) and at the end of the microchannel (position 3).

The experimental methodology for studying the dissolution caused Taylor drops shrinkage is schematically introduced in Figure 5.4. The dense CO_2 drop at three different positions of the straight microchannel, i.e., immediately after the drop generation (position 1), the midpoint of the microchannel (position 2) and the end of the microchannel (position 3), are visualized by using an upright microscope (BX51, Olympus) combined with a high speed camera (v210, Phantom). Images-stacked videos (3000 frames per second, fps) are recorded separately at the three positions after a waiting time of 20 minutes, each time when a different set of flow rates are applied, in order to reach a stable flow state. Later, these videos are firstly cropped into a standard size of 800×200 pixels (1 pixel ≈ 2 µm), and then analyzed in Matlab (R2014a, Mathworks) by using a series of self-developed Matlab codes based on identifying drops. Drop length (from the end of the back cap to the end of the front one on the flow direction) and drop speed are the two main parameters extracted from the video analyses. Under a given set of flow rates for CO_2 (Q_{CO2}) and water (Q_{H2O}) at one of the positions, the drop length is measured for all emerging drops in the video, and the averaged value is considered a characteristic drop length, as formulated below

$$L_x = \frac{1}{N}\sum_{i=1}^{N} L_i, \qquad x = 1, 2 \text{ or } 3, \tag{5.30}$$

and the standard deviation S_{Lx} is calculated from the following equation

$$s_{L_x} = \sqrt{\frac{1}{N-1}\sum_{i=1}^{N}(L_i - L_x)^2}, \qquad x = 1, 2 \text{ or } 3, \tag{5.31}$$

where N is the total number of complete drops that emerge in the video at position x (x = 1, 2 or 3). Focusing on one single drop of the N drops, if it emerges as a complete one (both the front cap and the back one are visible in the video) from the jth frame to the $(j + M)^{th}$ frame, its averaged speed (v_{sd}) at this position is determined from the following equation

$$v_{sd} = \frac{1}{M}\sum_{h=1}^{M} v_{h\to(h+1)}, \tag{5.32}$$

and $v_{h\to(h+1)}$ is the speed of this single drop calculated from two consecutive frames, i.e., the hth and the $(h+1)^{th}$ frame $(j \leq h < M)$, as formulated below

$$v_{h\to(h+1)} = \frac{\Delta d_{h\to(h+1)}}{1/\text{fps}}, \tag{5.33}$$

in which the Δd is the drop displacement from the hth and the $(h+1)^{th}$ frame. Based on the speed of a single drop v_{sd}, drop speed v_x by averaging on all the drops is considered a characteristic speed, which is calculated in the following,

$$v_x = \frac{1}{N}\sum_{i=1}^{N}(v_{sd})_i,, \qquad x = 1, 2 \text{ or } 3, \tag{5.34}$$

and the standard deviation S_{v_x} is calculated by

$$s_{v_x} = \sqrt{\frac{1}{N-1}\sum_{i=1}^{N}[(v_{sd})_i - v_x]^2}, \qquad x = 1, 2 \text{ or } 3, \tag{5.35}$$

5.4.2 Experimental Procedures

The procedures of preparing for the experiments and during the experiments is overall similar to those have been described in Chapter 4. Circulating water bath of (25±0.4) °C, used for maintaining liquid CO_2, are applied for controlling the temperature of CO_2 in the pump cylinder for 30 minutes to stabilize the temperature as well as the pressure of the CO_2 feedstock. Due to the generally low flow rates (10 ~ 100 µL/min) being worked with in the stainless steel tubing (inner diameter = 500 ~ 711 µm) that connects the pump and the micro system (comprised of the connector and the microchip), flow velocities of either CO_2 or water are below 10 mm/s, thus the residence time could be 3 ~ 5

minutes given a total length of 2 ~ 3 m of the tubing. Therefore, a tube-in-tube strategy for controlling the temperature of the fluids in the tubing is applied.

A pre-set back pressure of 6500 kPa (as shown by the nitrogen tank gas regulator) is loaded at the back pressure regulator for working with liquid CO_2. At the same time, the needle valve at downstream of the back pressure regulator is kept partly open. Then the CO_2 is filled at the tubing by slowly opening a first valve at the pump side, and as long as the pressure reading at the pump is stable, a second valve at the connector side is slowly opened and the CO_2 is further filled in the microchip together with its downstream tubing up to the back pressure regulator. During the filling process, the practical pressure values can be read from a LabVIEW (National Instrument) program on the computer that are measured exactly from the pressure transducer. Once the pressure reading is stabilized at an approximately constant value (note that the entire experimental system should have been inspected in advance and a leakage-free scenario can be achieved), an initial constant flow rate of the CO_2 is applied at the pump side, and the back pressure starts to increase. Until the back pressure increases to a close value to the pre-set one can the back pressure diaphragm be lifted and can the CO_2 be allowed to flow through the back pressure regulator.

On the other hand, the other two valves at the water side are kept closed. The pressure at the water pump is then increased to a same level as that at the CO_2 pump by using a rapid pressurization function of the pump. The two valves are sequentially opened, which is done very slowly too. Due to an insignificant pressure difference, two fluids will not infuse into the other's tubing. Instead, they will be very likely to meet at the micro T-junction. At this moment, a specific constant flow rate of water is applied at its pump. A waiting time of 20 minutes is required to obtain a stable flow regime of the two phase flow in the T-junction, which results in a Taylor flow regime. When the flow gets stable in terms of the generated drop size and the frequency of the drop generation, the videos at position 1, 2 and 3 are recorded, respectively and designated with order numbers that correspond to the flow rate conditions having been applied to those two fluids. When a different flow rate condition is applied, another waiting time of 20 minutes is required prior to the video recordings. During the whole process of the experiments, pump pressures, practical back pressures, and flow rates are measured and recorded.

5.4.3 Experimental Observations

Figure 5.5 shows an overview of all the liquid CO_2 drops under Taylor flows at the above specified three positions of the straight microchannel for nine flow rate conditions. Here, the flow rate ratio of

Q_{LCO2}/Q_{H2O} is tuned from 20/80 to 75/25, the total flow rate is controlled a constant of 100 µL/min. The capillary number (Ca_c) calculated by water ($Ca_c = \eta_c v_c/\gamma$) ranges from 8×10^{-4} to 2.5×10^{-3}. The viscosity η_c (890 µPa s) [337] and the interfacial tension γ (31.7 mN·m^{-1}) [338,339] are referred to 298 K and 65 bar. v_c is the superficial velocity of water from dividing the flow rate of water over the cross sectional area of the channel.
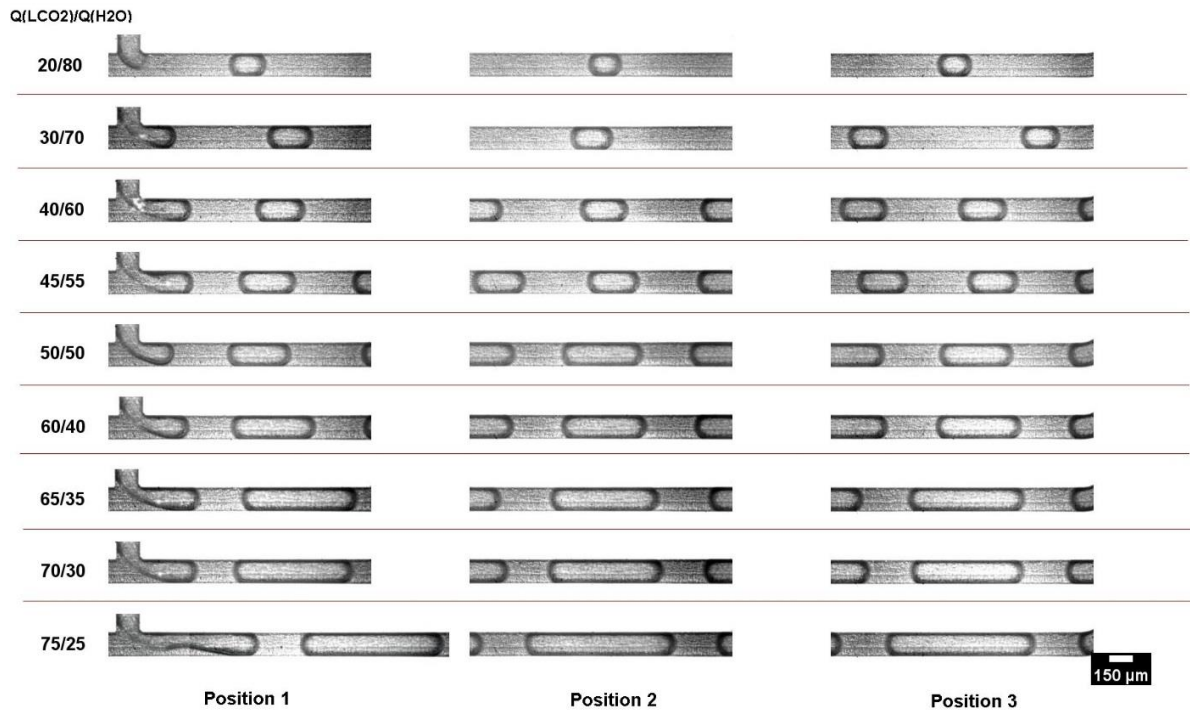
Figure 5.5 An overview of the liquid CO_2 drops at three specified positions under various Q_{LCO2}/Q_{H2O} in the straight microchannel. Scale bar for all images is 150 µm. The image video at position 1 for 75/25 results from combining two images in an end-to-end way showing both the T-junction and a completely generated drop.

At position 1, the CO_2 drop generation is periodic, the length of the generated drops increases as Q_{LCO2}/Q_{H2O} increases from 20/80 to 75/25. At position 2 and 3, CO_2 drops also periodically emerge in the imaging frames and flow in and through. The drop length and the drop speed are measured based on the aforementioned methodologies. It is noted that a complete drop will not be captured by our imaging methods at position 1 when $Q_{LCO2}/Q_{H2O} > 75/25$, and when $Q_{LCO2}/Q_{H2O} < 20/80$, the generation of drops becomes unstable and non-periodic. Therefore, flow rate ratios beyond these two thresholds are not covered in our work.

5.5 Results and Discussions

In this section, the experimental results covering various hydrodynamic aspects and the mass transfer phenomenon of the liquid CO_2 Taylor drop flow in the straight microchannel are reported and discussed.

5.5.1 Sizes of Generated Liquid CO_2 Drops at T-junction

The lengths (L_1) of the generated liquid CO_2 drops at the micro T-junction have been measured and normalized by the width (W) of the microchannel. The normalized drop lengths (L_1/W) have been plotted against to the flow rate ratios Q_{LCO2}/Q_{H2O} of the investigated cases, as shown in Figure 5.6. L_1 increases from around 1.5W to 6.3W as Q_{LCO2}/Q_{H2O} increases from 0.25 to 3. These data points have been fitted by using an analogous method as that applied in Chapter 4, i.e., a linear relation between the normalized drop length and the flow rate ratio (the ratio defined by the flow rate of the dispersed fluid to that of the continuous fluid). The fitting line, L_1/W = 1.15 + 1.79·(Q_{LCO2}/Q_{H2O}), is shown in Figure 5.6, which is characterized by an adjusted R-squared of 0.97. The Y-intercept is approximately 1 of a 15% deviation and the slope is 1.79 that is much larger than 1. The factor underlying the slope is related to the pinch-off time scale within a period of the drop generation, which has been elucidated in Chapter 4. The fitting line, on the other hand, suggests that different sized Taylor drops in terms of non-dimensional drop length are able to be produced by simply tuning the flow rate ratio in operations. However, there should exist an upper limit of Q_{LCO2}/Q_{H2O} beyond which Taylor flow starts to vanish and co-flow regimes occur, as evidenced in Chapter 4.
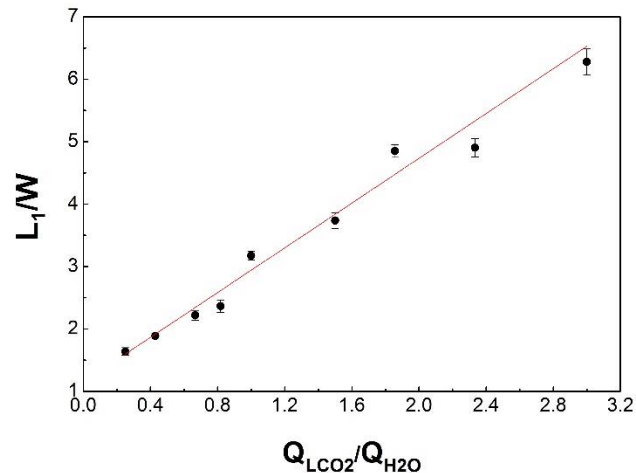
Figure 5.6 Non-dimensional length (L_1/W) of the generated liquid CO_2 drop at the micro T-junction under various Q_{LCO2}/Q_{H2O}.

5.5.2 Length and Length Reductions of Liquid CO_2 Drops

Drop length is not only measured at the micro T-junction but also visualized and measured at the midpoint and the ending point of the long straight microchannel. Figure 5.7 shows the absolute lengths of the liquid CO_2 drops at these three positions under various Q_{LCO2}/Q_{H2O}. The lengths at position 2 and 3 are derived from using equation (5.30) as well. Error bars calculated from equation (5.31) indicate the standard deviation of the mean drop length. As shown by the figure, for each flow rate condition, there is always a slight decline of the drop length from position 1 to 2 and to 3, and the declinations are approximately linear. Here, length reductions characterize the drop shrinkage which is considered caused by the dissolution-diffusion mechanism across the interface between the CO_2 drops and the continuously flowing water.

Detailed drop length reductions are plotted against Q_{LCO2}/Q_{H2O} in Figure 5.8. Three length reductions, namely, a total length reduction ΔL ($\Delta L = L_1 - L_3$), a first length reduction ΔL_1 ($\Delta L_1 = L_1 - L_2$), and a second length reduction ΔL_2 ($\Delta L_2 = L_2 - L_3$) are calculated and shown in the figure. The scattering data points of respective length reductions are linearly fitted by keeping the slopes as zeros. The mean values of drop length reductions ΔL, ΔL_1 and ΔL_2 are 24.35 µm, 16.52 µm and 7.83 µm, respectively. Correspondingly, the standard errors of these mean drop length reductions are 1.08 µm, 1.71 µm and 1.17 µm, respectively, which are calculated from dividing the standard deviations (see equation (5.31)) by the square root of the sample size (9 in our work). These mean drop length reductions may be able to be comprehended in such a way that, regardless of the sizes of the CO_2
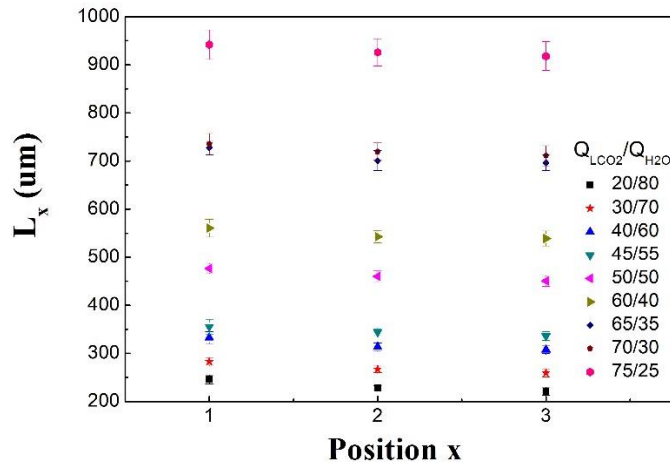
Figure 5.7 Lengths of the liquid CO_2 drops at the three positions under various flow rate ratios Q_{LCO2}/Q_{H2O}. Each error bar indicates one standard deviation of the mean drop length (i.e., the data point).
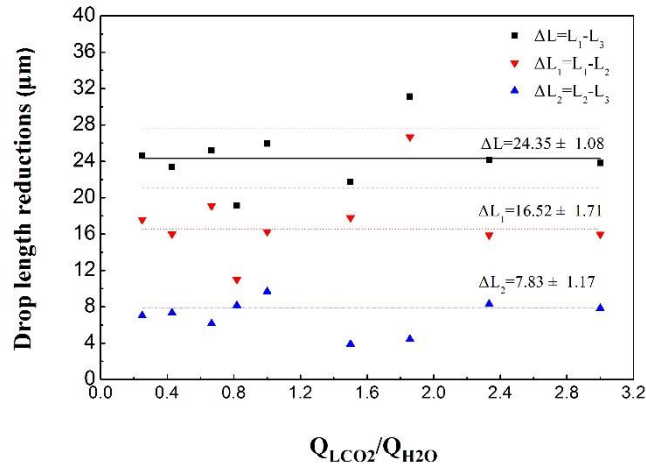
Figure 5.8 Length reductions (ΔL, ΔL_1 and ΔL_2) of liquid CO_2 drops and linear fittings of the three drop length reductions. ΔL (■): a total length reduction $\Delta L = L_1 - L_3$; ΔL_1 (▼): a first length reduction $\Delta L_1 = L_1 - L_2$; and ΔL_2 (▲): a second length reduction $\Delta L_2 = L_2 - L_3$. Solid line is the fitting line of ΔL. A positive and a negative one standard deviation band (dash lines above and below the solid line) of the mean ΔL are added for reference.

drops being produced from the T-junction and investigated later in the microchannel, absolute values of ΔL, ΔL_1 and ΔL_2 resulting from the dissolution-diffusion controlled mass transfer are generally constants, despite the two deviants at $Q_{LCO2}/Q_{H2O} = 45/55$ and $Q_{LCO2}/Q_{H2O} = 65/35$.

The relative total length reductions $\Delta L/L_1$ for all cases are plotted as a function of the flow rate ratios, as shown in Figure 5.9. Although the total drop length reductions (ΔL) may be a constant for all cases (see Figure 5.8), the relative drop length reductions ($\Delta L/L_1$) is likely to be an exponential decreasing function (whose base is < 1 but still > 0) of the increasing flow rate ratios. This result may be rational in view of the surface-volume ratios of the drops that are produced by low flow rate ratios which further enhance the mass transfer through the interface between CO_2 drops and the continuous flowing water. Also plotted in Figure 5.9 are averaged coefficients of variations (COVs) of the drop lengths at those three positions. Here, the COVs of drop lengths at each position is defined by dividing the standard deviation over the mean drop length as follows

$$COV_x = \frac{s_{Lx}}{L_x}, \quad x = 1, 2 \text{ or } 3, \tag{5.36}$$

where s_{Lx} and L_x are calculated from equation (5.31) and (5.30), respectively. The averaged COV as a characteristic of each investigated flow rate condition is obtained from averaging the ones at position 1, 2 and 3, as shown below

123

$$COV_{Q_{LCO2}/Q_{H2O}} = \frac{1}{3}\sum_{x=1}^{3}\frac{S_{L_x}}{L_x}, \qquad x = 1, 2 \text{ or } 3. \qquad (5.37)$$

The averaged COVs behave as a measure of the variability extent of the mean drop length for each flow rate condition. For almost all the flow rate conditions, averaged COVs are approximately a constant value of 0.029 ($\pm$0.003), and vast majority of them are well below the relative drop length reductions except when $Q_{LCO2}/Q_{H2O} = 75/25$. This comparison, in general, shows that the drop length reductions are beyond the error scopes and can be the real characteristics of drop shrinkage.
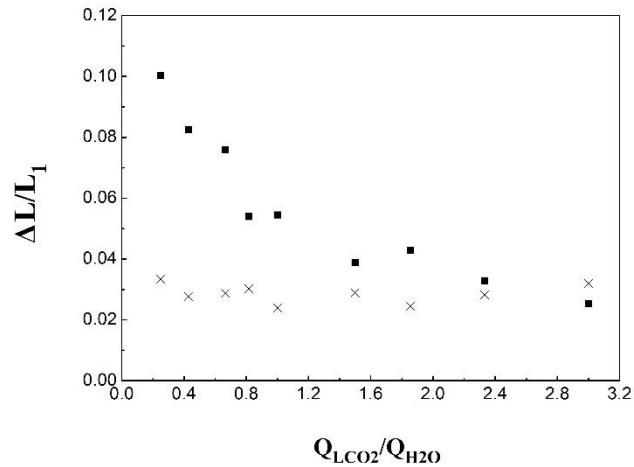
Figure 5.9 Relative total drop length reductions $\Delta L/L_1$ ($\blacksquare$) versus averaged coefficients of variations of drop lengths ($\times$) at various flow rate ratios.

5.5.3 Pressure Drop and Effects on Drop Volume Change

5.5.3.1 Total pressure drop ΔP_t

Given the experimentally obtained drop length and slug length, the pressure drop and the resulted drop volume change can be evaluated. Shown by equation (5.27) and (5.28), the length of the continuous slug needs to be known and an estimate of the initial pressure (P_0) at the micro T-junction is also required in order to gain the pressure drops ΔP_t. Figure 5.5 can not only provide a quick overview of the drops at the specified three positions in the straight microchannel but also provides one that delivers an intuitive scene of the slugs between two consecutive drops. However, the case $Q_{LCO2}/Q_{H2O} = 20/80$ is unable to show a complete slug length due to a size limitation of our field of view (1650 μm $\times$ 380 μm) within which CO_2 drops have been prioritized. Detailed water slug lengths, under all the other flow conditions, have been monitored at each of the three positions and plotted in a similar way as that for drop lengths, as shown in Figure 5.10. Almost all the cases except

124

$Q_{LCO2}/Q_{H2O} = 30/70$ are featured with invariant slug lengths (relative total slug length increases ($L_{s3,w}-L_{s1,w})/L_{s1,w} \leq 0.08$), which may be also true for $Q_{LCO2}/Q_{H2O} = 30/70$ given the error that has been introduced by the syringe pump at lower flow rates.
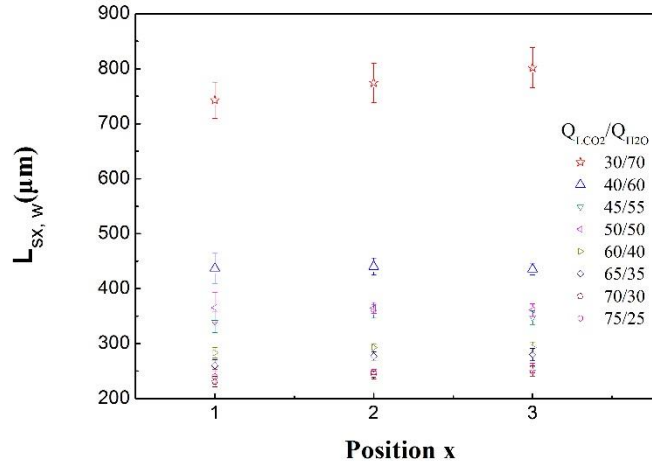
Figure 5.10 Lengths of the water slugs at the three positions under various flow rate ratios Q_{LCO2}/Q_{H2O}. Each error bar indicates one standard deviation of the mean slug length.

According to equation (5.27), total pressure drop is inversely proportional to the non-dimensional slug length L_c^*. The pressure drops are going to be calculated in a further-case scenario using the nominal minimum slug length among position 1, 2 and 3, which may introduce overestimated pressure drops. Apart from L_c^*, the other parameters on the right-hand side of equation (5.27) are listed in Table 5-1, their physical meanings and determinations are briefly introduced in the table captions. Based on the available data in Table 5-1 and equation (5.27), the pressure drops over the practical total length of the straight microchannel are calculated and have been plotted against the flow rate ratio in Figure 5.11(A). Although, as shown by Figure 5.11(A), there exists a slight decrease of ΔP_t subjected to increasing Q_{LCO2}/Q_{H2O} from 30/70 to 75/25, the decreases itself in comparison to the pressure drop are insignificant. The variations of ΔP_t are within 1.6% of a mean value of ~3175.4 Pa. Despite a constant ΔP_t, the decreasing trend of ΔP_t subjected to increasing Q_{LCO2}/Q_{H2O} reflects a dominant role of the water slugs in controlling the pressure drops. Moreover, the contribution of the second term on the right-hand side of equation (5.31) (non-dimensional as well) to the pressure drop comparatively, is almost two orders of magnitude smaller than the water as a continuous fluid.

As the focus shifts from an absolute pressure drops to a gradient of the pressure drops (i.e., $\Delta P_t/L_t^{'}$), as shown by Figure 5.11(B), smaller length fractions of water slugs (L_c^* in Table 5-1) generally result in a slight increase of $\Delta P_t/L_t^{'}$ as Q_{LCO2}/Q_{H2O} increases from 30/70 to 75/25, though the variations are

Table 5-1 The parameters that are applied to calculate the pressure drops over the total channel length by equation (5.27).

Q_{LCO2}/Q_{H2O}	$\eta_c \times 10^6$ (Pa·s)	$\bar{v}_c^1 \times 10^3$ (m/s)	$Ca_d^2 \times 10^3$	$R_h^3 \times 10^6$ (m)	L_c* (1)	$A_d^4 \times 10^{12}$ (m²)	$A_c^5 \times 10^{12}$ (m²)	L_t^6 (mm)	$L_t^{'7}$ (mm)	P_0^8 (10^5 Pa)
30/70	930.32	111.11	2.88	60	6.19	12978	15000	15	13.894	65.21
40/60	930.32	111.11	2.95	60	3.63	12978	15000	15	13.690	65.23
45/55	930.31	111.11	3.08	60	2.82	12978	15000	15	13.751	65.50
50/50	930.28	111.11	3.23	60	3.01	12978	15000	15	13.700	66.81
60/40	930.28	111.11	3.11	60	2.36	12978	15000	15	13.583	66.94
65/35	930.27	111.11	3.25	60	2.17	12978	15000	15	13.335	67.07
70/30	930.27	111.11	3.12	60	1.92	12978	15000	15	13.477	67.12
75/25	930.27	111.11	3.16	60	2.00	12978	15000	15	13.306	67.10

[1] $\bar{v}_c$ is a superficial velocity of the water slug at downstream of micro T-junction, calculated by dividing $(Q_{LCO2} + Q_{H2O})$ over the cross section of the microchannel.

[2] The capillary number calculated by the CO_2 drops.

[3] R_h is the hydrodynamic radius the microchannel, $R_h = (1/2)D_h = (1/2)\cdot 4(WD)/2(W+D) = (WD)/(W+D)$.

[4] The cross section area (A_d) of CO_2 drops is calculated by $A_d = (0.96WD-0.0632W^2)$, see section A.2.

[5] The cross section area (A_c) of water slugs is calculated by $A_c = WD$.

[6] L_t is a nominal total length of the straight channel and $L_t = 15mm$.

[7] $L_t^{'}$ is a real total length of the channel from experiments, the starting point is the back cap of the first generated drop (in a complete plus shape) at position 1 and the ending point is the front cap of the drop that closely approaches to the end of the channel at position 3.

[8] The initial pressure P_0 at the micro T-junction is estimated by the CO_2 pressure that read from the syringe pump.

126
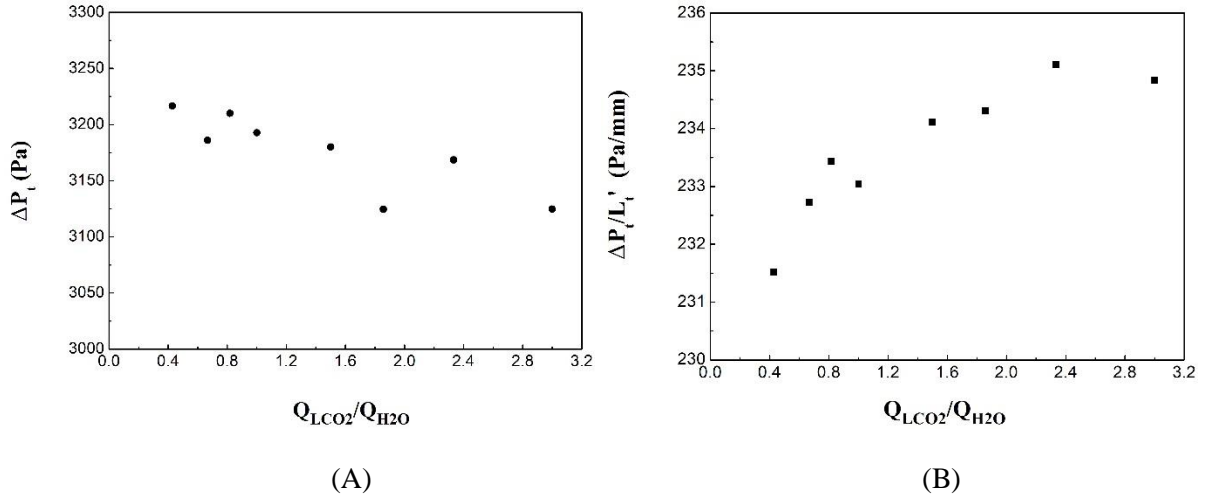
Figure 5.11 (A) Total pressure drop ΔP_t (Pa) over the practical straight microchannel length and (B) pressure drop gradient $\Delta P_t/L_t'$ (Pa/mm, or kPa/m), respectively, subjected to Q_{LCO2}/Q_{H2O}.

still subtle. This variation tendency reveals that larger occupations of the CO_2 drops may lower down the overall pressure drop on the one hand, but on the other hand, they may lead to a more rapid decline of the pressure drop.

5.5.3.2 Drop volume change subjected to ΔP_t

Since carbon dioxide (critical temperature $T_c = 304.15$ K and critical pressure $P_c = 73.8$ MPa) is applied as the drop fluid in this study and the experimental temperature is a room temperature (T = 298.15 K, thus $T_r = T/T_c = 0.98$), equation (2.21) combined with equation (2.22) can be specified as

$$P = \frac{RT}{V_m - 2.6659 \times 10^{-5}} - \frac{4.0183 \times 10^{-1}}{V_m{}^2 + 5.3318 \times 10^{-5} V_m - 7.107 \times 10^{-10}}, \quad (5.38)$$

for which the gas constant R = 8.31446 J/(mol·K) and an acentric factor $\omega = 0.228$ [251,380] of CO_2 are applied during the specification. In addition, the equation set in equation (5.28) can be rewritten as

$$\begin{cases} P_0 = \frac{RT}{V_{m0} - 2.6659 \times 10^{-5}} - \frac{4.0183 \times 10^{-1}}{V_{m0}{}^2 + 5.3318 \times 10^{-5} V_{m0} - 7.107 \times 10^{-10}}, \\ P_t = \frac{RT}{V_{mt} - 2.6659 \times 10^{-5}} - \frac{4.0183 \times 10^{-1}}{V_{mt}{}^2 + 5.3318 \times 10^{-5} V_{mt} - 7.107 \times 10^{-10}}, \\ \qquad\qquad \text{and } \Delta P_t = P_0 - P_t. \end{cases} \quad (5.39)$$

Note that V_m, V_{m0} and V_{mt} in the above equations have a unit of m³/mol. As argued at the end of section 5.3, an estimated initial pressure (P_0) in addition to the specific pressure decreases is required to evaluate the impact of ΔP_t on drop volume change. It is noted in Table 5-1 this initial pressure P_0 at

127

the micro T-junction may be estimated by the CO_2 pressure that read from the syringe pump, provided that CO_2 under the conditions of this study is characterized with much lower viscosities ((58.759 ± 0.114) µPa·s) compared with water and a much lower flow resistance from the pump to the micro T-junction. The estimated initial pressures at the T-junction for all studied flow conditions are listed in Table 5-1. By solving the two cubic equations in equation set (5.39) based on the known P_0 and P_t, molar volumes V_{m0} and V_{mt} of CO_2 at position 1 and 3 can be determined, during which only real and rational (specifically, verified by the calculated densities by dividing molar masses over molar volumes) solutions are employed. Figure 5.12(A) shows the calculated V_{m0} and V_{mt} with a unit 'ml/mol' (10^{-6} m^3/mol). As Q_{LCO2}/Q_{H2O} increases, the initial pressures P_0 has been slightly increasing from 65.2×10^5 Pa to 67.1×10^5 Pa. As a consequence, molar volume V_{m0} shows an overall decline, although small, from 69.4 ml/mol to 67.6 ml/mol. An almost same tendency arises for V_{mt}. Due to ΔP_t (presented in Figure 5.11(A)), P_t always has a very slightly smaller (~3.175 kPa) value than P_0. The difference between P_t and P_0 leads to a very small increase of 0.03 ml/mol from V_{m0} to V_{mt}. According to equation (5.29), relative drop volumes changes ($\Delta V/V_0$) subjected to the pressure drops can be determined via $\Delta V/V_0 \sim [(V_{mt}/V_{m0})-1]$. The results of $\Delta V/V_0$ (scaled by 1000) have been plotted in Figure 5.12(B). It shows that the relative drop volume changes as a result of the pressure drop is extremely small (approximately 0.39‰ to 0.52‰).

(A) (B)
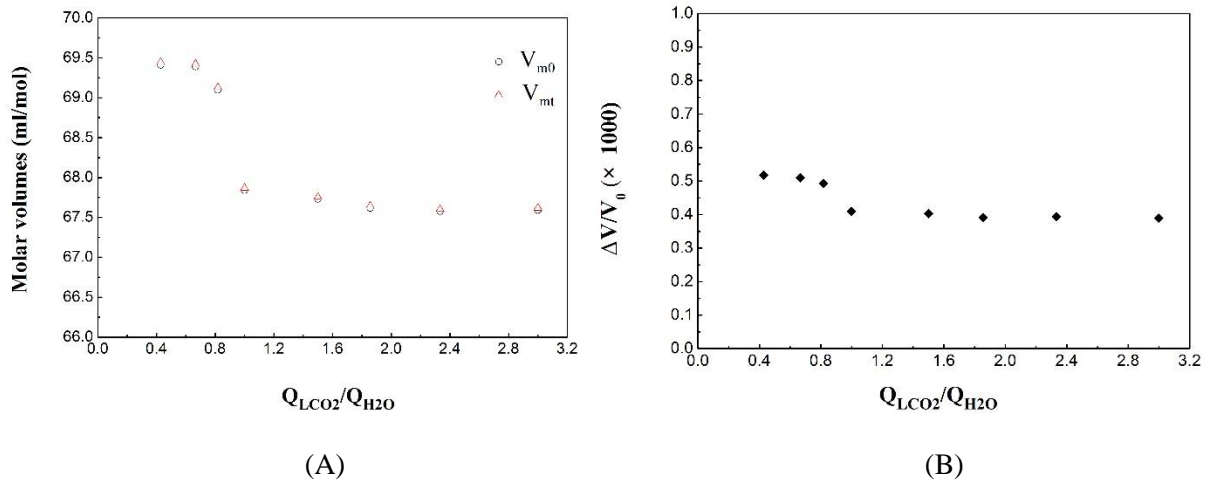
Figure 5.12 (A) Molar volumes V_{m0} (ml/mol) and V_{mt} (ml/mol) calculated from equation (5.39) based on initial pressures P_0 (see Table 5-1) and the pressure drops ΔP_t (Figure 5.11(A)). (B) Relative drop volume changes $\Delta V/V_0$ ($\times1000$) calculated from equation (5.29).

Taking advantage of $\Delta V/V_0$, relative drop length increases $\Delta L'/L_0$ as a result of volume expansions might be equivalent to $\Delta V/V_0$ based on an assumption that the drops, despite of volume changes, still

128

maintains a constant cross-sectional area. It should be noted that $\Delta L'$ and L_0 herein are not pertinent to the real drops, but instead, are equivalent ones to ΔL and L_1 (see Figure 5.9) accounting for a cylindrical body of the drop. Therefore, $\Delta L'/L_0$ may have the same magnitude as $\Delta V/V_0$ does, which then can be compared with $\Delta L/L_1$ in Figure 5.9. Clearly, relative drop length reductions ($\Delta L/L_1$) dedicated to the dissolution-diffusion of CO_2 in water are almost two orders of magnitude larger than the pressure drop resulted relative drop length expansions. It is thus concluded that the pressure drop due to the flow resistance of water and the existence of CO_2 Taylor drops in the straight channel does not lead to a significant drop size change, especially when this size change is compared with the shrinkage caused by the interfacial dissolution-diffusion of CO_2 in water.

5.5.4 Surface-Volume Ratios of Drops

Surface-volume ratio is one of the key parameters that controls the mass transfers (particularly the rates) between different substances, especially when it comes to those at the interfaces among fluids or even solids. In view of the shrinkages of CO_2 Taylor drops in this study, surface-volume ratios (S/V) of the drops in the microchannel undoubtedly play a key role. According to the formulations shown in equation (5.24) and (5.25), respectively, the drop surface area (A) and the drop volume (V) can be further specified, given that the channel sizes (width $W = 150$ µm and depth $D = 100$ µm) are known and a static contact angle θ_c ($\theta_c = 150°$, see Figure 5.5) may be applicable, as follows

$$A\ (\mu m^2) = 432.2 \cdot L - 522.2, \tag{5.40}$$

and

$$V\ (\mu m^3) = 12978 \cdot L + 99571. \tag{5.41}$$

in which L(µm) is the drop length, and $L = L_x$ (x = 1, 2 and 3) in experiments. Therefore, the surface-volume ratio (S/V, 1/mm) of the drops at position 1, 2 and 3 can be determined by the following formula

$$S/V\ (1/mm) = \frac{A}{V} \times 10^3 = \frac{432.2 \cdot L - 522.2}{12978 \cdot L + 99571} \times 10^3. \tag{5.42}$$

Substitute the drop lengths L (shown in Figure 5.7) into equation (5.42), the surface-volume ratio (S/V) at position 1, 2 and 3 for all the investigated flow rate ratios can be calculated. The calculated S/V are shown in Figure 5.13. For smaller CO_2 drops resulted from lower Q_{LCO2}/Q_{H2O}, their surface-volume ratios are generally smaller than those of the drops produced at higher Q_{LCO2}/Q_{H2O}. As the drop flows from position 1 to position 2 and position 3, it experiences a size reduction in terms of

length decrease (see Figure 5.8), which also results in a certain extent of decrease of the surface-volume ratio. The S/V decreases due to a size reduction are more notable for the smaller drops which have been produced at $Q_{LCO2}/Q_{H2O} < 1$), however, the S/V difference of the drop generated at $Q_{LCO2}/Q_{H2O} > 1$ among at position 1, 2 and 3 are not so obvious, which is attributed to the long drop lengths and relative small length reductions. Despite of the S/V differences among the various drops produced at Q_{LCO2}/Q_{H2O} ranging from 0.25 to 3, as shown in Figure 5.13, the S/V of all these Taylor drops can be averaged at 32.6 (mm^{-1}) with a standard error of 0.1 (mm^{-1}) which is small enough to neglect the S/V differences among all the drops. Further, given that the S/V of all drops are on a same level ($\sim 10^4\,m^{-1}$), the relative drop length reductions ($\Delta L/L_1$), as shown in Figure 5.9, are regarded independent of the S/V here in this study.
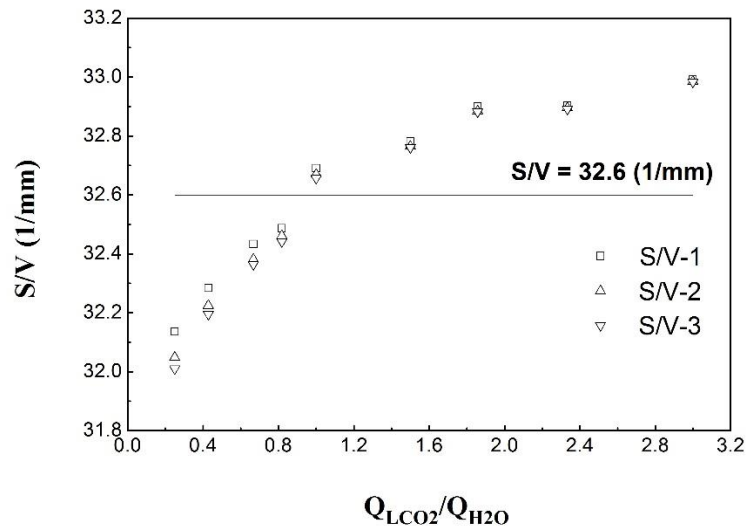
Figure 5.13 Surface-volume ratios of the CO_2 drops at position 1 (S/V-1, squares), position 2 (S/V-2, up triangles) and position 3 (S/V-3, down triangles), respectively. An horizontal line is added to show an averaged S/V which has a value of 32.6 mm^{-1}.

5.5.5 Drop Speeds at Three Specified Positions

Equation (5.26) reveals that the mass transfer between the drop phase and the slug phase is determined by not only the drop length L (more specifically, surface-volume ratio calculated based on L) but also the time scale that is of interest to the mass transfer. The CO_2 drop travel from position 1 (after their generations in the micro T-junction) to position 2 and up to position 3, which certainly takes time. On the other hand, mass transfer has also been in process within this time period.

130

Therefore, knowledge of the drop speeds in the microchannel, other than the drop sizes, are required to understand the mass transfer. Based on the experimental methodologies discussed in section 5.4.1 (shown by equation (5.32) to (5.35)), the drop speeds at position 1 (v-1), position 2 (v-2) and position 3 (v-3) can be measured in experiments and have been plotted in Figure 5.14(A) against Q_{LCO2}/Q_{H2O}. In addition, a horizontal dash line is added in the figure, which shows a constant superficial velocity (v_{Total}) calculated from dividing the constant total flow rates ($Q_{LCO2} + Q_{H2O}$) over the cross sectional area of the channel, i.e., $v_{Total} = (Q_{LCO2} + Q_{H2O})/A$. v_{Total} is introduced here for a purpose of comparison with the experimentally measured drop speeds.

When Q_{LCO2}/Q_{H2O} is below 1, all drop speeds at the three positions are lower than v_{Total} (111.1 mm/s). However, for one specific flow rate condition, those three drop speeds (i.e., v-1, v-2 and v-3) are very close (differences are less than 3 mm/s) to each other. As can be seen, each drop speed (e.g., v-1) are exactly within the error ranges of the other two speeds (v-2 and v-3). Thus, it is appropriate, in this work, to consider the drop flow a constant flow speed scenario when Q_{LCO2}/Q_{H2O} is below 1. An averaged drop speed from the three drop speeds will be applied in the next for such flow rate conditions ($Q_{LCO2}/Q_{H2O} < 1$). When Q_{LCO2}/Q_{H2O} is above 1, the dash line of v_{Total} always crosses with all the range lines of the measured drop speeds and separates these error bars nearly into two equivalent parts. It can be interpreted that the measured drop speeds, from wherever the drops are measured, are always in the vicinity of v_{Total}. Besides, focusing on any one of the flow rate conditions, it is likely that there exists a tendency of drop speed decreasing from v-1 to v-2 and down to v-3, which is clearer as Q_{LCO2}/Q_{H2O} is widely larger than 1. Analogous to the cases of $Q_{LCO2}/Q_{H2O} < 1$, averaged drop speeds based on the measured ones at position 1, 2 and 3 are to be used to determine the drop flowing time in the straight channel. Note that, however, it does not indicate the flow cases of $Q_{LCO2}/Q_{H2O} > 1$ are constant drop flows.

Based on averaged drop speeds from the ones at the three positions as well as the real channel lengths shown in Table 5-1, flowing time of the drops, $t_{flowing}$, in the straight microchannel can be calculated. The averaged drop speed $\bar{v}$ is determined as follows

$$\bar{v} = \frac{1}{3}\sum v_x, \qquad \text{x=1, 2 and 3} \tag{5.43}$$

and the corresponding standard deviation of $\bar{v}$, $\sigma_{\bar{v}}$, can be calculated based on an error propagation:

$$\sigma_{\bar{v}} \text{ (mm/s)} = \sqrt{(\frac{\partial \bar{v}}{\partial v_1})^2 \sigma_{v_1}{}^2 + (\frac{\partial \bar{v}}{\partial v_2})^2 \sigma_{v_2}{}^2 + (\frac{\partial \bar{v}}{\partial v_3})^2 \sigma_{v_3}{}^2}, \tag{5.44}$$

in which individual standard deviation σ_{v_x} (x = 1, 2, and 3) has been determined from experimental measurements. Consequently, the flowing time of the CO_2 drops in the straight channel is calculated from below

$$t_{flowing} \ (ms) = \frac{L_t'}{\bar{v}} \times 10^3, \tag{5.45}$$

where L_t' (mm) is the real total channel length for the CO_2 drops and has been introduced in Table 5-1. Analogously, the uncertainties of $t_{flowing}$ characterized by the standard deviation $\sigma_{t_{flowing}}$ can be quantified as follows

$$\sigma_{t_{flowing}}(ms) = \sqrt{(\frac{\partial t_{flowing}}{\partial \bar{v}})^2 \sigma_{\bar{v}}^2} = 1000 \frac{L_t'}{\bar{v}^2} \sigma_{\bar{v}}. \tag{5.46}$$

(A)   (B)
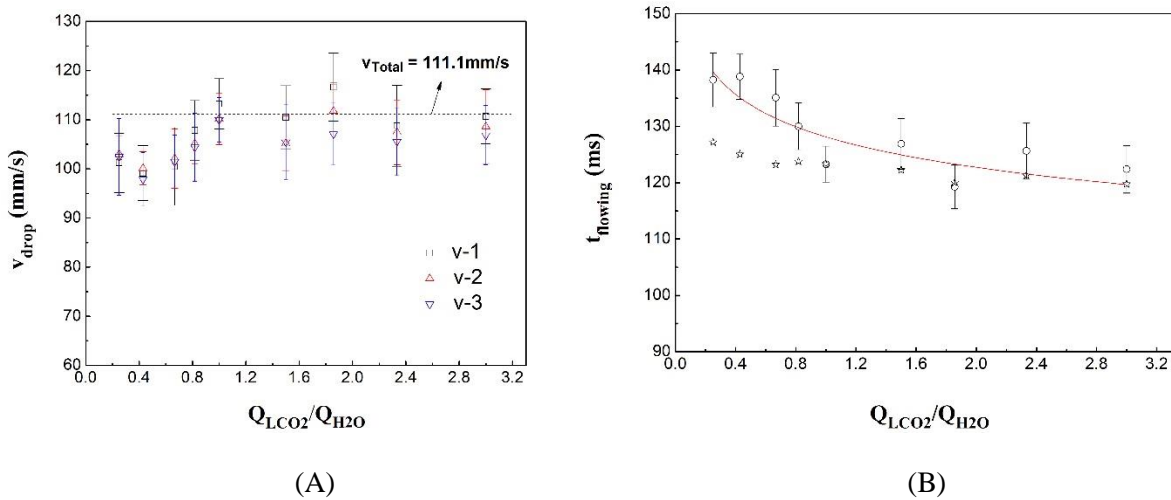
Figure 5.14 (A) Liquid CO_2 drop speed at position 1 (v-1, squares), position 2 (v-2, up triangles) and position 3 (v-3, down triangles) under various Q_{LCO2}/Q_{H2O}. A dash line added in the figure shows a superficial total flow velocity from dividing the total flow rate (Q_{Total} = $Q_{LCO2} + Q_{H2O} = 100 \ \mu L/min$) over the cross-sectional area (A=W·D) of the microchannel. Error bars show one standard deviation for the corresponding drop speed. The error bar caps for v-1, v-2 and v-3 at one specific flow rate ratio are characterized by their widths (the longest for v-1 and the shortest for v-3) for a differentiation purpose. (B) Flowing time ($t_{flowing}$) of CO_2 drops in the straight channel which are respectively determined based on equation (5.45), as shown by the circles, and based on a superficial total flow velocity v_{Total} (111.1mm/s), as shown by the stars.

According to the above two equations, the CO_2 drop flowing time are calculated and shown in Figure 5.14(B). As a reference, the flowing time calculated based on the superficial total flow velocity v_{Total} (111.1mm/s) are also plotted in Figure 5.14(B). As a consequence of a slight decrease of L_t' from 14 mm to 13.3 mm, there is also a slight decrease of the flowing time from 127.2 ms to 120 ms when v_{Total} instead of $\bar{v}$ is applied in equation (5.45). Apart from different L_t', the flowing time shown by the circles in Figure 5.14(B) are subjected to different averaged drop speeds (i.e., $\bar{v}$) as well. Generally, the averaged drop speeds at $Q_{LCO2}/Q_{H2O} < 1$ are marginally smaller than those at $Q_{LCO2}/Q_{H2O} > 1$. Consequently, the flowing time calculated for $Q_{LCO2}/Q_{H2O} < 1$ are approximately 10ms higher than those for $Q_{LCO2}/Q_{H2O} > 1$, as shown by Figure 5.14(B). Furthermore, as argued that the averaged drop speeds may be approximated by v_{Total} for $Q_{LCO2}/Q_{H2O} > 1$, the flowing time may also be approximated by those calculated by v_{Total} for such cases despite a slight difference (no larger than 4%) between the two sets of results. The trend line in the figure justifies the development of $\Delta L/L_1$, as shown in Figure 5.9, given that the surface-volume ratios S/V for all drops are at a same level (10^4 m^{-1}).

5.5.6 Mass Transfer Coefficient (k_d) Based on Drop Lengths and Flow Time

Based on the drop length and the CO_2 drop flowing time in the straight microchannel, as reported in previous sections, the overall solute-side mass transfer coefficients (k_d) can be determined by using equation (5.26). The channel width (W = 150 µm) and depth (D = 100 µm) are known. A nominal molar concentration ($C_d = \rho_{CO2}/M$) of pure CO_2 drop and an equilibrium concentration ($C_e \approx 1.27$ mol/L [321,322]) at an assumed sharp interface referring to the pressures listed in table 1 and a constant temperature (T = 298K) are going to be adopted in the calculations. A static contact angle θ_c = 150° estimated from Figure 5.5 is also applied. Thus, equation (5.26) can be specified as follows

$$k_d = 30.03 \frac{C_d}{C_d - 1.27} \left(\ln \frac{432.2L_0 - 522.2}{432.2L_x - 522.2} \right) \cdot \frac{1}{t}, \tag{5.47}$$

in which k_d has a unit of µm/ms, or equivalently, mm/s. In order to determine the nominal molar concentration of CO_2, densities of CO_2 at various initial pressures (P_0 in Table 5-1) and a constant temperature (298.15 K) are used, which are referred to the NIST chemistry webbook [381]. Based on the drop length and the drop flowing time in Figure 5.7 and Figure 5.14, respectively, the overall mass transfer coefficients $k_{d, 1-3}$, namely, the mass transfer coefficient of the drops from position 1 to 3, is calculated, as shown in Figure 5.15(A). Moreover, by combining the results in Figure 5.15(A) and Figure 5.13, $k_{d,1-3}*(S/V)_a$ (i.e., the volumetric mass transfer coefficient) can also be obtained,

133

which is simply accomplished by equation (5.47) and (5.42). Note that an averaged surface-volume ratio $(S/V)_a$ from the three at position 1, 2 and 3 is used for calculating $k_{d,1-3}*(S/V)_a$. The results of $k_{d,1-3}*(S/V)_a$ are plotted in Figure 5.15(B).

Figure 5.15 shows that a lower Q_{LCO2}/Q_{H2O} scenario usually results in a larger mass transfer coefficient, which is mainly attributed to a longer flowing time due to relatively slow drop flows (Figure 5.14(B)) despite a slightly lower surface-volume ratio (Figure 5.13). As Q_{LCO2}/Q_{H2O} increases, an elongated CO_2 drop will be produced which is characterized with slightly enhanced S/V and a shortened $t_{flowing}$. These factors lead to less significant drop shrinkages, which undoubtedly demonstrate smaller mass transfer coefficients. Based on the observations of drop length reductions and the calculations of mass transfer coefficients, it is clear that, although the CO_2 drops regardless of their sizes are featured with similar absolute drop length reductions, they may show different mass transfer capabilities by taking account of both the size effect and the flowing time, which is reflected by the drop shrinkages in a relative sense (Figure 5.9). Comparatively, flowing time becomes a dominant role over the rather unanimous surface-volume ratios of the CO_2 drops.

(A)   (B)
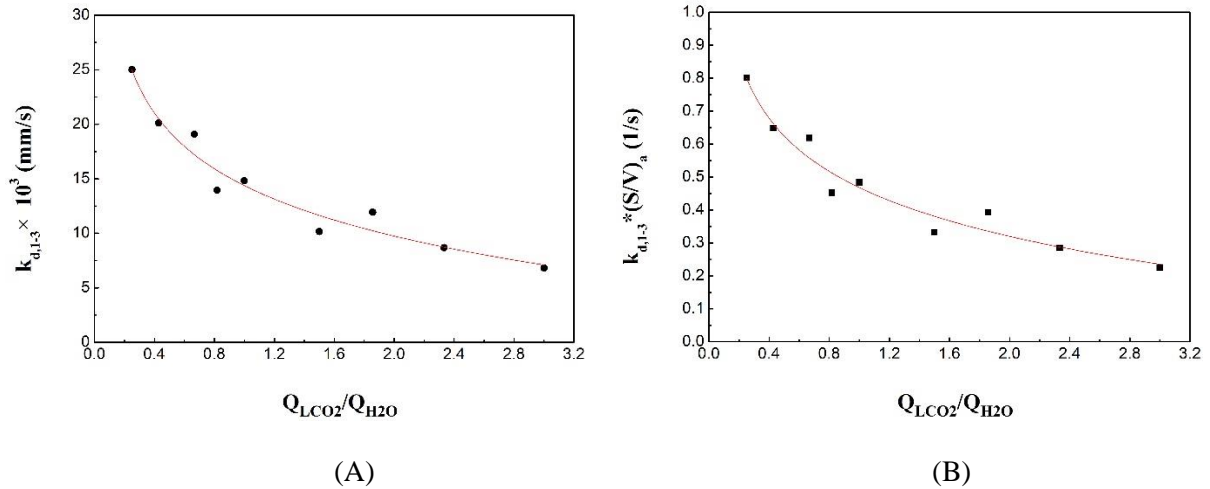
Figure 5.15 Overall solute-side mass transfer coefficients $k_{d,1-3}$ (A) and $k_{d,1-3}(S/V)_a$ (B) of liquid CO_2 drops in the straight microchannel. The data in the left figure have been scaled by 10^3.

5.6 Conclusion

In this study, hydrodynamic shrinkage of liquid carbon dioxide (CO_2) in water in a straight microchannel has been investigated, where the liquid CO_2 takes a form of flowing Taylor drops and water is applied as a continuously flowing solvent which behaves as a slug that separates the CO_2

drops. An experimental system introduced in Chapter 3 is utilized in this study. In particular, a micro T-junction with a uniform width (W = 150µm) and depth (D = 100µm) fabricated in a silicon/glass microchip is used to produce CO_2 drops, in which liquid CO_2 is injected from a side channel (perpendicular to the main channel) as a dispersed fluid and water as a continuous liquid flows in the main channel, respectively. As a result of various flow rate ratios (Q_{LCO2}/Q_{H2O}) of liquid CO_2 (Q_{LCO2}) over water (Q_{H2O}), different CO_2 drops in terms of non-dimensional drop length (L_1/W) are produced in the micro T-junction. Their drop length (L) and drop speed (V) have been monitored and measured at three specified positions in downstream straight microchannel, namely, position 1 where the drop is exactly pinched off by the continuously flowing water, position 2 which is the midpoint of the total length of the straight channel (approximately 7.35mm downstream of the inner point of the T-junction), and position 3 that is located at the very end of the straight channel. Main results are summarized as follows:

◆ Non-dimensional length (L_1/W) of the generated liquid CO_2 drops at the T-junction is correlated with Q_{LCO2}/Q_{H2O}. The correlation is found to be linear but the factor of Q_{LCO2}/Q_{H2O} is much larger than 1 (specifically, 1.79), which is similar to what have been reported in Chapter 4 that is essentially attributed to the squeezing-elongating effect of the interface during drop generations.

◆ The absolute drop length at position 1 (L_1), 2 (L_2) and 3 (L_3) shows a decreasing tendency. Detailed drop length reductions are manifested by a total length reduction ΔL ($\Delta L = L_1 - L_3$), a first length reduction ΔL_1 ($\Delta L_1 = L_1 - L_2$), and a second length reduction ΔL_2 ($\Delta L_2 = L_2 - L_3$). All these length reductions versus Q_{LCO2}/Q_{H2O} have been approximated constant reductions ($\Delta L = (24.35 \pm 1.08)$ µm, $\Delta L_1 = (16.52 \pm 1.71)$ um, $\Delta L_2 = (7.83 \pm 1.17)$ um), which indicates the absolute drop shrinkage may be independent of the original drop size. However, relative drop length reductions $\Delta L/L_1$ are different among the different flow rate conditions. $\Delta L/L_1$ decreases from 0.1 to 0.025 as Q_{LCO2}/Q_{H2O} increases from 20/80 to 75/25. Based on the formulations of drop surface area (A) and volume (V), surface-volume ratios (S/V) of all drops at the three specified positions are determined. In general, averaged S/V from at position 1, 2 and 3 show a decline tendency subjected to increasing Q_{LCO2}/Q_{H2O}. As $Q_{LCO2}/Q_{H2O} > 1$, there is almost no difference of S/V among all the three surface-volume ratios for each flow rate condition. Overall, S/V for all drops, regardless of locations, can be averaged at 32.6 mm^{-1} with a standard error of 0.1 mm^{-1}.

◆ Drop speeds at position 1 (v-1), 2 (v-2) and 3 (v-3) are measured, which will be applied to calculate the CO_2 drop flowing time in the channel, and as a further step, the mass transfer

coefficients. When $Q_{LCO2}/Q_{H2O} < 1$, these three drop speeds are very close and generally lower than a reference flow velocity v_{Total}, i.e., a superficial velocity by dividing the total flow rate ($Q_{LCO2} + Q_{H2O}$) over the channel cross section. When $Q_{LCO2}/Q_{H2O} > 1$, drop speed decreases from v-1 to v-2 and down to v-3 but still can be approximated by v_{Total}. In order to simplify the calculations of flowing time, an averaged drop speed based on these three speeds for all cases is adopted. Besides, a real channel length (see Table 5-1) rather than the total channel length dedicated to the CO_2 drop flow is applied. Due to the slightly longer real channel lengths and lower drop speeds, the flowing time for $Q_{LCO2}/Q_{H2O} < 1$ are roughly 10 ms longer than those for $Q_{LCO2}/Q_{H2O} > 1$.

◆ Starting from a general form of mass transfer coefficient k_d (equation (5.8)), a specific form of k_d (equation (5.26)) based on detailed drop surface area and volume by considering the microchannel size (width W and depth D), contact angle (θ_c) and drop lengths L_x (x = 1, 2, 3) has been developed. Two types of mass transfer coefficient, namely, k_d (mm/s) and $k_d(S/V)$ (1/s), are considered. Generally, lower Q_{LCO2}/Q_{H2O} results in relatively higher mass transfer coefficients in terms of both k_d and $k_d(S/V)$, which is essentially attributed to the flowing time $t_{flowing}$, given that S/V for all drops are rather unanimous (on a level of 10^4 m^{-1}). Moreover, mass transfer capabilities of different flow conditions are justified by the relative drop length reductions ($\Delta L/L_1$) as well.

◆ Potential effects of the pressure drop (ΔP_t) due to a drop flow in the straight microchannel on the drop volume have been discussed. Based on a modified Warnier's pressure drop model [221], the total pressure drops in the straight microchannel under the presence of CO_2 drops and water slugs are estimated. Despite a slight decrease (~100Pa) subjected to increasing Q_{LCO2}/Q_{H2O}, ΔP_t are of a mean value of 3175.4 Pa with a standard error of 1.6%. Combined with the Peng-Robinson Eos [251] and estimated initial pressures at the T-junction (from the CO_2 pump), liquid CO_2 drop volume changes relative to the original volumes are correlated to the molar volumes present in the Eos, which are further quantified. The resulted volume changes are calculated as relatively small quantities ($\Delta V/V_0 = 0.39‰ \sim 0.52‰$).

136

Chapter 6

Hydrodynamic Shrinkage of Super-critical CO_2 (scCO_2) Drops in a Straight Microchannel

In the previous chapter, the mass transfer and hydrodynamic shrinkage of liquid CO_2 drops in a Taylor flow regime in a straight microchannel are extensively studied. By increasing the working pressures and temperatures over the critical conditions of CO_2, the Taylor drop is easily tuned super-critical CO_2 (scCO_2). This chapter is dedicated to the study of the hydrodynamic shrinkage of super-critical CO_2 (scCO_2) Taylor drops in a straight microchannel.

6.1 Introduction

The combination of CO_2 and microfluidics has only started as a research topic from a decade ago. Limited literature related to this topic cover on either the CO_2 for applications or CO_2 itself. Among the reported applications of CO_2 in microsystems, scCO_2, as a unique form of CO_2, has been utilized to enhance chemical reactions as a solvent or reactant [68-70,72,73,79,383-385] and in extractions of non-polar compounds or emulsions [71,74,75,239,325,386-389], basically based on its liquid-like density ($500 \sim 700$ kg/m^3), a gas-like viscosity ($10 \sim 100$ µPa·S), an intermediate diffusion coefficient ($\sim 10^{-3}$ cm^2/s) between that of gas and that of liquid, and no surface tension. Besides, the density and viscosity of scCO_2 can be flexibly adjustable by tuning the pressure and/or temperature. Figure 6.1 is a schematic of the pressure-temperature phase diagram of CO_2 [382]. The critical pressure and temperature of CO_2 are 7.38 MPa and 31 °C (this is the so-called 'critical point'), respectively. Other than the applications of scCO_2, CO_2 itself, with most of the interests lying in its solubility in water and physical solvents [80,81,87,88,390-392] and its diffusivity in aqueous solution or even bitumen [326,327,393-396], has also become a research focus. Compared with conventional methods, microscale studies on these topics are advantageous in terms of increased resolution, less diffusion time, reduced convective effects, rapidness, reduced costs, enhanced high pressure applicability, less sample consumption and increased safety [397]. Moreover, the hydrodynamics of CO_2 with a presence of a second liquid phase (e.g., water, ethanol, methanol) at microscale have evoked interests in the microfluidics community in recent years, with the efforts mostly focused on the flow behaviors or regimes. Such studies have reveal the hydrodynamics in both regular microchannels (or capillaries) [329-331,333] and micromodel porous media [45,45,47,57,58,60,61,398,399].
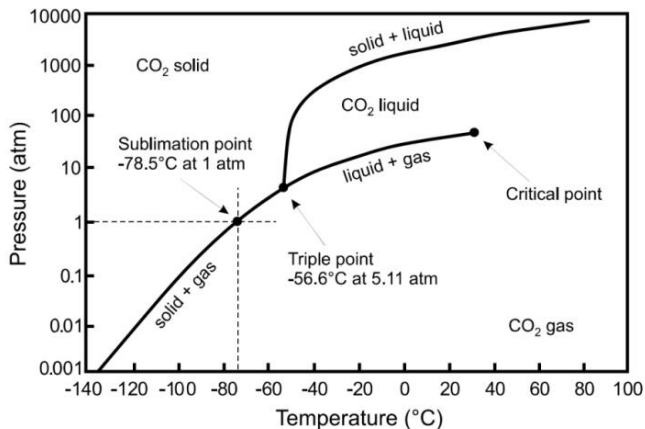
Figure 6.1 A pressure - temperature phase diagram of CO_2 (after Reference [382]).

By reviewing the research efforts on $scCO_2$ that may have been driven by either its application prospects in chemical processes or its importance in environmental sector, it is clear that CO_2 in a dense state (liquid CO_2, $scCO_2$) rather than gas have potentials to transform its conventional roles in chemical and food industries to others such as in advanced material production and underground carbon sequestration.

Following the experimental work in the previous chapter, in Chapter 6, highly pressurized $scCO_2$ in a Taylor flow regime is studied. De-ionized (DI) water is still utilized as the solvent as well as a continuously flowing liquid. The same micro T-junction for liquid CO_2 study is applied to generate the $scCO_2$ Taylor drops. The hydrodynamics and mass transfer coefficient of $scCO_2$ Taylor drops in water in the long straight microchannel are analyzed. To the best knowledge of author, this study is the first in research related to mass transfer caused $scCO_2$ drops' shrinkage in microfluidics.

In terms of the methodologies in experimental operations and for calculating the mass transfer coefficient, this chapter is analogous to Chapter 5. Therefore, the details of those sections will not be introduced again in Chapter 6. Instead, the experimental results and discussions are more focused here. Section 6.2 introduces the experimental methodologies and procedures specifically tailored for working with $scCO_2$, and an overview of observed $scCO_2$ drops at three specified positions of the channel is provided. In section 6.3, the experimental results are reported and discussions of the results are given. Section 6.4 is a summary of our experimental work.

6.2 Experimental Methodology

6.2.1 Setup and Measurements

The experimental system introduced in Chapter 3 is utilized to conduct the study of the hydrodynamic dissolution of $scCO_2$ Taylor drops in a straight microchannel. The same micro T-junction in a silicon/glass microchip having been used in Chapter 5 will be used to produce $scCO_2$ Taylor drops and to facilitate the hydrodynamic flows of the drops after their generations. The fabrication of this microchip has been detailed in Chapter 3. Briefly, it is sequentially carried out based on (1) standard photolithography, (2) deep reactive ion etching (DRIE), (3) inlet & outlet drilling, (4) anodic bonding of silicon and glass wafer, and (5) dicing of bonded wafers into a final rectangular shape ($74 \times 44 \times 1.2$ mm^3) which can be fitted and installed onto the non-permanent connector. The assembling methods for the microchip and the non-permanent connector have been introduced in Chapter 3 and in Appendix A.

In particular, super-critical carbon dioxide is prepared in the cylinder of the syringe pump based on increased pressures over the critical pressure of CO_2 (see Figure 6.1) and a circulating water bath for controlling the temperature of the cylinder (from its outside). During experiments, $scCO_2$ is used as the disperse fluid which is injected at constant flow rates into the side channel of the T-junction. Still, de-ionized (DI) water is used as the continuous liquid flowing at constant flow rates in the main channel of the T-junction, as shown in Figure 6.2. The downstream of the micro T-junction is a long straight microchannel with a total length of 14.7 mm. All the microchannels in the microchip are characterized by a constant width of 150 µm and a width of 100 µm. At the end of the straight microchannel is a 90 degree turning of the channel and a further 55 mm long microchannel (the same width and depth) connecting to the outlet of the microchip as well as that of the connector.

The back pressure of the entire flowing system is regulated by a back pressure regulator (model EB1ULF1, Equilibar) working simultaneously with a needle valve. A nitrogen gas tank as well as its gas regulator provides an initially appropriate back pressure at the top of back pressure regulator, and only when the upstream pressure of the back pressure regulator surpasses the reference one at the nitrogen gas regulator can the fluids flow through. In practice, the back pressure during experiments is actually measured by the precise pressure transducer (Swagelok) between the connector and the back pressure regulator. The circulating water bath (Thermo Scientific) for controlling the temperature of CO_2 (above 31 ℃) from within the pump cylinder, through the facilitating stainless steel tubing, up to the microchip is used to guarantee the super-critical state of the CO_2. In addition, a

miniature hot plate (model ph-121s, MSA Factory Japan) is installed between the bottom of the microchip (silicon side) and the top surface of the self-made stage for the microfluidic modulation, with the remaining gap between the hot plate and the chip filled with a thermal interface material – silicone (Dow Corning 340, thermal conductivity = 0.67 W/(m·K)). The temperature on the top surface (glass side) of the microchip can be measured by using an infrared thermometer (Fluke Corporation).
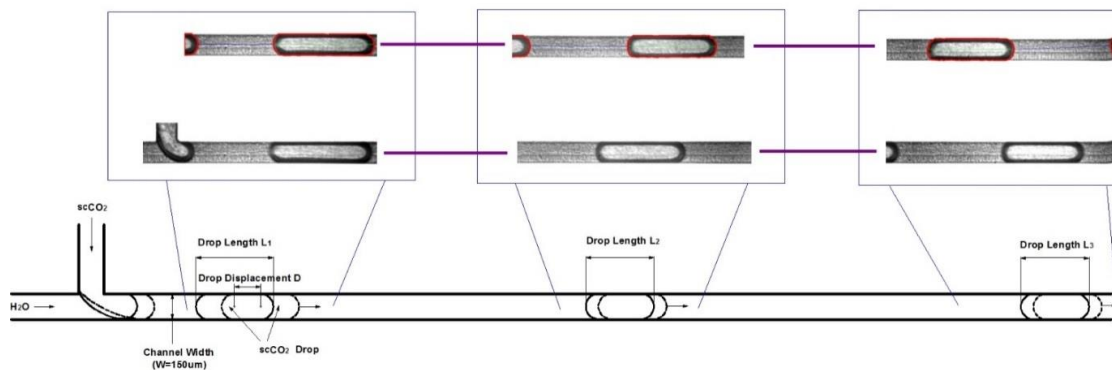
Figure 6.2 Schematic of the experimental methodology for investigating the hydrodynamic shrinkage of scCO$_2$ drops in a straight microchannel ($16 < L_t/L_x < 60$, x=1, 2, 3; W=150 µm). The drop length L_x and drop speeds v_x is measured at three positions, i.e., immediately after the drop generation (position 1), the midpoint of the microchannel length (position 2) and the end of the microchannel (position 3), as shown from left to right in sequence.

Figure 6.2 shows a schematic of the methodology of the measurements of drop size, drop speed, and slug (water) size (equivalent to the drop spacing) at three specified positions of the microchannel, i.e., immediately after the scCO$_2$ drop generation (position 1), at the midpoint of the channel (position 2, approximately 7.35mm from the T-junction), and the end point of the channel (position 3). The visualizations of the drops at these three positions are fulfilled by using a high speed camera (v210, Phantom) mounted with an upright microscope (BX51, Olympus). The video (3000 frames per second, fps) at each position is recorded after a waiting time of at least 20 minutes, also for each time when a different set of flow rate of the scCO$_2$ and DI water is applied, by which a stable Taylor flow regime can be reached. After experiments, all the videos (three videos for each studied case at the three positions) are processed in a same strategy as that applied in Chapter 5. The drop size and the drop speed as well as their standard deviations are determined in a same way as shown by equations (5.30-5.35). Therefore, in this chapter, the calculation details are not detailed again.

6.2.2 Experimental Procedures

The procedures of the experimental study on hydrodynamic shrinkage of $scCO_2$ Taylor drops are analogous to that introduced in Chapter 4 and Chapter 5 when working with liquid CO_2. However, there are two main differences for working with $scCO_2$ from working with liquid CO_2, i.e., (1) the working pressure should be over 7.38 MPa at all the flowing path; and (2) temperature control including a circulating water bath and a miniature hot plate for microchip are required. Therefore, the experimental procedures related to these two requirements are focused here.

At the beginning of the experiment, a reference back pressure of 8,000 kPa is applied to the back pressure regulator by purging nitrogen gas from the tank, and the pressure value is read from the pressure gauge on its pressure regulator at the outlet of the tank. Note that this pressure is approximately 8,000 kPa which is read from the pressure gauge but of a low precision. Afterwards, liquid CO_2 is filled into the entire system (water side valves are closed during this operation), which is done in a similar way as that in Chapter 4. Because of the applied back pressure, the filled CO_2 will be stopped and stored in the entire system. When the filling process is finished, the pressures read from the pump and the back pressure transducer are ~5.87 MPa. Next the valve at the CO_2 syringe pump exit is closed, and a temperature of (40 ± 0.4) °C of the circulating water bath is applied to increase the temperature of the CO_2 in the pump cylinder. During the waiting time of CO_2 temperature increases, the mercury lamp at the microscope is switched on which requires at least 15 minutes to reach a steady illumination. Due to the temperature increase, the pressure within the CO_2 pump also increases, for reference, the CO_2 in the pump has a pressure of 7,380 kPa at a volume of 200.1 ml when the circulating water bath reaches 33.3 °C. During this temperature increasing stage, the miniature hot plate is started and a temperature of 40 °C is applied, which can be confirmed by measuring the temperature on the microchip using an infrared thermometer.

As flowing water bath reaches ~ 40 °C (the pre-set temperature of the circulating water bath is 40 °C), CO_2 in the pump reaches a pressure of 8,330 kPa at a volume of 200.1mL. Then the CO_2 pump valve was slowly opened to fill the tubing between it and a second valve (which is kept closed) on the flow path but in front of the connector with this pressurized CO_2, after that, the first valve is closed and the second valve is slowly and gradually opened to let the pressurized CO_2 fill in the chip (which is initially filled with ~ 5.87 MPa CO_2). This procedure of alternately opening and closing these two valves could be repeated for a few times until the pressures from the pump to the chip as well as the downstream tubing are constant. As the CO_2 pressures everywhere in the flow path are steady and

constant, the pressure is 8,180 kPa (read from the pump) at the CO_2 pump and is approximately 7.8 MPa (measured by the back pressure transducer) at the back pressure regulator at downstream of the chip. For water, its pressure is rapidly increased (by doing a function of 'rapid pressure' on the water pump) to 8,000 kPa and is then stopped, during this operation the pump exit valve should be open and the second valve is closed. Then the second valve was gradually opened, and as observed from the live video transferred from the high speed camera on the computer, water is injected to the T-junction and pushes the CO_2 away within the T-junction while water pressure in the pump dropped to 7,700 kPa or so. Next, an initial flow rate set of the CO_2 and DI water are applied at the respective pump. After a waiting time of one hour, the microfluidic channels are deemed being filled with $scCO_2$ and the previous liquid CO_2 in the microchip has been pushed out further downstream.

As discussed during the operations with liquid CO_2 in Chapter 4 and Chapter 5, once the videos at those three specified positions are recorded to the applied flow rate set, another different flow rate condition is applied at the two pumps. After a waiting time of at least 20 minutes, the flow regime reaches a steady state, and videos are capture at those three positions. By doing so, various sets of flow rate for $scCO_2$ and water are studied in the T-junction.

6.2.3 Experimental Observations

Figure 6.3 shows an overview of all the $scCO_2$ drops in Taylor flow regime at the above specified three positions in the straight microchannel. Each group of the three snapshots is presented against the position at the horizontal axis and against the flow rate ratio (Q_{scCO2}/Q_{H2O}) at the vertical axis. In this experimental work, Q_{scCO2}/Q_{H2O} has been tuned from 10/90 up to 75/25. By keeping Q_{scCO2} as a constant of 50 µL/min, the author further study Q_{scCO2}/Q_{H2O} from 50/100 down to 50/280. It is worth noting that the minimum and the maximum flow rate ratio having been reached are not arbitrarily chosen, instead, they are the lower and the upper limit to render a $scCO_2$ drop flow in the micro T-junction which can be observable in the region of interest (1600 µm $\times$ 400 µm) in our study.

Similar to the experimental strategy in Chapter 4, two groups of flow rate conditions are investigated in this chapter, i.e., (1) a constant total flow rate $Q_{scCO2} + Q_{H2O} = 100$ µL/min and (2) a constant $Q_{scCO2} = 50$ µL/min. The capillary number (Ca_c) calculated by the continuous liquid - water ($Ca_c = \eta_c v_c/\gamma$) ranges from 5.44×10^{-4} to 6×10^{-3}, for which the viscosity η_c (655.48 µPa s) [337] and an interfacial tension γ (33.47 mN $\cdot$ m^{-1}) [338,339] are referred to 313 K and a pressure between 7,776 kPa to 7,940 kPa, and v_c is the mean velocity of water determined from its flow rates (Q_{H2O}) over the cross sectional area of the channel ($A_c =$ WD).
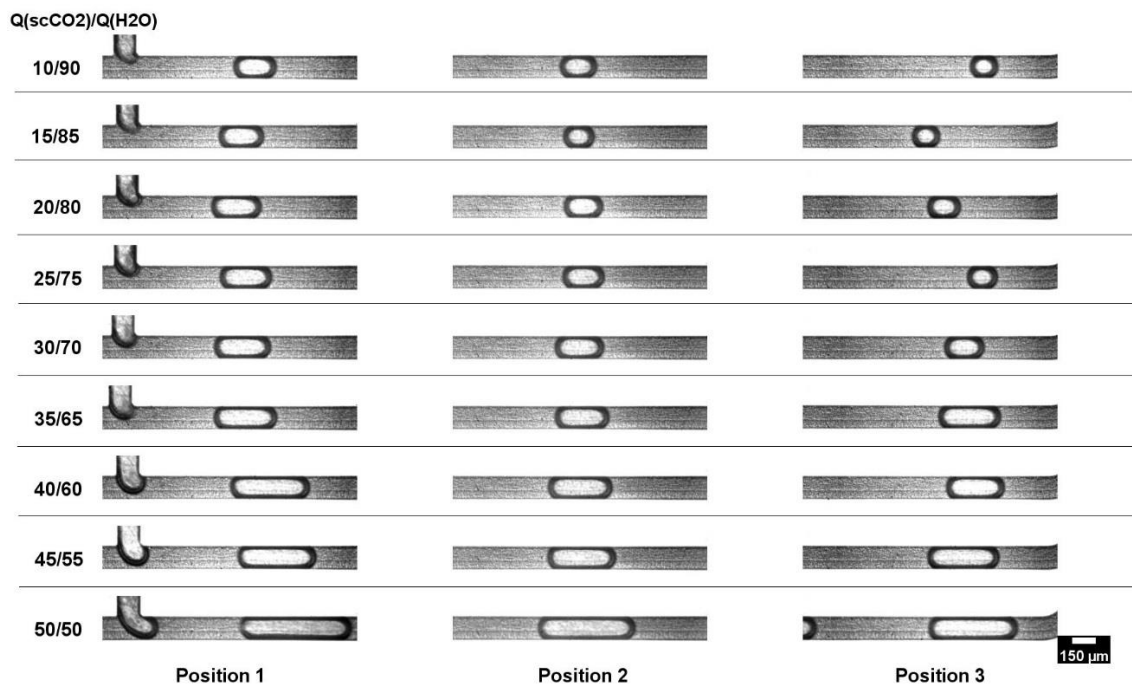
(A)
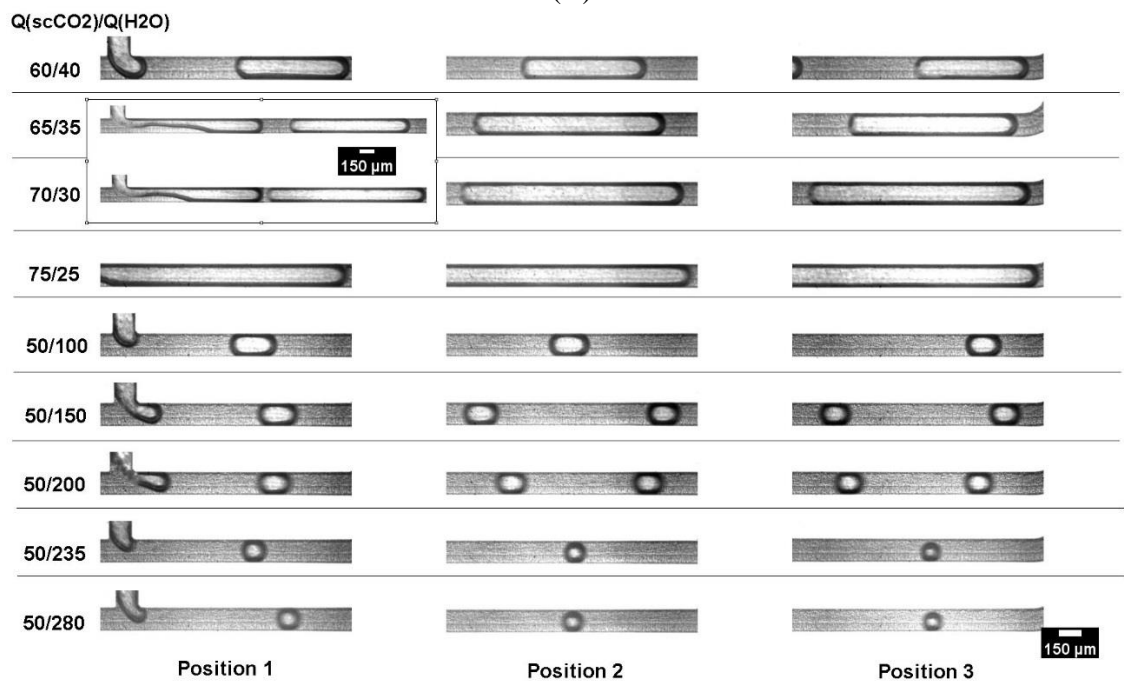
(B)

Figure 6.3 An overview of the scCO$_2$ drops (or segments) at the three specified positions in the straight microchannel at different flow rate conditions (Q_{scCO2}/Q_{H2O}). Scale bars in (A) and (B): 150µm.

143

Shown by Figure 6.3, $scCO_2$ drop length has been increasing visually as Q_{scCO2}/Q_{H2O} increases from 10/90 to 70/30. When Q_{scCO2}/Q_{H2O} reaches 65/35 and 70/30, the produced $scCO_2$ segments are too long to be observed in the region of interest. Therefore, the region of interest has been shift a little downstream in order to capture a complete $scCO_2$ segment, as shown by the snapshots at position 1 for $Q_{scCO2}/Q_{H2O} = 65/35$ and 70/30 in the figure. Also note that, in order to show the distance of the immediately produced $scCO_2$ segments in those two cases relative to the T-junction, the snapshots are shown in an combined end-to-end way showing both the T-junction and a completely generated drop. However, as Q_{scCO2}/Q_{H2O} is beyond 70/30, there is no way to capture a complete $scCO_2$ segment. By keeping Q_{scCO2} a constant of 50 µL/min, the drop size will be much smaller (length equals to channel width, not Taylor drops any more) as Q_{H2O} increases from 50 µL/min up to 280 µL/min. When Q_{H2O} is beyond 200 µL/min, the $scCO_2$ generation may have entered to a dripping regime, where the shear stress starts to dominate the pinching off the $scCO_2$ segments compared to the interfacial tension. However, the critical Ca number for an occurrence of dripping regime is still below 0.01, which makes it much earlier here than that have been shown in Chapter 4. Also, the maximum Q_{scCO2}/Q_{H2O} which renders a non-observable complete CO_2 segment in this study (i.e., $Q_{scCO2}/Q_{H2O} = 70/30$) is smaller than that reported in Figure 4.4. It is believed that a lower viscosity of $scCO_2$ than that of liquid CO_2 may have caused the difference.

6.3 Results and Discussions

In this section, experimental results based on the above observations of the $scCO_2$ drop at the three specified positions in the straight microchannel are reported. Related discussions are made as well. This section may be read and reviewed by comparison with the Section 5.5 in Chapter 5, despite the differences of the experimental results.

6.3.1 Size of Generated scCO$_2$ Drops

As introduced in Chapter 4 and Chapter 5, the size of the generated $scCO_2$ at the micro T-junction can be quantified by using a non-dimensional length L_1/W, in which L_1 is measured absolute drop length (L_1, µm) and W (150 µm) is the channel width. The non-dimensional lengths (L_1/W) of the $scCO_2$ drops generated at the micro T-junction have been plotted against the flow rate ratios (Q_{scCO2}/Q_{H2O}), as shown in Figure 6.4.

For the group of flow rate conditions with a constant total flow rate $Q_{scCO2} + Q_{H2O} = 100$ µL/min, the size of the generated $scCO_2$ has increased linearly as a result of increasing Q_{scCO2}/Q_{H2O} from 10/90
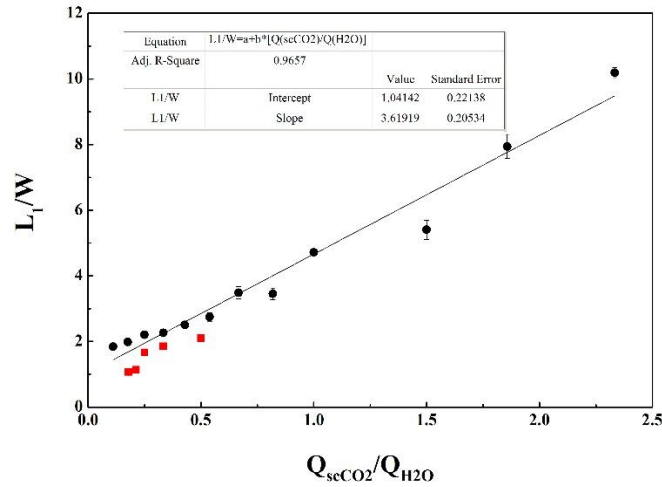
Figure 6.4 Non-dimensional lengths (L_1/W) of the generated $scCO_2$ drops at the micro T-junction versus Q_{scCO2}/Q_{H2O}. Black circles: $Q_{scCO2} + Q_{H2O} = 100$ µL/min; red squares: $Q_{scCO2} = 50$ µL/min. Error bar indicates one standard deviation of the mean value.

to 70/30. These data points are fitted by a linear function, as shown by the solid line in Figure 6.4, which is $L_1/W \approx 1.04 + 3.62 \cdot (Q_{scCO2}/Q_{H2O})$. The intercept and the factor of the flow rate ratio on the right side of the function have been discussed in Chapter 4. The factor in front of Q_{scCO2}/Q_{H2O}, in particular, reveals a more intensified effect of the elongating time on the final size of the $scCO_2$ drops than that when liquid CO_2 is involved (see Chapter 4 and Chapter 5).

For the group $Q_{scCO2} = 50$ µL/min, there also exists a monotonous increasing relation between L_1/W and Q_{scCO2}/Q_{H2O}, as shown by the squares in Figure 6.4. However, due to a limited range of the applied Q_{scCO2}/Q_{H2O}, there is a limited range of L_1/W from 1 to 2. Nevertheless, it is predictable that, under a same Q_{scCO2}/Q_{H2O}, the one in the group of a constant $scCO_2$ flow rate can result in a smaller drop size than that in the group of a constant total flow rate, as shown by the lower positions of the squares than the circles in the figure. This difference of the drop size for a same Q_{scCO2}/Q_{H2O} is attributed to a higher capillary number of the group of the circles due to larger flow rates of water. Therefore, flow rate ratio and capillary number are two main factors determining the $scCO_2$ drop size.

6.3.2 scCO$_2$ Drop Sizes and Size Reductions

The $scCO_2$ drops at three specified positions of the straight microchannel have been visualized and their sizes are measured based on equation (5.30) and (5.31). According to previous discussions in Chapter 5, a representative size always corresponds to a specific position of the microchannel.

145

Therefore, for a specific applied flow rate condition, each of those three positions (x = 1, 2, 3) is characterized with a representative drop length (L_x, x = 1, 2, 3).
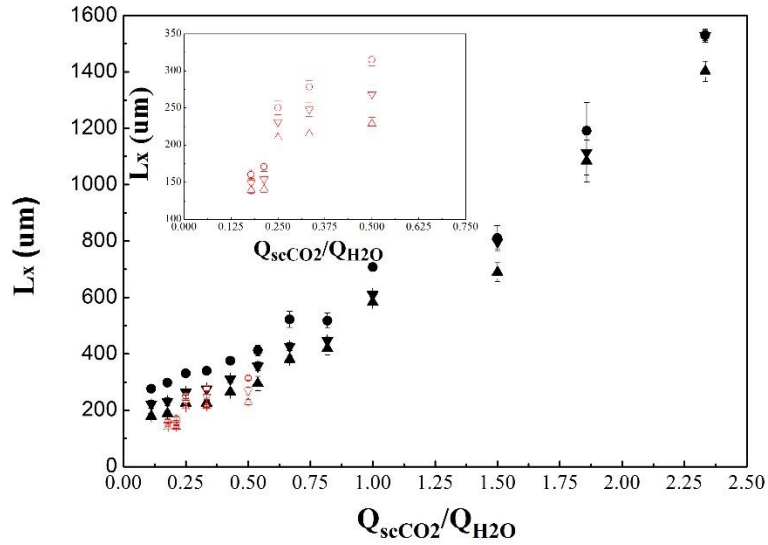
Figure 6.5 $scCO_2$ drop lengths at the three positions under various Q_{scCO2}/Q_{H2O}. Circles: drop length at position 1, L_1; down triangles: drop length at position 2, L_2; up triangles: drop length at position 3, L_3. Error bar indicates one standard deviation of the mean drop length. Inset in the figure shows an enlarged view of the details of the data points (hollow symbols) for $Q_{scCO2} = 50 \mu L/min$. Solid symbols: $Q_{scCO2} + Q_{H2O} = 100 \mu L/min$.

Figure 6.5 shows the absolute length of the $scCO_2$ drop at those three positions under various Q_{LCO2}/Q_{H2O}. For $Q_{scCO2} + Q_{H2O} = 100\mu L/min$ and $Q_{scCO2} = 50\mu L/min$, there are always a decline of the drop length from position 1 (circles in Figure 6.5) to position 2 (down triangles in Figure 6.5) and down to position 3 (up triangles in Figure 6.5), i.e., $L_1 > L_2 > L_3$. Analogous to the shrinkage study of liquid CO_2 drops in Chapter 5, length reductions characterize the $scCO_2$ drop shrinkage, which are resulted from a dissolution - diffusion mechanism across the interface between the $scCO_2$ drops and the continuously flowing water.

Three drop length reductions, i.e., ΔL_1 ($\Delta L_1 = L_1 - L_2$), ΔL_2 ($\Delta L_2 = L_2 - L_3$) and ΔL ($\Delta L = L_1 - L_3$), have been calculated based on the absolute drop lengths which are shown in Figure 6.5. Figure 6.6 shows these three detailed drop length reductions. Similar as liquid CO_2 in Chapter 5, ΔL_1 are almost always larger than ΔL_2 for the two groups of flow rate conditions. The differences between ΔL_1 and ΔL_2 are less significant at $Q_{scCO2}/Q_{H2O} < 35/65$ which results in generated $scCO_2$ drops shorter than 2.75W than $Q_{scCO2}/Q_{H2O} > 35/65$. By comparing ΔL_1 and ΔL_2 at $Q_{scCO2} = 50\mu L/min$, despite a

146
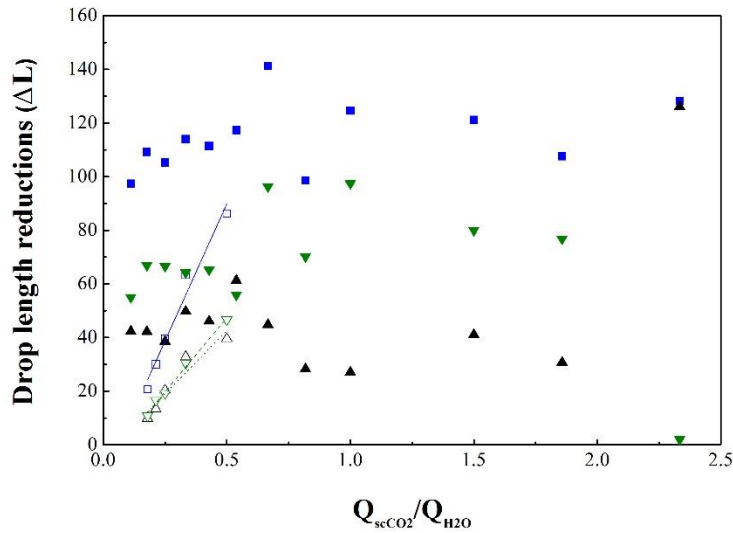
Figure 6.6 Three drop length reductions $\Delta L_1 = L_1 - L_2$ (down triangles), $\Delta L_2 = L_2 - L_3$ (up triangles) and $\Delta L = L_1 - L_3$ (squares) from position 1 (L_1) to position 2 (L_2) and to position 3 (L_3). Solid symbols: $Q_{scCO2} + Q_{H2O} = 100\ \mu L/min$; hollow symbols: $Q_{scCO2} = 50\ \mu L/min$.

tendency of increasing differences between these two length reductions with increasing Q_{scCO2}/Q_{H2O}, the differences are much less than those under $Q_{scCO2} + Q_{H2O} = 100\ \mu L/min$. This discrepancy is believed to be resulted from the flow hydrodynamics between the two groups of conditions, specifically, when $Q_{scCO2} = 50\ \mu L/min$ the water flow is much faster than the one in the other group, and the $scCO_2$ drops move at a speed mainly dominated by the continuously flowing water, thus they may have faster flowing speed in the channel as well as a shorter residence time, and there are barely relative motions between the $scCO_2$ and the water, which leads to almost no refreshing interface temporally and the shrinkage are totally relying on the diffusion – a relative hydrostatic diffusion. The effect of flowing time (or called 'residence time') of the $scCO_2$ in the microchannel is reflected by the data of ΔL for $Q_{scCO2} = 50\ \mu L/min$ which have been fitted into a linear straight line. Generally, the $scCO_2$ drops have a short flowing time in the channel under a small Q_{scCO2}/Q_{H2O}, thus the shrinkage in terms of drop length reductions is less significant for such small Q_{scCO2}/Q_{H2O}. However, the differences between various Q_{scCO2}/Q_{H2O} under a constant total flow rate $Q_{scCO2} + Q_{H2O} = 100\ \mu L/min$ are less obvious. ΔL for all the studied Q_{scCO2}/Q_{H2O} when $Q_{scCO2} + Q_{H2O} = 100\ \mu L/min$, as shown by the solid squares in Figure 6.6, can be averaged into a constant $\Delta L = 115\ \mu m$ with a standard error of 3.4 µm. This averaged total drop length reduction is consistent with the averaged length reductions of liquid CO_2 drops, as shown in Figure 5.8, both of which may be attributed to the approximately similar flowing time of the scCO2 drops among various Q_{scCO2}/Q_{H2O}. Therefore, Figure 6.6, to a

147

certain extent, verified the importance of flowing time on the shrinkage resulted from the dissolution-diffusion mechanism.

Other than drop flowing time, surface-volume ratio of the $scCO_2$ drops is the other important factor which could result in distinct shrinkage phenomenon. The effect of this factor can be reflected by a relative shrinkage of the $scCO_2$ drops, i.e., the drop length reductions relative to the original drop length (immediately after drops' generations), as expressed by $\Delta L/L_1$. Based on this inference and Figure 6.4 and 6.6, $\Delta L/L_1$ for the two groups of flow rate conditions has been plotted in Figure 6.7. Although ΔL as an overall absolute drop length reduction can be averaged as a constant for various Q_{scCO2}/Q_{H2O} under $Q_{scCO2} + Q_{H2O} = 100\ \mu L/min$, it leads to completely different $\Delta L/L_1$ when the original size of the generated $scCO_2$ drop is introduced. As shown by Figure 6.7, increasing Q_{scCO2}/Q_{H2O} leads to decreasing $\Delta L/L_1$ in an almost linear way for $Q_{scCO2} + Q_{H2O} = 100\ \mu L/min$. However, the tendency of $\Delta L/L_1$ with Q_{scCO2}/Q_{H2O} is a reverse one for $Q_{scCO2} = 50\ \mu L/min$, as shown by the hollow squares labelled data compared with solid squares denoted data points. The former tendency may be due to the flow rate ratio resulted $scCO_2$ drop size.
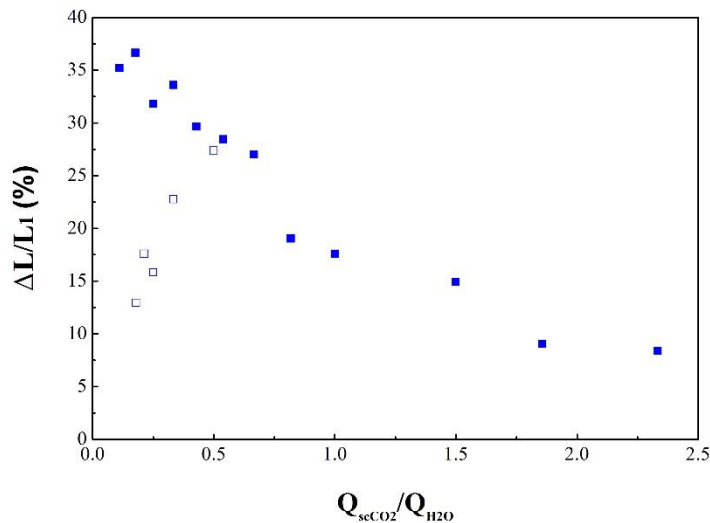
Figure 6.7 Relative overall length reductions ($\Delta L/L_1$) of $scCO_2$ drops versus flow rate ratios Q_{scCO2}/Q_{H2O}. Solid squares: $Q_{scCO2} + Q_{H2O} = 100\mu L/min$; hollow squares: $Q_{scCO2} = 50\mu L/min$.

The surface-volume ratio difference shows evidence to the relative drop length reduction, i.e., smaller drops featured with higher surface-volume ratios resulted from low Q_{scCO2}/Q_{H2O} are very likely to experience a significant relative drop length reduction, as shown by the solid squares in

148

Figure 6.7. Note that the conclusion made here is based on a similar flowing time of these drops under a constant total flow rate. On the other hand, when the flowing time of the drops are very different among one another, the factor of surface-volume ratio is no longer a primary role in determining the relative drop length reductions, instead, the drops which may have a longer flowing time at a higher Q_{scCO2}/Q_{H2O} will be characterized by a higher $\Delta L/L_1$, as shown by the hollow squares denoted data for $Q_{scCO2} = 50$ µL/min in Figure 6.7.

6.3.3 Surface-Volume Ratios of scCO$_2$ Drops

As discussed in previous section, surface-volume (S/V) ratio is one of the two parameters that may control the interfacial mass transfer between the scCO$_2$ drops and the continuously flowing water, especially when the flowing time of those drops are similar as a result of a constant total flow rate, as shown by the data points denoted by solid squares in Figure 6.7. Thus, it is necessary to quantify the surface-volume ratio of the scCO$_2$ drop at the three specified positions in the microchannel, which can be done based on equation (5.24) and (5.25). The channel geometry is the same as that has been applied for liquid CO$_2$ study in Chapter 5, i.e., the channel width and depth are 150 µm and 100 µm, respectively. In addition, the dynamic contact angle can be measured from the video frames (such as that shown in Figure 6.3) in which the drop meniscuses including the front and the back ones appear. Here, an average contact angle $\theta_c = (141\pm1.2)°$ having been measured from six representative frames at the drop meniscus is going to be used. Therefore, equation (5.24) and (5.25) can be specified for the scCO$_2$ drops in the microchannel as follows

$$A \ (\mu m^2) = 432.2 \cdot L_x + 2412, \tag{6.1}$$

and

$$V \ (\mu m^3) = 12978 \cdot L_x + 82260. \tag{6.2}$$

Thus, the surface-volume ratio S/V can be determined by

$$S/V \ (mm^{-1}) = \frac{A}{V} \times 10^3 = \frac{432.2 \cdot L_x + 2412}{12978 \cdot L_x + 82260} \times 10^3. \tag{6.3}$$

in which L_x (x = 1, 2, 3) indicates the scCO$_2$ drop length at the three specified positions. The calculated S/V of the drop at position 1, position 2 and position 3 have been plotted in Figure 6.8. For a single scCO$_2$ travelling from position 1 to 2 and down to 3, the S/V may slightly decrease during the shrinkage process, however, this decrease trend can be hardly seen when drops are very long (i.e., L/W is large) at a high flow rate ratio, as shown by those when $Q_{scCO2}/Q_{H2O} > 1$.

149
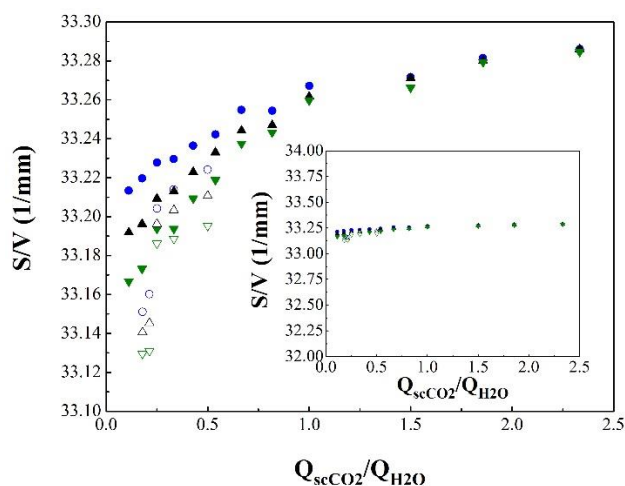
Figure 6.8 Surface-volume ratios (S/V) of scCO$_2$ drops at three specified positions in the straight channel against Q$_{scCO2}$/Q$_{H2O}$. Symbol meanings: circles – S/V at position 1, S/V-1; up triangles – S/V at position 2, S/V-2; down triangles – S/V at position 3, S/V-3. Solid and hollow symbols denote the data points for Q$_{scCO2}$ + Q$_{H2O}$ = 100µL/min and Q$_{scCO2}$ = 50µL/min, respectively.

For Q$_{scCO2}$ + Q$_{H2O}$ = 100 µL/min, S/V at one specific position of the three positions tends to increase slightly as the drops are elongated as a result of the increasing Q$_{scCO2}$/Q$_{H2O}$ from 0.1 to 2.3. This tendency of S/V is reverse, however, to the variations of the relative drop length reduction (ΔL/ L$_1$) with Q$_{scCO2}$/Q$_{H2O}$ in Figure 6.7. For Q$_{scCO2}$ = 50 µL/min, there exist similar tendencies of the S/V at one specific position and with the increasing Q$_{scCO2}$/Q$_{H2O}$. Nevertheless, for both groups of flow rate conditions, the overall variations of S/V at different Q$_{scCO2}$/Q$_{H2O}$ are very subtle among all the investigated cases. As shown by the inset in Figure 6.8, the S/V for all scCO$_2$ drops has a mean value of 33.25 mm^{-1} approximately. As a result, the shrinkage of scCO$_2$ drops is unlikely to be related to the surface-volume ratio. Therefore, the flowing time which can be determined by the flow speed of the scCO$_2$ drops in the channel might have dominated over S/V in controlling the shrinkage performance. Generally, those drops having a longer flowing time (i.e., the drops produced by a high Q$_{scCO2}$/Q$_{H2O}$) could have a more significant shrinkage characterized by a larger ΔL/L$_1$, as shown by the hollow squares in Figure 6.7.

6.3.4 scCO$_2$ Drop Speeds and Flowing Time

The roles of surface-volume ratio (S/V) and flowing time (t$_{flowing}$) in influencing the hydrodynamic shrinkage of the scCO$_2$ drops have been briefly introduced in previous two sub-sections. The S/V

150

values of the $scCO_2$ drops at all the studied flow conditions have been calculated and discussed as well. In this sub-section, the flowing time ($t_{flowing}$) of drops in the straight channel will be determined and discussed. According to equations from (5.32) to (5.35), the $scCO_2$ drop speed at the three positions can be measured, so does the standard deviation of the mean speed of the drops at one specific position. The measured $scCO_2$ drop speeds as well as the errors expressed by one standard deviation are plotted against the flow conditions in Figure 6.9, in which the speed at position 1, position 2 and position 3 is designated by V_1, V_2 and V_3, respectively.
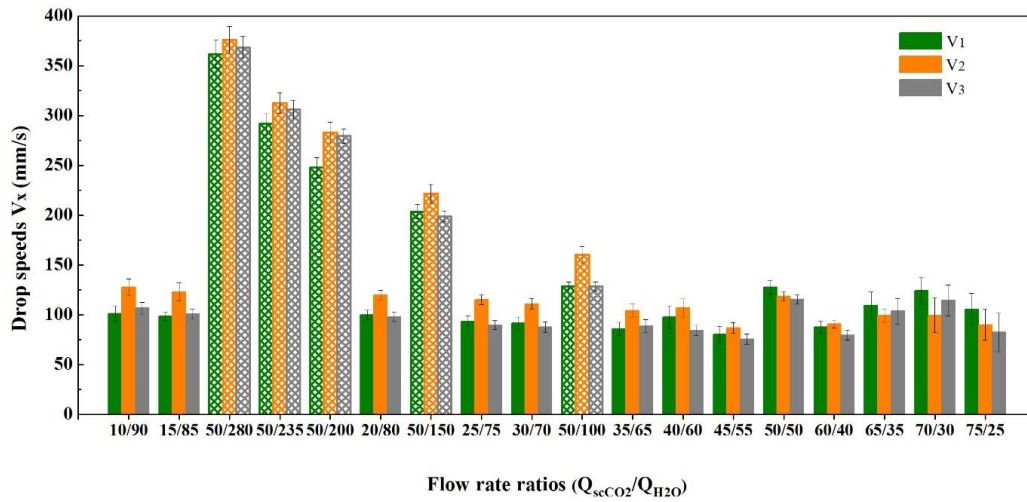
Figure 6.9 (Color in electronic version) Histogram of the $scCO_2$ drop speed at the three specified positions. V_1, V_2 and V_3 indicate the drop speeds at position 1, position 2 and position 3, respectively. Meshed histograms show the speed values of the group $Q_{scCO2} = 50\ \mu L/min$; solid ones show those at $Q_{scCO2} + Q_{H2O} = 100\ \mu L/min$. Error bar indicates one standard deviation of the mean speed value.

For the cases at $Q_{scCO2} + Q_{H2O} = 100\ \mu L/min$, the drop speeds at different Q_{scCO2}/Q_{H2O} are overall consistent with each other at a level of 100 mm/s. One interesting phenomenon is that eight cases which are characterized by $Q_{scCO2}/Q_{H2O} < 50/50$ are featured with an increasing-decreasing trend of the speed from position 1 to 2 and down to 3, i.e., $V_1 < V_2$ and $V_2 > V3$. The first increasing trend from V_1 to V_2 is due to the flow instabilities of the continuously flowing water at the T-junction, where the occupancy of $scCO_2$ in the T-junction blocks the water flow to certain extents, especially when the water flow rate is higher than that of $scCO_2$ stream the generated $scCO_2$ drops are not sufficiently advanced by the water stream. Thus its absolute speed will not be fully developed at

position 1. However, as the water flow regains its flow profile (very much likely a parabolic one) further downstream after passing through position 1, the scCO$_2$ drop will be more carried by the water with the speed increased. When the scCO$_2$ drop travels further downstream from position 2 to position 3, it will be dampened thanks to the viscous force between water and the drops, particularly in the thin films that separate the drops from touching the channel wall. Thus, there should be a decreasing development from position 2 to position 3, as shown by $V_2 > V_3$.

For cases $Q_{scCO2} = 50$ µL/min, as Q_{scCO2}/Q_{H2O} is decreased from 50/50 down to 50/280, there exists a same trend of increasing-decreasing of the drop speed from position 1 to 2 and to 3, though the differences between V_1 and V_2 as well as V_2 and V_3 may be not very consistent. During the decreasing development of Q_{scCO2}/Q_{H2O}, scCO$_2$ drop speeds at all three positions are increased almost in a linear way. When Q_{scCO2}/Q_{H2O} is lower than 50/200, the drop speeds are measured to be approximately 300 mm/s and even beyond. As observed in Figure 6.3, scCO$_2$ is not able to fully block the water stream in the T-junction any more, and the drop generations start to enter into a dripping regime where the shear stress becomes a prominent factor in pinching off the scCO$_2$ stream relative to the interfacial tension. The generated scCO$_2$ drops are very small, which have a characteristic length approximating to the channel width, i.e., $L_1/W \sim 1$. Another effect of such high drop speeds in the channel is that the flowing time of the scCO$_2$ becomes very short (less than 50 ms), The shortened flow time may not be enough for a visible drop length reduction which also tremendously undermines the potential of S/V in producing significant drop shrinkage.

In addition to the drop speed shown in Figure 6.9, the exact total flowing time ($t_{flowing}$) of the scCO$_2$ drops in the straight channel can be determined based on an average drop speed ($\bar{v}$) from those three speeds at the specified positions, i.e.,

$$\bar{v} = \frac{1}{3}\sum_{x=1}^{3} v_x, \tag{6.4}$$

$$s_{\bar{v}} = \sqrt{\frac{1}{3-1}\sum_{x=1}^{3}(v_x - \bar{v})^2} \,, \qquad x = 1, 2 \text{ or } 3, \tag{6.5}$$

in which $s_{\bar{v}}$ indicates the standard deviation calculated for $\bar{v}$. The total length of the straight channel (L_t) is 14.7 mm, however, a real total flowing channel length $L_t^{'}$ starting from position 1 to the very end of the channel should be applied to calculate the flowing time (see Table 5-1), as shown below,

$$t_{flowing} = \frac{L_t^{'}}{\bar{v}}. \tag{6.6}$$

Since $\bar{v}$ has a standard deviation of $s_{\bar{v}}$, as a function of $\bar{v}$, $t_{flowing}$ may have a standard deviation $s_{t_{flowing}}$ according to error propagation theory, which can be calculated as follows

$$s_{t_{flowing}} = \left| -\frac{L'_t}{\bar{v}^2} \right| s_{\bar{v}}. \tag{6.7}$$

Based on the above equations, average drop speeds in the straight channel are determined first, and consequently, the drop flowing time in the real total channel length are calculated. These two parameters have been plotted against the flow conditions in Figure 6.10 for both $Q_{scCO2} + Q_{H2O} = 100$ µL/min and $Q_{scCO2} = 50$ µL/min.
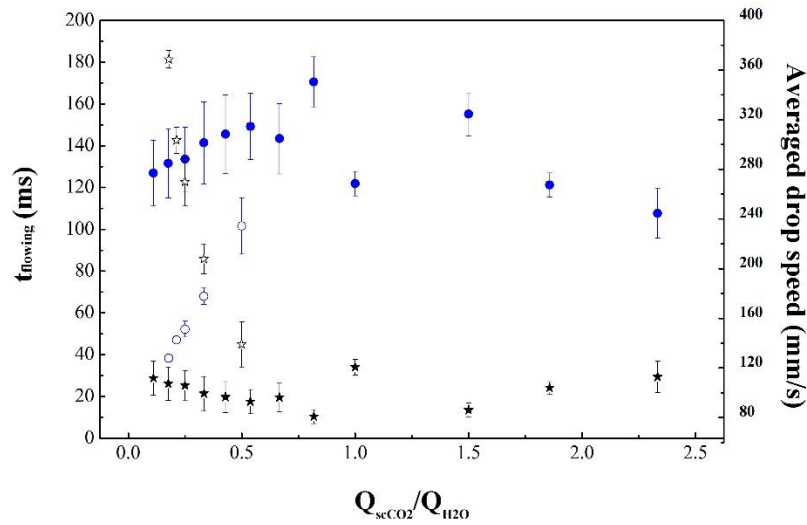
Figure 6.10 Flowing time of scCO$_2$ drops in the straight channel based on averaged drop speeds as characteristic drop speeds for specific Q_{scCO2}/Q_{H2O}. Circles: flow time $t_{flowing}$; stars: averaged drop speeds. Solid symbols: $Q_{scCO2} + Q_{H2O} = 100$µL/min; hollow symbols: $Q_{scCO2} = 50$µL/min. Error bar indicates one standard deviation of the mean value.

Overall, the average drop speeds at $Q_{scCO2} + Q_{H2O} = 100$ µL/min are at a level of 100 mm/s and it seems there exists a concave-like tendency line from left to right as Q_{scCO2}/Q_{H2O} increases from 0.1 to 2.3, i.e., the characteristic drop speeds approximated by the average drop speeds are declining as Q_{scCO2}/Q_{H2O} increases from 0.1 to 1 due to lowered Q_{H2O} and then maintain a constant value as Q_{scCO2} starts to contribute into the average drop speeds. As a result, the calculated drop flowing time $t_{flowing}$ are featured by a convex-like tendency line, as reverse relative to the average drop speeds. The contrary trend between $t_{flowing}$ and $\bar{v}$ reveals that the total channel length plays a less important role than the average drop speed, though the real overall flowing channel length L_t' is applied. This result

is also reflected by the data at $Q_{scCO2} = 50$ µL/min, in which the $t_{flowing}$ is linearly shortened from 101 ms to 38 ms as $\bar{v}$ is linearly increased from 140 mm/s to 360 mm/s. Relying on these calculated drop flowing time, the mass transfer coefficient k_d that characterizes the hydrodynamic shrinkage process of the scCO$_2$ drops in the straight channel can be determined, which is achieved by the specific model in section 5.2 of Chapter 5, as shown by equation (5.26).

6.3.5 Mass Transfer Coefficient (k_d) Based on Drop Length and Flowing Time

Based on the aforementioned scCO$_2$ drop lengths at position 1 (L_1) and position 3 (L_3) and the flowing time ($t_{flowing}$) of the scCO$_2$ drops in the straight channel, the solute-side mass transfer coefficient (k_d) can be determined according to equation (5.26). The channel width (W) and depth (D) are 150µm and 100µm, respectively. The nominal molar concentration (C_d) can be calculated as the ratio of scCO$_2$ density (ρ_{scCO2}) and molecular weight (M) of CO$_2$, i.e., $C_d = \rho_{scCO2}/M$, see Table 6-1. The equilibrium CO$_2$ concentration ($C_e = (1.153\pm0.005)$ mol/L) at an assumed sharp interface (a saturation scenario) is referred to a constant temperature (T = 313K) and the pressures ranging from 8,185 kPa ~ 8,284 kPa, which is mainly determined using a linear difference method [400]. A final parameter, namely, contact angle (θ_c) is $(141 \pm 1.2)°$. Therefore, equation (5.26) can be specified as

$$k_d \text{ (µm/ms)} = 30.03 \frac{C_d}{C_d - 1.153} \left(\ln \frac{432.2 \cdot L_1 + 2412}{432.2 \cdot L_3 + 2412}\right) \cdot \frac{1}{t_{flowing}}. \tag{6.8}$$

In addition, the standard deviations of k_d (s_{k_d}) as a function of L_1, L_3 and $t_{flowing}$ are determined based on the respective standard deviations of these three parameters either from the measurements or the calculation, namely, s_{L_1}, s_{L_3} and $s_{t_{flowing}}$ (see Figure 6.7), which are shown below

$$s_{k_d} = \sqrt{\left(\frac{\partial k_d}{\partial L_1}\right)^2 s_{L_1}^{~2} + \left(\frac{\partial k_d}{\partial L_3}\right)^2 s_{L_3}^{~2} + \left(\frac{\partial k_d}{\partial t_{flowing}}\right)^2 s_{t_{flowing}}^{~2}}. \tag{6.9}$$

Table 6-1a Nominal molar concentrations (C_d) of scCO$_2$ calculated by ρ_{scCO2}/M. M = 44 kg/kmol.

Q_{scCO2}/Q_{H2O}	10/90	15/85	50/280	50/235	50/200	20/80	50/150	25/75	30/70	50/100
P_{H2O} (kPa)	7897	7890	7940	7930	7923	7887	7909	7884	7878	7898
P_{scCO2} (kPa)	8260	8255	8284	8280	8276	8255	8268	8255	8251	8260
ρ_{H2O} (kg/m^3)	995.75	995.75	995.75	995.75	995.75	995.75	995.75	995.75	995.75	995.75
ρ_{scCO2} (kg/m^3)	311.75	311	315.4	314.78	314.17	311	312.95	311	310.4	311.75
C_d (mol/L)	7.085	7.068	7.168	7.154	7.140	7.068	7.113	7.068	7.055	7.085

Table 6-1b Nominal molar concentrations (C_d) of $scCO_2$ calculated as ρ_{scCO2}/M. M = 44 kg/kmol.

Q_{scCO2}/Q_{H2O}	35/65	40/60	45/55	50/50	60/40	65/35	70/30
P_{H2O} (kPa)	7871	7867	7858	7776	7811	7822	7836
P_{scCO2} (kPa)	8247	8246	8242	8185	8210	8217	8225
ρ_{H2O} (kg/m^3)	995.75	995.75	995.75	995.75	995.75	995.75	995.75
ρ_{scCO2} (kg/m^3)	309.81	309.66	309.07	300.97	304.46	305.45	306.6
C_d (mol/L)	7.041	7.038	7.024	6.840	6.920	6.942	6.968

Based on the $scCO_2$ drop lengths at position 1 and position 3, C_d and $t_{flowing}$ of $scCO_2$ drops in the channel, the mass transfer coefficient k_d are calculated by equation (6.8) and are plotted to all the flow conditions, as shown in Figure 6.11(A). For $Q_{scCO2} + Q_{H2O} = 100$ µL/min, the flowing time ($t_{flowing}$) of $scCO_2$ resulting from various Q_{scCO2}/Q_{H2O} are characterized by a mean value of 137.35 ms with a 4.94 standard error (see Figure 6.10). However, the mass transfer coefficient k_d tends to develop with increasing Q_{scCO2}/Q_{H2O} in a negative logarithmic way, as shown by the solid line in Figure 6.11(A). This result is comprehendible since k_d is determined based on equation (6.8) in which the drop length L_1 and L_3 determine k_d when $t_{flowing}$ is almost a constant. On the other hand, the drop lengths at position 1 and 3 originate from the flow rate ratios. Thus, there could be a logarithmic relation between k_d and Q_{scCO2}/Q_{H2O}, which may be interpreted by the relative drop length reduction (see Figure 6.7) at a rather constant surface-volume ratio (see the inset in Figure 6.8). It can be found that when the surface-volume ratios of $scCO_2$ drops in the straight channel are close, the flowing time (or the drop speed) is more likely to control the hydrodynamic shrinkage performance, as quantified by the mass transfer coefficient. For $Q_{scCO2} = 50$ µL/min, different Q_{H2O} lead to different Q_{scCO2}/Q_{H2O} as well as significantly different $t_{flowing}$. From $Q_{H2O} = 50$ µL/min to $Q_{H2O} = 100$ µL/min and up to $Q_{H2O} = 150$ µL/min, $t_{flowing}$ is decreased continuously from 122 ms to 101.6 ms and down to 68 ms, and at the same time, surface-volume ratios of the produced $scCO_2$ drops do not change substantially (less than 0.1 mm^{-1}, see Figure 6.8). As a result of the decreasing $t_{flowing}$, k_d has been increased from 57 µm/s to 133 µm/s. However, as Q_{H2O} further increases from 150 µL/min up to 280 µL/min, k_d starts to oscillate at a level of 130 µm/s despite of further decreasing $t_{flowing}$. This peak indicates that a critical $t_{flowing}$ (viz, a critical drop speed $\bar{v}$) may exist beyond which the dissolution-diffusion through interface will not result in any significant drop shrinkages due to a much too short flowing time (or residence time) in the straight channel, given that the S/V of the generated drops are still constant.

The effect of $t_{flowing}$ when surface-volume ratios are on a same level can be perceived by the fitting curve in Figure 6.11(A).

(A)   (B)
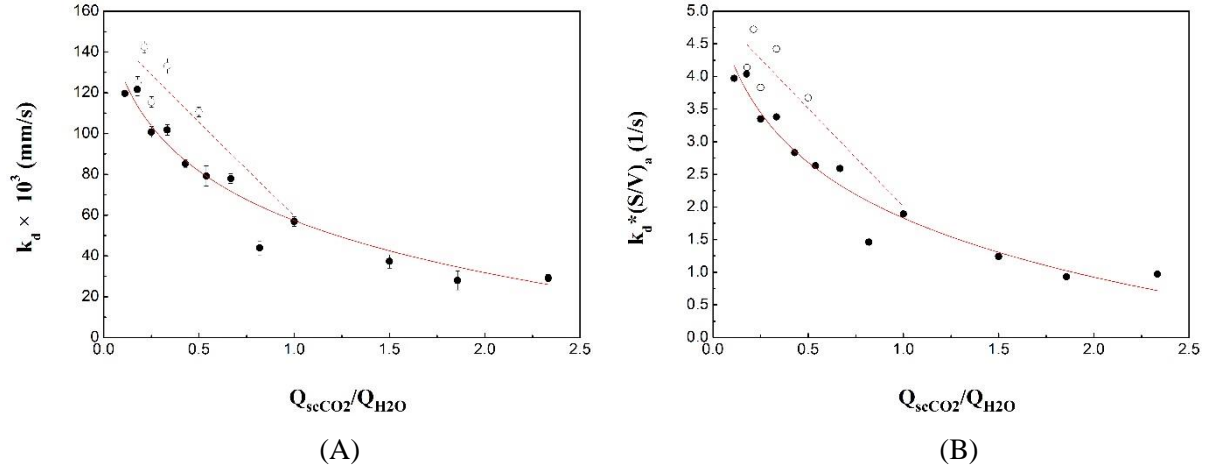
Figure 6.11 Mass transfer coefficients k_d (A) and volumetric mass transfer coefficients '$k_d*(S/V)_a$'
(B) of $scCO_2$ drops in the straight channel. Solid circles: $Q_{scCO2} + Q_{H2O} = 100$ µL/min
(except $Q_{scCO2}/Q_{H2O} = 70/30$ which results in no observable $scCO_2$ segments); hollow
circles: $Q_{scCO2} = 50$ µL/min. Error bar: one standard deviation of k_d calculated from
equation (6.9). Fitting curves are added only for discussion convenience.

In addition to k_d, the so-called volumetric mass transfer coefficient $k_d \cdot (S/V)$ can also be obtained
since surface-volume ratios are known. In order to derive a characteristic surface-volume ratio of the
$scCO_2$ under a specific flow rate condition (i.e., Q_{scCO2}/Q_{H2O}), an averaged S/V from the three S/V in
Figure 6.8 will be applied to calculate $k_d \cdot (S/V)$, which is designated as $(S/V)_a$. The calculated
volumetric mass transfer coefficient, namely, $k_d \cdot (S/V)_a$, have been plotted in Figure 6.11(B). Overall,
the correlations of $k_d \cdot (S/V)_a$ with flow conditions are analogous to those in Figure 6.11(A). For Q_{scCO2}
$+ Q_{H2O} = 100$ µL/min, the flowing time $t_{flowing}$ rather than surface-volume ratio might be the primary
factor in controlling the mass transfer from $scCO_2$ drops to the continuously flowing water through
interface,; and for $Q_{scCO2} = 50$ µL/min, the effect of $t_{flowing}$ (or say, drop speed $\bar{v}$) is more evidenced
and profound in governing the mass transport. And there could be a critical $t_{flowing}$ (or a critical drop
speed) below which (or beyond which) no significant drop shrinkage will be resulted.

6.3.6 Estimate of Total Pressure Drop and Its Effect on Volume Change

Analogous to the calculations of pressure drops for liquid CO_2 drops in the straight microchannel,
total pressure drops of $scCO_2$ in the straight channel can also be calculated according to equation

(5.27). From Figure 5.11(A), a low Q_{LCO2}/Q_{H2O} usually leads to a slightly higher total pressure drop ΔP_t; and as discussed in section 5.5.3 in Chapter 5, the total pressure drop is dominated by the single phase flow of the continuously flowing water, i.e., the first term on the right hand side of equation (5.27). Therefore, instead of calculating all the total pressure drop for all the flow conditions, the one which could cause the most significant pressure drop among all flow cases is chosen to be calculated here in this chapter. And all others will be characterized with the pressure drops lower than that of the chosen case. As shown by equation (5.27), this case should be the one which is characterized by a fastest flow velocity of the continuously flowing water. Thus the case $Q_{scCO2}/Q_{H2O} = 50/280$ is chosen for a pressure drop calculation example. Within the applied microchannel (W = 150 µm, D = 100 µm), the water slugs under this case will be of a mean velocity $\overline{v}_c = (Q_{scCO2} + Q_{H2O})/(W \cdot D) \approx 366.7$ mm/s. The viscosity (η_c) of water is approximately 655.5 µPa·s referring to a temperature of 40 °C and pressures ranging from 7,776 kPa to 7,936 kPa. Therefore, the total pressure drop ΔP_t will be

$$\Delta P_t = L_t \frac{32\eta_c\overline{v}_c}{(2R_h)^2}, \tag{6.10}$$

in which L_t (L_t = 14.7 mm) is the nominal total channel length; R_h is the hydrodynamic radius (R_h = 120 µm) of the rectangular channel. Based on these parameters, ΔP_t is calculated as 7.7 kPa. According to the Peng-Robinson's Eos, the equation set for $scCO_2$ at a temperature of 40 °C can be specified as below

$$\begin{cases} P_0 = \dfrac{RT}{V_{m0}-2.6659\times10^{-5}} - \dfrac{3.8797\times10^{-1}}{V_{m0}{}^2+5.3318\times10^{-5}V_{m0}-7.107\times10^{-10}}, \\ P_t = \dfrac{RT}{V_{mt}-2.6659\times10^{-5}} - \dfrac{3.8797\times10^{-1}}{V_{mt}{}^2+5.3318\times10^{-5}V_{mt}-7.107\times10^{-10}}, \\ \qquad\qquad\qquad \text{and } \Delta P_t = P_0 - P_t. \end{cases} \tag{6.11}$$

in which R is the gas constant and R = 8.31446 J/(mol·K); T = 313.15 K is the temperature. For the case $Q_{scCO2}/Q_{H2O} = 50/280$, P_0 is estimated from the CO_2 syringe pump, and P_0 = 8,284 kPa, thus P_t = 8276.3 kPa. Substitute P_0 and P_t into equation set (6.11), V_{mo} and V_{mt} are calculated to be 231.8 mL/mol and 232.2 mL/mol, respectively. According to equation (5.29), the relative volume change of the $scCO_2$ drop as a consequence of this total pressure drop can be calculate as

$$\Delta V_t/V_0 = N \cdot \Delta V_{mt}/V_0 = N \cdot (V_{mt} - V_{m0})/(N \cdot V_{m0}) = \frac{V_{mt}}{V_{m0}} - 1 \approx 1.49\text{‰}. \tag{6.12}$$

Although the effect of total pressure drop on $scCO_2$ drops are times higher than that on liquid CO_2 drops (see Figure 5.12(B)), it is still a small quantity compared with relative length reductions as shown in Figure 6.7. Therefore, the pressure drop effect on $scCO_2$ drop volume change can be

neglected, and the drop shrinkages are attributed to the mass transfer through the interface of the scCO$_2$ drop and the continuously flowing water.

6.4 Conclusion

As a follow-up study to Chapter 5, the hydrodynamic shrinkage of scCO$_2$ drops (or segments) in a straight microchannel has been experimentally studied in this chapter. The same microchip featured with a micro T-junction is used to produced scCO$_2$ drops. The hydrodynamic parameters including the size and the speed of the scCO$_2$ drop at three specified positions in the straight channel (total length = 14.7 mm) are measured. The experimental methodologies are mostly analogous to the ones in Chapter 5, but in this chapter, the procedures regarding the applications of even higher pressures and a temperature control are focused, as shown in section 6.2. Main results are summarized below:

◆ Correlation of the size of the generated scCO$_2$ drop at the T-junction indicates an even more significant effect of the elongating time on the final size of scCO$_2$ drop than that when liquid CO$_2$ is involved. This is reflected by the factor (3.62 in this chapter for scCO$_2$ drops) of the flow rate ratio.

◆ Based on measured drop sizes at position 1, 2 and 3, drop reductions from position 1 to position 2 and those from positon 2 to 3 are calculated, which reveal the hydrodynamic shrinkage of scCO$_2$ in the flowing path, as shown by the relative drop length reductions in Figure 6.7. The different behaviors for two groups of flow conditions, i.e., a constant total flow rate (Q_{scCO2} + Q_{H2O} = 100 µL/min) and a constant flow rate of scCO$_2$ (Q_{scCO2} = 50 µL/min) as a result of the flow rate ratio (Q_{scCO2}/Q_{H2O}) reveal that surface-volume ratios of the scCO$_2$ drops and the flowing time of the drops in the channel are the two main factors which controls the mass transfer resulted drop shrinkage.

◆ Surface-volume ratios and flowing time of scCO$_2$ drops in the straight channel are detailed. The tendency of relative drop length reduction characterized shrinkage with Q_{scCO2}/Q_{H2O} at Q_{scCO2} + Q_{H2O} = 100 µL/min may be more correlated with the flowing time of those scCO$_2$ drops at various Q_{scCO2}/Q_{H2O}, given that surface-volume ratios of those scCO$_2$ drops are similar among different flow conditions. More profoundly, the flowing time development with Q_{scCO2}/Q_{H2O} at the condition Q_{scCO2} = 50 µL/min justifies its dominant role in controlling the drop shrinkage phenomenon at a constant flow rate of scCO$_2$.

◆ Mass transfer coefficient k_d and volumetric transfer coefficient $k_d*(S/V)_a$ are calculated based on the mathematical model developed in Chapter 5. From the k_d data, it can be concluded that when surface-volume ratios of scCO$_2$ drops in the straight channel are similar, the flowing time is more likely to control the hydrodynamic shrinkage performance; as shown by the scenario $Q_{scCO2} = 50$ µL/min, the importance of flowing time in controlling the mass transport is justified, and there could be a critical drop flowing time (or critical drop speed) below which (or beyond which) no significant drop shrinkage will be resulted.

◆ The total pressure drop due to segmented flows in the straight microchannel is estimated, and its effect on drop volume change is quantified by using the same method as that in Chapter 5. The relative volume change thanks to the total pressure drop is no larger than 1.49‰ for all the flow cases studied. Therefore, drop shrinkages observed in this chapter can be confidently attributed to the mass transfer between the scCO$_2$ drops and the continuously flowing water which mainly occurs through the interface of these two fluids.

Chapter 7

Numerical Studies on Hydrodynamics of Single Liquid and Super-critical CO_2 Drop Flowing in Microchannel

Following the experimental studies of the hydrodynamic shrinkage of liquid and super-critical CO_2 ($scCO_2$) drops in the straight microchannel, as introduced in previous two chapters, this chapter is dedicated to preliminary CFD (computational fluid dynamics) studies of one single liquid CO_2 drop and one single $scCO_2$ drop traveling in a straight microchannel with water simultaneously. Despite various results can be shown from numerical simulations, issues such as drop profile, thin film, flow fields within single CO_2 drop as well as at the interface and interfacial distributions of CO_2 subjected to diffusion and flow streams in the interfacial regions are analyzed and discussed.

7.1 Introduction

Microfluidic geometries and fluid segments have always been characterized by large surface-volume ratios and short transfer distances among other merits, which may enhance heat and mass transfer. As two-phase flows involving gas-liquid and liquid-liquid are considered in the microscale devices, they are mostly characterized by an interface that separates one from the other. Thus, interfacial effects (e.g., interfacial tension, contact angle) start to dominate the flow behaviors (e.g., flow regimes) and topological changes (e.g., breakup or coalescence) relative to other factors, such as inertial and gravitational forces. Among all possible flow regimes, as introduced in Chapter 4, slug flows (may also be called 'segmented flow' or 'Taylor flow') have become one of the most studied patterns in experimental and numerical simulation studies, in terms of the flow pattern, flow fields in slugs, slug profiles, thin film thicknesses and effects etc. Compared with experiments, numerical simulations are much less implemented to study the two-phase microflows, which may be mainly due to the time consumption and not-fully developed numerical methods. However, rapid developments in computational methods and equipment have promoted the applications of numerical methods in two-phase microflow simulations, especially the interface involved and resolved ones over the last two decades [208,401-404].

Interface resolving is required in numerical simulations of slug flows in which the interface is often unsteady and deformable. Thus a numerical method for chosen to be used must be able to resolve interface evolution spatially and temporally, such as one among moving-grid and front-tracking in Lagrangian types or volume of fluid (VOF) and level-set (LS) in Eulerian types [404]. Moreover,

based on a continuum assumption of the discussed matter where the Knudsen number ($K_n = \lambda/L$, λ and L indicate a mean free path of molecules and a characteristic length, respectively) is extremely small (below 0.001), general governing equations of transport phenomena including the continuity equation, the momentum equation and energy equation are applicable to both phases as well as the interface on a micro length scale (i.e., tens to hundreds of microns) [403]. In the scope of continuum assumption, the interface can be described by either a zero thickness (i.e., sharp interface) or a non-zero thickness, for the former scenario there exist methods such as interface reconstruction VOF, LS, and front-tracking, and for the latter scenario methods may include color function VOF, conservation LS and phase-field. Detailed descriptions of the methods are referred to a review by Wörner [403].

Most of the above mentioned methods have been applied in numerical studies on slug flows in microchannel (mostly, the ones of circular cross sections). For example, Taha and Cui [207] used piece linear interface calculation (PLIC) (for interface reconstruction) based VOF for studying the hydrodynamics of long gas bubbles in capillaries. A similar strategy combined with a continuum surface force (CSF) model for modeling surface tension effects was applied by Gupta et al. [402] in simulating Taylor flows in horizontal microchannels. Fukagata et al. [405] numerically studied Taylor flow with a presence of heat transfer in a two-dimensional and axisymmetric tube using LS method. A phase-field method was utilized by He et al. [406] to probe the bubble shape, superficial velocities of gas and liquid in a two-dimensional and axisymmetric channel for gas-liquid two phase flows. Another popularly used method, Lattice-Boltzmann method was used by Yu et al. [407] in their numerical part study of gas-liquid flow in rectangular microchannels.

However, as argued by Wörner [403], Talimi et al. [208] and Falconi et al. [408], much fewer studies are dedicated to the slug flow in non-circular channels, such as rectangular or even triangular ones, which, however, have intrigued much attention in experimental studies, as reviewed in Chapter 2. The mass transfer across the interface in slug flows has become a promising mechanism for liquid extraction and phase separation [409]. And numerical methods can be applied to reveal the interphase mass transfer with and without reactions. Schuster et al. [410] computationally studied gas-liquid two-phase flow in mini/micro scale channels and the interphase mass transport in both a falling film and membrane reactor configurations with finite element method based software package FEMLAB (later known as COMSOL). Di Miceli Raimondi et al. [411] implemented direct two-dimensional simulations (self-developed codes called JADIM) in studying the mass transfer of liquid-liquid slug flow in square microchannel subjected to various flow velocities and channel geometries. Shao et al. [412] used COMSOL for simulations of chemical CO_2 adsorption to an alkaline solution in a gas-

liquid Taylor flow in capillaries, both a physical absorption and a chemical absorption at the interface were analyzed and compared in terms of absorption fraction and volumetric mass transfer coefficient. PLIC based VOF method was used by Onea et al. [413] and Kececi et al [414] in their three-dimensional simulations on mass transfer of upward and downward gas-liquid Taylor flow in rectangular microchannels.

In order to complement the experimental studies in Chapter 5 and Chapter 6, this chapter provides a numerical study on the hydrodynamics of both one single liquid CO_2 drop and one single $scCO_2$ drop in a long straight microchannel analogous to that applied in the experimental studies. Issues such as drop profile, thin film, flow fields and interfacial molar distribution subjected to diffusion effects and local convections at the interface are focused. In section 7.2, fundamentals of the numerical simulations regarding general assumptions and governing equations are introduced. The problems are formulated and the solution methods are detailed in section 7.3. In section 7.4, the results are shown and discussed. A final section 7.5 provided a conclusion of the simulation work.

7.2 Numerical Fundamentals

7.2.1 General Assumptions

Analogous to the configuration in experiments, liquid CO_2 and supercritical CO_2 are used as the drop phases, respectively. DI (de-ionized) water is the continuously flowing liquid in the microchannel. All fluids here are incompressible Newtonian fluids and are characterized by constant densities and viscosities. The problem is under an isothermal condition and the interfacial tension between CO_2 and water is constant as imported (thus Marangoni effects on the interface are not considered). Moreover, the interface between the CO_2 drop and water is a sharp interface, i.e., an interface with a zero thickness. In addition, gravitational forces are not considered, which can be rational based on the possible range of Bond number in the problem. Last but not least, the wettability of the channel wall is deemed uniform and steady, contact angles are constant and are implemented by referring to those in experiments.

7.2.2 Governing Equations

The CFD software FLUENT (Ansys Fluent 17.0) is used to carry out the simulations in this chapter. A finite volume based method is usually used in FLUENT to discretize the governing equations. In order for interface resolving, the volume of fluid (VOF) method is based on a fraction function of 'α'

in each cell which lies between 0 and 1. $\alpha = 1$ indicates the cell is full with one phase of interest; $\alpha = 0$ means the cell is full of the other phase; and one α falls in $0 < \alpha < 1$ indicates that the fluids co-exist in the cell. Thus the interface resolving is achieved based on a volume fraction equation (also called advection equation) of the main phase, as shown below

Volume fraction equation:

$$\frac{\partial \alpha_i}{\partial t} + \vec{u} \cdot \nabla \alpha_i = 0, \tag{7.1}$$

in which t is time and $\vec{u}$ is the velocity vector of the fluid. The volume fraction of the other phase will not be solved, instead, its volume fraction can be obtained based on

$$\sum_{i=1}^{2} \alpha_i = 1. \tag{7.2}$$

According to the assumptions of the fluids in section 7.2.1, such as Newtonian and incompressible, the continuity equation and the momentum equation can be applied to either or both of the two phases. Instead of an overall continuity equation, a convection-diffusion of the primary phase 'i' is introduced here and which can be written as

$$\frac{\partial}{\partial t}(\rho_i \alpha_i) + \nabla \cdot (\rho_i \alpha_i \vec{u}) = -\nabla \cdot \vec{J_i} + R_i, \tag{7.3}$$

where ρ_i is the density of i-phase, $\vec{J_i}$ is diffusion flux from phase i to the other phase through interface driven by concentration (and temperature as well) gradients, and R_i is the net production rate of phase i (or called specie 'i') due to chemical reaction. However, in this work, the chemical reaction is not considered, thus R_i is zero in equation (7.3). Further, $\vec{J_i}$ can be specified by a sum of mass diffusion and thermal diffusion. But here the thermal (or called Soret) diffusion is not considered based on an isothermal assumption, i.e., a uniform temperature distribution exists and there is no temperature gradient. Therefore, $\vec{J_i}$ may be specified under a dilute approximation (i.e., mass fraction of specie 'i' in the mixture region is much smaller than 1) as follows

$$\vec{J_i} = -D_{im} \nabla (\rho_i \alpha_i), \tag{7.4}$$

in which D_{im} is the mass diffusivity of specie 'i' in the mixture region. The form of equation (7.3) combined with equation (7.4) is applicable to the other phase as well since two phases are involved here, and their sum should result in a common overall continuity equation, as shown below

Overall continuity equation:

$$\frac{\partial}{\partial t}(\rho) + \nabla \cdot (\rho\vec{u}) = 0, \qquad (7.5)$$

in which ρ is the bulk density. Besides, a single momentum equation can be solved throughout the entire domain and the solved velocity field is shared among both phases. The momentum equation is detailed below

Momentum equation:

$$\frac{\partial}{\partial t}(\rho\vec{u}) + \nabla \cdot (\rho\vec{u}\vec{u}) = -\nabla P + \nabla \cdot [\mu(\nabla\vec{u} + \nabla\vec{u}^T)] + \rho\vec{g} + \vec{f}, \qquad (7.6)$$

where P is the pressure, μ is the bulk dynamic viscosity, $\vec{g}$ is the gravitational acceleration, and $\vec{f}$ is the volumetric interfacial force per unit area. On the right hand side of equation (7.6), the term $\mu(\nabla\vec{u} + \nabla\vec{u}^T)$ is the viscous stress tensor which may be designated as 'τ'.

Surface tension model

A surface tension model in FLUENT, namely, continuum surface force (CSF) treats surface tension as a source term in the momentum equation [415], as shown in equation (7.6). At the interface between the two phases, pressure difference across the interface is correlated to surface tension according to the Young-Laplace equation by

$$\Delta P = \sigma\left(\frac{1}{R_1 + R_2}\right) = \sigma\kappa, \qquad (7.7)$$

in which σ is the surface tension, ΔP is a capillary pressure induced by the surface tension, R_1 and R_2 are two principal radii of the interface, and κ indicates the curvature of the interface. If $\vec{n}$ is a surface normal at the interface, then it can be expressed as the gradient of the volume fraction (α_i) of the 'i' phase, as formulated below

$$\vec{n} = \nabla\alpha_i. \qquad (7.8)$$

Thus the unit normal $\hat{n}$ can be obtained and $\hat{n} = \frac{\vec{n}}{|\vec{n}|} = \frac{\nabla\alpha_i}{|\nabla\alpha_i|}$. Curvature κ is defined as the divergence of the unit normal $\hat{n}$, which can be expressed as follows

$$\kappa = \nabla \cdot \hat{n} = \nabla \cdot \left(\frac{\nabla\alpha_i}{|\nabla\alpha_i|}\right) = \frac{1}{|\nabla\alpha_i|}\nabla \cdot (\nabla\alpha_i) = \frac{1}{|\nabla\alpha_i|}\nabla^2\alpha_i = \frac{1}{|\nabla\alpha_i|}\Delta\alpha_i. \qquad (7.9)$$

in which Δ is a Laplace operator. When the two phases appear in the same cell, a volume force $\vec{f}$ can be resulted based on equation (7.7) – (7.9), and $\vec{f}$ is determined from below

$$\vec{f} = \sigma\kappa_i\nabla\alpha_i\delta. \tag{7.10}$$

where δ is a Dirac distribution correlated with the interface [403,408]. Note that equation (7.10) is only active in the interfacial region.

Fluid properties treatment:

Shown in equation (7.5) and (7.6), bulk density ρ and bulk dynamic viscosity μ are generally used in the continuity and the momentum equation, respectively. When the cell is purely filled by one phase 'i', the bulk density and viscosity are exactly the phase density and viscosity. However, in the interfacial region when the cell is filled with both phases, the bulk density ρ and the bulk viscosity μ are weighted by the volume fraction α and the mass fraction, respectively:

$$\rho = \sum_{i=1}^{2} \rho_i\,\alpha_i, \tag{7.11}$$

and

$$\mu = \sum_{i=1}^{2} \frac{\rho_i\alpha_i}{\rho}\mu_i, \tag{7.12}$$

where ρ_i and μ_i are the pure phase density and viscosity, respectively.

7.3 Problem Formulation

In this work, a two-dimensional (2D) computational domain for the flow field in a Cartesian coordinate system is considered, as shown in Figure 7.1. The computational domain falls into the group of a fixed frames type, as reported by [208]. Thus long CPU time are expected. The straight channel is horizontally oriented. A constant flow of water in terms of velocity ($\bar{v}_{H2O}$) starts from the inlet (boundary condition (B.C.) 1) on the left end, and the fluids will flow out of the channel eventually at the outlet on the right end (an outflow boundary, B.C. 3). The boundary conditions are fulfilled by the other two, i.e., B.C. 2 and B.C. 4, which are no slip walls.

Uniquely, none of the common geometries (e.g., T-junction, flow-focusing) for producing droplets is utilized in the simulation work here, instead, the to-be-investigated liquid CO_2 drop or $scCO_2$ drop is formed by marking a specific region located closely to the entrance area as an initialized CO_2 drop. The marked region (in a rectangular cuboid shape), at its left boundary, is 0.2 mm and 0.3 mm distance from the inlet for liquid CO_2 drops and $scCO_2$ drops, respectively, as shown by the x_0 in Figure 7.1. Note that the assigned x_0 should be larger than the entrance distance (related to the Re number) of the channel for water flow to be fully developed. Furthermore, the right-hand side

165
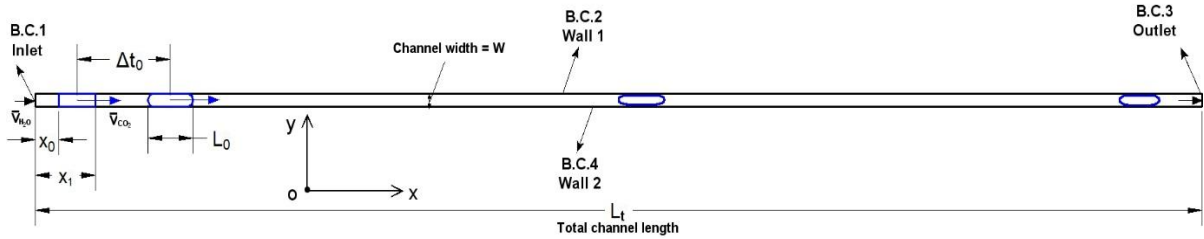
Figure 7.1 Schematic of the 2D computational domain for a single liquid CO_2 or a single $scCO_2$ drop flowing co-current with water in a straight microchannel (total length L_t = 15 mm and channel width W = 0.15 mm). Flows of the CO_2 drop and water are both from left to right. The origin of the coordinate is located at the center of the inlet, the x-axis is in the channel length direction and y-axis is in the channel width direction.

boundary is x_1 from the inlet. The difference between x_1 and x_0, i.e., (x_1-x_0) exactly defines the length of the initialized CO_2 drop. In addition to x-dimension, the width of the marked region on y-dimension is equivalent to the channel width. However, the initialized CO_2 drop needs some computation time to develop into a realistic cylindrical shaped drop (with a length of L_0), and this computation time is indicated by Δt_0. Generally, Δt_0 is a small quantity ($< 10\%$) compared with the subsequent overall flowing time of the CO_2 drop in the straight channel. After a certain computation time when the vertex of the front meniscus of the CO_2 drop reaches the outlet of the channel, the simulation is considered over and will then be manually terminated.

7.3.1 Meshing Information and Grid Resolution

The VOF method based on finite volume discretization is used to solve the equation (7.1), (7.5) and (7.6) on a 2D staggered Cartesian mesh. The computational domain, as shown in Figure 7.1, is meshed into 2999×119 (on x-axis and y-axis, respectively) quadrilateral cells. A total 356,881 cells result in 716,880 faces and 360,000 nodes as well.

Figure 7.2 shows a quick view of the partial meshing at the inlet region as well as a zoom-in view of the grids at the top left corner near the wall (Wall 1 in Figure 7.1). In the entire domain, each cell has a uniform length (in x-dimension) of 5 µm, and in the bulk central region, each cell is of a width (in y-dimension) of ~1.3 µm. Moreover, the grid is refined in terms of further reduced cell widths (approaching 0.1 µm) near the wall region (overall width is 3µm or so which equals to 2%W) in order to obtain the thin film that separates the CO_2 drop from touching the channel wall. Note that the meshing is axisymmetric, thus the meshing scenario is the same at the other channel wall (Wall 2 in

166

Figure 7.1). The meshing method and the grid resolutions are maintained as fixed over all the simulation work in this chapter.

(A)   (B)
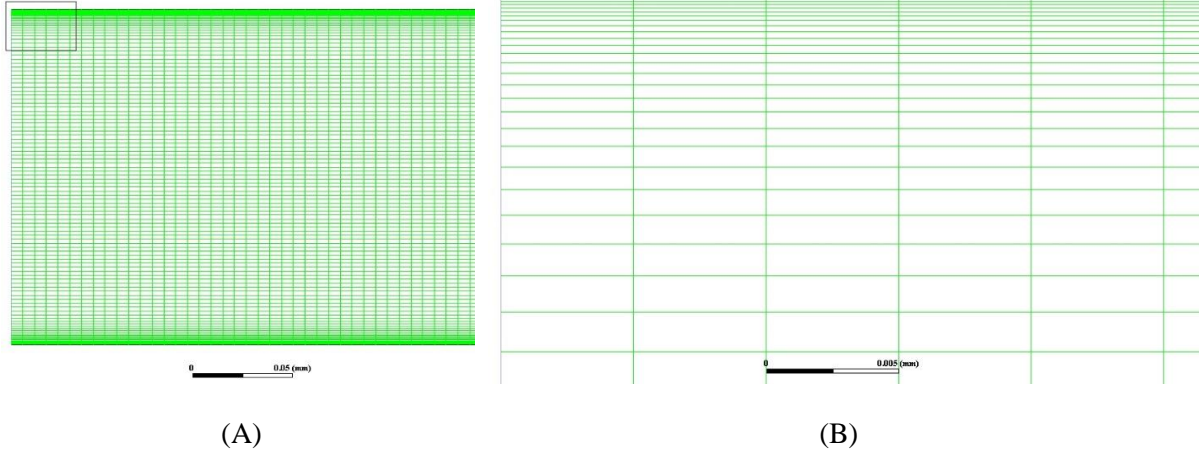
Figure 7.2 A quick view of the meshing at the channel inlet (A) and a detailed view of the fine mesh at the top left corner region (B). Scale bar in (A) and (B) are 0.05 mm and 0.005 mm, respectively.

7.3.2 Simulation Cases and Material Properties

In the simulation, six cases in total are investigated, which are designated by the specific ratios of the flow rate of CO_2 and that of water as inherited from the experiments in Chapter 5 and Chapter 6. Table 7-1 lists the detailed information of all the six simulation cases, including corresponding Q_{CO2}/Q_{H2O} in the experiments, the distance of the initialized drop at its left boundary to the channel inlet (x_0), the length of the initialized CO_2 drop that is determined by (x_1 - x_0), and the mean flow velocities of the continuously flowing water and the initialized drops. Note that (x_1 - x_0) for each case is assigned in accordance with the length of generated CO_2 drop under the corresponding Q_{CO2}/Q_{H2O}. Furthermore, mean flow velocities $\bar{v}_{H2O}$ and $\bar{v}_{CO2}$ of the continuous phase (water) and the CO_2 drop, as the initial conditions, are in accordance with the experimentally measured drop speeds. $\bar{v}_{CO2}$ is equivalent to $\bar{v}_{H2O}$ according to a single-field (or called 'shared-field') formulation in which the flow field is shared by the co-current phases as shown by the momentum equation (i.e., equation (7.6)).

For the simulation cases listed in Table 7-1, the material properties of the applied DI water and either the liquid CO_2 or the $scCO_2$ are referred to the experimental conditions, namely, pressures and temperatures, that have been used in Chapter 5 and Chapter 6. The material properties including density, viscosity, mass diffusivity, interfacial tension and contact angle are listed in Table 7-2.

167

Table 7-1. Simulation cases for a single liquid CO_2 drop and a single $scCO_2$ drop.

Parameters	A single liquid CO_2 drop			A single $scCO_2$ drop		
	Case 1	Case 2	Case 3	Case 4	Case 5	Case 6
Corresponding Q_{CO2}/Q_{H2O} (µL/min/µL/min)	45/55	65/35	75/25	20/80	45/55	50/280
x_0 (mm)	0.3	0.3	0.3	0.2	0.2	0.2
(x_1-x_0) (mm)	0.36	0.72	0.942	0.33	0.517	0.16
$\bar{v}_{H2O}$ (m/s)	0.1	0.11	0.11	0.11	0.085	0.3686
$\bar{v}_{CO2}$ (m/s)	0.1	0.11	0.11	0.11	0.085	0.3686

Table 7-2. Material properties of the applied water and CO_2.

Material properties		A single liquid CO_2 drop			A single $scCO_2$ drop		
		Case 1	Case 2	Case 3	Case 4	Case 5	Case 6
Corresponding Q_{CO2}/Q_{H2O} (µL/min/µL/min)		45/55	65/35	75/25	20/80	45/55	50/280
Water	density (kg/m^3)	1004	1004	1004	995.61	995.59	995.63
	viscosity (µPa·s)	930	930	930	653.66	653.66	653.66
CO_2	density (kg/m^3)	755.23	755.23	755.23	311	309.07	315.4
	viscosity (µPa·s)	65.76	65.76	65.76	23.89	23.975	24.11
	diffusivity (10^{-9} m^2/s)	1.79	1.79	1.79	58.193	58.423	57.666
Interfacial tension (mN/m)		33.2	33.2	33.2	33.47	33.47	33.47
Contact angle (°)		150	150	150	141	141	141

The temperatures for liquid CO_2 and $scCO_2$ are referred to the experimental temperatures, i.e., 25 °C and 40 °C, respectively. The pressures are referred to the applied fluid pressures in experiments for a specific case. By comparing the physical properties of liquid CO_2 with that of $scCO_2$, the density

and viscosity of liquid CO_2 are generally 2.5 ~ 3 times higher, but the mass diffusivity of $scCO_2$ is much higher than that of the liquid CO_2. Interfacial tension between CO_2 drops and water as well as the contact angle are referred to those having been used in the experimental work in the previous two chapters.

7.3.3 Solution Methods

A pressure based solver implementing a pressure-velocity coupled algorithm is used to solve the momentum equation (as shown by equation (7.6)) and the continuity equation simultaneously in a coupled way. The full implicit coupling is realized by an implicit discretization of the pressure gradient term in the momentum equation and an implicit discretization of the mass flux at faces. The volume fraction equation (shown by equation (7.1)) is solved using an implicit formulation. And a sharp-interface model is applied for the interface. In addition, an implicit treatment by considering the equilibrium between the body forces (e.g., gravitation forces and interfacial forces) and the pressure gradient in the momentum equation can improve the convergence of solutions. Last but not least, a species transport driven by diffusion is considered for the CO_2 in the water (equation (7.3) and (7.4)).

Spatial discretization and temporal discretization of the phase continuity equation (in which the scalar quantity is volume fraction α_i, see equation (7.3)) are achieved by using a second-order upwind scheme (i.e., the face value is determined by not only the cell center value but also its gradient in the upstream cell) and a first-order implicit scheme (i.e., the scalar quantity at next time level is determined by the quantity at current time level as well as an evolution function over the time difference). In order to solve the momentum equation (equation (7.6)), the discretization of momentum is achieved using a second-order upwind scheme which can minimize the numerical diffusion, and the pressure discretization is realized by using a body force weighted scheme. For the volume fraction value at faces of a cell, a compressive scheme which is a second-order interface reconstruction scheme is applied.

Time step sizing based on (flow) Courant number

To size an appropriate time step in the temporal discretization is vital to transient numerical simulations, which can be assisted by using a dimensionless number, namely, Courant number (Co) or flow Courant number (Co), as shown below

$$Co = \frac{v \cdot \Delta t}{\Delta x}, \tag{7.13}$$

where v is a velocity magnitude, m/s; Δt is a time step, s; and Δx is the control volume dimension, m. It generally compares the traveling distance of a fluid element over a time step with that of the dimension of a control volume (i.e., cell) [208]. If Co is too large, the simulations become unstable and the results will not be correct. As suggested in the reference [208], a typical time step of an order of magnitude of 10^{-5} s or 10^{-6} s is appropriate for numerical simulations in microfluidics. Here, a time step of 5×10^{-6} s is applied at the CO_2 drop preparation stage (i.e., during Δt_0 in Figure 7.1) and a time step of 1×10^{-5} s is used during the subsequent flowing stage in the channel.

Solution initialization and calculation settings

Prior to the calculation running of each case listed in Table 7-1 and Table 7-2, a solution initialization and calculation settings need to be done in advance.

A standard initialization is chosen in the CFD software FLUENT, and the reference frame of the computations is the one relative to cell zones which are fixed in the computation domains, see Figure 7.1 and Figure 7.2. An initialized gauge pressure of the entire domain is set 0 Pa, given that the gauge pressure is the only one meaningful pressure parameter rather than the very high absolute pressures working with. Alternatively, the absolute pressures can be considered as referenced pressures in the simulations. A purely water flow at one specific constant velocity (see Table 7-1) is assumed from the inlet to the outlet of the channel, see Figure 7.1. And moreover, the CO_2 drop including its region and velocity is initialized by adapting a specified region at a distance from the inlet and patching a velocity corresponding to that the water, respectively, see Figure 7.1 and Table 7-1.

Based on the aforementioned time steps for the two stages of the entire computation time, the simulation results are auto-saved every 50 time steps, i.e., every 0.25 ms and 0.5 ms during the CO_2 drop preparation stage and drop flowing stage, respectively. The maximum iterations of one single time step are 100. Based on the coupled algorithm as well as later observations of the calculation residuals of the relevant parameters, this iteration upper limit is sufficient.

7.4 Results and Discussions

In this section, simulation results and relevant discussions are shown and provided. The first part introduces the first stage of the computation for one specific case, which is a much shorter one compared with the following stage, namely, CO_2 drop flowing stage. Also introduced in this part is a formation of a complete wall film from the front meniscus to the end meniscus of the drop. In the second part, the flow fields within the CO_2 drop and near the interface during the second stage of

computation are probed. The third also the last part shows the distributions of CO_2 at the interfacial regions during the second stage which are subjected to both diffusion into water through interface and the local convection.

7.4.1 CO_2 Drop Preparation and Thin Film Formation

As discussed above, none of the commonly used geometries in microfluidics is used to produce neither liquid CO_2 drop nor $scCO_2$ drop in our simulation work. Instead, an initialized CO_2 drop by adapting one specific region that is close to the inlet of the channel with CO_2 properties (i.e., density, viscosity, diffusivity, velocity) is taken advantage of to provide the CO_2 drop, as shown in Figure 7.1, Table 7-1 and Table 7-2. Since interface tension between pure CO_2 phase and water phase is considered in the simulation, which is deemed a source term in the momentum equation, as shown in equation (7.6) to equation (7.10), the typical cylindrical drop profile can be expected under a collaboration of interfacial tension and pressure difference at the interface. However, a certain period of computation time are needed for the interfacial tension to show effects.

Taking case 1 as an example, the first stage of computation for preparing a complete cylindrical drop profile is shown in Figure 7.3. The initialized (liquid) CO_2 drop is 0.3 mm at its left boundary to the channel inlet and has a velocity of 0.1 m/s which equals to that of water. The initial profile of this drop is a perfect quadrilateral. After a computation for 0.25 ms, the front boundary of the drop shows a bending effect, so does the back one despite a slightly lower degree. As the computation further proceeds, water films near the channel wall start to be formed at the front part of the drop which separate the drop from touching the wall, and later the films continue to grow to the back part of the drop. At t = 9.2 ms, i.e., Δt_0 = 9.2 ms, a completely cylindrical profile of the CO_2 drop is preliminarily shaped, as shown in Figure 7.4. Both the front and the back past of the drop are of a meniscus shape. The drop is completely separated from contact with the channel wall by two thin water films, see Figure 7.4. The thin films' thickness is, by measurements, 2 ~ 2.3 μm, i.e., 1.3% ~ 1.5% of the channel width (W). Based on the water properties in Table 7.2, the capillary number (Ca) calculated by water is 2.8×10^{-3}, which may result in a film thickness of ~2%W according to the discussions and therein references in Chapter 5 and Chapter 6. Therefore, the formed thin water film in this simulation is justified.

Three more images of the liquid CO_2 drop at t = 10.2 ms, t = 11.2 ms, and t = 12.2 ms are provided in Figure 7.3. The purpose is to showcase a stabilized thin film as well as stabilized front and back meniscus following the preliminary formations of these drop features at t = 9.2 ms, which further

171
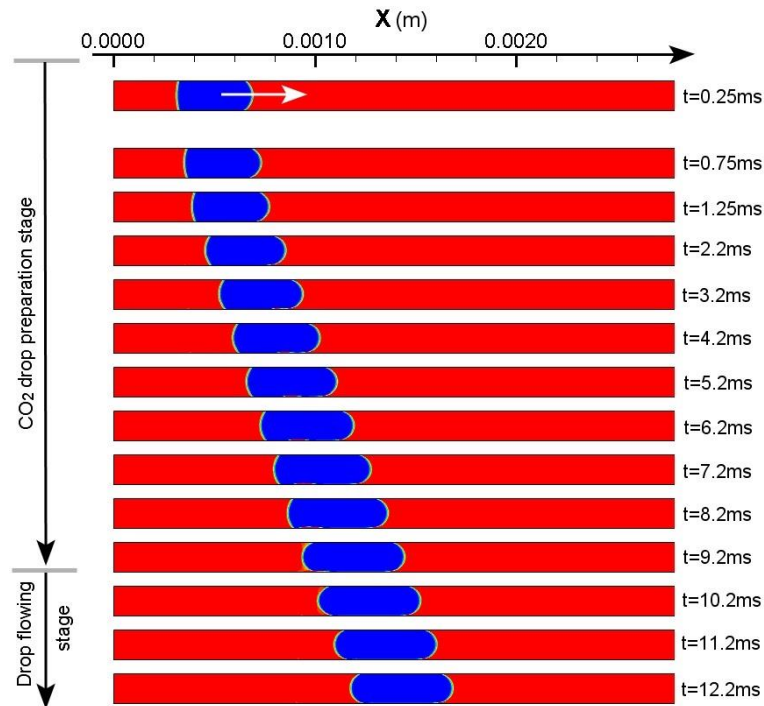
Figure 7.3 The CO_2 drop preparation stage of simulation case 1. Duration of this stage is $\Delta t_0 = 9.2$ ms. Red color indicates the volume fraction of water $\alpha_{H_2O} = 1$, blue color indicates $\alpha_{H_2O} = 0$ (i.e., $\alpha_{CO_2} = 1$), below figures until figure 7.6 are also applied.
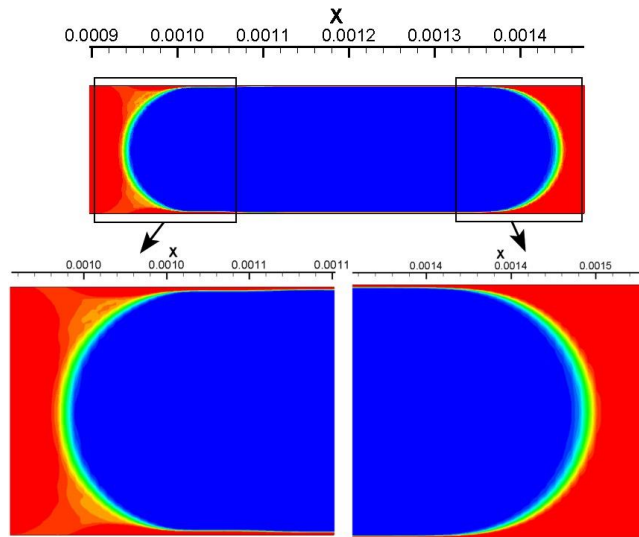
Figure 7.4 A completely cylindrical CO_2 drop is formed at t = 9.2 ms. Two meniscuses featured drop is formed. Thin water film (as shown in two below images) is 2 ~ 2.3 µm thick, compared to a 150 µm channel width.

172

verifies the appropriateness of dedicating t = 9.2 ms as an indication of the end of the CO_2 drop preparation stage. Figure 7.5, as a comparison to Figure 7.4, shows the profile of the liquid CO_2 drop at t = 12.2 ms, the drop length from the back vertex to the front vertex of the meniscus is approximately the same as that at t = 9.2 ms (in Figure7.4). The thin film thickness (measured from the two images below) is averaged by (2.09±0.06) µm which basically agrees with that (2 ~ 2.3 µm) has been measured at t = 9.2 ms as well.
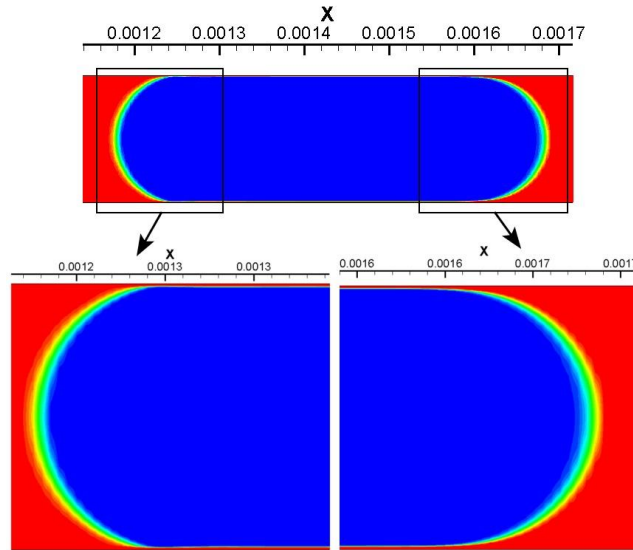
Figure 7.5 A completely cylindrical CO_2 drop is further stabilized at t = 12.2 ms.

Based on the above strategy to define the end of the CO_2 drop preparation stage for simulation 1, the other five simulation cases are analyzed, and three important parameters at the moment of the end of the first stage, including the time durations (Δt_0) of drop preparation stage, drop length (L_0) at the end of preparation stage and the film thickness (t_{film}), are summarized. These three parameters have been tabulated in Table 7-3. As argued in Table 7-1, (x_1-x_0) is the length of the initialized drop in a quadrilateral shape, of which the values are assigned based on the experimental data in Chapter 5 and Chapter 6. However, during the CO_2 drop preparation stage, there are certain expansions of initialized drops thanks to the effects of interfacial tension and pressure difference across the interface. Thus, the lengths of the prepared CO_2 drops are always larger than the initial ones, as shown in Table 7-3. Furthermore, the deviations between (x_1-x_0) and L_0 are less significant for scCO_2 drops than that for liquid CO_2 drops, which may be attributed to the slightly higher interfacial tension of the scCO_2 and water, as shown in Table 7-2.

173

Other than drop length (L_0), the time durations (Δt_0) of the CO_2 drop preparation stage are also listed. The determinations of Δt_0 are exactly the same as simulation case 1. Despite the values of Δt_0, they are small quantities compared with the expected time durations of the second stages of the computations, namely, drop flowing stage. The comparisons can be carried out by $\Delta t_0/(L_t/\bar{v}_{CO2} - \Delta t_0)$ which is well below 7.5% for all cases.

Table 7-3. Time durations of drop preparation stage (Δt_0), drop length (L_0) at the end of preparation stage and the film thickness (t_{film}) of all the simulation cases. (x_1-x_0), as an initialized drop length, is compared to the computed drop length L_0.

Parameters	A single liquid CO_2 drop			A single scCO$_2$ drop		
	Case 1	Case 2	Case 3	Case 4	Case 5	Case 6
Corresponding Q_{CO2}/Q_{H2O} (µL/min/µL/min)	45/55	65/35	75/25	20/80	45/55	50/280
(x_1-x_0) (mm)	0.36	0.72	0.942	0.33	0.517	0.16
Δt_0 (ms)	9.2	10.5	14	4.5	9	2.5
L_0 (µm)	540	915.5	1192.5	373	567	203
t_{film} (µm)	2.03±0.08	2.30±0.09	2.48±0.01	2.45±0.005	2.3±0.08	3.36 at narrowest places

The thin film thicknesses for all the simulation cases are measured and shown in Table 7-3. As can be seen, the film thickness generally ranges from 2 µm to 2.5 µm for most of the cases. Uniquely, cases 6 is characterized by a minimum film thickness of 3.36 µm which is very different from other cases. This increased film thickness actually results from a bullet-shaped scCO$_2$ drop for this case, which is determined by the much increased Ca (approaching 10^{-2}) due to a higher fluid velocity. Figure 7.6 shows the drop profile of the prepared scCO$_2$ drop for case 6. It shows a difference of curvature between the front and the back meniscus of the drop, and thus showcases the bullet-like drop profile. Two circles are added in the image to demonstrate the locations for measuring film thickness. Note that the indicated locations provide the minimum film thickness for this simulation case. Even though, it is much larger than those of the drops in the other five cases. Although case 6 is the only one case of a high flow velocity, same drop profile and increased film thickness are anticipated for even higher flow velocities leading to capillary numbers $\sim 10^{-2}$.
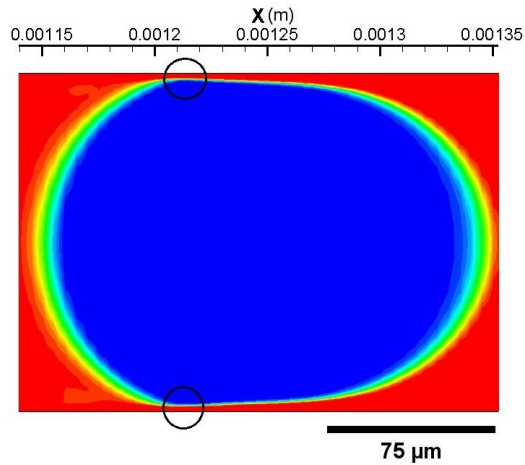
Figure 7.6 The drop profile of the scCO$_2$ drop for simulation case 6 at the end of the drop preparation stage. Two circles are added to indicate where the minimum film thickness are measured.

7.4.2 Flow Fields within CO$_2$ Drops and at Interface

Segmented drop flows or Taylor flows in microchannels have been placed with great expectations to enhance heat and mass transfer between phases such as gas-liquid and liquid-liquid. One important reason among others (e.g., high surface-volume ratios, short transport distances) is the convective hydrodynamics within the drops or bubbles as well as those lying in both sides of the interface between the phases. This factor is an active one which enables the transports of the thermal energy and mass along with diffusion. Thus, flow patterns within the discrete segments and the slugs particularly in the vicinity of the segment meniscus which qualitatively describe the convection have become interesting issues in both experiments and simulations, as reviewed in Chapter 2 and shown in the references in Chapter 5.

CO$_2$ molecules by diffusion and convection enter into the solvent phase – water, as a consequence, the shrinkage of CO$_2$ drop occurs. The shrinkage has been observed and investigated in previous two chapters. Prior to the discussion on drop shrinkage based on the simulation results in the next section, the flow patterns within the CO$_2$ drop and at the interface are probed in this section. Figure 7.7 shows the flow streamlines within the scCO$_2$ drop and in the vicinity of the interface at the drop meniscus at eight time moments during the drop flowing stage. The streamlines are plotted in a frame of reference of the CO$_2$ drop based on: (1) relative x-axis velocities that are calculated by subtracting the mean flow velocity (i.e., $\bar{v}_{CO2} = 0.11$ m/s, see Table 7-1) of the drop from the computed x-axis velocities, and (2) y-axis velocities (see Figure 7.1).

175

(a) t = 5 ms

(b) = 25.75 ms

(c) t = 44.75 ms

(d) t = 64.75 ms

(e) t = 84.75 ms

(f) t = 104.75 ms

(g) t = 124.75 ms

(h) t = 139.75 ms
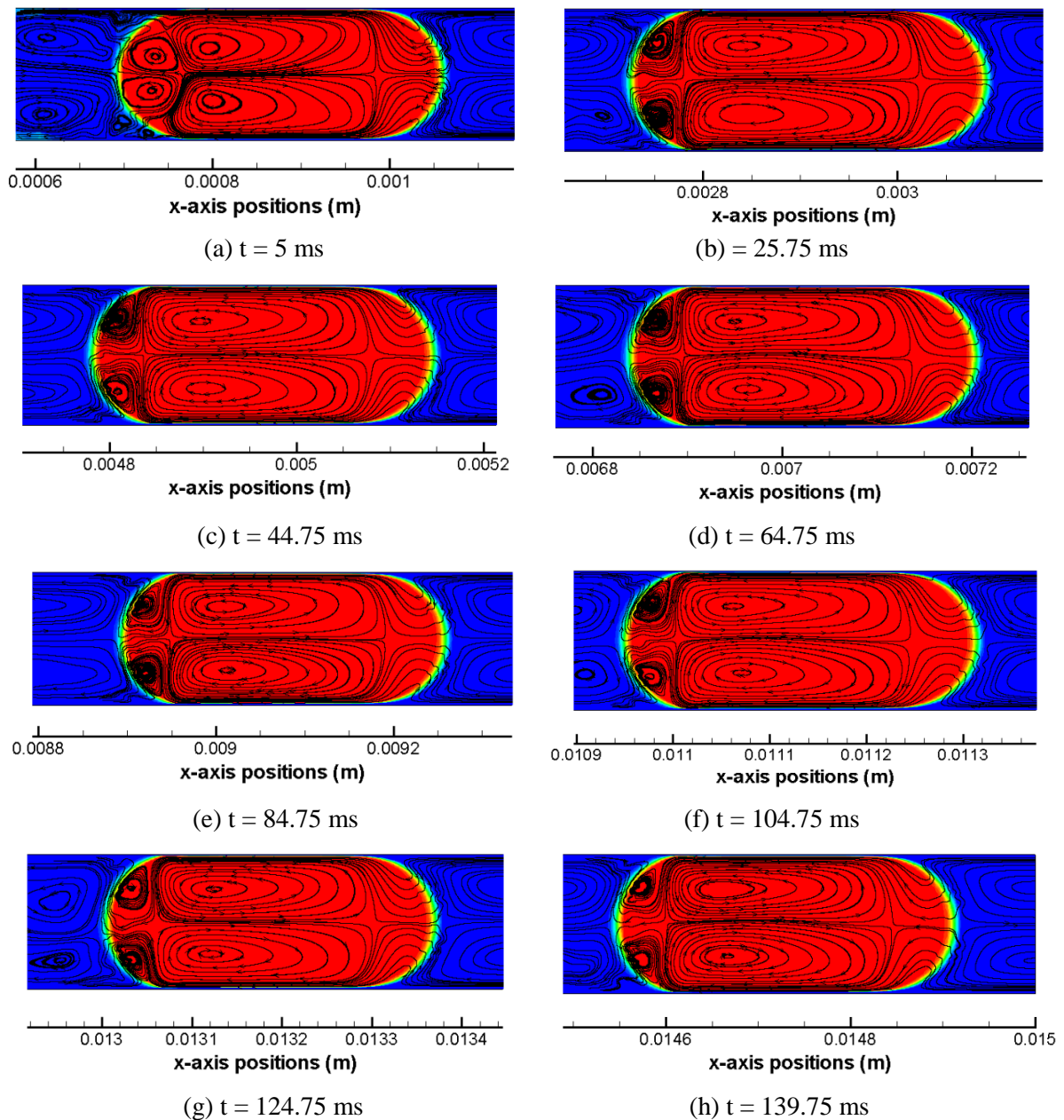
Figure 7.7 Flow field streamlines within the $scCO_2$ drop and in the vicinity of the interface for simulation case 4. The $scCO_2$ drop is tracked over the second stage, namely, drop flowing stage, of the computation, and the drop profile is shown at eight time moments (see above, from (a) to (h)). Red color indicates $\alpha_{CO_2} = 1$.

Focusing on the drop region (colored by red) at each of the eight time moments, there are generally four toroidal flow regions and one small front region that can be identified. Two large vortex regions which are axisymmetric are located in the center of the CO_2 drop. Along the x-axis, these two vortex

176

regions share a same flow path that is identical to the bulk flow; but the vortex directions are converse with each other, i.e., one is clockwise and the other is counter-clockwise, which should has been determined by the local shear stresses at the interface due to the presence of thin films. The shear stresses of the drop at the interface are opposite to the drop flow, and they induce the tangential flow velocities within the drop near the interface. Besides, there are two other vortices at the end of the CO_2 drop that are axisymmetric as well, and these two small vortices are in opposite directions too. At the back meniscus, the tangential flow velocities are dominated by the interface tension where shear stress becomes a weak role, which can be quantified by the local capillary numbers. On the other end of the drop, i.e., at the front meniscus of the drop, no vortex region is observed, instead, flows are in an opposite direction to the bulk drop flow. And due to the presence of the two larger vortex regions, the drop flows in the front region tend to be split and squeezed towards the thin film regions.

Out of the drop regions, the water slug parts both in the front and at the back of the drop in the vicinity of the meniscus are characterized by toroidal flow regions too, which can be found in any one of the images in Figure 7.7. In either the front or the back of the drop, there exist two vortex regions which are in opposite directions and axisymmetric with each other. These vortices are attributed to a combined effects of the shear stresses (in negative-x direction) at the near-wall regions and the net bulk flow (in positive-x direction) along the central axis under a presence of a drop meniscus. This elucidation can be made clear by considering the contours of the relative x-axis velocities (partly based on which the flow streamlines are plotted), as shown in Figure 7.8. The blue regions indicate that the thin film separating the drop from touching channel wall as well as the boundary layer regions (corner regions in Figure 7.8(a)) near the wall are featured with negative relative x-axis velocities. On the other hand, within the water regions and also on the axis, there exist net bulk flows which means positive relative x-axis velocities. These observations justify that shear stresses in near-wall regions are in a reverse direction with respect to the bulk flow, which may further result in the flow vortices in water slug.

From Figure 7.7, it can be seen that the patterns of the flow field streamlines are overall consistent among all the studied time moments of the simulation case 4. This result reflects that the governing forces as well as their relative strengths during the drop flowing stage in the straight channel, quantified by a group of dimensionless numbers such as Ca number, Weber numbers, Reynold numbers, are overall constants in a steady hydrodynamic scenario in terms of flow velocities. The

177

constant pattern of flow streamlines within CO_2 drops and at the interface, therefore, may also be applicable to all the other five simulation cases (i.e., case 1, 2, 3, 5, 6).

(a)   (b)
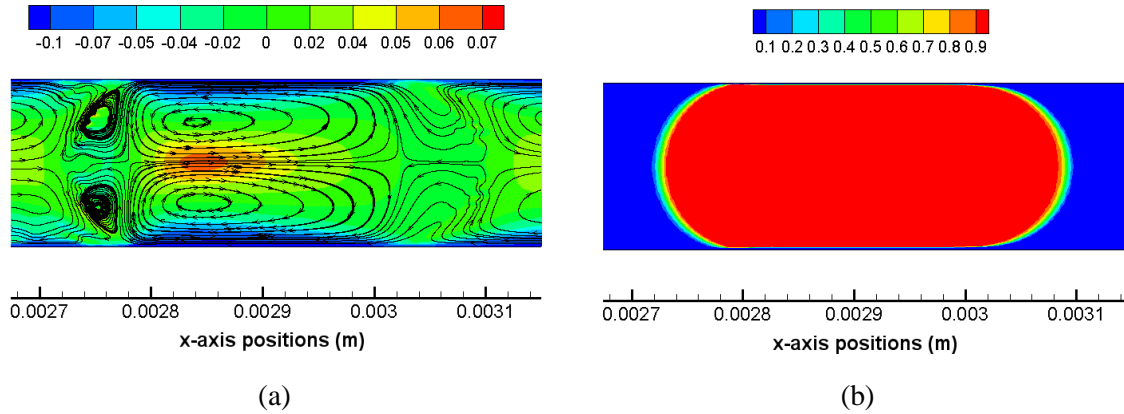
Figure 7.8 scCO$_2$ drop at the moment t = 5 ms in simulation case 4. (a) Contours of the relative x-axis velocities (absolute velocities subtracted by $\overline{v}_{CO2} = 0.11$ m/s) and flow streamlines, color levels of the band indicate the values of the relative x-axis velocities; (b) drop profile colored by the volume fraction of scCO$_2$ for reference, red indicates $\alpha_{CO_2} = 1$.

In view of a characteristic pattern of flow streamlines for each of these simulations cases, a time moment roughly during the middle of the a full computation process is selected to present a representative flow streamline pattern of these cases. Detailed flow streamlines of case 1, 2, 3, 5 and 6 are shown in Figure 7.10. For liquid CO_2 drops, as shown by Figure 7.10 (a), (b) and (c), the non-dimensional drop lengths (L_0/W) have a range from 2.4 to 6.3, and correspondingly, the capillary numbers of these three cases have an order of magnitude of 10^{-3}. It is noticed that at both the front meniscus and the back meniscus of the drops (still within the drop region) there exists a pair of vortex regions, thus there are totally six vortex areas can be identified for these liquid CO_2 drops. It is also clear that the front pair of vortex features a larger area than the back pair of vortex. Taking case 1 as an example, the y-axis velocities may be helpful to elucidate the vortex directions of the front vortex pair as well as the back vortex pair, as shown in Figure 7.9. It can be seen that across the interface there are always reverse y-axis velocities. For example in Figure 7.9(a), the colored small regions show a positive and a negative y-axis velocity in a neighboring domain across the meniscus. And the reverse directions between these two small regions further result in a small vortex region in between of them. Note that this resulted small vortex region is still located within the CO_2 drop. This inference, i.e., small vortex region in the drop caps is resulted from the shear between inside of the drop and outside of the drop, is also applied to the other pair of vortexes in the front meniscus

178

domain, as that shown in Figure 7.9(b). Based on the observations in Figure 7.8 and Figure 7.9, it can be concluded that the flow streamlines within the drops and in the interface domain are mainly caused by the shear directions, which concerns both the shear stresses in the thin film and the local ones at the drop meniscuses.

(a)   (b)
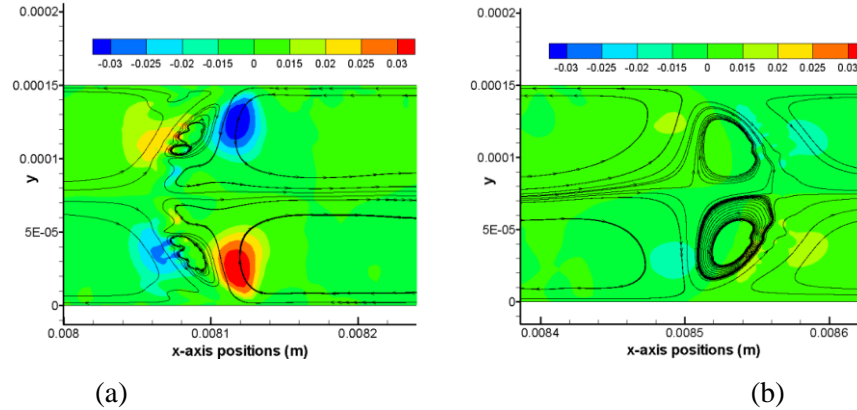
Figure 7.9 Contours of y-axis velocities and simple flow streamlines at (a) the back interface meniscus and (b) the front interface meniscus at time moment t = 98.7 ms in case 1. Color band on the top of each shows the magnitude of y-axis velocity, m/s.

Back to Figure 7.10, it can also be observed that for those Taylor liquid CO_2 drops, within the two larger vortexes in the middle of each drop there can be multiple smaller vortex regions acting as the centers of each of them. These smaller vortexes may have been produced due to the possibly uneven shears from place to place along the elongated drop interface on the x-dimension while on the axis of the drop strong inertia always maintains as a constant. Besides, six vortex regions are also found in case 5, as shown in Figure 7.10(d), where the $scCO_2$ drop has a non-dimensional length of 3.45 and a Ca number of 1.66×10^{-3}. However, as already discussed on case 4 using Figure 7.7 and 7.8, there are five vortex regions and no significant vortex is found at the front meniscus of the drop. Despite of a Ca number of 2.15×10^{-3} for case 4, the Weber number (We = $\rho v^2 L/\sigma$) has an approximate value of 5.4×10^{-2}. By comparison, inertia becomes 25 times larger than the viscous forces, which is quantified by the Re number (Re = We/Ca). Increased inertia justifies its influence on whether can vortexes be arisen in the front meniscus of the drop. An extreme condition of $scCO_2$ drop flowing at a very high velocity (~0.37 m/s) is provided by case 6, as shown in Figure 7.6 and Figure 7.10(e). The velocity increase has a much more profound effect on inertia than on viscous forces, as formulated by Re number which is approaching 100 for the $scCO_2$ drop in case 6. The strong inertia does not lead any formations of vortexes in the drop meniscus domain; nevertheless, shear stresses still dominate in

the thin film region which are still able to cause vortex regions in the middle of the drop, as shown in Figure 7.10(e).

(a) case 1 at t = 98.7 ms

(b) case 2 at t = 100 ms

(c) case 3 at t = 100 ms

(d) case 5 at t = 83.33 ms

(e) case 6 at t = 24.235 ms
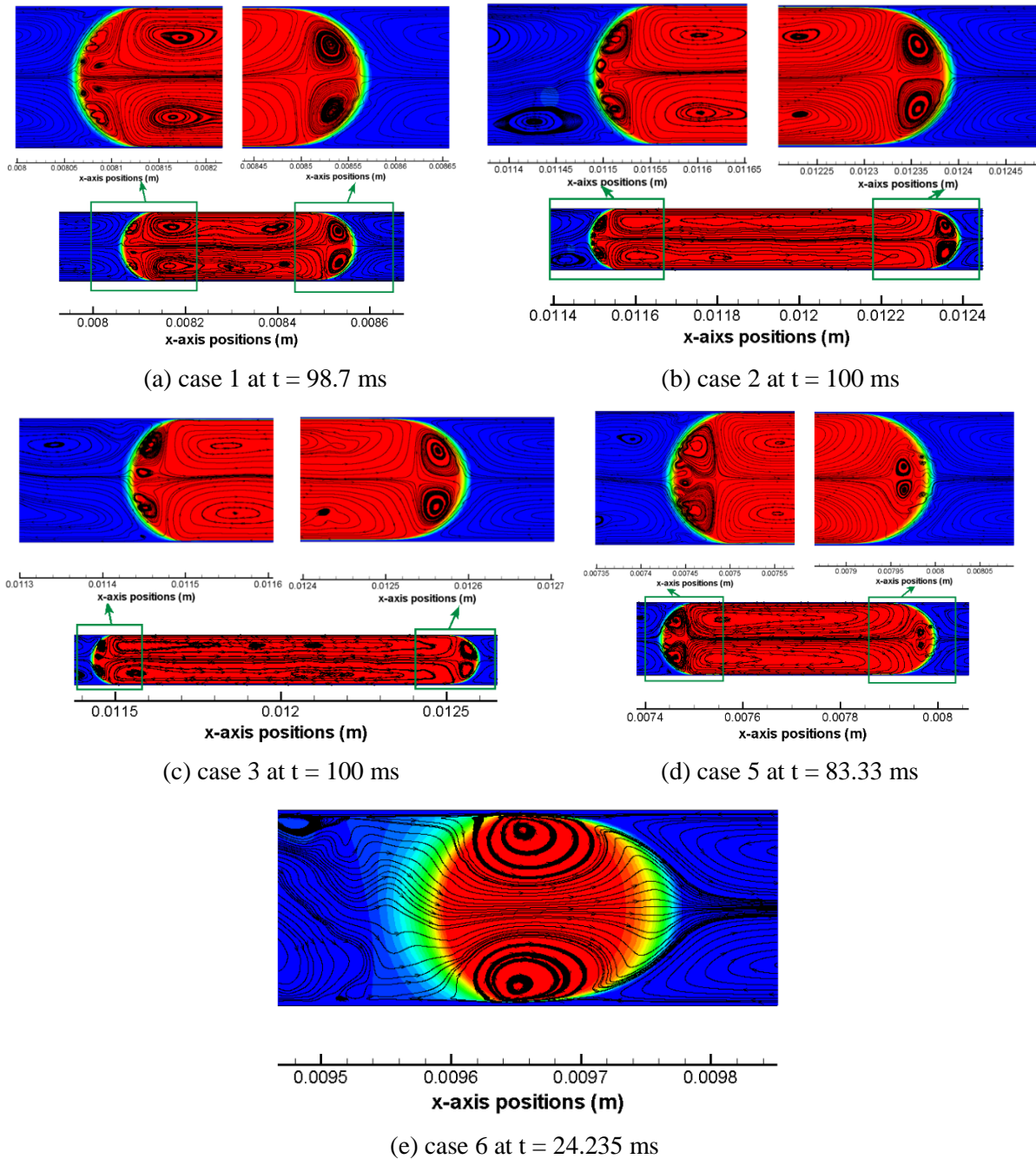
Figure 7.10 Representative pattern of flow streamlines within the CO_2 drops and at the interface for all the other five cases (other than case 4), i.e., (a) case 1; (b) case 2; (c) case 3; (d) case 5; and (e) case 6.

7.4.3 Interfacial Distributions of CO_2

Mass diffusivity (i.e., diffusion coefficient) has been assigned to the numerically studied liquid CO_2 and $scCO_2$ in the simulations in this chapter, see Table 7-2. Those diffusivities are determined based on the Stokes-Einstein equation, which has been shown by equation (4.14). Based on equation (7.3) and (7.4), the diffusion of CO_2 into water through the assumed 'sharp interface' is considered in all the simulations. Nevertheless, the diffusion should not be viewed as the only mechanism through which can CO_2 be transported but also the convection be considered as well.

(a)   (b)
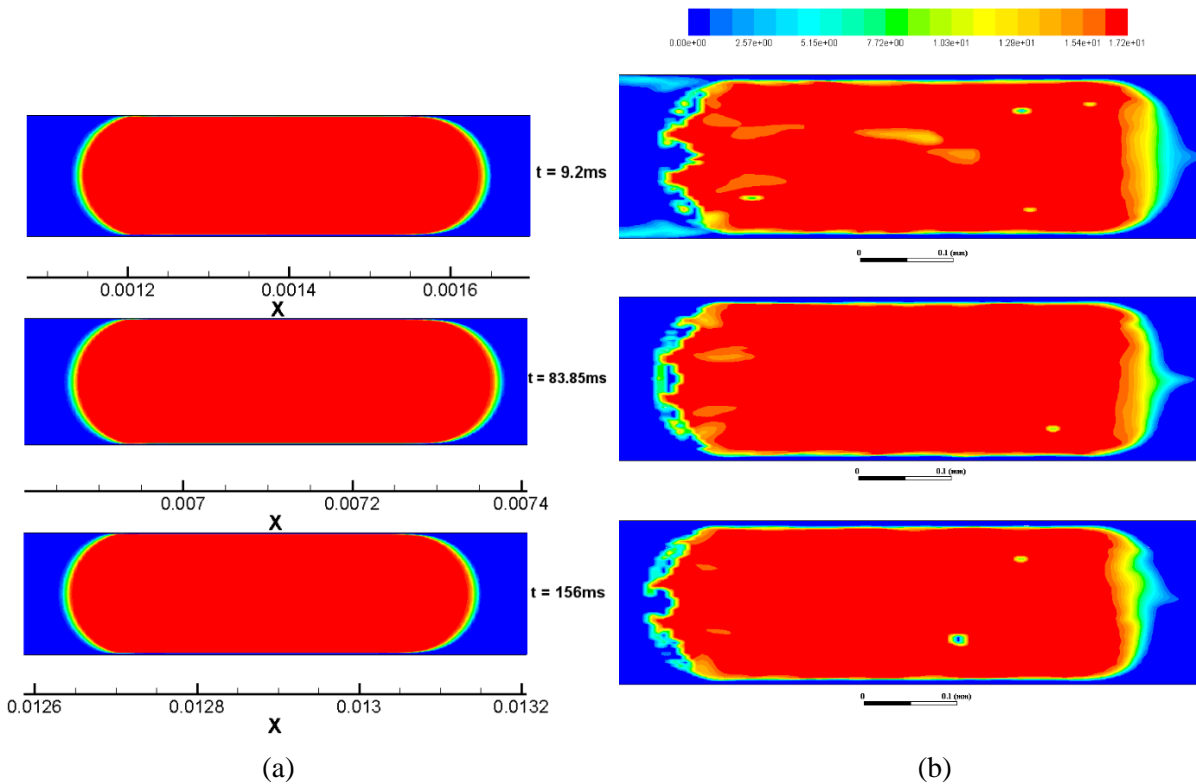
Figure 7.11 Liquid CO_2 drop at three time moments (t = 9.2 ms, t = 83.85 ms, t = 156 ms) in simulation case 1. (a) Drop profile in terms of volume fraction, red indicates $\alpha_{CO_2} = 1$; (b) contours of molar concentrations of CO_2 (c_{CO2}) in water, color map on the top indicates the values c_{CO2} and red indicates the nominal c_{CO2} of pure CO_2 (i.e., $c_{CO2} = \rho/M$).

Using case 1 as an example, Figure 7.11 shows comparisons of the volume fraction (of CO_2) featured drop profiles (see Figure 7.11(a)) with the molar concentrations of CO_2 in water featured drop profiles (see Figure 7.11(b)), at three moments of the drop flowing stage, i.e., at the beginning t = 9.2 ms, roughly at the middle of this stage t = 83.85 ms, and almost at the end of the drop flowing stage t = 156 ms. Quantified by a dimensionless number Peclet number (Pe) as formulated by

181

equation (2.26), diffusion is generally weaker in mass transport compared with the advection when these two mechanisms are both contributing to the transport process in the same direction. Here, the discussions of the CO_2 transport are limited to the x-axis direction. And on this dimension, despite of the strong effects of the drop advection in the straight microchannel, the drop travels at a same pace as with the continuously flowing water based on the assigned velocities of these two phases, see Table 7-2. Therefore, the first step of the CO_2 transport from its pure phase to the water phase should still be relying on diffusion. On the front meniscus of the scCO$_2$ drop, as shown in Figure 7.11(b), the concentration gradients of CO_2 which drives the diffusion are obvious, as shown by the color changes in red to yellow to green and to blue eventually from left to right. However, due to the vortexes on the water slug side, as shown in Figure 7.10(a), there are relative convections of the water flow from the channel wall towards the channel axis which tends to flush the interface of the meniscus. Consequently, a distortion of the diffusion profile is resulted from the neighboring convections. The distortions are justified by the triangular convex on the right end of each of the images in Figure 7.11(b). On the other end of the drop, i.e., the back meniscus, the profile of CO_2 molar concentrations are rather irregular. Different from the scenario in the front meniscus of the drop, the convections here near the back meniscus are overall in an opposite direction against the diffusion. Specifically, they are exactly opposite to diffusion on the axis, but at a bit deviated distance (a quarter of the channel width) from the axis, the resistive effects of the convections are weakened due to a reduced x-axis velocity component, and the diffusion there is less suppressed. Because of the varying relative strengths of the diffusions compared with the local convections, the profile of the CO_2 molar concentrations on the back meniscus generally presents a wavy pattern. In addition to the profiles at the meniscuses, there is almost a zero concentration as well as a zero concentration gradient of CO_2 in the thin film region. This result is not very surprising since the convections in the thin film region are extremely rapid in transporting the diffused CO_2 despite the flows near the wall are typically slow than that in the middle of the channel.

Although not shown here, the CO_2 concentration profiles along the interface between the pure CO_2 phase and the water phase for all the other CO_2 drops in a Taylor flow pattern in case 2, 3, 4, 5 are very likely the same, based on the flow field streamlines shown in Figure 7.10. Even so, there might exist a different local profile at the front meniscus of the scCO$_2$ drop in case 4, where the flow streams originate from the water side and continue into the drop through the meniscus, see Figure 7.7 and Figure 7.8. Since the flow streams are against to the diffusion in this region, the CO_2 molar concentration profile could be significantly suppressed by the reverse convections.

The other distinct scenario of the CO_2 distribution profile lies in the simulation case 6 which is characterized by an extremely high flow velocity. Uniquely, the flow streamlines within the $scCO_2$ drop and at the drop meniscuses are shown in Figure 7.10(e). There are only two vortex regions in the middle of the drop, and no vortex is found in the meniscus region. This is due to the relative small y-axis velocities compared with the x-axis velocities, and as discussed in previous section, the neglected y-axis velocities, even though there may be differences of these velocities across the meniscus, are not likely to induce vortex inside the meniscus. Actually, the relative x-axis velocities dominate the flow streams in the central region of the $scCO_2$ drop. Additionally, there are very rare relative convection between the water and CO_2 due to the quite uniform x-axis velocities. Figure 7.12 shows the $scCO_2$ drop in case 6 at three different moments which are chosen comparably as those in Figure 7.11. Instead of CO_2 molar concentrations, the volume fraction of CO_2 is applied to identify the $scCO_2$ drop. Different from Figure 7.11(a), volume fraction can be relied on to differentiate the pure CO_2, mixture of CO_2 and water, and pure water. As soon as the $scCO_2$ is prepared well during the first stage of the computation, the diffusive ring surrounding the pure $scCO_2$ is quite thin which is similar as those shown in Figure 11(a). However, as computation continues the diffusive ring becomes thicker in the x dimension, and significant wide regions of volume fraction gradients at the front and the back meniscus of the drop can be observed, as shown in Figure 7.12(b) and (c). The unidirectional gradients indicate that diffusion may be the only one effective transport mechanism for CO_2 into water although $scCO_2$ drop flows in a high velocity. This diffusion-only scenario can be comprehended based on the above discussions on the involved flow streamlines, in which the relative x-axis velocities override the differences of the y-axis velocities resulting in no formations of vortex in the meniscus regions of the drop, and on the other hand, the dominant x-axis velocity are so uniform that any significant relative convection between water and CO_2 do not exist. Thus, the effects of convection in a relative sense become subtle, and diffusion turns to be the only effective mechanism which achieves CO_2 transfer into water.

Based on Figure 7.12, the lengths ($L_{drop,x}$) of the $scCO_2$ drop at those three time moments are measured according to a nominal drop defined by a 0.5 cut-off volume fraction. The measured decreasing lengths demonstrate the hydrodynamic shrinkage of this $scCO_2$ drop over time. The numerically obtained drop lengths are first normalized to the channel width ($W = 150$ μm), and then are compared to the experimental results under the case $Q_{CO2}/Q_{H2O} = 50/280$, as shown in Figure 7.13. Generally, the simulated drop lengths overestimate the real drop lengths in the experiment. However, the decreasing tendency over time has been predicted. Note that the first drop length data point in our

simulation is originated from a drop initialization in which an initialized drop length (rather than the presented one) has been referred to the experimental drop length and applied in our simulation. If the length of the prepared $scCO_2$ drop is precisely predicted, it may enhance the predications further.

(a)   (b)   (c)
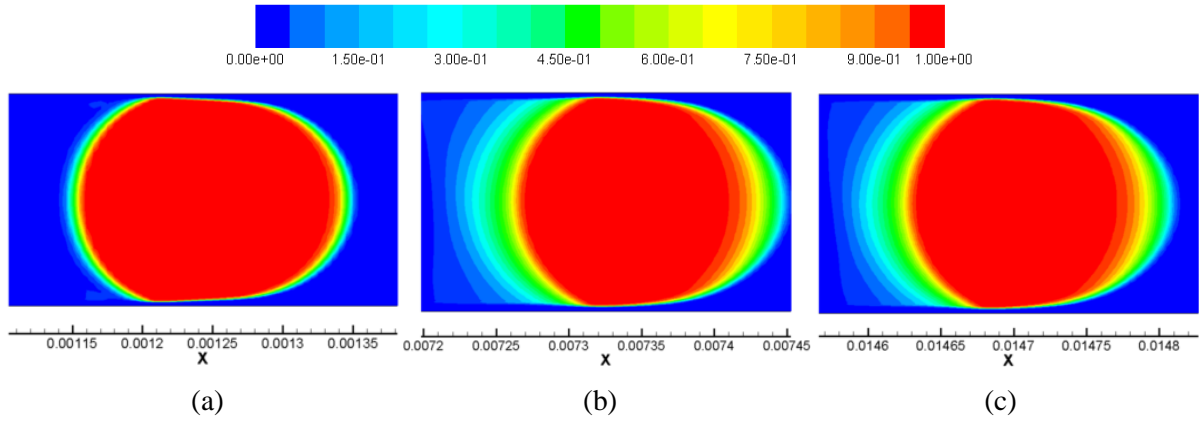
Figure 7.12 $scCO_2$ drop at three moments in simulation case 6. (a) t = 2.5 ms, $L_{drop,x}$ = (183±4) μm; (b) t = 18.235 ms, $L_{drop,x}$ = (155±5) μm; (c) t = 37.235 ms, $L_{drop,x}$ = (152.5±3.5) μm. Color map shows the magnitudes of the CO_2 volume fraction, where red indicates α_{CO_2} = 1.
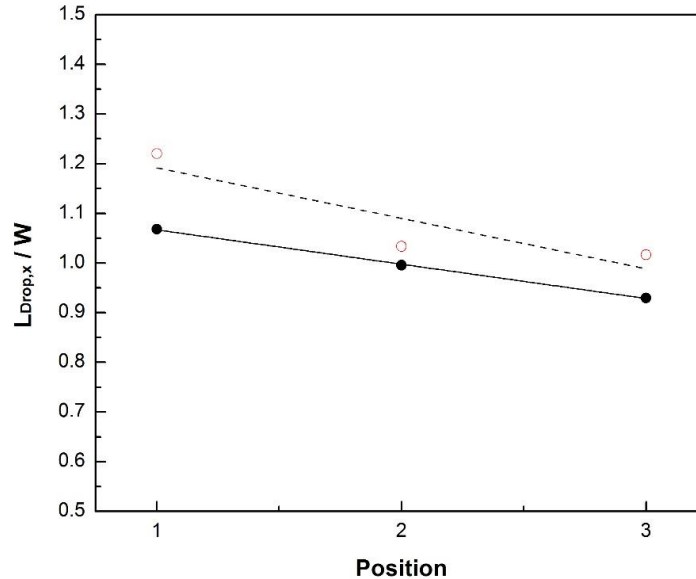
Figure 7.13 Development of the dimensionless $scCO_2$ drop length ($L_{drop,x}$/W). Simulation results are at three time moments (t = 2.5 ms, 18.235 ms, 37.235 ms) of case 6, shown by the open circles; experimental results are based on Q_{CO2}/Q_{H2O} = 50/280 in Chapter 6 in which the $scCO_2$ drop has a total flow time of 40ms in the straight channel, shown by the solid circles.

184

7.5 Conclusion

This chapter presents a preliminary numerical study on the hydrodynamics of one single liquid CO_2 drop and one single $scCO_2$ drop traveling in a straight microchannel, as configured with the same geometries as that has been used during the experimental work in Chapter 5 and Chapter 6. Six simulation cases in total, including three (case 1 to 3) for liquid CO_2 drop and three (case 4 to 6) for $scCO_2$ drop, are considered in this chapter. Each case is analogous to the corresponding experimental conditions in terms of the flow properties and the physical properties of the involved CO_2 and water, as shown in Table 7-1 and Table 7-2. Based on the numerical methods introduced in the section 7.2, three main governing equations are used to solve the segmented two phase problem, including: (1) a volume fraction equation (equation (7.1)), (2) continuity equations with respect to the two phases (equation (7.3)), and (3) an overall momentum equation of one-single fluid formulation (equation (7.6)). The diffusivities of liquid CO_2 and $scCO_2$ in water are considered. The interfacial tension between CO_2 and water is considered as a body force which is added to the right-hand side of the momentum equation. The numerical problem is formulated as a 2D and transient one. A pressure-velocity coupling algorithm is applied to solve the governing equations. Main simulation results are summarized as follows:

◆ The computation for each simulation case is composed of two sequential stages, namely, the first stage - CO_2 drop preparation stage and the second stage - CO_2 drop flowing stage. A full liquid CO_2 drop preparation stage ($\Delta t_0 = 9.2$ ms) for case 1 is shown, during which a cylindrical drop shape featured with two meniscuses at the front and the end of the drop is formed. And besides, thin films of water on two sides of the drop near the channel wall are formed as well, which separate the single CO_2 drop from contact with the wall. Generally, the drop preparation stages for all cases account for less than 7.5% of the entire computation time, and the thin film thickness ranges from 2 to 2.5 µm for all Taylor drops (case 1 to 5) and is the largest (3.36 µm) for case 6 which is characterized by the highest capillary number (approaching to 10^{-2}). The presence and thickness of the computed thin film are consistent with the experimentally reported ones, as reviewed in section 2.5.1 in Chapter 2.

◆ Flow fields within the single CO_2 drop and at the interfacial regions are probed in the second part of section 7.4. For the CO_2 drops in all the simulation cases, there are generally two major toroidal vortex regions in the middle of each single drop, which are attributed to the significant shear stresses in the thin film regions of the water towards the drop as well as upon the interface

185

(that are parallel to the x-axis). This inference is justified by the tangential flow streams of the vortex toroid at the interface which are always consistent with the shear stresses in terms of their directions. Moreover, small vortex regions are identified at the front and the back meniscus of the CO_2 drops in typical Taylor drop flows (case 1 to 3 and case 5), of which the formations are due to the reverse velocity components on y-dimension between the inner drop and out of the drop, see Figure 7.9. However, as the superficial velocity of the drop (as well as that of water) increases, the small vortex regions start to vanish, first at the front meniscus of the drop as shown in case 4 (see Figure 7.7 and Figure 7.8) and later at both the front and the back meniscus of the drop as shown in case 6 (Figure 7.10(e)). The vanishes of small vortexes in meniscus region are believed to be resulted from the weakening effects of the y-dimensional velocities under increasingly dominant x-axis velocities in case 4 and case 6, as more revealed in case 6 in which only the major vortexes in the middle of the $scCO_2$ drop are remained. In spite, increasing strengths of inertia relative to viscous forces in those regions are deemed the underlying causes.

◆ Interfacial distributions of CO_2 when the CO_2 drops are revealed. Diffusion tends to result in a one-dimensional concentration gradient featured region starting from the initialized sharp interface. However, the local convections are able to contribute to the CO_2 distributions as well. Specifically, radially inward convections out of the front meniscus of the drop at water side induce a distortion of the diffusion profile, and an approximately triangular convex of the concentration profile is formed, as shown Figure 7.11(b). On the other side of the drop, local convections at water side generally show an opposite effect to the diffusion, and uneven relative strengths of the convections in comparison with diffusion lead to irregular wavy profile of the CO_2 concentration distributions there. The CO_2 distribution profile scenarios of case 1 may also be applicable to other confident Taylor drop flow case, such as case 2, 3, 5, in which the local y-dimensional velocity components are comparable to the relative x-axis velocities in terms of magnitudes in the vicinities of the drop meniscus. But for case 4 and case 6 which are characterized by high x-axis velocities, relative convection between the CO_2 side and the water side turn to be tiny, which contribute little therefore to the CO_2 transport from its pure phase to pure water. During this moment, diffusion becomes the only effective mechanism controlling the CO_2 transport, and an only diffusion resulted CO_2 distribution profile is formed, as shown in Figure 7.12. Nevertheless, simulated $scCO_2$ drop length reductions in case 6 are analogous to those reported in experimental study in Chapter 6, despite of still slight overestimations.

186

Chapter 8

Conclusions and Recommendations

Conclusions of this thesis and recommendations for future work are made in this chapter.

8.1 Conclusions

Microfluidic devices have been proved effective and efficient means to support scientific exploration of transport phenomenon that are difficult to be obtained using macroscale systems. In this thesis, it has been applied to investigate the interactions between liquid CO_2 and $scCO_2$ with water aiming to provide insights to the questions faced by CCS such as capillary and dissolution mechanism particularly during the CO_2 injection and the early stage of storage. In particular, the author has constructed a unique experimental system for two-phase microfluidic studies related with extreme pressure/temperature conditions. Based on this system, experimental studies on the generation of dense CO_2 segments and hydrodynamic shrinkage of liquid CO_2 and $scCO_2$ drops in straight microchannel are conducted. Additionally, a numerical study of the hydrodynamics of a single liquid CO_2 and $scCO_2$ drop simultaneously water in a straight long microchannel is done, and the involved hydrodynamic issues are revealed.

The first effort of this thesis (in Chapter 4) is made upon experimentally engineering liquid CO_2 and DI water in a micro T-junction, where liquid CO_2 and DI water are injected into the T-junction perpendicularly. Over the probed flow conditions including a capillary number (Ca) ranging from $O(10^{-4}) \sim O(10^{-2})$ and various flow rate ratios of these two fluids, two main flow patterns, namely, drop flow ($Ca \sim O(10^{-3}) \sim O(10^{-2})$) and co-flow ($Ca \sim O(10^{-4})$) have been identified. Uniquely, the observed drop flows are characterized by an elongating-squeezing stage, preceded by a filling and followed by a pinch-off stage, respectively, in which both squeezing and elongating effects co-exist. Thus, the common 'necking' time for CO_2 stream truncation is increased and the truncation point is located further downstream from the corner of the T-junction. This extra elongating effect results in a modified factor (much larger than 1) in a well-known 'flow-rate-controlled' droplet size formulation '$L/W = 1 + \alpha(Q_c/Q_d)^{-1}$'. Detailed analyses of a relation between time development and drop size increase in the sequential three stages of one drop generation period provide interpretations to the modified flow-rate-ratio factors. Besides, the speeds of liquid CO_2 drops flowing through the microchannels after generation can be approximated by dividing the total flow rates of the two fluids by the channel cross-sectional area. Finally, the drop spacing development between the generated

drop and the emerging drop within one drop generation period is reported. A linear model is developed to predict the spacing as a function of the time. In view of a periodical spacing development, the model yields a good agreement with experimental results.

Following liquid CO_2 drop generation in the micro T-junction in Chapter 4, hydrodynamic shrinkage of liquid CO_2 drops travelling through a straight long microchannel is experimentally investigated in Chapter 5. The liquid CO_2 drops that are in a form of flowing Taylor drops (whose equivalent diameters are several or even tens of times larger than the channel hydrodynamic diameter) are formed using the same T-junction as that used in Chapter 4 with water as the continuous phase. Based on various flow rate ratios of liquid CO_2 (Q_{LCO2}) over water (Q_{H2O}), variously sized CO_2 drops in terms of non-dimensional drop length (L/W) are produced, and the drop lengths (L) and drop speeds (V) have been measured at three specified positions along the straight microchannel, namely, the drop pinch-off position, the midpoint of the total channel length, and the very end of the channel. A correlation between the non-dimensional length (L_1/W) of the (generated) liquid CO_2 drops and the flow rate ratio Q_{LCO2}/Q_{H2O} presents a much larger than 1 (specifically, 1.79) factor of Q_{LCO2}/Q_{H2O}, which has been discussed in details in Chapter 4. It is found that drop length reductions is not highly dependent on flow rate ratios, indicating that the absolute drop shrinkage may be independent of the original drop sizes. However, relative drop length reduction $\Delta L/L_1$ shows differences among all the flow rate conditions, which has decreased from 0.1 to 0.025 as Q_{LCO2}/Q_{H2O} increases from 20/80 to 75/25. It shows that slightly longer flowing time of smaller drops (produced by lower Q_{LCO2}/Q_{H2O}) may have promoted the mass transfers through the interface between CO_2 drops and water. Mathematical formulations of drop surface area (A) and volume (V) are provided in this chapter by considering a typical Taylor drop in square microchannels with a presence of the thin film. The surface-volume ratios (S/V) of all the drops at the specified three positions are evaluated against the flow rate ratio Q_{LCO2}/Q_{H2O}, which indicates that there is almost no significant difference of S/V among all the flow rate conditions. Other than drop lengths, drop speeds at position 1 (v-1), 2 (v-2) and 3 (v-3) are measured as well, which assist in calculating the flowing time of the CO_2 drops in the channel and, as a further step, the mass transfer coefficients of CO_2 in water. For Q_{LCO2}/Q_{H2O} < 1, those three drop speeds are almost constant and generally lower than the reference velocity v_{Total}, i.e., a superficial velocity by dividing the total flow rate (Q_{LCO2} + Q_{H2O}) by the channel cross section; for Q_{LCO2}/Q_{H2O} > 1, the velocities can still be approximated by v_{Total} despite of a decrease from v-1 to v-2 and down to v-3. Based on an averaged drop speed and a real channel length (see Table 5-1), the real drop flowing time are estimated. Because of a slightly longer real channel length and a lower drop

speed, the flowing time for $Q_{LCO2}/Q_{H2O} < 1$ are roughly 10ms higher than those for $Q_{LCO2}/Q_{H2O} > 1$. Furthermore, the mass transfer coefficient can be determined depending on a mathematically developed form of k_d. Two types of mass transfer coefficient, i.e., k_d (mm/s) and $k_d \cdot (S/V)$ (1/s) are considered. Generally, lower Q_{LCO2}/Q_{H2O} results in relatively higher mass transfer coefficients in terms of both k_d and $k_d \cdot (S/V)$, which is essentially attributed to the corresponding flowing time given that surface-volume ratios are on the same level (10^4 m^{-1}). Moreover, mass transfer capabilities of different flow conditions are also justified by the relative drop length reductions. Also considered are the potential effects of the pressure drops due to the drop flows in the straight microchannel on the drop volume. Despite a slight decrease (~100 Pa) subjected to increasing Q_{LCO2}/Q_{H2O}, the values of total pressure drop ΔP_t are averaged at ~3,175 Pa with a standard error of 1.6%. Combined with the Peng-Robinson Eos (equation of state) for liquid CO_2 and estimated initial pressures at the T-junction from the CO_2 pump, drop volume changes relative to the original volumes are correlated to the molar volumes present in the Eos. Overall, the resulted volume changes are calculated as relatively small quantities ($\Delta V/V_0 = 0.39‰ \sim 0.52‰$).

A follow-up experimental study concerning hydrodynamic shrinkage of scCO$_2$ drops (or segments) in a straight microchannel is provided in Chapter 6. The experimental methodologies are mostly analogous to the ones applied in Chapter 5, but in this chapter the procedures regarding the applications of even higher pressures and a temperature control are different from that in Chapter 4 and are specifically introduced, as shown in section 6.2. A correlation of the sizes of generated scCO$_2$ drops at the T-junction with the flow rate ratios indicates a more intensified effect of the elongating time on the final sizes of scCO$_2$ drops than that when liquid CO_2 is involved. This is reflected by the factor (3.62 in chapter 6 for scCO$_2$) of the flow rate ratios. Also based on scCO$_2$ drop sizes at three similarly specified positions on the straight channel, the drop reductions from position 1 to position 2 and those from positon 2 to 3 are calculated, which reveal the hydrodynamic shrinkage of scCO$_2$ in the flowing path, as shown by the relative drop length reductions in Figure 6.7. Different behaviors of two groups of flow conditions, i.e., a constant total flow rate ($Q_{scCO2} + Q_{H2O} = 100$ µL/min) and a constant flow rate of scCO$_2$ ($Q_{scCO2} = 50$ µL/min) as functions of flow rate ratios (Q_{scCO2}/Q_{H2O}), reveal that surface-volume ratios of the scCO$_2$ drops and the flowing time of the drops in the channel are the two main factors which control the mass-transfer-led drop shrinkage. Based on the surface-volume ratios and the flowing time of scCO$_2$ drops, the tendency of relative drop length reduction characterized shrinkage with Q_{scCO2}/Q_{H2O} at the condition $Q_{scCO2} + Q_{H2O} = 100$ µL/min may be correlated with the flowing time of those scCO$_2$ drops at various Q_{scCO2}/Q_{H2O}, given that the surface-

volume ratios are similar among different flow conditions. Moreover, the flowing time development with Q_{scCO2}/Q_{H2O} at the condition $Q_{scCO2} = 50$ µL/min justifies its dominant role in controlling the drop shrinkage phenomenon at a constant flow rate of scCO$_2$. Similar to Chapter 5, the mass transfer coefficient k_d and the volumetric transfer coefficient $k_d*(S/V)_a$ are calculated based on the developed mathematical model of k_d. It is concluded that the flowing time of scCO$_2$ drops in the straight channel rather than surface-volume ratio controls the hydrodynamic shrinkage performance; for $Q_{scCO2} = 50$ µL/min, the flowing time becomes more influential, and there could exist a critical drop flowing time below which no significant drop shrinkage will occur. The total pressure drop due to segmented flows in the straight microchannel is estimated as well, and the corresponding relative volume changes are no larger than 1.49‰ for all the studied flow cases. Therefore, the drop shrinkages observed can be confidently attributed to the mass transfer between the scCO$_2$ drops and the continuously flowing water which mainly occurs through the interface of these two fluids.

The final part of the thesis (Chapter 7) is a preliminary numerical study on the hydrodynamics of one single liquid CO$_2$ drop and one single scCO$_2$ drop traveling simultaneously with water in a straight microchannel. The two-dimensional numerical domain is configured with the same geometries as that has been used during the experimental work in Chapter 5 and Chapter 6. Analogous to the corresponding experimental conditions of the involved CO$_2$ and water, as shown in Table 7-1 and Table 7-2, six cases in total are considered in this chapter, including three (case 1 to 3) for liquid CO$_2$ drop and three (case 4 to 6) for scCO$_2$ drop. Three main governing equations including: (1) a volume fraction equation (equation (7.1)), (2) continuity equations with respect to the two phases (equation (7.3)), and (3) an overall momentum equation of one-single fluid formulation (equation (7.6)) are solved in the simulations. In addition, the diffusivities of liquid CO$_2$ and scCO$_2$ in water are considered, the interfacial tensions between CO$_2$ and water regarded as a body force is also considered, as shown by the term on the right-hand side of the momentum equation. The computation of each case is believed to be composed of two sequential stages, namely, a first stage - CO$_2$ drop preparation stage and a second stage - CO$_2$ drop flowing stage. Taking case 1 as an example, liquid CO$_2$ drop preparation stage ($\Delta t_0 = 9.2$ ms) is fulfilled when a cylindrical drop shape featured with two meniscuses at the front and the end of the drop is formed and thin water films near the channel walls are formed as well. In general, the drop preparation stages for all cases account for less than 7.5% of the entire computation time, the thin films have a thickness range of 2 ~ 2.5 µm for all Taylor drops (case 1 to 5) and shows a largest value (3.36 µm) for case 6 that is characterized by the highest capillary number (~10^{-2}). Besides, flow fields within the single CO$_2$ drop and at the interfacial regions

190

are probed. There are generally two major toroidal vortex regions in the middle of each single CO_2 drop, which are a result of the significant shear stress lying in between the central axis and the near-wall interface. The inference is justified by the tangential flow streams of the vortex toroid at the interface which are consistent with the shear stress in terms of directions. Additionally, small vortex regions are identified as well at the front and the back meniscus of the CO_2 drops in typical Taylor drop flows (i.e., case 1 to 3 and case 5), whose formations are due to the near-meniscus y-axial shears, as evidenced by the reverse y-axial velocity components. As the superficial velocity of the drop (as well as that of water) increases, these small vortex regions vanish at the front meniscus of the drop first (see Figure 7.7 and Figure 7.8) and later at both the front and the back meniscus of the drop (Figure 7.10(e)). The disappearance of these small vortexes results from the weakening effects of the y-dimensional velocities along with the increasingly dominant x-axial velocities in case 4 and case 6. Fundamentally, increasing strength of inertia relative to viscous forces in those regions is deemed the underlying causes. Finally, interfacial distributions of CO_2 are shown. Diffusion tends to present a one-dimensional concentration gradient starting from an initialized sharp interface, however, local convection contributes to the CO_2 distributions as well. As observed, radially inward convection out of the front meniscus of the drop at water side distort the diffusion profile, and a triangular convex of the concentration profile is formed. Focusing on the back meniscus, local convection in water generally shows an opposite effect on the diffusion. Non-uniformities of the relative strength of convection compared with diffusion lead to an irregular wavy profile of the CO_2 concentration. The observed CO_2 distribution profile of case 1 is applicable to other Taylor drop flow cases in which the local y-axial velocity components can be comparable to the relative x-axial velocities in terms of magnitudes within the vicinities of the drop meniscus. However, for case 4 and case 6 that are characterized by high x-axial velocities, relative convection between CO_2 and water should be tiny, resulting in little contribution to the CO_2 transport, thus diffusion becomes the only effective mechanism for the CO_2 transport. Despite slight overestimations, simulated $scCO_2$ drop length reductions in case 6 agree with those reported in the experimental study in Chapter 6.

8.2 Future Work Recommendations

Based on the accomplished work in this thesis and experimentally as well as numerically observed phenomenon, a few recommendations for future work are put forward here, as detailed below:

(1) *Dynamic interfacial effects led interface deformation*

From the experimental observations of liquid CO_2/water as well as $scCO_2$/water two phases flows in the micro T-junction, the CO_2 drop generation has been characterized by an elongating-squeezing stage, which results in a significant increase of the common 'necking' time of the dispersed CO_2 streams as well as the entire drop generation period. Dynamic interfacial effects, either dynamic contact angles or a non-uniform interfacial tension distribution on the interface (thus Marangoni stresses are induced) between CO_2 stream and water stream, may have led to a deformation of the interface at its clear upper section (see Chapter 4) during the second stage and the third stage of the drop generation, which no longer assists in squeezing the dispersed CO_2 stream. Therefore, dynamic interfacial effects led interface deformation becomes one suggested topic for future work. This investigation can be carried out by using an appropriate three-dimensional optical visualization technology to show the interface on the channel depth dimension. On the other hand, the visualization requirement is one key limitation as well.

(2) *After-generation drop speeds interpretation*

As discussed in Chapter 4, experimentally measured after-generation CO_2 drops' speeds can be approximated by dividing total flow rates over the channel cross sectional area. This finding has also been reported by other researchers. However, no insightful explanations about this approximation is provided. Also in this thesis, only experimentally measured drop speeds are reported and compared to the calculated ones based on flow rates. It is advised here that the approximation might be interpreted from two perspectives: (1) conservation of momentum and kinetic energy, based on which the kinetics of the generated drop are composed by one inherited from the original dispersed fluid flow and the other due to the 'pushing' effect of the continuous fluid; and (2) lubrication theory, in which both a strong shear stress in the thin film (separates the CO_2 stream from contact with the channel wall) and a pressure difference between the two ends of the thin film (in the flow direction) contribute to the towing of the emerging drop downstream. If the latter perspective is chosen, a physical model of the thin film between the drop head and the channel wall may be required, and a scenario of Stokes flow in this film (in flow direction) may also need to be considered. In addition, appropriate boundary conditions are also necessary.

(3) *Verifications on calculations of Taylor drop surface area and volume*

As shown by equation (5.24) and (5.25), the surface area (A, m^2) and volume (V, m^3) of one single Taylor drop in a rectangular cross-section microchannel can be calculated. The thin film at the channel wall and gutter region in the corner region are considered, and the drop caps at the front and

the back of the drop are assumed as a half of a general triaxial ellipsoid. Nevertheless, the mathematical formulations of surface area and volume in this thesis have to be verified, either by experiments or numerical methods. However, it should be noted that a precise determination of these two geometrical parameters of a typical Taylor drop (or bubble) is not an easy job, unless an extremely reliable measurement technology in experiments or a more accurate computation method in numerical results are applied.

(4) *Numerical considerations of mass transfer mechanisms*

Although the diffusion and the convection mechanism are considered in our simulation work in Chapter 7, they do not induce analogous drop length reductions as those reported in experimental work in Chapter 5 and Chapter 6 for case 1 to 5. It also explains why the CO_2 drop shrinkage is not calculated and compared with the experimental data. Instead, the discussions have been limited to the hydrodynamic issues of the numerical problems and only the interfacial CO_2 distributions surrounding the drop are discussed (however, case 6 is an exception). Unobservable drop length reductions for typical Taylor CO_2 drops (in case 1 to case 5) are mainly due to no setting of any mass transfer mechanisms, which calls for either a mass transfer coefficient or a mass transfer rate being known. Therefore, in future numerical work on not only the hydrodynamics but also the mass transfer issues, an appropriate treatment of the mass transfer properties of CO_2 in water is required.

(5) *More possible projects realizable in the experimental system*

The core of the experimental system lies in the microfluidic module, i.e., the non-permanent connector and the microfluidic model, which would enable three-phase flow and flow in two-dimensional porous media. Due to its excellence in working at extreme pressure/temperature conditions, other supercritical fluids (e.g., supercritical water, supercritical ethane, supercritical propane, etc.) could be implemented in this system under purposely regulated pressure and temperature conditions.

Bibliography

[1]   Canadell, J. G., Le Quere, C., Raupach, M. R., Field, C. B., Buitenhuis, E. T., Ciais, P., . . . Marland, G. (2007). Contributions to accelerating atmospheric CO_2 growth from economic activity, carbon intensity, and efficiency of natural sinks. *Proceedings of the National Academy of Sciences of the United States of America, 104*(47), 18866-18870.

[2]   Benson, S. M. (2005). Carbon dioxide capture and storage in underground geologic formations. In *Proceedings Workshop 'the 10-50 Solution: technologies and policies for a low-carbon future.*

[3]   Ciais, P., Sabine, C., Bala, G., Bopp, L., Brovkin, V., Canadell, J., ... & Jones, C. (2014). Carbon and other biogeochemical cycles. In *Climate change 2013: the physical science basis. Contribution of Working Group I to the Fifth Assessment Report of the Intergovernmental Panel on Climate Change* (pp. 465-570). Cambridge University Press.

[4]   Falkowski, P., Scholes, R. J., Boyle, E., Canadell, J., Canfield, D., Elser, J., . . . Steffen, W. (2000). The global carbon cycle: A test of our knowledge of earth as a system. *Science, 290*(5490), 291-296.

[5]   Metz, B., Davidson, O., de Coninck, H., Loos, M., Meyer, L., & Working Group III of the Intergovernmental Panel on Climate Change. (2005). *IPCC, 2005: IPCC special report on carbon dioxide capture and storage*. Cambridge University Press.

[6]   Oelkers, E. H., & Cole, D. R. (2008). Carbon Dioxide Sequestration: A Solution to a Global Problem. *Elements, 4*(5), 305-310.

[7]   Manabe, S., & Stouffer, R. J. (1994). Multiple-Century Response of a Coupled Ocean-Atmosphere Model to an Increase of Atmospheric Carbon-Dioxide. *Journal of Climate, 7*(1), 5-23.

[8]   Rowley, R. J., Kostelnick, J. C., Braaten, D., Li, X., & Meisel, J. (2007). Risk of rising sea level to population and land area. *Eos*, *Transactions American Geophysical Union 88*(9), 105-107.

[9]   Cole, D. R., & Monger, H. C. (1994). Influence of Atmospheric CO_2 on the Decline of C4 Plants during the Last Deglaciation. *Nature, 368*(6471), 533-536.

[10]   Bruant, R. G., Guswa, A. J., Celia, M. A., & Peters, C. A. (2002). Safe storage of CO_2 in deep saline aquifers. *Environmental Science & Technology, 36*(11), 240-245.

[11]   Metz, B., Davidson, O. R., Bosch, P. R., Dave, R., & Meyer, L. A. (2007). *IPCC, 2007: Climate Change 2007: Mitigation Contribution of Working Group III to the Fourth Assessment Report of the Intergovernmental Panel on Climate Change*. Cambridge University Press.

[12]   Rubin, E. S. (2008). CO_2 Capture and Transport. *Elements*, *4*(5), 311-317.

[13]   Page, S. C., Williamson, A. G., & Mason, I. G. (2009). Carbon capture and storage: Fundamental thermodynamics and current technology. *Energy Policy, 37*(9), 3314-3324.

[14]   Michael, K., Arnot, M., Cook, P., Ennis-King, J., Funnell, R., Kaldi, J., ... & Paterson, L. (2009). CO2 storage in saline aquifers I—Current state of scientific knowledge. *Energy Procedia*, *1*(1), 3197-3204.

[15]   Middleton, R. S., Keating, G. N., Stauffer, P. H., Jordan, A. B., Viswanathan, H. S., Kang, Q. J., ... & Esposito, R. (2012). The cross-scale science of CO 2 capture and storage: from pore scale to regional scale. *Energy & Environmental Science*, *5*(6), 7328-7345.

[16]   Ellis, J. S., & Bazylak, A. (2012). Dynamic pore network model of surface heterogeneity in brine-filled porous media for carbon sequestration. *Physical Chemistry Chemical Physics*, *14*(23), 8382-8390.

[17]   Houghton, J.T., Callander, B.A., & Varney, S.K. (eds.) (1992). *Climate Change 1992: The Supplementary Report to the IPCC Scientific Assessment. Report prepared for Intergovernmental Panel on Climate Change by Working Group I combined with Supporting Scientific Material*. Cambridge University Press.

[18]   Sauerbeck, D. R. (1993). CO$_2$-Emissions from Agriculture - Sources and Mitigation Potentials. *Water Air and Soil Pollution, 70*(1-4), 381-388.

[19]   Marchetti, C. (1977). On geoengineering and the CO$_2$ problem. *Climatic change*, *1*(1), 59-68.

[20]   Adams, E. E., & Caldeira, K. (2008). Ocean storage of CO$_2$. *Elements*, *4*(5), 319-324.

[21]   Dunsmore, H. E. (1992). A geological perspective on global warming and the possibility of carbon dioxide removal as calcium carbonate mineral. *Energy Conversion and Management*, *33*(5), 565-572.

[22]   Lackner, K. S., Wendt, C. H., Butt, D. P., Joyce, E. L., & Sharp, D. H. (1995). Carbon dioxide disposal in carbonate minerals. *Energy*, *20*(11), 1153-1170.

[23]   Herzog, H. (2002). Carbon sequestration via mineral carbonation: overview and assessment. *Cambridge, Massachusetts: Massachusetts Institute of Technology, Laboratory for Energy and the Environment*.

[24]   Van der Meer, L. G. H. (1992). Investigations regarding the storage of carbon dioxide in aquifers in the Netherlands. *Energy Conversion and Management*, *33*(5), 611-618.

[25]   Kaarstad, O. (1992). Emission-free fossil energy from Norway. *Energy Conversion and Management*, *33*(5), 781-786.

[26]   Koide, H., Tazaki, Y., Noguchi, Y., Nakayama, S., Iijima, M., Ito, K., & Shindo, Y. (1992). Subterranean containment and long-term storage of carbon dioxide in unused aquifers and in depleted natural gas reservoirs. *Energy Conversion and management*, *33*(5), 619-626.

[27] Herzog, H., Drake, E., Tester, J., & Rosenthal, R. (1993). A research needs assessment for the capture, utilization, and disposal of carbon dioxide from fossil fuel-fired power plants. *Report to the US Department of Energy, Grant No. DEFG02-92ER30194. AOOO, from MIT Energy Laboratory, Cambridge*.

[28] Gunter, W. D., Perkins, E. H., & McCann, T. J. (1993). Aquifer disposal of CO_2-rich gases: reaction design for added capacity. *Energy Conversion and management*, *34*(9), 941-948.

[29] Bachu, S., Gunter, W. D., & Perkins, E. H. (1994). Aquifer disposal of CO_2: hydrodynamic and mineral trapping. *Energy Conversion and Management*, *35*(4), 269-279.

[30] Herzog, H., Drake, E., & Adams, E. (1997). *CO_2 Capture, Reuse, and Storage Technologies for Mitigating Global Climate Change,* Report to US DOE Order No. DE-AF22-96PC01257, January 1997.

[31] Kikuta, K., Hongo, S., Tanase, D., & Ohsumi, T. (2005). Field test of CO_2 injection in Nagaoka, Japan. In *Proceedings of seventh international conference on greenhouse gas control technologies* (2), 1367-1372.

[32] Hovorka, S. D., Benson, S. M., Doughty, C., Freifeld, B. M., Sakurai, S., Daley, T. M., ... & Myer, L. R. (2006). Measuring permanence of CO_2 storage in saline formations: the Frio experiment. *Environmental Geosciences*, *13*(2), 105-121.

[33] Frster, A., Norden, B., Zinck-Jrgensen, K., Frykman, P., Kulenkampff, J., Spangenberg, E., ... & Juhlin, C. (2006). Baseline characterization of the CO2SINK geological storage site at Ketzin, Germany. *Environmental Geosciences*, *13*(3), 145-161.

[34] http://www.energy.gov/fe/science-innovation/carbon-capture-and-storage-research/regional-partnerships. Accessed in June 2014.

[35] Plasynski, S. I., Litynski, J. T., McIlvried, H. G., & Srivastava, R. D. (2009). Progress and new developments in carbon capture and storage. *Critical Reviews in Plant Science*, *28*(3), 123-138.

[36] Michael, K., Golab, A., Shulakova, V., Ennis-King, J., Allinson, G., Sharma, S., & Aiken, T. (2010). Geological storage of CO_2 in saline aquifers—a review of the experience from existing storage operations. *International Journal of Greenhouse Gas Control*, *4*(4), 659-667.

[37] Hitchon, B. (Ed.). (2012). *Best practices for validating CO_2 geological storage: Observations and guidance from the IEAGHG Weyburn-Midale CO_2 monitoring and Storage project*. IEA Greenhouse Gas R & D Programme, Geoscience Publishing.

[38] Riddiford, F. A., Tourqui, A., Bishop, C. D., Taylor, B., & Smith, M. (2003). A cleaner development: the In Salah Gas project, Algeria. In *Proceedings of the 6th International Conference on Greenhouse Gas Control Technologies*, 1-4 October 2002, Kyoto, Japan, volume 1, 601–606.

[39] Riddiford, F., Wright, I., Bishop, C., Espie, T., & Tourqui, A. (2004). Monitoring geological storage: The In Salah gas CO_2 storage project: GHGT-7. *Presented at: 7th International Conference on Greenhouse Gas Control*, Vancouver, Canada.

[40]   Maldal, T., & Tappel, I. M. (2004). CO_2 underground storage for Snøhvit gas field development. *Energy*, *29*(9), 1403-1411.

[41]   http://www.chevronaustralia.com/our-businesses/gorgon. Accessed in June 2014.

[42]   Liu, N. (2013). *Microfluidique supercritique pour la compréhension des systèmes CO_2/eau sous pression et en température: Application à la gestion durable de la filière CO_2*. Ph.D. Thesis. University of Bordeaux, France.

[43]   Doughty, C., Pruess, K., Benson, S. M., Hovorka, S. D., Knox, P. R., & Green, C. T. (2001). Capacity investigation of brine-bearing sands of the Frio Formation for geologic sequestration of CO_2. In *Proceedings of First National Conference on Carbon Sequestration*, 14-17 May 2001, Washington, D.C., United States Department of Energy, Paper P.32, 16pp.

[44]   Ennis-King, J., Gibson-Poole, C. M., Lang, S. C., & Paterson, L. (2002). Long term numerical simulation of geological storage of CO_2 in the Petrel sub-basin, North West Australia. In *Greenhouse Gas Control Technologies, Proceedings of the 6th International Conference on Greenhouse Gas Control Technologies*, 1-4 October 2002, Kyoto, Japan, volume 1, 507–511.

[45]   Doughty, C., & Pruess, K. (2004). Modeling supercritical carbon dioxide injection in heterogeneous porous media. *Vadose Zone Journal*, *3*(3), 837-847.

[46]   Kumar, A., Noh, M. H., Ozah, R. C., Pope, G. A., Bryant, S. L., Sepehrnoori, K., & Lake, L. W. (2005). Reservoir simulation of CO_2 storage in aquifers. *SPE Journal*, *10*(3), 336-348.

[47]   Ghanbari, S., Al-Zaabi, Y., Pickup, G. E., Mackay, E., Gozalpour, F., & Todd, A. C. (2006). Simulation of CO2 storage in saline aquifers. *Chemical Engineering Research and Design*, *84*(9), 764-775.

[48]   Ennis-King, J. P., & Paterson, L. (2005). Role of convective mixing in the long-term storage of carbon dioxide in deep saline formations. *SPE Journal*, *10*(03), 349-356.

[49]   Juanes, R., Spiteri, E. J., Orr, F. M., & Blunt, M. J. (2006). Impact of relative permeability hysteresis on geological CO_2 storage. *Water Resources Research*, *42*(12).

[50]   Suekane, T., Soukawa, S., Iwatani, S., Tsushima, S., & Hirai, S. (2005). Behavior of supercritical CO_2 injected into porous media containing water. *Energy*, *30*(11), 2370-2382.

[51]   Krevor, S., Pini, R., Zuo, L., & Benson, S. M. (2012). Relative permeability and trapping of CO_2 and water in sandstone rocks at reservoir conditions. *Water Resources Research*, *48*(2), W02532.

[52]   Ma, J., Petrilli, D., Manceau, J. C., Xu, R., Audigane, P., Shu, L., ... & Le-Nindre, Y. M. (2013). Core scale modelling of CO_2 flowing: identifying key parameters and experiment fitting. *Energy Procedia*, *37*, 5464-5472.

[53]   Rimmelé, G., Barlet-Gouédard, V., & Renard, F. (2010). Evolution of the petrophysical and mineralogical properties of two reservoir rocks under thermodynamic conditions relevant for

CO$_2$ geological storage at 3 km depth. *Oil & Gas Science and Technology–Revue de l'Institut Français du Pétrole*, *65*(4), 565-580.

[54]   Zemke, K., Liebscher, A., & Wandrey, M. (2010). Petrophysical analysis to investigate the effects of carbon dioxide storage in a subsurface saline aquifer at Ketzin, Germany (CO$_2$ SINK). *International Journal of Greenhouse Gas Control*, *4*(6), 990-999.

[55]   Gutiérrez, B., Juarez, F., Ornelas, L., Zeppieri, S., & de Ramos, A. L. (2008). Experimental study of gas–liquid two-phase flow in glass micromodels. *International Journal of Thermophysics*, *29*(6), 2126-2135.

[56]   Joseph, J., Gunda, N. S. K., & Mitra, S. K. (2013). On-chip porous media: Porosity and permeability measurements. *Chemical Engineering Science*, *99*, 274-283.

[57]   Kim, Y., Wan, J., Kneafsey, T. J., & Tokunaga, T. K. (2012). Dewetting of silica surfaces upon reactions with supercritical CO2 and brine: pore-scale studies in micromodels. *Environmental science & technology*, *46*(7), 4228-4235.

[58]   Majlaton, N.I.. (2012). *A Visual Study of CO$_2$ Injection at the Pore Scale using Micromodels*. M.S. Thesis. University of Bergen, Norway.

[59]   Cottin, C., Bodiguel, H., & Colin, A. (2010). Drainage in two-dimensional porous media: From capillary fingering to viscous flow. *Physical Review E*, *82*(4), 046315.

[60]   Zhang, C., Oostrom, M., Grate, J. W., Wietsma, T. W., & Warner, M. G. (2011). Liquid CO$_2$ displacement of water in a dual-permeability pore network micromodel. *Environmental science & technology*, *45*(17), 7581-7588.

[61]   Wang, Y., Zhang, C., Wei, N., Oostrom, M., Wietsma, T. W., Li, X., & Bonneville, A. (2012). Experimental study of crossover from capillary to viscous fingering for supercritical CO$_2$–water displacement in a homogeneous pore network. *Environmental science & technology*, *47*(1), 212-218.

[62]   Smith, D. H., Bromhal, G. S., & Ferer, M., (2000). Pore-level modeling of carbon dioxide sequestration in deep aquifers. *Papers of the American Chemical Society* 220: U397-U398, 751-755.

[63]   Ellis, J. S., & Bazylak, A. (2013). Investigation of contact angle heterogeneity on CO$_2$ saturation in brine-filled porous media using 3D pore network models. *Energy Conversion and Management*, *68*, 253-259.

[64]   Jessop, P. G., & Leitner, W. (1999). Supercritical fluids as media for chemical reactions. *Chemical Synthesis Using Supercritical Fluids*, Wiley-VCH Verlag GmbH, 1-36.

[65]   Taylor, L. T. (1996). *Supercritical fluid extraction* (volume 4). John Wiley & Sons, Inc., New York, NY.

[66]   York, P., Kompella, U. B., & Shekunov, B. Y. (Eds.). (2004). *Supercritical fluid technology for drug product development* (1 edition). CRC Press.

[67] Marre, S., Roig, Y., & Aymonier, C. (2012). Supercritical microfluidics: Opportunities in flow-through chemistry and materials science. *The Journal of Supercritical Fluids*, *66*, 251-264.

[68] Kobayashi, J., Mori, Y., & Kobayashi, S. (2005). Hydrogenation reactions using $scCO_2$ as a solvent in microchannel reactors. *Chemical communications*, (20), 2567-2568.

[69] Tiggelaar, R. M., Benito-López, F., Hermes, D. C., Rathgen, H., Egberink, R. J., Mugele, F. G., ... & Gardeniers, H. J. (2007). Fabrication, mechanical testing and application of high-pressure glass microreactor chips. *Chemical Engineering Journal*, *131*(1), 163-170.

[70] Benito-Lopez, F., Tiggelaar, R. M., Salbut, K., Huskens, J., Egberink, R. J., Reinhoudt, D. N., ... & Verboom, W. (2007). Substantial rate enhancements of the esterification reaction of phthalic anhydride with methanol at high pressure and using supercritical CO_2 as a co-solvent in a glass microreactor. *Lab on a Chip*, *7*(10), 1345-1351.

[71] Ohashi, A., Sugaya, M., & Haeng-Boo, K. I. M. (2011). Development of a microfluidic device for measurement of distribution behavior between supercritical carbon dioxide and water. *Analytical Sciences*, *27*(6), 567-567.

[72] Trachsel, F., Hutter, C., & von Rohr, P. R. (2008). Transparent silicon/glass microreactor for high-pressure and high-temperature reactions. *Chemical Engineering Journal*, *135*, S309-S316.

[73] Trachsel, F., Tidona, B., Desportes, S., & von Rohr, P. R. (2009). Solid catalyzed hydrogenation in a Si/glass microreactor using supercritical CO_2 as the reaction solvent. *The Journal of Supercritical Fluids*, *48*(2), 146-153.

[74] Assmann, N., Kaiser, S., & von Rohr, P. R. (2012). Supercritical extraction of vanillin in a microfluidic device. *The Journal of Supercritical Fluids*, *67*, 149-154.

[75] Assmann, N., Werhan, H., Ładosz, A., & von Rohr, P. R. (2013). Supercritical extraction of lignin oxidation products in a microfluidic device. *Chemical Engineering Science*, *99*, 177-183.

[76] Marre, S., Adamo, A., Basak, S., Aymonier, C., & Jensen, K. F. (2010). Design and packaging of microreactors for high pressure and high temperature applications. *Industrial & Engineering Chemistry Research*, *49*(22), 11310-11320.

[77] Ilin, E. S., Marre, S., Jubera, V., & Aymonier, C. (2013). Continuous supercritical synthesis of high quality UV-emitting ZnO nanocrystals for optochemical applications. *Journal of Materials Chemistry C*, *1*(33), 5058-5063.

[78] Roig, Y., Marre, S., Cardinal, T., & Aymonier, C. (2011). Synthesis of exciton luminescent ZnO nanocrystals using continuous supercritical microfluidics. *Angewandte Chemie International Edition*, *50*(50), 12071-12074.

[79] Gendrineau, T., Marre, S., Vaultier, M., Pucheault, M., & Aymonier, C. (2012). Microfluidic synthesis of palladium nanocrystals assisted by supercritical CO_2: tailored surface properties for applications in boron chemistry. *Angewandte Chemie International Edition*, *51*(34), 8525-8528.

[80] Liu, N., Aymonier, C., Lecoutre, C., Garrabos, Y., & Marre, S. (2012). Microfluidic approach for studying CO_2 solubility in water and brine using confocal Raman spectroscopy. *Chemical Physics Letters*, *551*, 139-143.

[81] Abolhasani, M., Singh, M., Kumacheva, E., & Günther, A. (2012). Automated microfluidic platform for studies of carbon dioxide dissolution and solubility in physical solvents. *Lab on a Chip*, *12*(9), 1611-1618.

[82] Marre, S., Roig, Y., & Aymonier, C. (2012). Supercritical microfluidics: Opportunities in flow-through chemistry and materials science. *The Journal of Supercritical Fluids*, *66*, 251-264.

[83] Abolhasani, M., Günther, A., & Kumacheva, E. (2014). Microfluidic studies of carbon dioxide. *Angewandte Chemie International Edition*, 53(31), 7992-8002.

[84] Leitner, W. (2002). Supercritical carbon dioxide as a green reaction medium for catalysis. *Accounts of chemical research*, *35*(9), 746-756.

[85] Licence, P., Ke, J., Sokolova, M., Ross, S. K., & Poliakoff, M. (2003). Chemical reactions in supercritical carbon dioxide: from laboratory to commercial plant. *Green Chemistry*, *5*(2), 99-104.

[86] Sun, R., & Cubaud, T. (2011). Dissolution of carbon dioxide bubbles and microfluidic multiphase flows. *Lab on a Chip*, *11*(17), 2924-2928.

[87] Cubaud, T., Sauzade, M., & Sun, R. (2012). CO_2 dissolution in water using long serpentine microchannels. *Biomicrofluidics*, *6*(2), 022002.

[88] Tumarkin, E., Nie, Z., Park, J. I., Abolhasani, M., Greener, J., Sherwood-Lollar, B., ... & Kumacheva, E. (2011). Temperature-controlled 'breathing' of carbon dioxide bubbles. *Lab on a Chip*, *11*(20), 3545-3550.

[89] Lefortier, S. G., Hamersma, P. J., Bardow, A., & Kreutzer, M. T. (2012). Rapid microfluidic screening of CO_2 solubility and diffusion in pure and mixed solvents. *Lab on a Chip*, *12*(18), 3387-3391.

[90] Shim, S., Wan, J., Hilgenfeldt, S., Panchal, P. D., & Stone, H. A. (2014). Dissolution without disappearing: multicomponent gas exchange for CO_2 bubbles in a microfluidic channel. *Lab on a Chip*, *14*(14), 2428-2436.

[91] Zhu, C., Li, C., Gao, X., Ma, Y., & Liu, D. (2014). Taylor flow and mass transfer of CO_2 chemical absorption into MEA aqueous solutions in a T-junction microchannel. *International Journal of Heat and Mass Transfer*, *73*, 492-499.

[92] Young, T. (1805). An essay on the cohesion of fluids. *Philosophical Transactions of the Royal Society of London*, *95*, 65-87.

[93] Hetsroni, G. (1982). *Handbook of multiphase systems*. Hemisphere Publishing Corporation, New York.

[94] Brennen, C. E. (2005). *Fundamentals of multiphase flow*. Cambridge University Press.

[95] Günther, A., & Jensen, K. F. (2006). Multiphase microfluidics: from flow characteristics to chemical and materials synthesis. *Lab on a Chip*, *6*(12), 1487-1503.

[96] Zhao, C. X., & Middelberg, A. P. (2011). Two-phase microfluidic flows. *Chemical Engineering Science*, *66*(7), 1394-1411.

[97] Basaran, O. A. (2002). Small-scale free surface flows with breakup: Drop formation and emerging applications. *AIChE J.*, 48: 1842–1848.

[98] Stone, H. A., Stroock, A. D., & Ajdari, A. (2004). Engineering flows in small devices: microfluidics toward a lab-on-a-chip. *Annu. Rev. Fluid Mech.*, *36*, 381-411.

[99] Cristini, V., & Tan, Y. C. (2004). Theory and numerical simulation of droplet dynamics in complex flows—a review. *Lab on a Chip*, *4*(4), 257-264.

[100] Baroud, C. N., & Willaime, H. (2004). Multiphase flows in microfluidics. *Comptes Rendus Physique*, *5*(5), 547-555.

[101] Christopher, G. F., & Anna, S. L. (2007). Microfluidic methods for generating continuous droplet streams. *Journal of Physics D: Applied Physics*, *40*(19), 319.

[102] Huebner, A., Sharma, S., Srisa-Art, M., Hollfelder, F., & Edel, J. B. (2008). Microdroplets: a sea of applications?. *Lab on a Chip*, *8*(8), 1244-1254.

[103] Umbanhowar, P. B., Prasad, V., & Weitz, D. A. (2000). Monodisperse emulsion generation via drop break off in a coflowing stream. *Langmuir*, *16*(2), 347-351.

[104] Gañán-Calvo, A. M., & Gordillo, J. M. (2001). Perfectly monodisperse microbubbling by capillary flow focusing. *Physical review letters*, *87*(27), 274501.

[105] Garstecki, P., Gitlin, I., DiLuzio, W., Whitesides, G. M., Kumacheva, E., & Stone, H. A. (2004). Formation of monodisperse bubbles in a microfluidic flow-focusing device. *Applied Physics Letters*, *85*(13), 2649-2651.

[106] Anna, S. L., Bontoux, N., & Stone, H. A. (2003). Formation of dispersions using "flow focusing" in microchannels. *Applied physics letters*, *82*(3), 364-366.

[107] Rodríguez-Rodríguez, J., Sevilla, A., Martínez-Bazán, C., & Gordillo, J. M. (2015). Generation of microbubbles with applications to industry and medicine. *Annual Review of Fluid Mechanics*, *47*, 405-429.

[108] Angeli, P., & Gavriilidis, A. (2008). Hydrodynamics of Taylor flow in small channels: a review. *Proceedings of the Institution of Mechanical Engineers, Part C: Journal of Mechanical Engineering Science*, *222*(5), 737-751.

[109] Squires, T. M., & Quake, S. R. (2005). Microfluidics: Fluid physics at the nanoliter scale. *Reviews of modern physics*, *77*(3), 977.

[110] Dullien, F. A. (1992). *Porous Media: Fluid Transport And Pore Structure* (edition 2). Academic Press Inc.

[111] Defay, R., Bellemans, A., & Prigogine, I. (1966). *Surface Tension and Adsorption*. Longmans, Green and Co. Ltd., London.

[112] De Gennes, P. G., Brochard-Wyart, F., & Quéré, D. (2013). *Capillarity And Wetting Phenomena: Drops, Bubbles, Pearls, Waves*. Springer Science & Business Media.

[113] Pawar, Y., & Stebe, K. J. (1996). Marangoni effects on drop deformation in an extensional flow: The role of surfactant physical chemistry. I. Insoluble surfactants. *Physics of Fluids*, *8*(7), 1738-1751.

[114] Würger, A. (2014). Thermally driven Marangoni surfers. *Journal of Fluid Mechanics*, *752*, 589-601.

[115] Sahimi, M. (2011). *Flow and Transport in Porous Media And Fractured Rock: from classical methods to modern approaches*. John Wiley & Sons.

[116] Xu, J. H., Li, S. W., Tan, J., Wang, Y. J., & Luo, G. S. (2006). Controllable preparation of monodisperse O/W and W/O emulsions in the same microfluidic device. *Langmuir*, *22*(19), 7943-7946.

[117] Xu, J. H., Li, S. W., Tan, J., Wang, Y. J., & Luo, G. S. (2006). Preparation of highly monodisperse droplet in a T-junction microfluidic device. *AIChE journal*, *52*(9), 3005-3010.

[118] Jonathan Levine. (2011). *Relative permeability experiments of carbon dioxide displacing brine & their implications for carbon sequestration*. Ph.D thesis, Columbia University.

[119] Willhite, G. P. (1986). *Waterflooding*. SPE Textbook Series, volume 3, Richardson.

[120] Nisisako, T., Torii, T., & Higuchi, T. (2002). Droplet formation in a microchannel network. *Lab on a Chip*, *2*(1), 24-26.

[121] Van der Graaf, S., Steegmans, M. L. J., Van Der Sman, R. G. M., Schroën, C. G. P. H., & Boom, R. M. (2005). Droplet formation in a T-shaped microchannel junction: a model system for membrane emulsification. *Colloids and Surfaces A: Physicochemical and Engineering Aspects*, *266*(1), 106-116.

[122] Garstecki, P., Fuerstman, M. J., Stone, H. A., & Whitesides, G. M. (2006). Formation of droplets and bubbles in a microfluidic T-junction—scaling and mechanism of break-up. *Lab on a Chip*, *6*(3), 437-446.

[123] Thorsen, T., Roberts, R. W., Arnold, F. H., & Quake, S. R. (2001). Dynamic pattern formation in a vesicle-generating microfluidic device. *Physical review letters*, *86*(18), 4163-4166.

[124] Xu, J. H., Luo, G. S., Li, S. W., & Chen, G. G. (2006). Shear force induced monodisperse droplet formation in a microfluidic device by controlling wetting properties. *Lab on a Chip*, *6*(1), 131-136.

[125] De Menech, M., Garstecki, P., Jousse, F., & Stone, H. A. (2008). Transition from squeezing to dripping in a microfluidic T-shaped junction. *Journal of fluid mechanics*, *595*, 141-161.

[126] Tice, J. D., Lyon, A. D., & Ismagilov, R. F. (2004). Effects of viscosity on droplet formation and mixing in microfluidic channels. *Analytica chimica acta*, *507*(1), 73-77.

[127] Steegmans, M. L., Schroën, K. G., & Boom, R. M. (2009). Characterization of emulsification at flat microchannel Y junctions. *Langmuir*, *25*(6), 3396-3401.

[128] Steegmans, M. L., Warmerdam, A., Schroën, K. G., & Boom, R. M. (2009). Dynamic interfacial tension measurements with microfluidic Y-junctions. *Langmuir*, *25*(17), 9751-9758.

[129] Anna, S. L., Bontoux, N., & Stone, H. A. (2003). Formation of dispersions using "flow focusing" in microchannels. *Applied physics letters*, *82*(3), 364-366.

[130] Lee, W., Walker, L. M., & Anna, S. L. (2009). Role of geometry and fluid properties in droplet and thread formation processes in planar flow focusing. *Physics of Fluids*, *21*(3), 032103.

[131] Cubaud, T., & Mason, T. G. (2008). Capillary threads and viscous droplets in square microchannels. *Physics of Fluids*, *20*(5), 053302.

[132] Cramer, C., Fischer, P., & Windhab, E. J. (2004). Drop formation in a co-flowing ambient fluid. *Chemical Engineering Science*, *59*(15), 3045-3058.

[133] Utada, A. S., Fernandez-Nieves, A., Gordillo, J. M., & Weitz, D. A. (2008). Absolute instability of a liquid jet in a coflowing stream. *Physical review letters*, *100*(1), 014502.

[134] Kobayashi, I., Nakajima, M., Chun, K., Kikuchi, Y., & Fujita, H. (2002). Silicon array of elongated through-holes for monodisperse emulsion droplets. *AIChE Journal*, *48*(8), 1639-1644.

[135] Sugiura, S., Nakajima, M., & Seki, M. (2002). Prediction of droplet diameter for microchannel emulsification. *Langmuir*, *18*(10), 3854-3859.

[136] Barbier, V., Willaime, H., Tabeling, P., & Jousse, F. (2006). Producing droplets in parallel microfluidic systems. *Physical Review E*, *74*(4), 046306.

[137] Pollack, M. G., Fair, R. B., & Shenderov, A. D. (2000). Electrowetting-based actuation of liquid droplets for microfluidic applications. *Applied Physics Letters*, *77*(11), 1725-1726.

[138] Gascoyne, P. R., Vykoukal, J. V., Schwartz, J. A., Anderson, T. J., Vykoukal, D. M., Current, K. W., ... & Andrews, C. (2004). Dielectrophoresis-based programmable fluidic processors. *Lab on a Chip*, *4*(4), 299-309.

[139] Ahn, K., Kerbage, C., Hunt, T. P., Westervelt, R. M., Link, D. R., & Weitz, D. A. (2006). Dielectrophoretic manipulation of drops for high-speed microfluidic sorting devices. *Applied Physics Letters*, *88*(2), 024104.

[140] Nguyen, N. T., Ng, K. M., & Huang, X. (2006). Manipulation of ferrofluid droplets using planar coils. *Applied Physics Letters*, *89*(5), 052509.

[141] Ozen, O., Aubry, N., Papageorgiou, D. T., & Petropoulos, P. G. (2006). Monodisperse drop formation in square microchannels. *Physical review letters*, *96*(14), 144501.

[142] Kim, H., Luo, D., Link, D., Weitz, D. A., Marquez, M., & Cheng, Z. (2007). Controlled production of emulsion drops using an electric field in a flow-focusing microfluidic device. *Applied Physics Letters*, *91*(13), 133106.

[143] Malloggi, F., Vanapalli, S. A., Gu, H., van den Ende, D., & Mugele, F. (2007). Electrowetting-controlled droplet generation in a microfluidic flow-focusing device. *Journal of Physics: Condensed Matter*, *19*(46), 462101.

[144] Gañán-Calvo, A. M. (2007). Electro-flow focusing: the high-conductivity low-viscosity limit. *Physical review letters*, *98*(13), 134503.

[145] Ting, T. H., Yap, Y. F., Nguyen, N. T., Wong, T. N., Chai, J. C. K., & Yobas, L. (2006). Active control for droplet-based microfluidics. In *Smart Materials, Nano-and Micro-Smart Systems*. International Society for Optics and Photonics, 64160E.

[146] Nguyen, N. T., Ting, T. H., Yap, Y. F., Wong, T. N., Chai, J. C. K., Ong, W. L., ... & Yobas, L. (2007). Thermally mediated droplet formation in microchannels. *Applied Physics Letters*, *91*(8), 084102.

[147] Baroud, C. N., Delville, J. P., Gallaire, F., & Wunenburger, R. (2007). Thermocapillary valve for droplet production and sorting. *Physical Review E*, *75*(4), 046302.

[148] Yeo, L. Y., & Friend, J. R. (2009). Ultrafast microfluidics using surface acoustic waves. *Biomicrofluidics*, *3*(1), 012002.

[149] Friend, J., & Yeo, L. Y. (2011). Microscale acoustofluidics: Microfluidics driven via acoustics and ultrasonics. *Reviews of Modern Physics*, *83*(2), 647.

[150] Ding, X., Li, P., Lin, S. C. S., Stratton, Z. S., Nama, N., Guo, F., ... & Huang, T. J. (2013). Surface acoustic wave microfluidics. *Lab on a Chip*, *13*(18), 3626-3649.

[151] Yeo, L. Y., & Friend, J. R. (2014). Surface acoustic wave microfluidics. *Annual Review of Fluid Mechanics*, *46*, 379-406.

[152] Hewitt, G.F., & Butterworth, D. (1977). *Two phase flow and heat transfer*, Oxford University Press.

[153] Suo, M., & Griffith, P. (1964). Two-phase flow in capillary tubes. *J. Basic Engng*. 86, 576-582.

[154] Fukano, T., & Kariyasaki, A. (1993). Characteristics of gas-liquid two-phase flow in a capillary tube. *Nuclear Engineering and Design*, *141*(1-2), 59-68.

[155] Taitel, Y., & Dukler, A. E. (1976). A model for predicting flow regime transitions in horizontal and near horizontal gas-liquid flow. *AIChE Journal*, *22*(1), 47-55.

[156] Barnea, D., Luninski, Y., & Taitel, Y. (1983). Flow pattern in horizontal and vertical two phase flow in small diameter pipes. *The Canadian Journal of Chemical Engineering*, *61*(5), 617-620.

[157] Triplett, K. A., Ghiaasiaan, S. M., Abdel-Khalik, S. I., & Sadowski, D. L. (1999). Gas–liquid two-phase flow in microchannels Part I: two-phase flow patterns. *International Journal of Multiphase Flow*, *25*(3), 377-394.

[158] Rebrov, E. V. (2010). Two-phase flow regimes in microchannels. *Theoretical foundations of chemical engineering*, *44*(4), 355-367.

[159] Cubaud, T., & Ho, C. M. (2004). Transport of bubbles in square microchannels. *Physics of fluids*, *16*(12), 4575-4585.

[160] Hassan, I., Vaillancourt, M., & Pehlivan, K. (2005). Two-phase flow regime transitions in microchannels: a comparative experimental study. *Microscale Thermophysical Engineering*, *9*(2), 165-182.

[161] Chung, P. Y., & Kawaji, M. (2004). The effect of channel diameter on adiabatic two-phase flow characteristics in microchannels. *International journal of multiphase flow*, *30*(7), 735-761.

[162] Yue, J., Luo, L., Gonthier, Y., Chen, G., & Yuan, Q. (2008). An experimental investigation of gas–liquid two-phase flow in single microchannel contactors. *Chemical Engineering Science*, *63*(16), 4189-4202.

[163] Barajas, A. M., & Panton, R. L. (1993). The effects of contact angle on two-phase flow in capillary tubes. *International Journal of Multiphase Flow*, *19*(2), 337-346.

[164] Cubaud, T., Ulmanella, U., & Ho, C. M. (2006). Two-phase flow in microchannels with surface modifications. *Fluid Dynamics Research*, *38*(11), 772-786.

[165] Lee, C. Y., & Lee, S. Y. (2008). Pressure drop of two-phase plug flow in round mini-channels: influence of surface wettability. *Experimental Thermal and Fluid Science*, *32*(8), 1716-1722.

[166] Waelchli, S., & von Rohr, P. R. (2006). Two-phase flow characteristics in gas–liquid microreactors. *International journal of multiphase flow*, *32*(7), 791-806.

[167] Pohorecki, R., Sobieszuk, P., Kula, K., Moniuk, W., Zieliński, M., Cygański, P., & Gawiński, P. (2008). Hydrodynamic regimes of gas–liquid flow in a microreactor channel. *Chemical Engineering Journal*, *135*, S185-S190.

[168] Shao, N., Salman, W., Gavriilidis, A., & Angeli, P. (2008). CFD simulations of the effect of inlet conditions on Taylor flow formation. *International journal of heat and fluid flow*, *29*(6), 1603-1611.

[169] Dreyfus, R., Tabeling, P., & Willaime, H. (2003). Ordered and disordered patterns in two-phase flows in microchannels. *Physical review letters*, *90*(14), 144505.

[170] Zhao, Y., Chen, G., & Yuan, Q. (2006). Liquid-liquid two-phase flow patterns in a rectangular microchannel. *AIChE journal*, *52*(12), 4052-4060.

[171] Dessimoz, A. L., Cavin, L., Renken, A., & Kiwi-Minsker, L. (2008). Liquid–liquid two-phase flow patterns and mass transfer characteristics in rectangular glass microreactors. *Chemical Engineering Science*, *63*(16), 4035-4044.

[172] Cherlo, S. K. R., Kariveti, S., & Pushpavanam, S. (2009). Experimental and numerical investigations of two-phase (liquid− liquid) flow behavior in rectangular microchannels. *Industrial & Engineering Chemistry Research*, *49*(2), 893-899.

[173] Kashid, M. N., Renken, A., & Kiwi-Minsker, L. (2011). Gas–liquid and liquid–liquid mass transfer in microstructured reactors. *Chemical Engineering Science*, *66*(17), 3876-3897.

[174] Betz, A. R., & Attinger, D. (2010). Can segmented flow enhance heat transfer in microchannel heat sinks?. *International Journal of Heat and Mass Transfer*, *53*(19), 3683-3691.

[175] Kandlikar, S. G., Colin, S., Peles, Y., Garimella, S., Pease, R. F., Brandner, J. J., & Tuckerman, D. B. (2013). Heat transfer in microchannels—2012 status and research needs. *Journal of Heat Transfer*, *135*(9), 091001.

[176] Garstecki, P., Stone, H. A., & Whitesides, G. M. (2005). Mechanism for flow-rate controlled breakup in confined geometries: a route to monodisperse emulsions. *Physical Review Letters*, *94*(16), 164501.

[177] Husny, J., & Cooper-White, J. J. (2006). The effect of elasticity on drop creation in T-shaped microchannels. *Journal of non-newtonian fluid mechanics*, *137*(1), 121-136.

[178] van Sint Annaland, M., Dijkhuizen, W., Deen, N. G., & Kuipers, J. A. M. (2006). Numerical simulation of behavior of gas bubbles using a 3-D front-tracking method. *AIChE Journal*, *52*(1), 99-110.

[179] Weber, M. W., & Shandas, R. (2007). Computational fluid dynamics analysis of microbubble formation in microfluidic flow-focusing devices. *Microfluidics and Nanofluidics*, *3*(2), 195-206.

[180] Hua, J., Zhang, B., & Lou, J. (2007). Numerical simulation of microdroplet formation in coflowing immiscible liquids. *AIChE Journal*, *53*(10), 2534-2548.

[181] Goel, D., & Buwa, V. V. (2008). Numerical simulations of bubble formation and rise in microchannels. *Industrial & Engineering Chemistry Research*, *48*(17), 8109-8120.

[182] Sang, L., Hong, Y., & Wang, F. (2009). Investigation of viscosity effect on droplet formation in T-shaped microchannels by numerical and analytical methods. *Microfluidics and Nanofluidics*, *6*(5), 621-635.

[183] Tice, J. D., Song, H., Lyon, A. D., & Ismagilov, R. F. (2003). Formation of droplets and mixing in multiphase microfluidics at low values of the Reynolds and the capillary numbers. *Langmuir*, *19*(22), 9127-9133.

[184] Xu, J. H., Li, S. W., Tan, J., & Luo, G. S. (2008). Correlations of droplet formation in T-junction microfluidic devices: from squeezing to dripping. *Microfluidics and Nanofluidics*, *5*(6), 711-717.

[185] Van der Graaf, S., Nisisako, T., Schroen, C. G. P. H., Van Der Sman, R. G. M., & Boom, R. M. (2006). Lattice Boltzmann simulations of droplet formation in a T-shaped microchannel. *Langmuir*, *22*(9), 4144-4152.

[186] Ganán-Calvo, A. M. (2004). Perfectly monodisperse microbubbling by capillary flow focusing: An alternate physical description and universal scaling. *Physical Review E*, *69*(2), 027301.

[187] Cubaud, T., Tatineni, M., Zhong, X., & Ho, C. M. (2005). Bubble dispenser in microfluidic devices. *Physical Review E*, *72*(3), 037302.

[188] Xiong, R., Bai, M., & Chung, J. N. (2007). Formation of bubbles in a simple co-flowing micro-channel. *Journal of Micromechanics and Microengineering*, *17*(5), 1002.

[189] Yasuno, M., Sugiura, S., Iwamoto, S., Nakajima, M., Shono, A., & Satoh, K. (2004). Monodispersed microbubble formation using microchannel technique. *AIChE journal*, *50*(12), 3227-3233.

[190] Xu, J. H., Li, S. W., Chen, G. G., & Luo, G. S. (2006). Formation of monodisperse microbubbles in a microfluidic device. *AIChE journal*, *52*(6), 2254-2259.

[191] Fu, T., Ma, Y., Funfschilling, D., & Li, H. Z. (2009). Bubble formation and breakup mechanism in a microfluidic flow-focusing device. *Chemical Engineering Science*, *64*(10), 2392-2400.

[192] Dietrich, N., Poncin, S., Midoux, N., & Li, H. Z. (2008). Bubble formation dynamics in various flow-focusing microdevices. *Langmuir*, *24*(24), 13904-13911.

[193] Tan, J., Li, S. W., Wang, K., & Luo, G. S. (2009). Gas–liquid flow in T-junction microfluidic devices with a new perpendicular rupturing flow route. *Chemical Engineering Journal*, *146*(3), 428-433.

[194] Xiong, R., & Chung, J. N. (2009). Bubble generation and transport in a microfluidic device with high aspect ratio. *Experimental Thermal and Fluid Science*, *33*(8), 1156-1162.

[195] Zhang, Y., & Wang, L. (2009). Experimental investigation of bubble formation in a microfluidic T-shaped junction. *Nanoscale and Microscale Thermophysical Engineering*, *13*(4), 228-242.

[196] Gupta, R., Leung, S. S., Manica, R., Fletcher, D. F., & Haynes, B. S. (2013). Hydrodynamics of liquid–liquid Taylor flow in microchannels. *Chemical Engineering Science*, *92*, 180-189.

[197] Kreutzer, M. T., Kapteijn, F., Moulijn, J. A., Kleijn, C. R., & Heiszwolf, J. J. (2005). Inertial and interfacial effects on pressure drop of Taylor flow in capillaries. *AIChE Journal*, *51*(9), 2428-2440.

[198] Fries, D. M., Trachsel, F., & von Rohr, P. R. (2008). Segmented gas–liquid flow characterization in rectangular microchannels. *International Journal of Multiphase Flow*, *34*(12), 1108-1118.

[199] Kolb, W. B., & Cerro, R. L. (1993). Film flow in the space between a circular bubble and a square tube. *Journal of colloid and interface science*, *159*(2), 302-311.

[200] Taylor, G. I. (1961). Deposition of a viscous fluid on the wall of a tube. *Journal of fluid mechanics*, *10*(2), 161-165.

[201] Baroud, C. N., Gallaire, F., & Dangla, R. (2010). Dynamics of microfluidic droplets. *Lab on a Chip*, *10*(16), 2032-2045.

[202] Aussillous, P., & Quéré, D. (2000). Quick deposition of a fluid on the wall of a tube. *Physics of fluids*, *12*(10), 2367-2371.

[203] Thulasidas, T. C., Abraham, M. A., & Cerro, R. L. (1995). Bubble-train flow in capillaries of circular and square cross section. *Chemical Engineering Science*, *50*(2), 183-199.

[204] Hazel, A. L., & Heil, M. (2002). The steady propagation of a semi-infinite bubble into a tube of elliptical or rectangular cross-section. *Journal of fluid mechanics*, *470*, 91.

[205] Chaoqun, Y., Yuchao, Z., Chunbo, Y., Minhui, D., Zhengya, D., & Guangwen, C. (2013). Characteristics of slug flow with inertial effects in a rectangular microchannel. *Chemical Engineering Science*, *95*, 246-256.

[206] Edvinsson, R. K., & Irandoust, S. (1996). Finite-element analysis of Taylor flow. *AIChE Journal*, *42*(7), 1815-1823.

[207] Taha, T., & Cui, Z. F. (2004). Hydrodynamics of slug flow inside capillaries. *Chemical Engineering Science*, *59*(6), 1181-1190.

[208] Talimi, V., Muzychka, Y. S., & Kocabiyik, S. (2012). A review on numerical studies of slug flow hydrodynamics and heat transfer in microtubes and microchannels. *International Journal of Multiphase Flow*, *39*, 88-104.

[209] Abadie, T., Aubin, J., Legendre, D., & Xuereb, C. (2012). Hydrodynamics of gas–liquid Taylor flow in rectangular microchannels. *Microfluidics and nanofluidics*, *12*(1-4), 355-369.

[210] Xu, B., Cai, W., Liu, X., & Zhang, X. (2013). Mass transfer behavior of liquid–liquid slug flow in circular cross-section microchannel. *Chemical Engineering Research and Design*, *91*(7), 1203-1211.

[211] Biswas, K. G., Das, G., Ray, S., & Basu, J. K. (2015). Mass transfer characteristics of liquid–liquid flow in small diameter conduits. *Chemical Engineering Science*, *122*, 652-661.

[212] John, J. J., Kuhn, S., Braeken, L., & Van Gerven, T. (2016). Ultrasound assisted liquid–liquid extraction in microchannels—A direct contact method. *Chemical Engineering and Processing: Process Intensification*, *102*, 37-46.

[213] Che, Z., Wong, T. N., Nguyen, N. T., & Yang, C. (2014). Asymmetric heat transfer in liquid–liquid segmented flow in microchannels. *International Journal of Heat and Mass Transfer*, *77*, 385-394.

[214] Romano, M., Pradere, C., Toutain, J., Hany, C., & Batsale, J. C. (2014). Quantitative thermal analysis of heat transfer in liquid–liquid biphasic millifluidic droplet flows. *Quantitative InfraRed Thermography Journal*, *11*(2), 134-160.

[215] Dai, Z., Guo, Z., Fletcher, D. F., & Haynes, B. S. (2015). Taylor flow heat transfer in microchannels—Unification of liquid–liquid and gas–liquid results. *Chemical Engineering Science*, *138*, 140-152.

[216] Kashid, M. N., & Agar, D. W. (2007). Hydrodynamics of liquid–liquid slug flow capillary microreactor: flow regimes, slug size and pressure drop. *Chemical Engineering Journal*, *131*(1), 1-13.

[217] Ghaini, A., Mescher, A., & Agar, D. W. (2011). Hydrodynamic studies of liquid–liquid slug flows in circular microchannels. *Chemical engineering science*, *66*(6), 1168-1178.

[218] Jovanović, J., Zhou, W., Rebrov, E. V., Nijhuis, T. A., Hessel, V., & Schouten, J. C. (2011). Liquid–liquid slug flow: hydrodynamics and pressure drop. *Chemical Engineering Science*, *66*(1), 42-54.

[219] Eain, M. M. G., Egan, V., Howard, J., Walsh, P., Walsh, E., & Punch, J. (2015). Review and extension of pressure drop models applied to Taylor flow regimes. *International Journal of Multiphase Flow*, *68*, 1-9.

[220] Bretherton, F. P. (1961). The motion of long bubbles in tubes. *Journal of Fluid Mechanics*, *10*(02), 166-188.

[221] Warnier, M. J. F., De Croon, M. H. J. M., Rebrov, E. V., & Schouten, J. C. (2010). Pressure drop of gas–liquid Taylor flow in round micro-capillaries for low to intermediate Reynolds numbers. *Microfluidics and Nanofluidics*, *8*(1), 33.

[222] Tsaoulidis, D., Dore, V., Angeli, P., Plechkova, N. V., & Seddon, K. R. (2013). Flow patterns and pressure drop of ionic liquid–water two-phase flows in microchannels. *International Journal of Multiphase Flow*, *54*, 1-10.

[223] Tsaoulidis, D., & Angeli, P. (2016). Effect of channel size on liquid-liquid plug flow in small channels. *AIChE Journal*, *62*(1), 315-324.

[224] Walsh, E., Muzychka, Y., Walsh, P., Egan, V., & Punch, J. (2009). Pressure drop in two phase slug/bubble flows in mini scale capillaries. *International Journal of Multiphase Flow*, *35*(10), 879-884.

[225] Fairbrother, F., & Stubbs, A. E. (1935). 119. Studies in electro-endosmosis. Part VI. The "bubble-tube" method of measurement. *Journal of the Chemical Society (Resumed)*, 527-529.

[226] Wong, H., Radke, C. J., & Morris, S. (1995). The motion of long bubbles in polygonal capillaries. Part 1. Thin films. *Journal of Fluid Mechanics*, *292*, 71-94.

[227] Wong, H., Radke, C. J., & Morris, S. (1995). The motion of long bubbles in polygonal capillaries. Part 2. Drag, fluid pressure and fluid flow. *Journal of Fluid Mechanics*, *292*, 95-110.

[228] Sarrazin, F., Bonometti, T., Prat, L., Gourdon, C., & Magnaudet, J. (2008). Hydrodynamic structures of droplets engineered in rectangular micro-channels. *Microfluidics and Nanofluidics*, *5*(1), 131-137.

[229] Jousse, F., Lian, G., Janes, R., & Melrose, J. (2005). Compact model for multi-phase liquid–liquid flows in micro-fluidic devices. *Lab on a Chip*, *5*(6), 646-656.

[230] Fuerstman, M. J., Lai, A., Thurlow, M. E., Shevkoplyas, S. S., Stone, H. A., & Whitesides, G. M. (2007). The pressure drop along rectangular microchannels containing bubbles. *Lab on a Chip*, *7*(11), 1479-1489.

[231] Jakiela, S., Makulska, S., Korczyk, P. M., & Garstecki, P. (2011). Speed of flow of individual droplets in microfluidic channels as a function of the capillary number, volume of droplets and contrast of viscosities. *Lab on a Chip*, *11*(21), 3603-3608.

[232] Cox, B. G. (1964). An experimental investigation of the streamlines in viscous fluid expelled from a tube. *Journal of Fluid Mechanics*, *20*(2), 193-200.

[233] Udell, K. S. (1989). Boundary integral analysis of the creeping flow of long bubbles in capillaries. *Journal of applied mechanics*, *56*, 211.

[234] Westborg, H., & Hassager, O. (1989). Creeping motion of long bubbles and drops in capillary tubes. *Journal of Colloid and Interface Science*, *133*(1), 135-147.

[235] Thulasidas, T. C., Abraham, M. A., & Cerro, R. L. (1997). Flow patterns in liquid slugs during bubble-train flow inside capillaries. *Chemical Engineering Science*, *52*(17), 2947-2962.

[236] Giavedoni, M. D., & Saita, F. A. (1997). The axisymmetric and plane cases of a gas phase steadily displacing a Newtonian liquid—A simultaneous solution of the governing equations. *Physics of Fluids*, *9*(8), 2420-2428.

[237] Heil, M. (2001). Finite Reynolds number effects in the Bretherton problem. *Physics of Fluids*, *13*(9), 2517-2521.

[238] Taha, T., & Cui, Z. F. (2006). CFD modelling of slug flow inside square capillaries. *Chemical Engineering Science*, *61*(2), 665-675.

[239] Günther, A., Jhunjhunwala, M., Thalmann, M., Schmidt, M. A., & Jensen, K. F. (2005). Micromixing of miscible liquids in segmented gas−liquid flow. *Langmuir*, *21*(4), 1547-1555.

[240] Lindken, R., Rossi, M., Große, S., & Westerweel, J. (2009). Micro-particle image velocimetry (μPIV): recent developments, applications, and guidelines. *Lab on a Chip*, *9*(17), 2551-2567.

[241] Kashid, M. N., Gerlach, I., Goetz, S., Franzke, J., Acker, J. F., Platte, F., ... & Turek, S. (2005). Internal circulation within the liquid slugs of a liquid− liquid slug-flow capillary microreactor. *Industrial & engineering chemistry research*, *44*(14), 5003-5010.

[242] Sarrazin, F., Loubiere, K., Prat, L., Gourdon, C., Bonometti, T., & Magnaudet, J. (2006). Experimental and numerical study of droplets hydrodynamics in microchannels. *AIChE Journal*, *52*(12), 4061-4070.

[243] Kinoshita, H., Kaneda, S., Fujii, T., & Oshima, M. (2007). Three-dimensional measurement and visualization of internal flow of a moving droplet using confocal micro-PIV. *Lab on a Chip*, *7*(3), 338-346.

[244] van Steijn, V., Kreutzer, M. T., & Kleijn, C. R. (2007). μ-PIV study of the formation of segmented flow in microfluidic T-junctions. *Chemical Engineering Science*, *62*(24), 7505-7514.

[245] Malsch, D., Kielpinski, M., Merthan, R., Albert, J., Mayer, G., Köhler, J. M., ... & Henkel, T. (2008). μPIV-analysis of Taylor flow in micro channels. *Chemical Engineering Journal*, *135*, 166-172.

[246] Miessner, U., Lindken, R. & Westerweel, J. (2008). 3D-velocity measurements in microscopic two-phase flows by means of micro PIV. In *Proceedings of the 14th Int. Symp. on Applications of Laser Techniques to Fluid Mechanics*, Lisbon, Portugal, paper 04, 1-2.

[247] Oishi, M., Kinoshita, H., Fujii, T., & Oshima, M. (2011). Simultaneous measurement of internal and surrounding flows of a moving droplet using multicolour confocal micro-particle image velocimetry (micro-PIV). *Measurement Science and Technology*, *22*(10), 105401.

[248] Waals, J. D., & Rowlinson, J. S. (1988). *JD van der Waals: On the Continuity of the Gaseous and Liquid States* (vol. 14). North Holland, Amsterdam, Netherlands.

[249] Redlich, O., & Kwong, J. N. (1949). On the thermodynamics of solutions. V. An equation of state. Fugacities of gaseous solutions. *Chemical reviews*, *44*(1), 233-244.

[250] Soave, G. (1972). Equilibrium constants from a modified Redlich-Kwong equation of state. *Chemical Engineering Science*, *27*(6), 1197-1203.

[251] Peng, D. Y., & Robinson, D. B. (1976). A new two-constant equation of state. *Ind. Eng. Chem. Fundam*, *15*(1), 59-64.

[252] Martin, J. J. (1979). Cubic equations of state-which?. *Industrial & Engineering Chemistry Fundamentals*, *18*(2), 81-97.

[253] Péneloux, A., Rauzy, E., & Fréze, R. (1982). A consistent correction for Redlich-Kwong-Soave volumes. *Fluid Phase Equilibria*, *8*(1), 7-23.

[254] Patel, N. C., & Teja, A. S. (1982). A new cubic equation of state for fluids and fluid mixtures. *Chemical Engineering Science*, *37*(3), 463-473.

[255] Valderrama, J. O. (2003). The state of the cubic equations of state. *Industrial & engineering chemistry research*, *42*(8), 1603-1618.

[256] Bird, R.B., Stewart, W.E. & Lightfoot, E.N. (2002). *Transport Phenomena*, John Wiley & Sons, New York, US.

[257] Higbie, R. (1935). The rate of absorption of a pure gas into still liquid during short periods of exposure. *Transactions of the AIChE*, 31, 365-389.

[258] Ward, C. A., & Fang, G. (1999). Expression for predicting liquid evaporation flux: Statistical rate theory approach. *Physical Review E*, *59*(1), 429.

[259] Handlos, A. E., & Baron, T. (1957). Mass and heat transfer from drops in liquid-liquid extraction. *AIChE Journal*, *3*(1), 127-136.

[260] Danckwerts, P. V. (1955). Gas absorption accompanied by chemical reaction. *AIChE Journal*, *1*(4), 456-463.

[261] Olander, D. R. (1960). Simultaneous mass transfer and equilibrium chemical reaction. *AIChE Journal*, *6*(2), 233-239.

[262] Whitman, W. G. (1923). A preliminary experimental confirmation of the two film theory of gas absorption. *Chemical and Metallurgical Engineering*, 29, 146-148.

[263] Kuo, J. S., & Chiu, D. T. (2011). Controlling mass transport in microfluidic devices. *Annual Review of Analytical Chemistry*, *4*, 275-296.

[264] Kashid, M. N., Renken, A., & Kiwi-Minsker, L. (2011). Gas–liquid and liquid–liquid mass transfer in microstructured reactors. *Chemical Engineering Science*, *66*(17), 3876-3897.

[265] Fick, A. (1855). Ueber diffusion. *Annals of Physics*, *170* (1), 59-86.

[266] Ranz, W. E., & Marshall, W. R. (1952). Evaporation from drops. *Chemical Engineering Progress*, *48*(3), 141446.

[267] Cussler, E. L. (2009). *Diffusion: mass transfer in fluid systems*. Cambridge University Press.

[268] Toor, H. L., & Marchello, J. M. (1958). Film-penetration model for mass and heat transfer. *AIChE Journal*, *4*(1), 97-101.

[269] Whitman, W. G. (1962). The two film theory of gas absorption. *International journal of heat and mass transfer*, *5*(5), 429-433.

[270] Jensen, K. F. (2006). Silicon-based microchemical systems: characteristics and applications. *MRS bulletin*, *31*(02), 101-107.

[271] Lang, W. (1996). Silicon microstructuring technology. *Materials Science and Engineering: R: Reports*, *17*(1), 1-55.

[272] Anderson, J. R., Chiu, D. T., Wu, H., Schueller, O. J., & Whitesides, G. M. (2000). Fabrication of microfluidic systems in poly (dimethylsiloxane). *Electrophoresis*, *21*(1), 27-40.

[273] Chen, Q., Chen, Q., & Maccioni, G. (2013). Fabrication of microfluidics structures on different glasses by simplified imprinting technique. *Current Applied Physics*, *13*(1), 256-261.

[274] Becker, H., & Locascio, L. E. (2002). Polymer microfluidic devices. *Talanta*, *56*(2), 267-287.

[275] Pan, Y. J., & Yang, R. J. (2006). A glass microfluidic chip adhesive bonding method at room temperature. *Journal of Micromechanics and Microengineering*, *16*(12), 2666.

[276] Kopp, M. U., De Mello, A. J., & Manz, A. (1998). Chemical amplification: continuous-flow PCR on a chip. *Science*, *280*(5366), 1046-1048.

[277] Reyes, D. R., Iossifidis, D., Auroux, P. A., & Manz, A. (2002). Micro total analysis systems. 1. Introduction, theory, and technology. *Analytical chemistry*, *74*(12), 2623-2636.

[278] McCreedy, T. (2000). Fabrication techniques and materials commonly used for the production of microreactors and micro total analytical systems. *TrAC Trends in Analytical Chemistry*, *19*(6), 396-401.

[279] Rodriguez, I., Spicar-Mihalic, P., Kuyper, C. L., Fiorini, G. S., & Chiu, D. T. (2003). Rapid prototyping of glass microchannels. *Analytica Chimica Acta*, *496*(1), 205-215.

[280] Becker, H., & Gärtner, C. (2008). Polymer microfabrication technologies for microfluidic systems. *Analytical and bioanalytical chemistry*, *390*(1), 89-111.

[281] Gibbs, J. H., & DiMarzio, E. A. (1958). Nature of the glass transition and the glassy state. *The Journal of Chemical Physics*, *28*(3), 373-383.

[282] Mayes, A. M. (1994). Glass transition of amorphous polymer surfaces. *Macromolecules*, *27*(11), 3114-3115.

[283] Ahn, C. H., Choi, J. W., Beaucage, G., Nevin, J. H., Lee, J. B., Puntambekar, A., & Lee, J. Y. (2004). Disposable smart lab on a chip for point-of-care clinical diagnostics. *Proceedings of the IEEE*, *92*(1), 154-173.

[284] Mela, P., van Den Berg, A., Fintschenko, Y., Cummings, E. B., Simmons, B. A., & Kirby, B. J. (2005). The zeta potential of cyclo-olefin polymer microchannels and its effects on insulative (electrodeless) dielectrophoresis particle trapping devices. *Electrophoresis*, *26*(9), 1792-1799.

[285] Yang, Y., Li, C., Kameoka, J., Lee, K. H., & Craighead, H. G. (2005). A polymeric microchip with integrated tips and in situ polymerized monolith for electrospray mass spectrometry. *Lab on a Chip*, *5*(8), 869-876.

[286] Berthier, E., Young, E. W., & Beebe, D. (2012). Engineers are from PDMS-land, Biologists are from Polystyrenia. *Lab on a Chip*, *12*(7), 1224-1237.

[287] Quake, S. R., & Scherer, A. (2000). From micro-to nanofabrication with soft materials. *Science*, *290*(5496), 1536-1540.

[288] Marre, S., Adamo, A., Basak, S., Aymonier, C., & Jensen, K. F. (2010). Design and packaging of microreactors for high pressure and high temperature applications. *Industrial & Engineering Chemistry Research*, *49*(22), 11310-11320.

[289] Anderson, T. L. (1991). *Fracture Mechanics: Fundamentals and Applications*, Taylor & Francis Group, London.

[290] http://www.schott.com/tubing/english/download/schott-tubing_brochure_technical-glasses_english.pdf

[291] Gere, J. M., & Goodno, B. J. (2012). *Mechanics of Materials* (edition 8). Cengage Learning, CT, 763-765.

[292] http://mems.stanford.edu/~hopcroft/Publications/Hopcroft_Youngs_Modulus_Silicon.pdf

[293] Laermer, F., & Schilp, A. (1996). Method of anisotropically etching silicon, *U.S. Patent No. 5,501,893*. Washington, DC: U.S. Patent and Trademark Office.

[294] Kenis, P. J., Ismagilov, R. F., & Whitesides, G. M. (1999). Microfabrication inside capillaries using multiphase laminar flow patterning. *Science*, *285*(5424), 83-85.

[295] Garstecki, P., Fuerstman, M. J., & Whitesides, G. M. (2005). Nonlinear dynamics of a flow-focusing bubble generator: An inverted dripping faucet. *Physical review letters*, *94*(23), 234502.

[296] Leshansky, A. M., & Pismen, L. M. (2009). Breakup of drops in a microfluidic T junction. *Physics of Fluids*, *21*(2), 023303.

[297] van Steijn, V., Kleijn, C. R., & Kreutzer, M. T. (2009). Flows around confined bubbles and their importance in triggering pinch-off. *Physical review letters*, *103*(21), 214501.

[298] Van Hoeve, W., Dollet, B., Versluis, M., & Lohse, D. (2011). Microbubble formation and pinch-off scaling exponent in flow-focusing devices. *Physics of Fluids*, *23*(9), 092001.

[299] Hoang, D. A., Portela, L. M., Kleijn, C. R., Kreutzer, M. T., & Van Steijn, V. (2013). Dynamics of droplet breakup in a T-junction. *Journal of Fluid Mechanics*, *717*, R4.

[300] Guillot, P., & Colin, A. (2005). Stability of parallel flows in a microchannel after a T junction. *Physical Review E*, *72*(6), 066301.

[301] Christopher, G. F., Noharuddin, N. N., Taylor, J. A., & Anna, S. L. (2008). Experimental observations of the squeezing-to-dripping transition in T-shaped microfluidic junctions. *Physical Review E*, *78*(3), 036317.

[302] van Steijn, V., Kleijn, C. R., & Kreutzer, M. T. (2010). Predictive model for the size of bubbles and droplets created in microfluidic T-junctions. *Lab on a Chip*, *10*(19), 2513-2518.

[303] Atencia, J., & Beebe, D. J. (2005). Controlled microfluidic interfaces. *Nature*, *437*(7059), 648-655.

[304] Seemann, R., Brinkmann, M., Pfohl, T., & Herminghaus, S. (2011). Droplet based microfluidics. *Reports on progress in physics*, *75*(1), 016601.

[305] Taylor, G. I. (1934). The formation of emulsions in definable fields of flow. *Proceedings of the Royal Society of London. Series A, Containing Papers of a Mathematical and Physical Character*, *146*(858), 501-523.

[306] Xu, J. H., Luo, G. S., Chen, G. G., & Wang, J. D. (2005). Experimental and theoretical approaches on droplet formation from a micrometer screen hole. *Journal of Membrane Science*, *266*(1), 121-131.

[307] Sang, L., Hong, Y., & Wang, F. (2009). Investigation of viscosity effect on droplet formation in T-shaped microchannels by numerical and analytical methods. *Microfluidics and Nanofluidics*, *6*(5), 621-635.

[308] Abate, A. R., Mary, P., van Steijn, V., & Weitz, D. A. (2012). Experimental validation of plugging during drop formation in a T-junction. *Lab on a Chip*, *12*(8), 1516-1521.

[309] Liu, H., & Zhang, Y. (2009). Droplet formation in a T-shaped microfluidic junction. *Journal of applied physics*, *106*(3), 034906.

[310] Anna, S. L. (2016). Droplets and bubbles in microfluidic devices. *Annual Review of Fluid Mechanics*, *48*, 285-309.

[311] Glawdel, T., Elbuken, C., & Ren, C. L. (2012). Droplet formation in microfluidic T-junction generators operating in the transitional regime. I. Experimental observations. *Physical Review E*, *85*(1), 016322.

[312] Glawdel, T., Elbuken, C., & Ren, C. L. (2012). Droplet formation in microfluidic T-junction generators operating in the transitional regime. II. Modeling. *Physical Review E, 85*(1), 016323.

[313] Gobby, D., Angeli, P., & Gavriilidis, A. (2001). Mixing characteristics of T-type microfluidic mixers. *Journal of Micromechanics and microengineering*, *11*(2), 126.

[314] Akpa, B. S., Matthews, S. M., Sederman, A. J., Yunus, K., Fisher, A. C., Johns, M. L., & Gladden, L. F. (2007). Study of miscible and immiscible flows in a microchannel using magnetic resonance imaging. *Analytical chemistry*, *79*(16), 6128-6134.

[315] Dogan, H., Nas, S., & Muradoglu, M. (2009). Mixing of miscible liquids in gas-segmented serpentine channels. *International Journal of Multiphase Flow*, *35*(12), 1149-1158.

[316] Tang, S. K., Derda, R., Quan, Q., Lončar, M., & Whitesides, G. M. (2011). Continuously tunable microdroplet-laser in a microfluidic channel. *Optics express*, *19*(3), 2204-2215.

[317] Cubaud, T., & Notaro, S. (2014). Regimes of miscible fluid thread formation in microfluidic focusing sections. *Physics of Fluids*, *26*(12), 122005.

[318] Nguyen, P., Mohaddes, D., Riordon, J., Fadaei, H., Lele, P., & Sinton, D. (2015). Fast fluorescence-based microfluidic method for measuring minimum miscibility pressure of CO_2 in crude oils. *Analytical chemistry*, *87*(6), 3160-3164.

[319] Carroll, J. J., Slupsky, J. D., & Mather, A. E. (1991). The solubility of carbon dioxide in water at low pressure. *Journal of Physical and Chemical Reference Data*, *20*(6), 1201-1209.

[320] Logan, S. R. (1998). The behavior of a pair of partially miscible liquids. *J. Chem. Educ*, *75*(3), 339.

[321] Spycher, N., Pruess, K., & Ennis-King, J. (2003). CO_2-H_2O mixtures in the geological sequestration of CO_2. I. Assessment and calculation of mutual solubilities from 12 to 100C and up to 600 bar. *Geochimica et cosmochimica acta*, *67*(16), 3015-3031.

[322] Diamond, L. W., & Akinfiev, N. N. (2003). Solubility of CO_2 in water from −1.5 to 100C and from 0.1 to 100 MPa: evaluation of literature data and thermodynamic modelling. *Fluid phase equilibria*, *208*(1), 265-290.

[323] Wang, S., & Clarens, A. F. (2012). The effects of CO_2-brine rheology on leakage processes in geologic carbon sequestration. *Water Resources Research*, *48*(8).

[324] Anderson, D. M., McFadden, G. B., & Wheeler, A. A. (1998). Diffuse-interface methods in fluid mechanics. *Annual review of fluid mechanics*, *30*(1), 139-165.

[325] Luther, S. K., & Braeuer, A. (2012). High-pressure microfluidics for the investigation into multi-phase systems using the supercritical fluid extraction of emulsions (SFEE). *The Journal of Supercritical Fluids*, *65*, 78-86.

[326] Fadaei, H., Scarff, B., & Sinton, D. (2011). Rapid microfluidics-based measurement of CO_2 diffusivity in bitumen. *Energy & Fuels*, *25*(10), 4829-4835.

[327] Sell, A., Fadaei, H., Kim, M., & Sinton, D. (2012). Measurement of CO_2 diffusivity for carbon sequestration: A microfluidic approach for reservoir-specific analysis. *Environmental science & technology*, *47*(1), 71-78.

[328] Marre, S., Baek, J., Park, J., Bawendi, M. G., & Jensen, K. F. (2009). High-pressure/high-temperature microreactors for nanostructure synthesis. *JALA: Journal of the Association for Laboratory Automation*, *14*(6), 367-373.

[329] Marre, S., Aymonier, C., Subra, P., & Mignard, E. (2009). Dripping to jetting transitions observed from supercritical fluid in liquid microcoflows. *Applied Physics Letters*, *95*(13), 134105.

[330] Blanch-Ojea, R., Tiggelaar, R. M., Pallares, J., Grau, F. X., & Gardeniers, J. G. E. (2012). Flow of CO_2–ethanol and of CO_2–methanol in a non-adiabatic microfluidic T-junction at high pressures. *Microfluidics and nanofluidics*, *12*(6), 927-940.

[331] Guillaument, R., Erriguible, A., Aymonier, C., Marre, S., & Subra-Paternault, P. (2013). Numerical simulation of dripping and jetting in supercritical fluids/liquid micro coflows. *The Journal of Supercritical Fluids*, *81*, 15-22.

[332] Luther, S. K., Schuster, J. J., Leipertz, A., & Braeuer, A. (2013). Microfluidic investigation into mass transfer in compressible multi-phase systems composed of oil, water and carbon dioxide at elevated pressure. *The Journal of Supercritical Fluids*, *84*, 121-131.

[333] Ogden, S., Bodén, R., Do-Quang, M., Wu, Z. G., Amberg, G., & Hjort, K. (2014). Fluid behavior of supercritical carbon dioxide with water in a double-Y-channel microfluidic chip. *Microfluidics and nanofluidics*, *17*(6), 1105-1112.

[334] Knaust, S., Andersson, M., Hjort, K., & Klintberg, L. (2016). Influence of surface modifications and channel structure for microflows of supercritical carbon dioxide and water. *The Journal of Supercritical Fluids*, *107*, 649-656.

[335] Kim, M., Sell, A., & Sinton, D. (2013). Aquifer-on-a-Chip: understanding pore-scale salt precipitation dynamics during CO_2 sequestration. *Lab on a Chip*, *13*(13), 2508-2518.

[336] Kazemifar, F., Blois, G., Kyritsis, D. C., & Christensen, K. T. (2015). A methodology for velocity field measurement in multiphase high-pressure flow of CO_2 and water in micromodels. *Water Resources Research*, *51*(4), 3017-3029.

[337] Lide, D. R. (2005). *CRC Handbook of Chemistry and Physics*, CRC Press.

[338] Hebach, A., Oberhof, A., Dahmen, N., Kögel, A., Ederer, H., & Dinjus, E. (2002). Interfacial tension at elevated pressures measurements and correlations in the water + carbon dioxide system. *Journal of Chemical & Engineering Data*, *47*(6), 1540-1546.

[339] Georgiadis, A., Maitland, G., Trusler, J. M., & Bismarck, A. (2010). Interfacial tension measurements of the (H_2O+ CO_2) system at elevated pressures and temperatures. *Journal of Chemical & Engineering Data*, *55*(10), 4168-4175.

[340] Zagnoni, M., Anderson, J., & Cooper, J. M. (2010). Hysteresis in multiphase microfluidics at a T-Junction. *Langmuir*, *26*(12), 9416-9422.

[341] Housecroft, C. E., & Sharpe, A. G. (2005). *Inorganic Chemistry*, Prentice Hall.

[342] Johnson, K. S. (1982). Carbon dioxide hydration and dehydration kinetics in seawater. *Limnol. Oceanogr*, *27*(5), 849-855.

[343] Schulz, K. G., Riebesell, U., Rost, B., Thoms, S., & Zeebe, R. E. (2006). Determination of the rate constants for the carbon dioxide to bicarbonate inter-conversion in pH-buffered seawater systems. *Marine chemistry*, *100*(1), 53-65.

[344] Greenwood, N. N., & Earnshaw, A. (1997). *Chemistry of the Elements*, Butterworth-Heinemann.

[345] Bandura, A. V., & Lvov, S. N. (2006). The ionization constant of water over wide ranges of temperature and density. *Journal of physical and chemical reference data*, *35*(1), 15-30.

[346] Einstein, A. (1905). The motion of elements suspended in static liquids as claimed in the molecular kinetic theory of heat. *Ann Phys*, *17*(8), 549-560.

[347] Li, J. R., Ma, Y., McCarthy, M. C., Sculley, J., Yu, J., Jeong, H. K., ... & Zhou, H. C. (2011). Carbon dioxide capture-related gas adsorption and separation in metal-organic frameworks. *Coordination Chemistry Reviews*, *255*(15), 1791-1823.

[348] Pruess, K., & Zhang, K. (2008). *Numerical modeling studies of the dissolution-diffusion-convection process during CO_2 storage in saline aquifers*. Lawrence Berkeley National Laboratory.

[349] Carslaw, H. S., & Jaeger, J. C. (1959). *Conduction of Heat in Solids*. Oxford University Press.

[350] Perez, N. (2004). *Electrochemistry and Corrosion Science*. Kluwer Academic Publishers.

[351] Perry, R. H., & Green, D. W. (2008). *Perry's chemical engineers' handbook*, McGraw-Hill, New York, US.

[352] Visscher, F., Van der Schaaf, J., Nijhuis, T. A., & Schouten, J. C. (2013). Rotating reactors–a review. *Chemical Engineering Research and Design*, *91*(10), 1923-1940.

[353] Klaewkla, R., Arend, M., & Hoelderich, W. F. (2011). *A review of mass transfer controlling the reaction rate in heterogeneous catalytic systems* (Volume 5). INTECH Open Access Publisher.

[354] Löffler, D. G., & Schmidt, L. D. (1977). Influence of external mass transfer on catalytic reaction rates on metals. *Industrial & Engineering Chemistry Fundamentals*, *16*(3), 362-366.

[355] Angeli, P., & Hewitt, G. F. (2000). Drop size distributions in horizontal oil-water dispersed flows. *Chemical Engineering Science*, *55*(16), 3133-3143.

[356] Simmons, M. J. H., & Azzopardi, B. J. (2001). Drop size distributions in dispersed liquid–liquid pipe flow. *International journal of multiphase flow*, *27*(5), 843-859.

[357] Lovick, J., & Angeli, P. (2004). Droplet size and velocity profiles in liquid–liquid horizontal flows. *Chemical engineering science*, *59*(15), 3105-3115.

[358] Suh, Y. K., & Kang, S. (2010). A review on mixing in microfluidics. *Micromachines*, *1*(3), 82-111.

[359] Au, A. K., Huynh, W., Horowitz, L. F., & Folch, A. (2016). 3D-printed microfluidics. *Angewandte Chemie International Edition*.

[360] Demello, A. J. (2006). Control and detection of chemical reactions in microfluidic systems. *Nature*, *442*(7101), 394-402.

[361] McMullen, J. P., & Jensen, K. F. (2011). Rapid determination of reaction kinetics with an automated microfluidic system. *Organic Process Research & Development*, *15*(2), 398-407.

[362] Riechers, B., Maes, F., Akoury, E., Semin, B., Gruner, P., & Baret, J. C. (2016). Surfactant adsorption kinetics in microfluidics. *Proceedings of the National Academy of Sciences*, *113*(41), 11465-11470.

[363] Kashid, M. N., & Kiwi-Minsker, L. (2009). Microstructured reactors for multiphase reactions: state of the art. *Industrial & Engineering Chemistry Research*, *48*(14), 6465-6485.

[364] Van Baten, J. M., & Krishna, R. (2004). CFD simulations of mass transfer from Taylor bubbles rising in circular capillaries. *Chemical Engineering Science*, *59*(12), 2535-2545.

[365] Yue, J., Chen, G., Yuan, Q., Luo, L., & Gonthier, Y. (2007). Hydrodynamics and mass transfer characteristics in gas–liquid flow through a rectangular microchannel. *Chemical Engineering Science*, *62*(7), 2096-2108.

[366] Sobieszuk, P., Pohorecki, R., Cygański, P., & Grzelka, J. (2011). Determination of the interfacial area and mass transfer coefficients in the Taylor gas–liquid flow in a microchannel. *Chemical engineering science*, *66*(23), 6048-6056.

[367] Tan, J., Lu, Y. C., Xu, J. H., & Luo, G. S. (2012). Mass transfer performance of gas–liquid segmented flow in microchannels. *Chemical Engineering Journal*, *181*, 229-235.

[368] Kastens, S., Hosoda, S., Schlüter, M., & Tomiyama, A. (2015). Mass transfer from single taylor bubbles in minichannels. *Chemical Engineering & Technology*, *38*(11), 1925-1932.

[369] Abolhasani, M., Kumacheva, E., & Günther, A. (2015). Peclet number dependence of mass transfer in microscale segmented gas–liquid flow. *Industrial & Engineering Chemistry Research*, *54*(36), 9046-9051.

[370] Burns, J. R., & Ramshaw, C. (2001). The intensification of rapid reactions in multiphase systems using slug flow in capillaries. *Lab on a Chip*, *1*(1), 10-15.

[371] Kashid, M. N., Harshe, Y. M., & Agar, D. W. (2007). Liquid− liquid slug flow in a capillary: an alternative to suspended drop or film contactors. *Industrial & Engineering Chemistry Research*, *46*(25), 8420-8430.

[372] Raimondi, N. D. M., Prat, L., Gourdon, C., & Tasselli, J. (2014). Experiments of mass transfer with liquid–liquid slug flow in square microchannels. *Chemical Engineering Science*, *105*, 169-178.

[373] N. Kashid, M., Renken, A., & Kiwi-Minsker, L. (2011). Influence of flow regime on mass transfer in different types of microchannels. *Industrial & Engineering Chemistry Research*, *50*(11), 6906-6914.

[374] Nunes, J. K., Tsai, S. S. H., Wan, J., & Stone, H. A. (2013). Dripping and jetting in microfluidic multiphase flows applied to particle and fibre synthesis. *Journal of physics D: Applied physics*, *46*(11), 114002.

[375] Ito, Y., & Komori, S. (2008). Mass Transfer Across Gas–Liquid Interface in a Capillary Tube. *Journal of chemical engineering of Japan*, *41*(10), 947-952.

[376] Bercic, G., & Pintar, A. (1997). The role of gas bubbles and liquid slug lengths on mass transport in the Taylor flow through capillaries. *Chemical Engineering Science*, *52*(21-22), 3709-3719.

[377] Günther, A., Khan, S. A., Thalmann, M., Trachsel, F., & Jensen, K. F. (2004). Transport and reaction in microscale segmented gas–liquid flow. *Lab on a Chip*, *4*(4), 278-286.

[378] Dore, V., Tsaoulidis, D., & Angeli, P. (2012). Mixing patterns in water plugs during water/ionic liquid segmented flow in microchannels. *Chemical engineering science*, *80*, 334-341.

[379] http://www.numericana.com/answer/ellipsoid.htm. Accessed on November 11, 2016.

[380] Martynov, S., Brown, S., & Mahgerefteh, H. (2013). An extended Peng-Robinson equation of state for carbon dioxide solid-vapor equilibrium. *Greenhouse Gases: Science and Technology*, *3*(2), 136-147.

[381] http://webbook.nist.gov/chemistry/fluid/, accessed on December 21, 2016.

[382] http://scifun.chem.wisc.edu/chemweek/pdf/carbondioxide.pdf

[383] Kobayashi, J., Mori, Y., Okamoto, K., Akiyama, R., Ueno, M., Kitamori, T., & Kobayashi, S. (2004). A microfluidic device for conducting gas-liquid-solid hydrogenation reactions. *Science*, *304*(5675), 1305-1308.

[384] Cansell, F., & Aymonier, C. (2009). Design of functional nanostructured materials using supercritical fluids. *The Journal of Supercritical Fluids*, *47*(3), 508-516.

[385] Marre, S., & Jensen, K. F. (2010). Synthesis of micro and nanostructures in microfluidic systems. *Chemical Society Reviews*, *39*(3), 1183-1202.

[386] Eckert, C. A., Knutson, B. L., & Debenedetti, P. G. (1996). Supercritical fluids as solvents for chemical and materials processing. *Nature*, *383*(6598), 313.

[387] Marr, R., & Gamse, T. (2000). Use of supercritical fluids for different processes including new developments—a review. *Chemical Engineering and Processing: Process Intensification*, *39*(1), 19-28.

[388] Lang, Q., & Wai, C. M. (2001). Supercritical fluid extraction in herbal and natural product studies—a practical review. *Talanta*, *53*(4), 771-782.

[389] Brunner, G. (2010). Applications of supercritical fluids. *Annual Review of Chemical and Biomolecular Engineering*, *1*, 321-342.

[390] Gibbs, R. E., & Van Ness, H. C. (1972). Vapor-liquid equilibria from total-pressure measurements. A new apparatus. *Industrial & Engineering Chemistry Fundamentals*, *11*(3), 410-413.

[391] Puhl, H. (1991). *Solubility of Gases in Liquids*, John Wiley & Sons Ltd., Chichester-New York.

[392] Chai, X. S., & Zhu, J. Y. (1998). Indirect headspace gas chromatographic method for vapor–liquid phase equilibrium study. *Journal of Chromatography A*, *799*(1), 207-214.

[393] Riazi, M. R. (1996). A new method for experimental measurement of diffusion coefficients in reservoir fluids. *Journal of Petroleum Science and Engineering*, *14*(3-4), 235-250.

[394] Jamialahmadi, M., Emadi, M., & Müller-Steinhagen, H. (2006). Diffusion coefficients of methane in liquid hydrocarbons at high pressure and temperature. *Journal of Petroleum Science and Engineering*, *53*(1), 47-60.

[395] Zhang, X., Fulem, M., & Shaw, J. M. (2007). Liquid-phase mutual diffusion coefficients for athabasca bitumen+ pentane mixtures. *Journal of Chemical & Engineering Data*, *52*(3), 691-694.

[396] Zhang, X., & Shaw, J. M. (2007). Liquid-phase mutual diffusion coefficients for heavy oil+ light hydrocarbon mixtures. *Petroleum science and technology*, *25*(6), 773-790.

[397] Whitesides, G. M. (2006). The origins and the future of microfluidics. *Nature*, *442*(7101), 368-373.

[398] Krevor, S., Pini, R., Li, B., & Benson, S. M. (2011). Capillary heterogeneity trapping of CO_2 in a sandstone rock at reservoir conditions. *Geophysical Research Letters*, *38*(15).

[399] Follesø, H.N. (2012). *Fluid Displacements during Multiphase Flow Visualized at the Pore Scale using Micromodels*. M.S. Thesis, University of Bergen, Norway.

[400] Wiebe, R., & Gaddy, V. L. (1940). The solubility of carbon dioxide in water at various temperatures from 12 to 40 and at pressures to 500 atmospheres. Critical phenomena. *Journal of the American Chemical Society*, *62*(4), 815-817.

[401] Erickson, D. (2005). Towards numerical prototyping of labs-on-chip: modeling for integrated microfluidic devices. *Microfluidics and Nanofluidics*, *1*(4), 301-318.

[402] Gupta, R., Fletcher, D. F., & Haynes, B. S. (2009). On the CFD modelling of Taylor flow in microchannels. *Chemical Engineering Science*, *64*(12), 2941-2950.

[403] Wörner, M. (2012). Numerical modeling of multiphase flows in microfluidics and micro process engineering: a review of methods and applications. *Microfluidics and nanofluidics*, *12*(6), 841-886.

[404] Hoang, D. A., van Steijn, V., Portela, L. M., Kreutzer, M. T., & Kleijn, C. R. (2013). Benchmark numerical simulations of segmented two-phase flows in microchannels using the Volume of Fluid method. *Computers & Fluids*, *86*, 28-36.

[405] Fukagata, K., Kasagi, N., Ua-arayaporn, P., & Himeno, T. (2007). Numerical simulation of gas–liquid two-phase flow and convective heat transfer in a micro tube. *International Journal of Heat and Fluid Flow*, *28*(1), 72-82.

[406] He, Q., & Kasagi, N. (2008). Phase-field simulation of small capillary-number two-phase flow in a microtube. *Fluid dynamics research*, *40*(7), 497-509.

[407] Yu, Z., Hemminger, O., & Fan, L. S. (2007). Experiment and lattice Boltzmann simulation of two-phase gas–liquid flows in microchannels. *Chemical Engineering Science*, *62*(24), 7172-7183.

[408] Falconi, C. J., Lehrenfeld, C., Marschall, H., Meyer, C., Abiev, R., Bothe, D., ... & Wörner, M. (2016). Numerical and experimental analysis of local flow phenomena in laminar Taylor flow in a square mini-channel. *Physics of Fluids*, *28*(1), 012109.

[409] Mary, P., Studer, V., & Tabeling, P. (2008). Microfluidic droplet-based liquid− liquid extraction. *Analytical chemistry*, *80*(8), 2680-2687.

[410] Schuster, A., Sefiane, K., & Ponton, J. (2008). Multiphase mass transport in mini/micro-channels microreactor. *chemical engineering research and design*, *86*(5), 527-534.

[411] Raimondi, N. D. M., Prat, L., Gourdon, C., & Cognet, P. (2008). Direct numerical simulations of mass transfer in square microchannels for liquid–liquid slug flow. *Chemical Engineering Science*, *63*(22), 5522-5530.

[412] Shao, N., Gavriilidis, A., & Angeli, P. (2010). Mass transfer during Taylor flow in microchannels with and without chemical reaction. *Chemical Engineering Journal*, *160*(3), 873-881.

[413] Onea, A., Woerner, M., & Cacuci, D. G. (2009). A qualitative computational study of mass transfer in upward bubble train flow through square and rectangular mini-channels. *Chemical Engineering Science*, *64*(7), 1416-1435.

[414] Kececi, S., Wörner, M., Onea, A., & Soyhan, H. S. (2009). Recirculation time and liquid slug mass transfer in co-current upward and downward Taylor flow. *Catalysis Today*, *147*, S125-S131.

[415] Brackbill, J. U., Kothe, D. B., & Zemach, C. (1992). A continuum method for modeling surface tension. *Journal of computational physics*, *100*(2), 335-354.

Appendix A

Connector/Microchip Assembling Tests

This appendix details the assembling tests of the connector and the microchip done in the year 2015. The contents of each test including test durations, assembling conditions, main results, possible reasons and suggestions have been tabulated.

A.1. Test Method
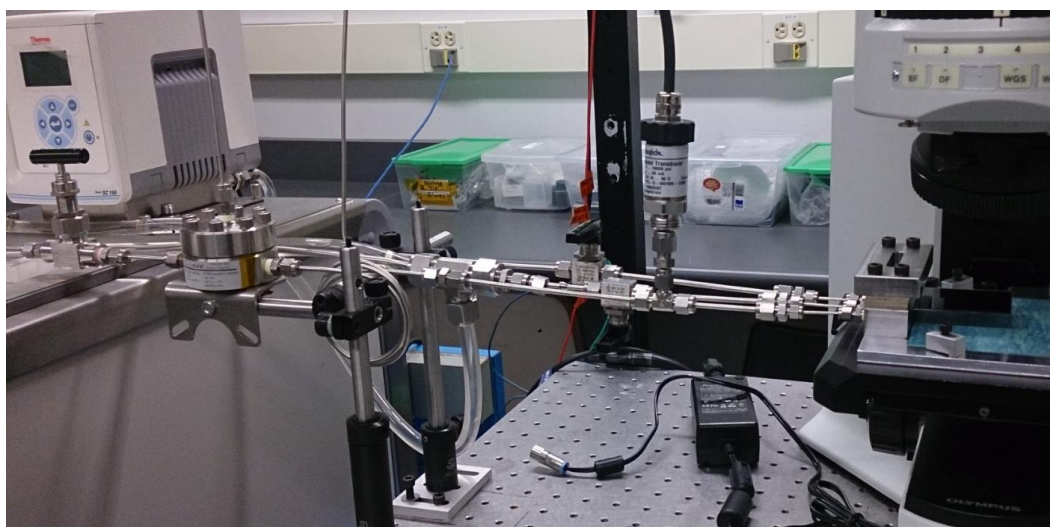
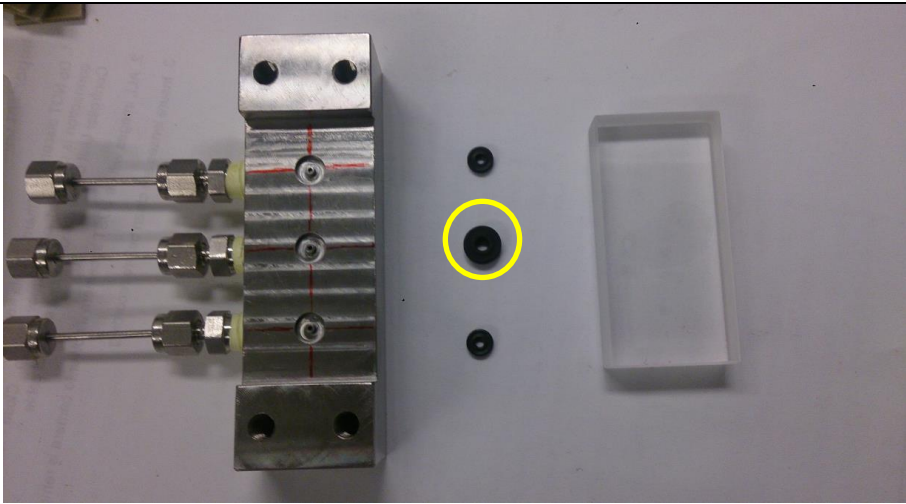**Figure A.1** The setup for testing the assembling quality of the connector/microchip

Figure A.2 A close look at the assembly of connector/microchip.

A.2. Details of the five tests

Table A-1. First time assembling test.

Date & Time & Duration	Starting	Ending	Duration
	April 2, 6:38 pm	April 6, 11:00 am	3 days 16hs 22 mins
Conditions	X-ring AS568-004, 75A; **Channel width-100um microchip;** Glass block (49.8mm $\times$ 25mm $\times$ 10.2mm); Original upper part (80mm $\times$ 25mm $\times$ 7mm); Initial pressure: 59.1 bar, ending pressure: 58.7 bar.		
Results	 Central x-ring expanded; **Microchip cracked at its contact region with the x-ring**; Glass block cracked at its middle; The upper part (stainless steel) of the connector was slightly bended.		
Possible reasons	In the order from a larger possibility to a smaller: The upper part is not robust enough, resulting in an extent of bending; Glass block is not thick enough; X-ring's hardness is not enough; Test time is too long, leading to a significant x-ring expansion.		
Suggestions	Robust upper part; Thick compression block; Hard O-rings; Shorter test time if using a real microchip.		

Table A-2. Second time assembling test.
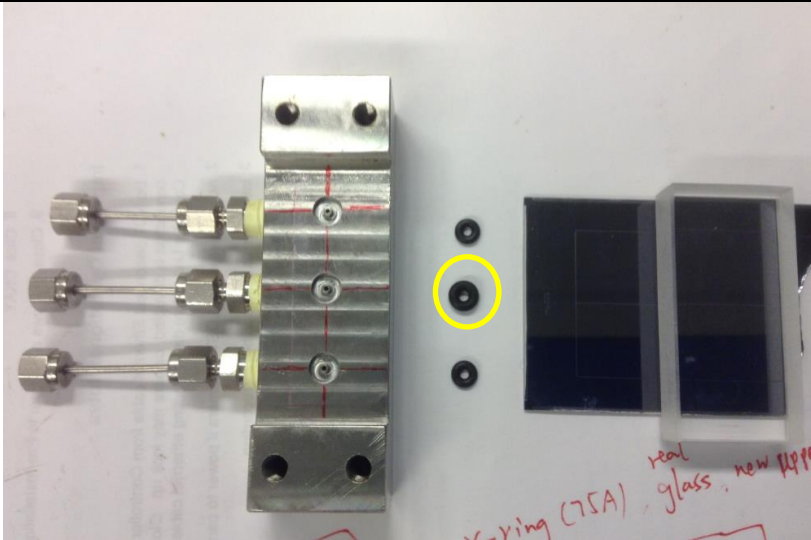
Date & Time & Duration	Starting	Ending	Duration
	April 10, 1:00 pm	April 13, 3:15 pm	3 days 2hs 15 mins
Conditions	X-ring AS568-004, 75A; Glass block; **New upper part (80mm $\times$ 37mm $\times$12mm)**; Initial pressure: 80 bar, ending pressure: ~80 bar; Without microchip.		
Results	 Central x-ring expanded (Original size: D_{out}=5.38mm, D_{in}=2mm, t=1.7mm; after expansion: D_{out}=7.6mm, D_{in}=3mm, t=2.7mm; as measured by a caliper); Glass block remains;		
Possible reasons	In the order from a larger possibility to a smaller: The upper part is robust enough, providing enough supportive compression to the glass block; Test time and CO_2 pressure is too long and too high, leading to a significant x-ring expansion.		
Suggestions	Robust upper part; Hard O-rings; Shorter test time.		
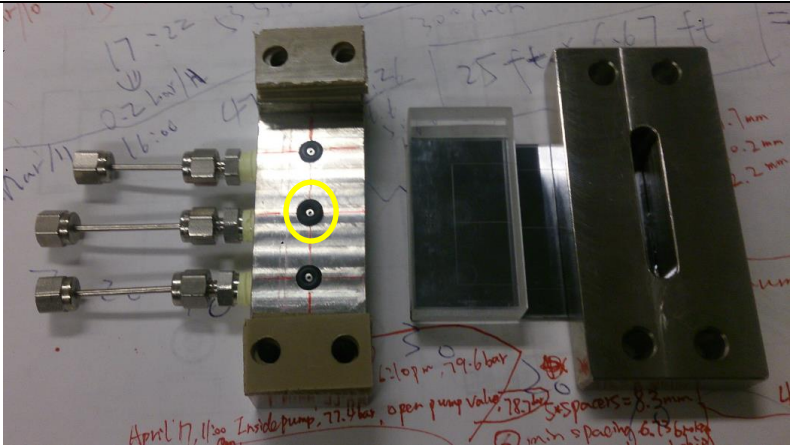
Table A-3. Third time assembling test.

Date & Time & Duration	Starting	Ending	Duration
	April 13, 4:05 pm	April 14, 2:50 pm	22hs 45 mins
Conditions	**O-ring AS568-004, 90A;** **New PMMA plastic glass block (49.3mm × 23.9mm ×12.1mm);** **New upper part;** Initial pressure: 77 bar, ending pressure: ~77 bar		
Results	 Central x-ring hardly expands; **CO_2 reacts with PMMA, resulting in a small bulge.**		
Possible reasons	In the order from a larger possibility to a smaller: The upper part is robust enough, providing enough supportive compression to the plastic glass block; The compression results in a tight-enough sealing and a limited space for o-ring expansion. CO_2 tends to react with PMMA naturally, particularly under extreme high pressures.		
Suggestions	Robust upper part; Thick compression block; Hard O-rings; Never contact PMMA with CO_2.		
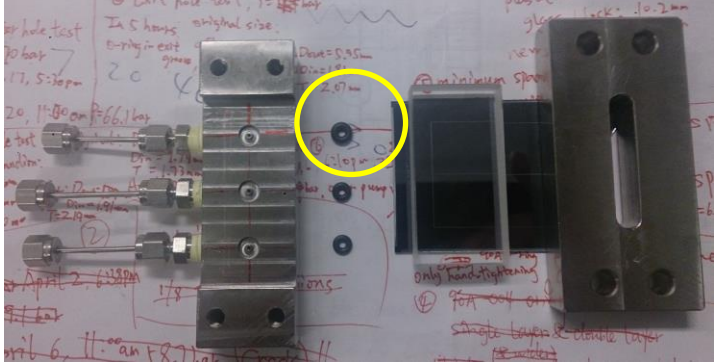
Table A-4. Fourth time assembling tests: hand tightening attempts and toward all three holes.
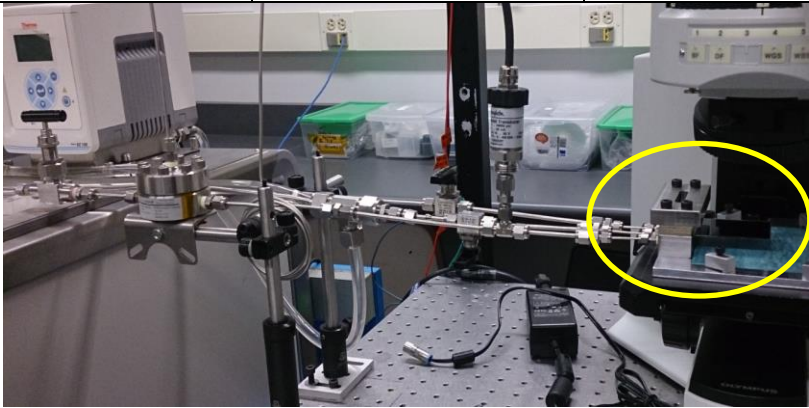
Date & Time & Duration	Starting	Ending	Duration
	April 14, 4:00 pm	April 15, 6:45 pm	1 day 2hs 45 mins
Conditions	O-ring AS568-004, 90A; Glass block; New upper part; **Hand-tightened the compression screws;** **A piece of a broken microchip;** Initial pressure: 79.5 bar, ending pressure: 75.6 bar		
Results	 Central O-ring expands (after expansion: D_{out}=6.1mm, D_{in}=2.14mm, T=2.1mm，as measured by a caliper); Hand-tightening maybe good enough for leakage free.		
Possible reasons	In the order from a larger possibility to a smaller: The upper part is robust enough, providing enough supportive compression to the glass block; The deformation of the o-ring resulted from hand tightening works well in terms of a leakage free sealing for a pressure up to 80bar.		

Date & Time & Duration	Starting	Ending	Duration
	April 16, 6:10 pm	April 17, 11:00 am	17hs 10 mins
Conditions	O-ring AS568-004, 90A; Glass block; New upper part; Hand tightened the compression screws; A piece of a broken microchip; Initial pressure: 80 bar, ending pressure: 80 bar		
Results	Central O-ring expands (Original size: D_{out}=5.34mm, D_{in}=1.79mm, T=1.73mm; after expansion: D_{out}=5.99mm, D_{in}=1.91mm, T=2.19mm; as measured by a caliper); Hand tightening good enough for leakage free.		
Possible reasons	In the order from a larger possibility to a smaller: The upper part is robust enough, providing enough supportive compression to the glass block; The deformation of the O-ring resulted from hand tightening works well in terms of a leakage free sealing for a pressure up to 80bar.		
Suggestions	1. Robust upper part; 2. Whether 75A or 90A, they both can suffer from CO_2 diffusion into themselves under a long time and a high pressure. 3. A uniform hand-tightening of the compression screws is good enough for sealing. 4. Always release CO_2 off from inside device once the test or experiment finishes; 5. For filling and releasing liquids from the system, always do slowly and gently.		

Date & Time & Duration	Starting	Ending	Duration
	April 17, 12:00 pm	April 17, 5:00 pm	5hs

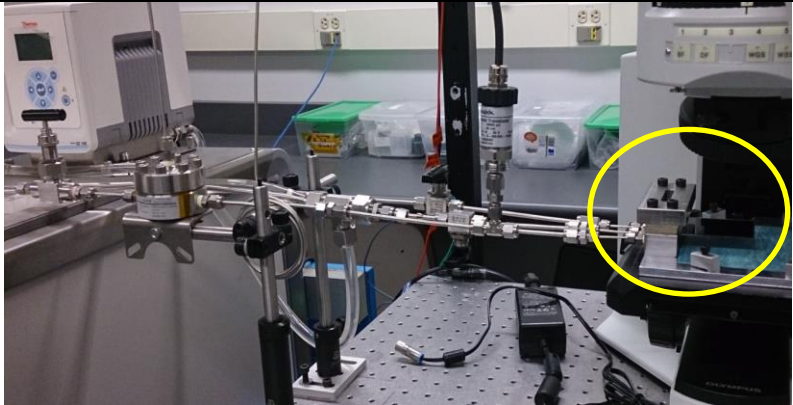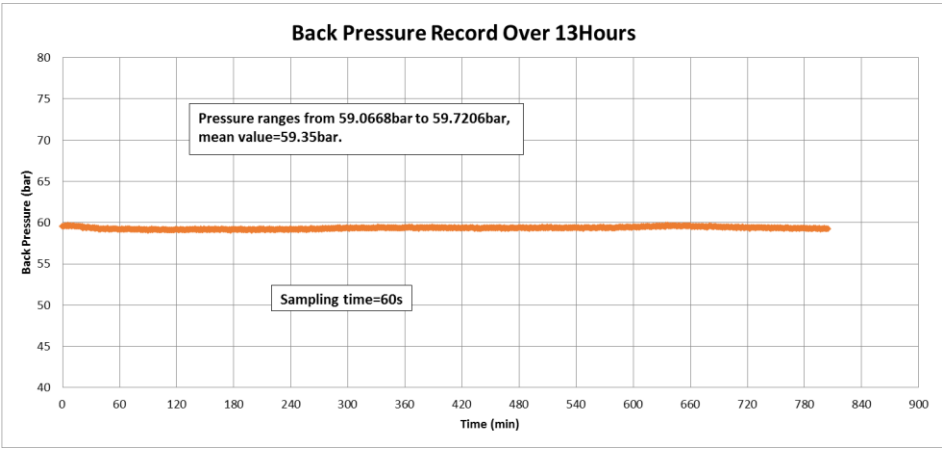|	
Conditions	O-ring AS568-004, 90A; Glass block; New upper part; Hand tightened the compression screws; A piece of a broken microchip; Initial pressure: 77.2 bar, ending pressure: 77.2 bar
Results	 Exit O-ring expands (Original size: D_{out}=5.34mm, D_{in}=1.79mm, T=1.73mm; after expansion: D_{out}=5.95mm, D_{in}=1.81mm, T=2.07mm; as measured by a caliper); Hand tightening good enough for leakage free.
Possible reasons	In the order from a larger possibility to a smaller: The upper part is robust enough, providing enough supportive compression to the glass block; The deformation of the O-ring resulted from hand tightening works well in terms of a leakage free sealing for a pressure up to 80bar.
Suggestions	1. Robust upper part; 2. Whether 75A or 90A, they both can suffer from CO_2 diffusion into themselves under a long time and a high pressure. 3. A uniform hand-tightening of the compression screws is good enough for sealing. 4. Always release CO_2 off from inside device once the test or experiment finishes; 5. For filling and releasing liquids from the system, always do slowly and gently.

Date & Time & Duration	Starting	Ending	Duration
	April 17, 5:30 pm	April 20, 11:00 am	2days 17hs 30mins
Conditions	O-ring AS568-004, 90A; Glass block; New upper part; Hand tightened the compression screws; A piece of a broken microchip; Initial pressure: 70 bar, ending pressure: 66.3bar		
Results	 Water-hole-side O-ring expands (Original size: D_{out}=5.34mm, D_{in}=1.79mm, T=1.73mm; after expansion: D_{out}=6.35mm, D_{in}=2.12mm, T=2.20mm; as measured by a caliper); Hand tightening good enough for leakage free.		
Possible reasons	In the order from a larger possibility to a smaller: The upper part is robust enough, providing enough supportive compression to the glass block; The deformation of the O-ring resulted from hand tightening works well in terms of a leakage free sealing.		
Suggestions	1. Robust upper part; 2. Whether 75A or 90A, they both can suffer from CO_2 diffusion into themselves under a long time and a high pressure. 3. A uniform hand-tightening of the compression screws is good enough for sealing. 4. Always release CO_2 off from inside device once the test or experiment finishes; 5. For filling and releasing liquids from the system, always do slowly and gently.		

Table A-5. Fifth time assembling tests using a microchip.

Date & Time & Duration	Starting	Ending	Duration
	April 20, 4:40 pm	April 21, 12:30 pm	19hs 50mins
Conditions	 O-ring AS568-004, 90A; Glass block; New upper part; Hand tightened the compression screws; **w-150um microchip**; Initial pressure: 60.1 bar, ending pressure: 59.7 bar		
Results	Speculation: O-rings should have expanded. Hand tightening good enough for leakage free.		
Possible reasons	In the order from a larger possibility to a smaller: The upper part is robust enough, providing enough supportive compression to the glass block; The deformation of the O-ring resulted from hand tightening works well in terms of a leakage free sealing.		
Suggestions	1. Robust upper part; 2. Whether 75A or 90A, they both can suffer from CO_2 diffusion into themselves under a long time and a high pressure. 3. A uniform hand-tightening of the compression screws is good enough for sealing. 4. Always release CO_2 off from inside device once the test or experiment finishes; 5. For filling and releasing liquids from the system, always do slowly and gently.		

Date & Time & Duration	Starting	Ending	Duration
	April 21, 09:00 pm	April 22, 10:25 am	13hs 25mins
Conditions	O-ring AS568-004, 90A; Glass block; New upper part; Hand tightened the compression screws; **w-150um microchip**;		
Results	Back pressure data recording via LabVIEW		
Suggestions	1. Robust upper part; 2. Whether 75A or 90A, they both can suffer from CO_2 diffusion into themselves under a long time and a high pressure. 3. A uniform hand-tightening of the compression screws is good enough for sealing. 4. Always release CO_2 off from inside device once the test or experiment finishes; 5. For filling and releasing liquids from the system, always do slowly and gently.		

Appendix B

Matlab Codes for Drop Measurements

This appendix details the Matlab (R2014a, MathWorks, Inc.) codes which have been applied to identify the flowing liquid CO_2 drops and $scCO_2$ drops in the recorded videos from using a microscope (BX51, Olympus) and a high speed camera (V210, Phantom). Parameters including drop length, drop width, drop spacing (or say, water slug length) and drop speeds can be extracted and stored based on the following Matlab codes. My lab colleague, Mr. Yuk Hei David, Wong during the year 2014 to 2016, is acknowledged here for his assistance in writing the Matlab codes.

```
clear

clc

close all


% IMPORT PARAMETERS

in_path = 'x:\xx\xxx\xxxx\'; % indicate the path for the imported video file

in_file_name = xxxx.tif'; % indicate the imported file name


% EXPORT PARAMETERS

ex_path = 'x:\xx\xxx\xxxx\'; % indicate the path for the exported video file

ex_filename = 'xxxx.avi'; % indicate the exported file name

ex_fps = 10;

ex_quality = 100;


% BACKGROUND SELECTION PARAMETERS

bg_start_frame = x; % from which frame a background selection starts
```

```matlab
bg_interval = x; % at what an interval the background selection proceeds

bg_n = x; % indicate how many frames are used for selecting the background


bg_y_top = y; % from what y-dimensional value the background originates

% bg_x_left = 135;

bg_boxsize = 70;


% DROPPLET IDENTIFICATION PARAMETERS

dp_thresh = 20/255;

dp_inside_pixel = 8000;

dp_morph_radius = 7;


% POST PROCESS

pp_original_fps = xxxx;  % frame per second (fps) of the original video


%% Import TIFF

info = imfinfo([in_path,'\',in_file_name]);

f = 1;

while 1

  try

    I8 = imread([in_path,'\',in_file_name],f);

  catch

    break

  end

  raw(:,:,f) = I8;
```

```matlab
    f = f+1;
end
clear i I8 in_*


%% Select Background
end_frame = bg_start_frame + bg_n*bg_interval;
frames = [bg_start_frame:bg_interval:end_frame];
background =[];
figure;
for f = 1:bg_n;
    subplot(1,bg_n,f)
%     subplot(bg_n,1,f)
    imshow(raw(:,:,frames(f)));
    hold on
    axis manual


    y = bg_y_top + bg_boxsize*(f-1);
%     x = bg_x_left + bg_boxsize*(f-1);
%     box(:,f) = [x,1,bg_boxsize-1,size(raw,1)];
    box(:,f) = [1,y,size(raw,2),bg_boxsize-1];
    rectangle('Position',box(:,f));


    piece = imcrop(raw(:,:,frames(f)),box(:,f));
    background = cat(1,background,piece);
%     background = cat(2,background,piece);
```

```matlab
end

rect = [1,min(box(2,:)),size(raw,2),sum(box(4,:))+bg_n-1];

% rect = [min(box(1,:)),1,sum(box(3,:))+bg_n-1,size(raw,1)];


figure; imshowpair(imcrop(raw(:,:,1),rect),background,'montage')

clear  end_frame frames i piece x y box


pause on

pause

pause off


%% Main Loop

SE = strel('disk',dp_morph_radius);

time_step = 1/pp_original_fps;


figure;

for f = 1:size(raw,3)

    display(f)


    %IMAGE PROCESSING identifying droplet

    tic

    cropped = imcrop(raw(:,:,f),rect); % apply crop

    foreground = imabsdiff(cropped,background); % isolate foreground

    BW = im2bw(foreground,dp_thresh); % convert to binary

    BW2 = imfill(BW,'holes'); % fill intact droplet
```

```matlab
WB = imcomplement(BW2);

WB2 = bwareaopen(WB,dp_inside_pixel); % fill entrance exit droplet

BW2 = imcomplement(WB2);

BW3 = imopen(BW2,SE); % clean edges and noise

timer_improc(f) = toc;




% IMAGE PROCESSING extracting data
tic

B = bwboundaries(BW3); % find boundaries

stat = regionprops(BW3, 'Centroid', 'Area', 'Perimeter','BoundingBox');

frame_data(f).boundaries = B;

frame_data(f).centroids = cat(1,stat.Centroid);

frame_data(f).areas = cat(1,stat.Area);

frame_data(f).perimeters = cat(1,stat.Perimeter);

frame_data(f).boundingbox = cat(1,stat.BoundingBox);

timer_data(f) = toc;



% POST PROCESS spacing --> bounding box limits
tic

bb = frame_data(f).boundingbox;

for j = 1:size(bb,1)

    l(j) = bb(j,1);

    t(j) = bb(j,2);

    r(j) = bb(j,1) + bb(j,3);
```

```matlab
        b(j) = bb(j,2) + bb(j,4);

    end



    % POST PROCESS spacing --> sort from top to bottom / left to right

    if ~isempty(bb)

        [t_sorted,ind] = sort(t);

        b_sorted = b(ind);

        l_sorted = l(ind);

        r_sorted = r(ind);

%       [l_sorted,ind] = sort(l);

%       r_sorted = r(ind);

%       t_sorted = t(ind);

%       b_sorted = b(ind);

        sorted_data(f).time_ms = f*time_step*1000;

        sorted_data(f).left = l_sorted';

        sorted_data(f).top = t_sorted';

        sorted_data(f).right = r_sorted';

        sorted_data(f).bottom = b_sorted';

        sorted_data(f).drop_width = (r_sorted - l_sorted)';

        sorted_data(f).drop_length = (b_sorted - t_sorted)';

    end



    % POST PROCESS spacing --> plot spacing in blue

    for j = 1:size(bb,1)-1

        spacing(j) = t_sorted(j+1) - b_sorted(j);
```

238

```matlab
        spaceline_x(j,1) = (r_sorted(j)+l_sorted(j))/2;

        spaceline_x(j,2) = (r_sorted(j+1)+l_sorted(j+1))/2;

        spaceline_y(j,1) = b_sorted(j);

        spaceline_y(j,2) = t_sorted(j+1);

%       spacing(j) = l_sorted(j+1) - r_sorted(j);

%       spaceline_y(j,1) = (b_sorted(j)+t_sorted(j))/2;

%       spaceline_y(j,2) = (b_sorted(j+1)+t_sorted(j+1))/2;

%       spaceline_x(j,1) = r_sorted(j);

%       spaceline_x(j,2) = l_sorted(j+1);

    end

    try

        sorted_data(f).spacing = spacing';

        sorted_data(f).spaceline_x = spaceline_x;

        sorted_data(f).spaceline_y = spaceline_y;

    catch

        sorted_data(f).spacing = NaN;

        sorted_data(f).spaceline_x = NaN;

        sorted_data(f).spaceline_y = NaN;

    end


    % POST PROCESS size --> pick only whole droplets, plot size in green

%    for j = 1:size(sorted_data(f).drop_width)

%       if sorted_data(f).left(j)<1 || ...

%               sorted_data(f).right(j)> rect(3) + 1

%           sorted_data(f).size(j) = NaN;
```

239

```matlab
%         sorted_data(f).sizeline_x(j,1) = NaN;

%         sorted_data(f).sizeline_x(j,2) = NaN;

%         sorted_data(f).sizeline_y(j,1) = NaN;

%         sorted_data(f).sizeline_y(j,2) = NaN;

%     else

%         sorted_data(f).size(j) = sorted_data(f).drop_width(j);

%         sorted_data(f).sizeline_x(j,1) = l_sorted(j);

%         sorted_data(f).sizeline_x(j,2) = r_sorted(j);

%         sorted_data(f).sizeline_y(j,1) = (b_sorted(j) + t_sorted(j))/2;

%         sorted_data(f).sizeline_y(j,2) = (b_sorted(j) + t_sorted(j))/2;

%     end

%   end

    for j = 1:size(sorted_data(f).drop_length)

      if sorted_data(f).top(j)<1 || ...

            sorted_data(f).bottom(j)> rect(4) + 1

        sorted_data(f).size(j) = NaN;

        sorted_data(f).sizeline_x(j,1) = NaN;

        sorted_data(f).sizeline_x(j,2) = NaN;

        sorted_data(f).sizeline_y(j,1) = NaN;

        sorted_data(f).sizeline_y(j,2) = NaN;

      else

        sorted_data(f).size(j) = sorted_data(f).drop_length(j);

        sorted_data(f).sizeline_x(j,1) = (l_sorted(j) + r_sorted(j))/2;

        sorted_data(f).sizeline_x(j,2) = (l_sorted(j) + r_sorted(j))/2;

        sorted_data(f).sizeline_y(j,1) = t_sorted(j);
```
240

```matlab
            sorted_data(f).sizeline_y(j,2) = b_sorted(j);

    end

end


% POST PROCESS velocity --> construct Separation matrix

for j = 1:size(frame_data(f).centroids,1)

    curr_centroid = frame_data(f).centroids(j,:);

    if f > 1

        for i = 1:size(frame_data(f-1).centroids,1)

            last_centroid = frame_data(f-1).centroids(i,:);

            separation(i,j) = sqrt((last_centroid(1)-curr_centroid(1))^2 +...

                (last_centroid(2)-curr_centroid(2))^2);

        end

    end

end


% POST PROCESS velocity --> construct droplet_data base on S matrix

if exist('separation') % both curr_centroids and last_centroids exist

    [min1 cgli] = min(separation,[],1); %current_guess_last_index

    [min2 lgci] = min(separation,[],2); %last_guess_current_index

    for i = 1:length(lgci) % i is last index

        if cgli(lgci(i)) == i % those are non exiting droplets

            num = find(drop_ind(:,f-1)==i);

            drop_ind(num,f) = lgci(i);

            drop_x(num,f) = frame_data(f).centroids(lgci(i),1);
```
241

```matlab
            drop_y(num,f) = frame_data(f).centroids(lgci(i),2);

            clear num

        end

    end

    for j = 1:length(cgli) % j is current index

        if lgci(cgli(j)) ~= j % those are extrance droplets

            drop_ind(size(drop_ind,1)+1,f) = j;

            drop_x(size(drop_x,1)+1,f) = frame_data(f).centroids(j,1);

            drop_y(size(drop_y,1)+1,f) = frame_data(f).centroids(j,2);

        end

    end

elseif exist('curr_centroid') % going from 0 to 1 drop

    for j = 1:size(frame_data(f).centroids,1) % j is current index

        drop_ind(j,f) = j;

        drop_x(j,f) = frame_data(f).centroids(j,1);

        drop_y(j,f) = frame_data(f).centroids(j,2);

    end

end


% Post PROCESS velocity --> calculate velocity of whole droplets

if f > 1

    try % incase no droplet

    for j = 1:size(drop_ind(:,f))

        % reject entrance droplets so bb works

        if drop_ind(j,f)>0 && drop_ind(j,f-1) > 0
```

242

```matlab
bb = frame_data(f).boundingbox(drop_ind(j,f),:);

l = bb(1);

t = bb(2);

r = bb(1) + bb(3);

b = bb(2) + bb(4);

if l>1 && r<rect(3)+1 && t>1 && b<rect(4)+1

    is_whole_current_frame = 1;

else

    is_whole_current_frame = 0;

end

bb = frame_data(f-1).boundingbox(drop_ind(j,f-1),:);

l = bb(1);

t = bb(2);

r = bb(1) + bb(3);

b = bb(2) + bb(4);

if l>1 && r<rect(3)+1 && t>1 && b<rect(4)+1

    is_whole_last_frame = 1;

else

    is_whole_last_frame = 0;

end

if is_whole_current_frame && is_whole_last_frame

    drop_u_ppms(j,f) = ...

        (drop_x(j,f)-drop_x(j,f-1))/time_step/1000;

    drop_v_ppms(j,f) = ...

        (drop_y(j,f)-drop_y(j,f-1))/time_step/1000;
```

```matlab
                frame_data(f).is_whole(drop_ind(j,f),:) = 1;

                frame_data(f).u_ppms(drop_ind(j,f),:) = drop_u_ppms(j,f);

                frame_data(f).v_ppms(drop_ind(j,f),:) = drop_v_ppms(j,f);

            else

                frame_data(f).is_whole(drop_ind(j,f),:) = 0;

                frame_data(f).u_ppms(drop_ind(j,f),:) = NaN;

                frame_data(f).v_ppms(drop_ind(j,f),:) = NaN;

            end

        % write data to entrance droplets

        elseif drop_ind(j,f)>0

                frame_data(f).is_whole(drop_ind(j,f),:) = 0;

                frame_data(f).u_ppms(drop_ind(j,f),:) = NaN;

                frame_data(f).v_ppms(drop_ind(j,f),:) = NaN;

        end

    end

    end

end

timer_post(f) = toc;


% Plot

tic

cla

imshow(cropped);

hold on

axis manual
```

```matlab
        xl = sorted_data(f).spaceline_x;

        yl = sorted_data(f).spaceline_y;

        xs = sorted_data(f).sizeline_x;

        ys = sorted_data(f).sizeline_y;

        for j = 1:size(xl,1)

            plot(xl(j,:),yl(j,:),'b')

        end

        for j = 1:size(xs,1)

            plot(xs(j,:),ys(j,:),'g')

        end

        B = frame_data(f).boundaries;

        try

            A = cell2mat(B);

            plot(A(:,2),A(:,1),'r.','markersize',5);

        end

        mov(f) = getframe;

        timer_plot = toc;


        clear I BW BW2 BW3 WB WB2 foreground stat cropped

        clear bb l t r b b_sorted l_sorted r_sorted t_sorted ind

        clear spacing spaceline_x spaceline_y sizeline_x sizeline_y

        clear curr_centroid last_centroid separation min1 min2 cgli lgci

        clear xl yl xs ys A B

    end
```

```matlab
display('average image processing time')

display(mean(timer_improc));

display('average data extract time')

display(mean(timer_data));

display('average post process time')

display(mean(timer_post));

display('average_plotting time')

display(mean(timer_plot));

% display('average ?????? per frame per million pixel')

% display(mean(??????)/rect(3)*rect(4))


clear bg_* dp_* pp_* SE  time_step i j f timer_*

clear rect background


figure;

v = drop_v_ppms;

v(v == 0) = NaN;

v_avg = nanmean(v,1);

plot([sorted_data.time_ms],v_avg)

xlabel('time [millisecond]')

ylabel('vertical velocity [pixel per millisecond]')

title('Average Speed of Whole Droplets in each Frame')

clear v*


%% export movie
```

```matlab
export = VideoWriter([ex_path, '\', ex_filename])%,'Uncompressed AVI');

export.FrameRate = ex_fps;

export.Quality = ex_quality;

open(export);

writeVideo(export,mov);

close(export);

clear export ex_*
```

Appendix C

Structural Annotations of the Bottom Connector Part